
Diffuse Boundary Modelling in the Digital Waveguide Mesh

Simon Benedict Shelley

Submitted in partial fulfilment of the requirements
for the degree of Doctor of Philosophy

THE UNIVERSITY *of York*

Department of Electronics
November, 2007

Abstract

Diffuse reflection has a significant effect on an acoustic environment, and is an important consideration in any acoustic modelling application. A study of diffuse reflection and diffuser types is presented, and current methods to measure and analyse the scattering effects of acoustic boundaries are reviewed. An overview of different approaches to room acoustic simulation is also presented, including existing techniques for modelling diffuse reflection.

The Digital Waveguide Mesh is a wave-based time-domain approach to the simulation of sound wave propagation in an acoustic system, in which the problem domain is considered using spatial sampling points arranged in a regular grid. The focus of this thesis is on the simulation of diffuse reflection in a Digital Waveguide Mesh. Diffusion models, based on both physical mapping and statistical approaches, are presented and compared. The scattering characteristics of the models are analysed in detail using a number of different techniques, and are quantified in the form of frequency dependent diffusion coefficients. A detailed analysis of diffusion models in the 2-D Digital Waveguide Mesh is presented. Models are also implemented and analysed in some detail in the 3-D Digital Waveguide Mesh.

Contents

Acknowledgements	18
Declaration	19
1 Introduction	20
1.1 Boundary Diffusion	21
1.2 Acoustical Modelling	23
1.3 Motivation	24
1.4 Thesis Outline	26
1.5 Contributions of Research	27
2 Acoustic theory	29
2.1 Introduction	29
2.2 Wave Motion and the Wave Equation	30
2.2.1 Simple Harmonic Oscillation	30
2.2.2 The Equation of Wave Motion	32
2.3 Sound Pressure and Particle Velocity	33
2.4 The Speed of Sound	34
2.5 Acoustic Impedance	35
2.6 Sound intensity	36
2.7 Air Absorption	36
2.8 Plane Waves	37
2.9 Boundary Interaction	38
2.10 Sound Wave Interference	40
2.11 Diffraction of Sound	41
2.12 Standing Waves and Room Modes	42

2.13	The Room Impulse Response	45
3	Diffuse Reflection	47
3.1	Acoustic Diffusers	47
3.1.1	Random Rough Diffuser	48
3.1.2	Geometric Diffusers	48
3.2	Measurement of Diffuse Reflections	51
3.2.1	The Diffusion Coefficient	51
3.2.2	The Scattering Coefficient	58
3.2.3	Comparison of Diffusion and Scattering Coefficients	61
3.2.4	The Correlation Scattering Coefficient	64
4	Acoustical Modelling	65
4.1	Acoustic Scale Modelling	65
4.2	Ray-based Computer Modelling	67
4.2.1	Image Source Method	68
4.2.2	Ray-Tracing	70
4.2.3	Approximate Beam-Tracing	73
4.2.4	The Room Acoustic Rendering Equation	76
4.2.5	Hybrid Models	76
4.2.6	Discussion	77
4.3	Wave-based Computer Modelling	79
4.3.1	Element Methods	79
4.3.2	Finite Difference Time Domain Methods	83
4.4	The Digital Waveguide Mesh	86
4.4.1	The One Dimensional Digital Waveguide	86
4.4.2	The Scattering Junction	87
4.4.3	Comparison of K-Modelling and W-Modelling and Mixed Modelling	90
4.4.4	Mesh Topology	92
4.4.5	Sampling Rate	94
4.4.6	Dispersion	96
4.4.7	Boundary Termination	98
4.4.8	Diffuse Reflection in Digital Waveguide Mesh	103

5	Diffuse Reflection in the Digital Waveguide Mesh	105
5.1	Introduction	105
5.2	Physical Mapping	106
5.2.1	Quadratic Residue Diffuser	106
5.2.2	Large Scale Boundary Irregularities	109
5.3	Statistical Diffusion Modelling	109
5.3.1	Random Roughness	109
5.3.2	A Diffusion Model Using Circulant Matrices	110
5.3.3	The Diffusing Layer Model	117
6	Characterisation of Diffuse Boundary Models in the DWM	121
6.1	Introduction	121
6.2	Mesh Excitation	122
6.3	Diffusion Coefficient Measurement in the 2-D DWM	124
6.3.1	Test Set-up and Geometry	124
6.4	Results and Discussion	125
6.4.1	Plane Boundary	125
6.4.2	Simple Geometric Diffusing Objects	131
6.4.3	Quadratic Residue Diffuser	138
6.4.4	The Diffusing Boundary Diffusion Model	146
6.4.5	The Diffusing Layer Model	154
6.4.6	Mesh Orientation	172
6.5	Modal Analysis of Diffusion Models in a 2-D Lossless DWM	173
6.5.1	Discussion	174
6.6	Early Reflection Testing in a 2-D DWM	176
6.7	Effect of Diffusion Models on Boundary Absorption	178
6.8	An Investigation of Diffusion Based on Room Diffuseness	182
6.8.1	The 2-D Triangular Mesh	182
6.8.2	The 3-D Rectilinear Mesh	185
6.9	Computational Analysis of the Diffusing Layer Model in the 2-D DWM	188
6.10	Auditory Demonstration	189
6.10.1	Test Description	189
6.10.2	Discussion	191

7	Summary and Conclusions	193
7.1	Diffusion Coefficient Measurements	193
7.2	Further Investigation	197
7.2.1	Modal Analysis	197
7.2.2	Early Reflection Testing	197
7.2.3	Effect on Boundary Absorption	197
7.3	An Alternative Investigation into Boundary Diffusion	198
7.4	Audio Demonstration	198
7.5	Conclusion	198
7.6	Future Work	199
A	Mathematical Derivation	202
A.1	The d’Alambert Solution of the 1-D Wave Equation	202
B	Software Implementation	204
B.1	Class Description	205
B.1.1	Main Class	205
B.1.2	JunctionControl Class	205
B.1.3	Junction Class	207
B.2	Software Testing	207
C	Accompanying CD-ROM	210
C.1	Directory Structure	210
	References	213

List of Figures

2.1	Diagram of particles in a medium with alternating areas of compressions and rarefactions.	29
2.2	A simple harmonic oscillator (a) in equilibrium and (b) with displacement ξ	30
2.3	A one dimensional travelling wave $\xi(x, t)$ in simple harmonic oscillation, represented at (a) a fixed point in space x and (b) a fixed point in time t	31
2.4	Spherical propagation of sound from a source.	37
2.5	The interaction of sound with an acoustic boundary.	38
2.6	Examples of (a) constructive and (b) destructive wave interference, showing five snapshots at different points in time as two waves travel in opposite directions.	41
2.7	Illustration of Wave Diffraction (a) at the edge of a solid object, (b) through a gap in an object and (c) around the sides of an object. . . .	42
2.8	Pressure components of standing waves between two parallel reflective boundaries for $n = 1, 2$ and 3	43
2.9	A simple cuboid shaped room showing examples of cyclic reflection paths that result in (a) a tangential and (b) an oblique room mode. . .	44
3.1	Illustration of (a) specular reflections and (b) diffuse reflections. . . .	47
3.2	Cross section of three simple geometric diffuser designs.	49
3.3	Cross section of a Quadratic Residue Schroeder diffuser with sequence length of 13.	49

3.4	Diagram showing possible test geometry for obtaining (a) semi-circular 2-D and (b) hemispherical 3-D polar responses, leading to diffusion coefficient measurement.	52
3.5	The specular zone of reflection.	54
3.6	Diagram showing angles of azimuth ϕ and elevation ω of a receiver with respect to the test surface.	56
3.7	Diagram showing the test geometry used for measuring the scattering coefficient.	59
3.8	Hypothetical polar responses of a reflective surface that (a) yields a high scattering coefficient but a low diffusion coefficient and (b) yields both a high scattering coefficient and a high diffusion coefficient.	62
4.1	Graph showing calculated air absorption of sound in dB attenuation per metre in relationship to frequency.	66
4.2	A first order specular reflection with its corresponding image source.	68
4.3	Diagram showing reflections of sound in a room and the corresponding image sources.	68
4.4	Flow chart describing a technique for implementing diffuse reflection in the ray-tracing model.	72
4.5	Illustration of (a) conical and (b) pyramidal diverging beams radiating from source.	74
4.6	Simplified diagram showing the hybrid ray-based approach used in ODEON.	77
4.7	A mechanical system with a single degree of freedom	79
4.8	Discrete time implementation of lossless 1-D wave propagation, observed at the spatial sampling points $x = 0$ and $x = 3X$	87
4.9	A general scattering junction J with N connected waveguides for $i = 1, 2, \dots, N$	88
4.10	A digital signal functional block diagram representation of a W -model scattering junction J_W with N connected waveguides for $i = 1, 2, \dots, N$	89
4.11	A digital signal functional block diagram representation of a K -model scattering junction K with N connected waveguides for $i = 1, 2, \dots, N$	90

4.12	A digital signal functional block diagram representation of a W-model scattering junction J interfaced with a K-model scattering junction K using a KW-pipe	91
4.13	A digital signal functional block diagram representation of a KW-junction KW with two K-model ports and two W-model ports	92
4.14	(a) A 4-port 2-D rectilinear mesh structure and (b) a 6-port 2-D triangular mesh structure.	93
4.15	(a) 6-port 3-D rectilinear, (b) 4-port 3-D tetrahedral, (c) 12-port 3-D dodecahedral (CCP) and (d) 8-port 3-D octahedral mesh structures	93
4.16	Diagram showing a junction in a 2-D rectilinear DWM with its 8 neighbours.	93
4.17	Decomposition of the 2-D rectilinear mesh into sub-grids.	95
4.18	Dispersion factor k_d in the 2-D rectilinear mesh.	96
4.19	Dispersion factor k_d in the 2-D triangular mesh.	97
4.20	Simple termination of a 1-D waveguide string.	98
4.21	Simple termination of a DWM at an N -port boundary junction.	100
4.22	Modelling a smooth, curved boundary using ringguides	102
4.23	Modelling diffuser wells at the boundary of a 2-D Digital Waveguide Mesh	103
5.1	Quadratic residue diffuser implementation in a triangular DWM with well widths (a) $w = x$ and (b) $w = 2 \times x$	107
5.2	Quadratic residue diffuser implementation in a triangular DWM applied to an irregular boundary.	108
5.3	3-D diagram of a simple Schroeder diffuser with cross section.	108
5.4	Section of a DWM structure with a randomly generated boundary mapping.	110
5.5	(a) A 3-port boundary junction and (b) a 6-port junction with connecting waveguides.	112
5.6	Plots of the rotation error for different perimeter junction structures	113
5.7	A section of a DWM showing the <i>diffusing</i> junctions on the mesh boundary.	113
5.8	(a) 2-port, (b) 3-port, (c) 4-port, (d) 5-port and (e) 2-port scattering junctions from a 2-D triangular DWM with connecting waveguides	114

5.9	Incoming signals at a 5-port diffusing junction J (a) before rotation and (b) after rotation. The resulting incoming signals, p'_{ji}^+ are then used in the scattering equations rather than the original signals, p_{ji}^+ .	116
5.10	Probability density function of the uniform distribution used in the diffuse boundary model.	116
5.11	A section of a DWM showing the <i>diffusing</i> junctions in the diffusing layer model.	118
5.12	Incoming signals at a 6-port diffusing junction J (a) before rotation and (b) after rotation. The resulting incoming signals, p'_{ji}^+ are then used in the scattering equations rather than the original signals, p_{ji}^+ .	119
5.13	Rotation of wave direction in a 6-port air-junction in the 3-D rectilinear DWM.	120
6.1	Graphs showing the low-pass filtered impulse used as the excitation signal.	123
6.2	Screen shots showing excitation and wave propagation in a 2-DDWM of triangular topology.	123
6.3	Diagram showing the set-up used for the diffusion testing leading to the measurement of the diffusion coefficient in the 2D DWM.	124
6.4	Spectrograms showing reflection magnitude of a flat plane boundary varying with angle of reflection across the semicircular range of receivers.	127
6.5	Polar responses showing scattering of reflected sound energy from a flat plane boundary.	128
6.6	Graph showing directional diffusion coefficients measured from a flat plane boundary in third octave bands from 1 kHz to 10 kHz.	129
6.7	Graph showing random incidence diffusion coefficients measured from a flat plane boundary in third octave bands from 1 kHz to 10 kHz.	130
6.8	Diagram of a triangular shaped diffusing object	131
6.9	Spectrograms showing reflection magnitude of a triangular object varying with angle of reflection across the semicircular range of receivers.	132

6.10	Polar responses showing scattering of reflected sound energy from a triangular shaped diffuser with a frequency independent prediction from ray-tracing simulation	133
6.11	Graph showing random incidence diffusion coefficients measured from a triangular shaped diffuser in third octave bands from 1 kHz to 10 kHz.	134
6.12	Diagram of a semicircular diffusing object.	134
6.13	Spectrograms showing reflection magnitude of a semicircular object varying with angle of reflection across the semicircular range of receivers.	135
6.14	Polar responses showing scattering of reflected sound energy from a semi-circular shaped diffuser	136
6.15	Graph showing random incidence diffusion coefficients measured from a semi-circular shaped diffuser in third octave bands from 1 kHz to 10 kHz.	137
6.16	Illustration showing the lengths of the modelled quadratic diffuser wells in comparison with apparent depth of the diffuser object as used in the diffusion coefficient measurement.	138
6.17	Spectrograms showing reflection magnitude of the quadratic diffuser model Q-A varying with angle of reflection across the semicircular range of receivers.	140
6.18	Polar responses showing scattering of reflected sound energy from quadratic diffuser model Q-A	141
6.19	Graph showing random incidence diffusion coefficients measured from the quadratic diffuser model Q-A in third octave bands from 1 kHz to 10 kHz.	142
6.20	Spectrograms showing reflection magnitude of the quadratic diffuser model Q-B varying with angle of reflection across the semicircular range of receivers.	143
6.21	Spectrograms showing reflection magnitude of the quadratic diffuser models (a) Q-A and (b) Q-B across the semicircular range of receivers for the 0° angle of incidence, with theoretical optimal diffusion frequencies marked using dotted lines.	144

6.22	Polar response showing scattering of reflected sound energy from quadratic diffuser model Q-B for normal incidence at the frequency 11.025 kHz.	144
6.23	Graph showing random incidence diffusion coefficients measured from the quadratic diffuser models Q-A and Q-B in third octave bands from 1 kHz to 10 kHz.	146
6.24	Spectrograms showing reflection magnitude for -30° incidence, varying with angle of reflection across the semicircular range of receivers with a range of diffusive materials modelled with the circulant matrix technique.	148
6.25	Spectrograms showing reflection magnitude for 0° incidence, varying with angle of reflection across the semicircular range of receivers with a range of diffusive materials modelled with the circulant matrix technique.	149
6.26	Polar responses showing scattering of reflected sound energy from diffuser models CM00 , CM45 and CM90 for incident angle -60°	150
6.27	Polar responses showing scattering of reflected sound energy from diffuser models CM00 , CM45 and CM90 for incident angle -30°	150
6.28	Polar responses showing scattering of reflected sound energy from diffuser models CM00 , CM45 and CM90 for incident angle 0°	151
6.29	Graphs showing directional diffusion coefficients for the modelled boundaries CM00-CM90	151
6.30	Random incidence diffusion coefficients for the 7 boundary models CM00-CM90	153
6.31	Spectrograms showing reflection magnitude for -30° incidence, varying with angle of reflection across the semicircular range of receivers with a range of diffusive materials modelled with the diffusing layer technique.	155
6.32	Spectrograms showing reflection magnitude for 0° incidence, varying with angle of reflection across the semicircular range of receivers with a range of diffusive materials modelled with the diffusing layer technique.	156

6.33	Polar responses showing scattering of reflected sound energy from diffuser models DL00 , DL45 and DL90 for incident angle -60°	157
6.34	Polar responses showing scattering of reflected sound energy from diffuser models DL00 , DL45 and DL90 for incident angle -30°	157
6.35	Polar responses showing scattering of reflected sound energy from diffuser models DL00 , DL45 and DL90 for incident angle 0°	158
6.36	Graphs showing directional diffusion coefficients for the modelled boundaries DL00-DL90	159
6.37	Random incidence diffusion coefficients for the 7 boundary models DL00-DL90	160
6.38	Random incidence diffusion coefficients for the boundary models (a) DDL00-DDL90 and (b) TDDL00-TDDL90	161
6.39	Spectrograms showing reflection magnitude for -30° incidence, varying with angle of reflection across the semicircular range of receivers with a range of diffusive materials modelled with the diffusing layer technique for sample rate 22050Hz.	164
6.40	Spectrograms showing reflection magnitude for 0° incidence, varying with angle of reflection across the semicircular range of receivers with a range of diffusive materials modelled with the diffusing layer technique for sample rate 22050Hz.	165
6.41	Spectrograms showing reflection magnitude for -30° incidence, varying with angle of reflection across the semicircular range of receivers with a range of diffusive materials modelled with the diffusing layer technique for sample rate 33075Hz.	166
6.42	Spectrograms showing reflection magnitude for 0° incidence, varying with angle of reflection across the semicircular range of receivers with a range of diffusive materials modelled with the diffusing layer technique for sample rate 33075Hz.	167
6.43	Random incidence diffusion coefficients for the boundary models (a) HRL00-HRL90 and (b) TRDL00-TRDL90	168
6.44	Random incidence diffusion coefficients for the boundary models (a) RDL00-RDL90 and (b) DL00-DL90 for comparison.	170

6.45	Graph Showing the average of the absolute values of the differences between the measured diffusion coefficients in boundary models RDL00-RDL90 and DL00-DL90 for each third octave band.	171
6.46	Diagram of the set-up used for the diffusion testing in the 2-D DWM showing the orientation of the mesh both for the triangular and rectilinear topologies.	172
6.47	Graphs showing the average amplitudes of the outputs from (a) Model DL and (b) Model CM at 3 modal frequencies for each 4 second simulation.	173
6.48	Graphs showing the 10dB modal bandwidths of the outputs from (a) Model DL and (b) Model CM at 3 modal frequencies for each 4 second simulation.	174
6.49	Graphs showing early part of impulse responses for room simulations with boundary diffusion models (a) DL00 , (b) DL45 and (c) DL90 implemented at each boundary.	177
6.50	Graphs showing RT_{60} times of a DWM structure for boundary models (a) CM00-CM90 with $r = 0.3$ (Test A), (b) CM00-CM90 with $r = 0.5$ (Test B), (c) DL00-DL90 with $r = 0.3$ (Test C) and (d) DL00-DL90 with $r = 0.5$ (Test D).	181
6.51	Diagram of DWM with alternating absorbent walls and diffusing walls.	182
6.52	Graph showing RT_{60} times of the DWM structure described by Figure 6.51 with boundary models DL00-DL90 implemented at the diffusing boundaries and reflection coefficient $r = 0.3$ applied at the absorbing boundaries.	184
6.53	Wave propagation in a cuboid shaped 3-D DWM.	187
6.54	Graph showing RT_{60} times of the DWM structure described by Figure 6.53 with boundary models 3DDL00-3DDL90 implemented at the diffusing boundaries and reflection coefficient $r = 0.8$ applied at the absorbing boundaries.	188
6.55	Diagram showing the mesh geometry used to create the 2-D auditory examples.	189
6.56	Diagram showing the mesh geometry used to create the 3-D auditory examples.	190

B.1	A class diagram describing the core of the software used to create all results in this thesis.	204
B.2	Frequency Analysis of test output with the lowest 26 modal frequencies marked on.	208
B.3	Screen shots showing wave propagation during diffusion coefficient measurement simulation for a flat plane boundary, with an incident angle of -60°	209
C.1	Diagram describing the directory structure and location of files contained in the attached CD-ROM.	212

List of Tables

2.1	Frequency dependent random incidence absorption coefficients for a selection of common building materials	40
6.1	Table showing Directional Diffusion Coefficients and Random Incidence Diffusion Coefficients measured from a flat plane boundary. .	129
6.2	Table showing Directional Diffusion Coefficients and Random Incidence Diffusion Coefficients measured from a triangular shaped diffuser.	131
6.3	Table showing directional diffusion coefficients and random incidence diffusion coefficients measured from a semi-circular shaped diffuser.	135
6.4	Table showing directional diffusion coefficients and random incidence diffusion coefficients measured from the quadratic diffuser model Q-A	141
6.5	Table showing directional diffusion coefficients and random incidence diffusion coefficients measured from the quadratic diffuser model Q-B	145
6.6	Table showing random incidence diffusion coefficients for the 7 boundary models CM00-CM90	152
6.7	Table showing random incidence diffusion coefficients for the 7 boundary models DL00-DL90	159
6.8	Table showing random incidence diffusion coefficients for the 7 boundary models DDL00-DDL90	161
6.9	Table showing random incidence diffusion coefficients for the 7 boundary models TDL00-TDL90	161

6.10	Table showing random incidence diffusion coefficients for the 7 boundary models HRDL00-HRDL90	168
6.11	Table showing random incidence diffusion coefficients for the 7 boundary models TRDL00-TRDL90	168
6.12	Table showing random incidence diffusion coefficients for the 7 boundary models RDL00-RDL90	170
6.13	Table showing measured RT_{60} times of a DWM structure at different octave bands for the 7 boundary models CM00-CM90 with boundary reflection coefficient $r = 0.3$ (Test A).	179
6.14	Table showing measured RT_{60} times of a DWM structure at different octave bands for the 7 boundary models CM00-CM90 with boundary reflection coefficient $r = 0.5$ (Test B).	179
6.15	Table showing measured RT_{60} times of a DWM structure at different octave bands for the 7 boundary models DL00-DL90 with boundary reflection coefficient $r = 0.3$ (Test C).	180
6.16	Table showing measured RT_{60} times of a DWM structure at different octave bands for the 7 boundary models DL00-DL90 with boundary reflection coefficient $r = 0.5$ (Test D).	180
6.17	Table showing RT_{60} times of the DWM structure described by Figure 6.51 with boundary models DL00-DL90 implemented at the diffusing boundaries and reflection coefficient $r = 0.3$ applied at the absorbing boundaries.	183
6.18	Table showing RT_{60} times of the DWM structure described by Figure 6.53 with boundary models 3DDL00-3DDL90 implemented at the diffusing boundaries and reflection coefficient $r = 0.8$ applied at the absorbing boundaries.	187

Acknowledgements

I would first like to thank my supervisor Dr. Damian Murphy, who has provided me with nothing but dedicated support, guidance, motivation and inspiration during the period of my research. The time spent on this work would not have been the highly educational and enjoyable experience it was without his truly excellent supervision. I am extremely grateful to Damian for making it all possible, for his confidence in my work, and of course for his extensive tutelage and advice.

I would also like to give thanks to David Howard for providing me with his informed guidance and motivation at important stages during my time in York, and to Lauri Savioja whose input also proved to be extremely useful.

I must also express gratitude to all those with whom I shared an office in the Department of Electronics at the University of York. They have always been welcoming, friendly and most helpful. Their constant support and generosity has helped in many different ways, from solving complicated mathematical problems related to my research to providing a constant stream of interesting biscuits. I would particularly like to thank Jack Mullen for sharing with me his knowledge in many areas, for his well informed advice and for his friendliness. I would also like to show my gratitude to Antti Kelloniemi for his inspiration, support and discussion during his time spent working in the Audio Lab.

I would like to thank my father, Chris, for providing me with so much love and encouragement, and inspiring me through his kindness. I would also like to thank my brothers Julian and Adrian for being my friends through difficult times.

Above all, I would like to express my most sincere gratitude to my mother, Linda, for the strength she has given me and whose immense courage, love and kindness I will always aspire to.

Declaration

I hereby declare that this thesis is entirely my own work and all contributions from outside sources, through direct contact or publications, have been explicitly stated and referenced. I also declare that some parts of this program of research have been presented previously, at conferences and in journals. These publications are listed as follows:

- **The Modeling of Diffuse Surfaces in the 2-D Digital Waveguide Mesh**, S. Shelley and D. T. Murphy, journal paper accepted on the 4th of October 2007 to *IEEE Transactions on Audio, Speech and Language Processing*, awaiting publication.
- **Measuring Diffusion in a 2-D Digital Waveguide Mesh**, S. Shelley and D. T. Murphy, paper and oral presentation at the *8th International Conference on Digital Audio Effects (DAFx'05)*, Madrid, Spain, September 2005 [1].
- **Diffusion Modelling at the Boundary of a Digital Waveguide Mesh**, S. Shelley and D. T. Murphy, paper and oral presentation at the *13th European Signal Processing Conference (EUSIPCO2005)*, Antalya, Turkey, September 2005 [2].
- **Acoustic Modeling Using the Digital Waveguide Mesh**, Damian Murphy, Antti Kelloniemi, Jack Mullen and Simon Shelley, *IEEE Signal Processing Magazine*, volume 24(2), 2007 [3].

Chapter 1

Introduction

The work presented in this thesis is concerned with the modelling of sound propagation in an acoustic space or system. The main focus of this work is on the issue of room acoustic modelling, as part of the *auralization* process, but it is also applicable to other fields in which the modelling of sound propagation is required, such as vocal tract modelling [4] and musical instrument modelling [5,6]. The definition of auralization, taken from [7], is as follows:

Auralization is the process of rendering audible, by physical or mathematical modelling, the sound field in a space, in such a way as to simulate the binaural listening experience at a given position in the modelled space.

A number of methods exist that are designed to model and predict the movement of sound energy in an enclosed acoustic space, such as a room or a concert hall. An important problem in such models is the complex wave activity that takes place when sound comes into contact with acoustic boundaries. One outcome of such an interaction is the resulting scattering of the sound energy. Specular reflection of sound occurs only in certain conditions, providing the boundary is flat, the wavelength of the sound is very small in comparison with its size and that the reflection takes place far away from its edges. Specular reflection results in the reflected energy being concentrated in the angle of reflection, which is equal to the angle of incidence of the wave. In reality however, boundaries are often irregular with respect to the wavelength of incident sound, resulting in diffuse reflections and causing a redistribution of sound energy across a range of angles

upon reflection. The scattering of sound at boundaries in many situations has a significant effect on the overall acoustic characteristics of a system, or space, and must therefore not be overlooked in any acoustic model. However accurate reproduction of scattering or diffuse boundaries is often problematic, particularly for boundaries with numerous complex irregularities that are relatively small in size in comparison with the size of the boundary itself. A model is therefore required where the diffuse behaviour of boundaries is approximated in a more general way using a statistical approach. Such a model should ideally be adjustable so that the diffusive effects of the simulated boundaries can be optimized to match those of a wide range of real, irregularly shaped boundaries as closely as possible.

1.1 Boundary Diffusion

It is important at this stage to clarify the definitions used in this work in relation to boundary diffusion. The terms *diffuse reflection* and *scattering* describe the process that occurs when reflected sound energy is redistributed away from the specular direction of reflection. The term *diffusion* is sometimes used to describe reflections that are in general diffuse, however this is potentially ambiguous as it may also be used to describe the general diffusion - or spread - of sound in a space. This describes a process that is heavily affected by the presence and nature of diffuse reflections at the boundaries of a space, but not the process of diffuse reflection itself. To avoid confusion, the term *boundary diffusion* is used to explicitly refer to the process of sound diffusion that takes place at boundaries. The terms *diffuse boundary* and *diffuse surface* are used to describe an acoustic boundary that results in diffuse reflection. The term *diffuser* is also used to describe such a boundary. *Diffraction* is a property of sound waves that should not be confused with diffuse reflection, but often plays an important part in the behaviour of sound at diffuse boundaries and must be taken into account.

The scale of the irregularities of a boundary determines the range of frequencies for which the effect of boundary diffusion occurs. In the situation where these irregularities are very small compared to the wavelength of the incident sound wave, very little diffusion is observed and the reflection tends to the specular case [8].

To understand the importance of diffuse reflection, it is useful to look at the effects that diffuse boundaries can have on the characteristic acoustics of an enclosed space. A summary of the so-called *macroscopic* effects of diffuse reflection are presented in [9] and a selection of these effects are repeated here.

The introduction of diffuse boundaries to a space can potentially result in:

- a “softer” acoustic response [10].
- a shorter reverberation time and a decay curve that shows increasingly exponential properties [11].
- diminished “comb filter” effects caused by strong early reflections.
- a “smoother” impulse response.

As well as this, it is also argued in [12] that the concentrated energy found at certain modal frequencies are attenuated as standing waves become less prominent due to the scattering of energy, at boundaries, away from the modal cyclic paths present in the room.

Unfortunately, these terms are vague and difficult to quantify and measure. Also, the effects are heavily dependent on other parameters of the room like its geometry for example. Techniques to measure the quality of diffuse reflection have been developed so far on a more *microscopic* level. Recent advances in this field have led to the development of two coefficients designed to characterise and quantify the diffusive characteristics of a boundary: the *scattering* coefficient [13] and the *diffusion* coefficient [14]. These coefficients are designed to quantify boundary diffusion in such a way that the diffusive characteristics of the boundary are well represented, but in an efficient way that does not result in an overwhelming collection of data.

Scattering coefficients are suitable for geometric modelling techniques as they are compatible with the boundary scattering algorithms they currently use. Scattering coefficient data, however, only contains information about the quantity of energy that is moved from the specular direction and is not concerned with the more detailed diffusive characteristics of the boundary. Diffusion coefficient data holds more information about the nature of scattering at a boundary. The diffusion coefficient is designed as a detailed measure of the diffusive quality of acoustic

boundaries and diffusers, however it is not compatible with the diffuse reflection algorithms currently used in ray-based modelling techniques [15].

1.2 Acoustical Modelling

The techniques used in the computer modelling of sound propagation in an enclosed space can, on the whole, be divided into two different types. These are referred to as *ray-based* acoustic modelling and *wave-based* acoustic modelling. Ray-based acoustic modelling includes approaches such as ray-tracing [16] and the image-source method [17]. They have an advantage over wave-based methods in that they are less computationally expensive but phenomena such as sound diffraction and wave interference have to be considered in addition to the basic implementation and can be very difficult to successfully build into the model. In general, ray-based implementations are most effective for room acoustic modelling situations where the upper limit of the simulated wavelength is much shorter than the boundary dimensions of the space. Wave-based acoustic modelling methods, on the other hand, are generally more computationally expensive than ray-based solutions, with the computational requirement increasing with the upper frequency limit of the simulated sound, although sound diffraction and wave interference are modelled inherently. This makes such approaches particularly suited for situations where the modelling of low frequency sound wave propagation is required. For wave-based acoustic simulations, the smallest value of the modelled wavelength (the upper limit on the frequency) becomes more of an issue, and is limited by the computation power and time available. The largest value of the modelled wavelength is no longer an issue however.

The *Digital Waveguide Mesh* (DWM) is an implementation of the Finite Difference Time Domain (FDTD) modelling technique, a wave-based approach that models sound waves in a multidimensional acoustic system in discrete points in time and space [18, 19, 20, 21, 22]. 3-D Digital Waveguide Mesh structures can be used to fully model an acoustic space, although with current computer systems, the modelling of sound with wavelengths that are very small in comparison to the size of the system becomes problematic, as the computational load for these high frequencies becomes very large. 2-D Digital Waveguide Mesh models have

been used extensively to model wave propagation in membranes and plates [23] as well as in vocal tract models [4]. Their relatively low computation load in comparison with the 3-D case means that they are also a useful tool for room acoustic modelling [20, 24]. For example, hybrid systems can be implemented where low frequency wave propagation is modelled accurately with a 3-D DWM structure and wave propagation at higher frequencies are approximated using 2-D DWM structures. Other possible scenarios for room acoustic modelling include hybrid systems that take advantage of the efficiency of ray-based modelling systems for high frequencies (where the wavelengths are much smaller than the proportions of the room) and the accuracy of the DWM system at relatively low frequencies (where the wavelengths are a similar size to or larger than the room proportions). The work in this thesis is concentrated on the modification of 2-D and 3-D DWM systems used in room acoustic modelling to include diffusing boundaries. The work can also be applied to other applications of DWM systems however, and is not limited to room acoustic modelling. For example it may be desirable to implement diffusing boundaries at the edge of a drum membrane, or at the boundaries of DWM structure used in a vocal tract model.

1.3 Motivation

Recent work in modelling diffuse reflection in ray-based computer models has shown much improvement in the quality of results [25, 26, 27]. The methods used to achieve these improved results are based on statistical approaches and, although showing a degree of success on a macroscopic scale, are in fact far from accurate on a microscopic level. A commonly used technique is to change the direction of reflected waves (or rays) after they strike the boundary using a random probability distribution designed to distribute the reflected energy according to Lambert's Cosine Law [28]. This law states that the amount of reflected energy found at a particular direction from the point of reflection at the boundary is proportional to the cosine of the angle between the direction of the reflected energy and the normal of the boundary, irrespective of the incident angle of the sound wave. Partial diffuse boundaries are modelled by allowing a proportion of the reflected rays to reflect in the specular direction. A random number is typically chosen between 0 and

1 in order to decide whether the boundary acts as a diffuse or specular reflector for each particular ray. If the number is above a certain threshold the reflection is determined as diffuse with the implication that a certain amount of the reflected energy at certain times will be treated as specular.

Previous work in implementing diffusing boundaries for a DWM details the successful implementation of a highly diffusive boundary in a 2-D mesh using a quadratic residue diffuser [29]. Another technique has been developed that simulates diffusion by randomly rotating incident waves as they approach the boundary of the mesh [30] (for convenience this is later referred to as the *diffusing boundary* technique). Although effective, neither method offers a complete, controllable and accurate boundary diffusion model and a full analysis of these techniques and their effects is limited.

The technique described in [30] allows for control over the diffusivity of the modelled boundary, however the method is limited by an inherent error. The error, described in section 5.3.2, is caused by differences between ideal and actual mesh configuration conditions, and results in undesirable inconsistency in measured boundary diffusion results. With the aim of improving this technique, a new modified version of the boundary diffusion method, *the diffusing layer*, is introduced in this thesis, which eliminates the previously identified error. In addition, a multi-layered adaptation of the diffusing layer model is proposed which offers some control over the frequency dependent nature of the resultant diffusive characteristics.

The work presented in this thesis aims to bring together methods for modelling diffusion in the DWM, including the diffusing layer techniques, and to analyse and compare them in detail. On a microscopic scale, a measurement technique for obtaining the diffusion coefficients of the models is described and applied. The aim is both to observe and characterise the diffusive effects of the surfaces, and also to provide data that can be used as a reference when designing and simulating diffuse boundaries in a DWM. Tests that are designed to measure the macroscopic effect of the modelled boundary diffusers are also developed and the results are presented and discussed. The results give a greater understanding of the behaviour of the model and show that the model can be used to simulate diffuse boundaries, with properties comparable to that observed in real diffusing boundaries. The techniques

described in this thesis can be used to test any diffuse boundary models designed for a 2-D DWM or a 3-D DWM, and to compare them with both each other and with real diffuse boundaries.

A further aim is to bring together and review current developments and theories in the field of diffuse reflections, and also to discuss both existing and suggested methods for modelling diffuse reflections in different acoustic modelling scenarios.

1.4 Thesis Outline

The theoretical foundations behind the topics discussed in this thesis are presented in Chapter 2. An overview of the mechanical process involved with sound propagation is given, as well as the mathematics that describe simple harmonic motion and the equation of wave motion. Definitions and descriptions are given for sound pressure, particle velocity, the speed of sound, acoustic impedance and sound intensity. Phenomena related to sound wave propagation in space are described and discussed, including the interaction of sound with acoustic boundaries, sound wave interference and the formulation of standing waves. Finally the *room impulse response* and its measurement are described.

In Chapter 3, an overview of diffuse reflection is presented, along with current characterisation and measurement techniques in this field. Acoustic diffusers are split into different classes, depending on their nature, geometry and design. These diffuser types are defined as *random rough diffusers*, *geometric diffusers* and *Schroeder diffusers*. Diffusion and scattering coefficients are also defined and discussed, and standard techniques for measuring these coefficients are described.

Chapter 4 consists of a review of current acoustical modelling techniques. These are split into three different types, referred to as *acoustical scale modelling*, *ray-based computer modelling* and *wave-based computer modelling*. Each approach is described and discussed. Methods that are used, or have been suggested, for modelling diffuse reflection in specific computer acoustical modelling techniques are also described and discussed. The *Digital Waveguide Mesh* modelling technique is described in detail, including its limitations. A review of previous research in modelling boundary absorption and diffuse reflection in the Digital Waveguide Mesh is also presented.

A detailed review of diffuse reflection modelling in the Digital Waveguide Mesh is given in Chapter 5. Implementation of diffusers based on modelling their physical structure, including the quadratic residue diffuser, at the DWM boundary is described. Statistical approaches and their implementation, namely the *diffusing boundary* and *diffusing layer* approaches, are also detailed. Considerations are made for implementation in both 2-D and 3-D DWM structures.

A series of tests designed to measure the diffusive properties of diffuse boundary models in the DWM is described in Chapter 6. These tests are applied to a number of different boundary models and the results are presented and discussed in detail. Tests designed to measure the scattering characteristics both on a microscopic scale and on a macroscopic scale are presented. The entire set of results of these tests are included in digital format in the accompanying CD-ROM attached to this thesis. Demonstration sound files designed to evidence the audible effects of the models, are also included on the CD. A description and review of these sound files makes up the final section of this chapter.

Chapter 7 contains a final summary of the work presented here, and the results presented in the previous chapter. Conclusions are drawn from the results concerning the measurement techniques used and the diffuse boundary models. Possible directions for future work are then discussed.

1.5 Contributions of Research

Novel contributions of research contained in this thesis are as follows:

- A new diffuse boundary model that offers high degree of control is presented. This *diffusing layer* approach provides a statistical method to implement boundary diffusion without altering the physical make-up of the DWM.
- The new diffuse boundary model is successfully implemented in the 2-D triangular DWM, the 2-D rectilinear DWM and the 3-D rectilinear DWM. A quadratic residue diffuser is also implemented in the 2-D triangular DWM for the first time.
- A detailed analysis of diffuse boundary models in the DWM is presented, and the diffusivity is quantified in the form of frequency dependent diffusion

coefficients.

- An analysis of the resulting effect on the diffusing layer model of both changing the DWM topogoly and changing the update frequency of the mesh is described.
- All diffuse boundary methods so far implemented in the DWM are discussed and compared.
- New methods for measuring the diffusion characteristics of DWM boundaries are described which are concerned with the macroscopic effects of boundary diffusion, and their effect on the effect of absorbing boundary implementation.
- Audio examples are presented, which clearly demonstrate the audible effect of diffuse reflection when implemented as part of a DWM room acoustics auralization system.

Chapter 2

Acoustic theory

2.1 Introduction

In order to model sound and its interaction with the surrounding environment, an understanding of the physics that govern its behaviour is required. From a physical perspective, sound is a mechanical energy disturbance that propagates through a solid, liquid or gas as waves. The nature of such disturbance is that molecules, or particles in the medium are moved from their natural state. As a result, the density of particles in the medium fluctuate as the sound propagates through it. Areas within the medium that become more dense, when particles are moved closer to each other than they would be in their natural state, are called compressions; areas that become less dense, when particles are moved apart from each other, are called rarefactions [31, 8]. Despite this disturbance of particles on a local scale, it is important to note that the net movement of the medium itself that results is zero, and particles return to their original state once the disturbance has passed.

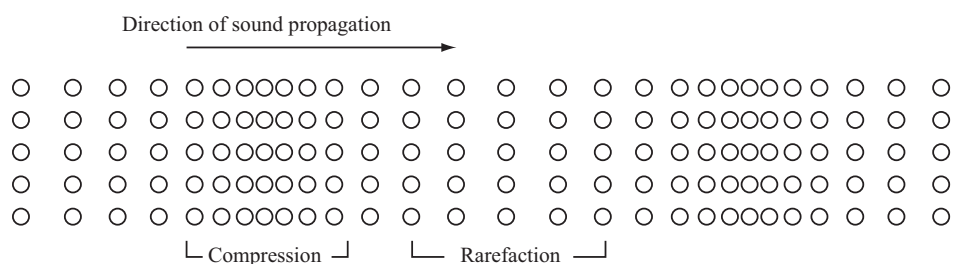


Figure 2.1: Diagram of particles in a medium with alternating areas of compressions and rarefactions.

2.2 Wave Motion and the Wave Equation

Mathematically, the disturbance caused by a wave at a position in space and time is considered as a function. For a one dimensional wave, the wave disturbance ξ at position x (m) and time t (s) can be expressed as:

$$\xi = f(x, t) \quad (2.1)$$

A one-dimensional travelling wave is described by (2.2), with a travelling velocity c (ms^{-1}):

$$\xi = f(x - ct) \quad (2.2)$$

2.2.1 Simple Harmonic Oscillation

The most fundamental oscillating system is known as the *simple harmonic oscillator* and is defined by (2.3), where F is the force (N), ξ is the displacement of the system from equilibrium (m) and k is a constant.

$$F = -k\xi \quad (2.3)$$

A mechanical example of such a system is a mass connected to a linear spring (a spring that conforms to Hooke's law of elasticity), which is in turn connected to a fixed point, as shown in Figure 2.2:

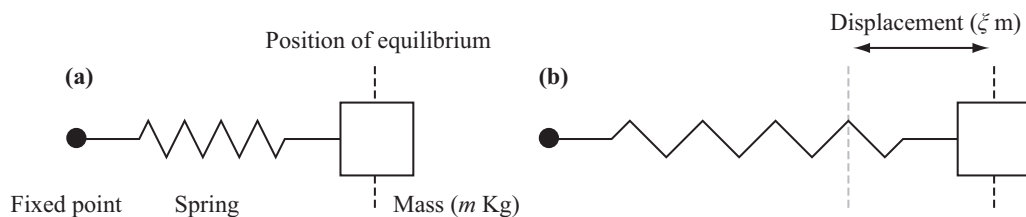


Figure 2.2: A simple harmonic oscillator (a) in equilibrium and (b) with displacement ξ .

It is assumed in this case that the spring is a perfect linear spring conforming to Hooke's law of elasticity, that the fixed point is perfectly rigid and also that displacement is small in relation to the length of the spring. If, under these conditions, the mass is given an initial displacement from rest and then allowed

to move freely, as shown in Figure 2.2, then the system is in simple harmonic oscillation. Using Newton's Second Law of Motion:

$$F = -k\xi = m \frac{d^2\xi}{dt^2} \quad (2.4)$$

Rearranging (2.4) gives the differential equation:

$$\frac{d^2\xi}{dt^2} + \frac{k}{m}\xi = 0 \quad (2.5)$$

The general solution to (2.5) is given by (2.6), where $\omega_0 = \sqrt{k/m}$ is the natural angular frequency of oscillation (rad s^{-1}), A is the amplitude (m) and ϕ_0 is the phase constant.

$$\xi = A \cos(\omega_0 t + \phi_0) \quad (2.6)$$

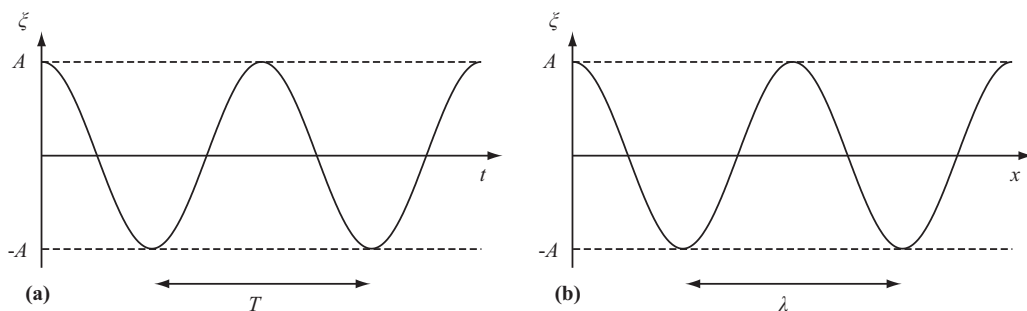


Figure 2.3: A one dimensional travelling wave $\xi(x, t)$ in simple harmonic oscillation, represented at (a) a fixed point in space x and (b) a fixed point in time t .

A one dimensional travelling wave that is oscillating harmonically, illustrated in Figure 2.3, can therefore be described by (2.7), the 1-D *Harmonic Wave Function*:

$$\xi(x, t) = A \cos[\omega_0(x \pm ct) + \phi_0] \quad (2.7)$$

The amplitude A is the maximum value that ξ can reach in this function. The phase of the oscillation, $\phi(x, t)$ is the argument to the trigonometric function and describes the state of oscillation in the system at a particular point in space and time:

$$\phi(x, t) = \omega_0(x \pm ct) + \phi_0 \quad (2.8)$$

The phase constant ϕ_0 is the phase of oscillation at $t = 0$ and $x = 0$. By shifting the value of ϕ_0 by $\pi/2$ it is possible to express the Harmonic Wave Function in the form:

$$\xi = A \sin[\omega_0(x \pm ct) + \phi_0] \quad (2.9)$$

The angular frequency ω_0 is the rate of change of phase (in radians per second) in the system. One phase revolution is equal to 2π radians, therefore the angular frequency can be expressed in terms of the period T (length of time for system to complete one oscillation in seconds) and also its frequency $f = 1/T$ (number of oscillations per second in Hz):

$$\omega_0 = \frac{2\pi}{T} = 2\pi f \quad (2.10)$$

The wavelength λ (m) is the distance the wave travels in the time it takes to complete one oscillation. This can be calculated by multiplying the period T of the wave by its speed of travel c :

$$\lambda = cT = \frac{c}{f} \quad (2.11)$$

2.2.2 The Equation of Wave Motion

The equation of wave motion, or wave equation, is a differential equation that describes the passage of harmonic waves through an elastic medium [32,11]. (2.12) is the general wave equation in n dimensions, where c m/s is the speed of propagation in the medium and ξ m represents the displacement of the medium as a function of the variables describing its location ($x_1, x_2 \dots x_n$ m) and time, t s. ∇ is the Laplacian with respect to the location variables, which in cartesian terms is described by (2.13).

$$\frac{\partial^2 \xi}{\partial t^2} = c^2 \nabla^2 \xi \quad (2.12)$$

$$\nabla^2 = \frac{\partial^2}{\partial x_1^2} + \frac{\partial^2}{\partial x_2^2} + \dots + \frac{\partial^2}{\partial x_n^2} \quad (2.13)$$

For a one dimensional travelling wave, the equation of motion is as follows:

$$\frac{\partial^2 \xi(x, t)}{\partial t^2} = c^2 \frac{\partial^2 \xi(x, t)}{\partial x^2} \quad (2.14)$$

By introducing a change in variables, described by $e = x - ct$ and $h = x + ct$, a general solution to this equation can be derived, known as d'Alembert's solution (2.15). The solution describes the displacement, $\xi(x, t)$, at a given point in time and one dimensional space as the sum of two waves travelling in opposite directions. A full derivation of d'Alembert's solution is given in Appendix A.1.

$$\xi(x, t) = \xi^+(t - x/c) + \xi^-(t + x/c) \quad (2.15)$$

ξ^+ and ξ^- are functions representing waves travelling in the positive and negative x directions respectively, and with velocity $c \text{ ms}^{-1}$.

2.3 Sound Pressure and Particle Velocity

The compressions and rarefactions caused by a propagating sound wave in a medium result in a fluctuation of pressure within the medium. Sound pressure is the varying difference, at a fixed point, between the pressure caused by a sound wave and the average pressure of the medium at that point. The instantaneous sound pressure is this difference measured at a particular location at a particular point in time. The effective sound pressure is the root mean square of the instantaneous sound pressure measured over a period of time. Sound pressure is measured in pascals (symbol: Pa).

The human ear is sensitive to a wide range of sound pressure, in the region of between $20 \text{ }\mu\text{Pa}$ and 20 Pa [33]. As a result of this, and of the nature by which sound is perceived, sound pressure is commonly expressed in relation to a reference sound pressure on a logarithmic decibel scale. This is known as the sound pressure level. The reference pressure level p_0 is usually the threshold of hearing, which according to [34], is defined in air in (2.16). It should be noted that the threshold of hearing is dependent on frequency and the definition given here is the threshold for the most sensitive range of human hearing.

$$p_0 = 2 \times 10^5 \text{ Pa} \quad (2.16)$$

The sound pressure level (SPL) is defined in (2.17), where p is the actual sound

pressure level, measured in Pa, and p_0 is the reference pressure level:

$$SPL = 20 \log_{10} \left(\frac{p}{p_0} \right) \quad (2.17)$$

The fluctuation in pressure that describes the propagation of sound within a medium results in a movement of particles as they travel closer to each other and further apart. This movement of particles means that they have a velocity that is explicitly caused by the propagating sound wave, known as *particle velocity*.

2.4 The Speed of Sound

The speed of sound describes the speed at which sound waves travel through a medium, and therefore is dependent on both the inertial and elastic properties of that medium. In the general case the speed of sound, c can be calculated using (2.18), where B is the bulk (elastic) modulus of the medium and ρ is its density:

$$c = \sqrt{\frac{B}{\rho}} \quad (2.18)$$

For the case where the medium is an ideal gas, the bulk modulus, B_{gas} is given by (2.19). In this equation, P is the pressure of the gas and γ is the adiabatic index, or heat capacity ratio of the gas:

$$B_{gas} = \gamma P \quad (2.19)$$

Substituting (2.19) in (2.18), the speed of sound in an ideal gas c_{gas} can be given by:

$$c_{gas} = \sqrt{\frac{\gamma P}{\rho}} \quad (2.20)$$

(2.21) is the *ideal gas law*, the equation of state of a quantity of ideal gas [35], determined by its pressure P , volume V and temperature T . In the equation, n is the amount of substance of the gas (expressed in Moles) and R is the ideal gas constant.

$$P = \frac{nRT}{V} \quad (2.21)$$

The density, ρ of a gas is expressed in terms of the amount of substance n , its molar mass M and its volume V by (2.22):

$$\rho = \sqrt{\frac{nM}{V}} \quad (2.22)$$

By substituting (2.21) and (2.22) in (2.20), we get the following expression for the speed of sound in an ideal gas, showing that it is dependent on the absolute temperature and the molar weight of the gas, and not by its pressure:

$$c_{gas} = \sqrt{\frac{\gamma RT}{M}} \quad (2.23)$$

Given that for air, the heat capacity ratio $\gamma = 1.4$, the molecular mass $M = 2.897 \times 10^{-2} \text{ kg mol}^{-1}$ and the gas constant is $R = 8.314 \text{ J mol}^{-1} \text{ K}^{-1}$, the speed of sound in air c_{air} can be expressed as a function of its absolute temperature T :

$$c_{air} = 20.04 \sqrt{T} \quad (2.24)$$

2.5 Acoustic Impedance

The ratio of sound pressure p and particle velocity v at a given frequency gives the *acoustic impedance*, Z at that frequency:

$$Z = \frac{p}{v} \quad (2.25)$$

For a sound wave travelling in a homogeneous medium, undisturbed and without interruption from boundaries, the acoustic impedance will be constant, and will be equal to the *characteristic impedance* of the medium. The characteristic impedance of the medium, Z_0 can be calculated from its density ρ and its Bulk modulus B using (2.26):

$$Z = \sqrt{\rho B} \quad (2.26)$$

By rearranging (2.18) and substituting in (2.26), the characteristic acoustic impedance Z_0 can also be defined as the product of its density ρ and the speed of sound in the medium c :

$$Z_0 = \rho c \quad (2.27)$$

2.6 Sound intensity

Sound intensity I is defined as the sound power per unit area at a certain location within an acoustic medium. For a plane travelling wave it can be calculated using (2.28), where p is the sound pressure and v is the particle velocity:

$$I = pv \quad (2.28)$$

Rearranging (2.25) and substituting in (2.28) gives:

$$I = \frac{p^2}{Z} \quad (2.29)$$

This shows that sound intensity is proportional to the sound pressure squared. As with sound pressure level, measurements of sound intensity in air are often made relative to a reference sound intensity level, usually the threshold of hearing defined in air, according to [34], as:

$$I_0 = 10^{-12} \text{ Wm}^{-2} \quad (2.30)$$

The sound intensity level (SIL), in dB, is defined in (2.31):

$$SIL = 10 \log_{10} \left(\frac{I}{I_0} \right) \quad (2.31)$$

2.7 Air Absorption

An acoustic travelling wave experiences absorption as it travels through a medium, resulting in an attenuation of sound intensity that increases with distance. This absorption is brought about by a conversion of sound energy to other forms of energy, the most common being heat. The absorption that occurs in air is subtle and depends on the temperature and humidity of the atmosphere [36,37,38]. Air absorption is also highly dependent on frequency. When modelling acoustics, the absorption of sound in air should be considered if the problem space is large, or if boundaries are highly reflective, resulting in long reverberation decays. The net result of air absorption under such conditions is a slight attenuation of the later part of a room response that increases with frequency. The relationship between air absorption and frequency is not linear however, and a formulation

for this relationship is given in the International Organization for Standardization (ISO) document entitled “Acoustics – Attenuation of Sound During Propagation Outdoors – Part 1: Calculation of the Absorption of Sound by the Atmosphere.” (ISO 9613-1) [39].

2.8 Plane Waves

As an uninterrupted spherical sound wave travels away from a point source, its intensity decreases according to the inverse square law, defined in 2.32 [31]. This law states that the intensity of a sound wave I is inversely proportional to the square of the distance from its source r , where W is the power of sound at the source:

$$I = \frac{W}{4\pi r^2} \quad (2.32)$$

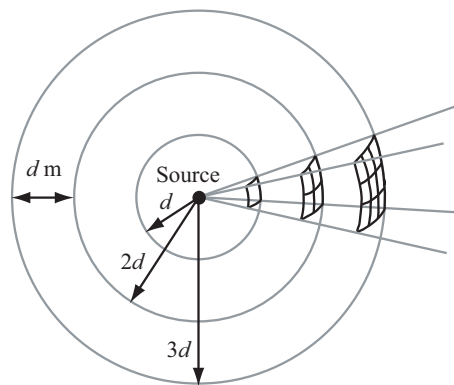


Figure 2.4: Spherical propagation of sound from a source.

Figure 2.4 shows sound spreading from a point source, illustrating how intensity is spread over a greater area as the sound travels away from the source. The area for part of the spherical wave is illustrated at distances $r = d, 2d$ and $3d$ from the source, showing how the area covered by this part of the wave increases in proportion to the square of the distance travelled. Therefore, assuming no air absorption in the system, the intensity of the wave is spread across an increasing area and is therefore inversely proportional to the square of the distance travelled from the source.

A plane wave is a wave that has consistent amplitude and phase across any plane that is perpendicular to its direction of travel [32]. At large distances from its source, a sound wave, if considered on a relatively small scale, has properties

similar to that of a plane wave.

2.9 Boundary Interaction

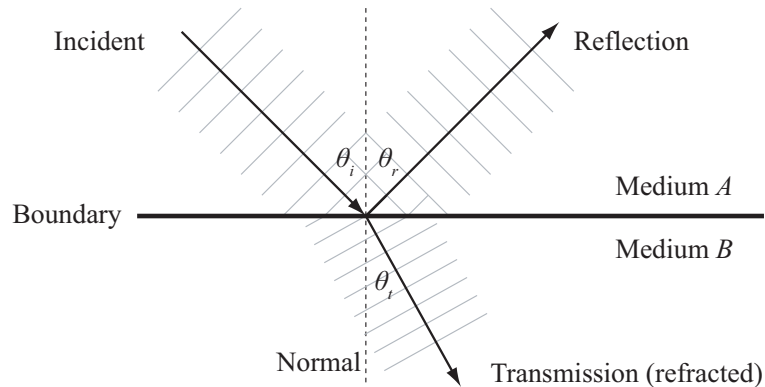


Figure 2.5: The interaction of sound with an acoustic boundary.

The interaction of sound waves with a boundary between two different acoustic media may result in the phenomenon of sound reflection, diffraction, transmission and/or refraction, depending on the nature of the boundary and frequency spectrum of the sound waves [32,28]. Figure 2.5 shows a cross section of a plane sound wave interacting with a smooth and straight boundary between two isotropic acoustic media. The boundary is relatively large compared to the wavelength of the sound waves and Medium *B* has a greater acoustic impedance than Medium *A*. Reflection is caused by change in impedance between two mediums and when the change in impedance increases, for example if a sound wave travelling in air interacts with a solid wall, the phase of the sound pressure wave is preserved and the phase of the particle velocity wave component is reversed. Conversely, if the acoustic impedance of Medium *B* is relatively smaller than that of Medium *A*, the phase of the sound pressure wave is inverted upon reflection and the phase of the particle velocity wave component is preserved. This type of reflection is observed in musical instruments, for example at the open end of a trumpet or clarinet.

In the case where the boundary is relatively large compared to the wavelength of the sound wave, the law of reflection applies, which states that the angle of

incidence θ_i is equal to the angle of reflection θ_r :

$$\theta_i = \theta_r \quad (2.33)$$

The angle of the transmitted sound wave, that is refracted, can be determined using Snell's law if the speed of sound in each medium is known [40]. If the speed of sound in medium A is c_A and the speed of sound in medium B is c_B then Snell's law states that:

$$\frac{\sin \theta_i}{\sin \theta_t} = \frac{c_A}{c_B} \quad (2.34)$$

The speed of sound also depends on the medium. A change in the speed of sound upon transmission from one medium to another results in a change in its direction of travel, known as refraction. The transmitted wave shown in Figure 2.5 for example is subject to a decrease in transmission speed upon transmission. This change in propagation speed results in a change in wavelength, with an increase in speed resulting in an increase in wavelength and visa versa. The frequency of the wave however remains constant. The relationship between speed of wave propagation, wavelength and frequency is given by:

$$\lambda = \frac{c}{f} \quad (2.35)$$

In the field of acoustics, it is important to consider the boundary between air and other acoustic media. Sound travelling in air is absorbed upon interaction with other media. Absorption in the case is defined as the attenuation in energy in the reflected sound wave, compared with the incident sound wave [8, 32, 28]. The degree to which the sound is absorbed depends on the medium or material at the boundary. The *sound absorption coefficient* is a measure of the absorptive qualities of a material. In general the absorption coefficient varies with angle of incidence and frequency. For plane wave with a given angle of incidence and frequency, the absorption coefficient α is defined by (2.36), where I_a is the absorbed sound intensity (Wm^{-2}) and I_i is the sound intensity of the incident wave (Wm^{-2}).

$$\alpha = \frac{I_a}{I_i} \quad (2.36)$$

Absorption coefficients are commonly given in octave bands starting at either 125 Hz

or sometimes 63 Hz. Table 2.1 lists absorption coefficients that have been measured for a selection of common building materials [41]. These coefficients are *random incidence absorption coefficients*, meaning that they are based on measurements where the sound energy approaches the materials' surface randomly from all directions rather than applying to a specific angle of incidence.

Material	Absorption Coefficients α at different Octave Bands						
	63 Hz	125 Hz	250 Hz	500 Hz	1000 Hz	2000 Hz	4000 Hz
Brickwork (plain or painted)	0.05	0.05	0.04	0.02	0.04	0.05	0.05
Concrete (tooled stone or granolithic)	0.01	0.02	0.02	0.02	0.03	0.04	0.04
Cork tiles (22mm thick on solid backing)	-	0.05	0.1	0.2	0.55	0.6	0.55
Glass (4mm thick)	-	0.3	0.2	0.1	0.07	0.05	0.02
Glass (6mm thick)	-	0.1	0.08	0.04	0.03	0.02	0.02

Table 2.1: Frequency dependent random incidence absorption coefficients for a selection of common building materials, from [41]

This information can also be represented using reflection coefficients. The reflection coefficient r is defined by (2.37), where I_r is the absorbed sound intensity and I_i is again the sound intensity of the incident wave.

$$r = \frac{I_r}{I_i} \quad (2.37)$$

At a rigid boundary where the phase of the sound pressure is preserved, interference (see next section) between the incident and reflected wave results in a pressure amplitude that is up to twice as great as the pressure of the incident wave itself. This phenomena only occurs in a thin region near the boundary known as the *pressure zone*. In contrast to this, the phase of velocity component of the wave is reversed, resulting in particle velocity of near zero at the boundary. It should also be noted again from (2.29) that the intensity of sound is proportional to the sound pressure squared.

2.10 Sound Wave Interference

Interference occurs when sound waves that are travelling in the same medium meet and interact with each other [31]. The particles in the medium at a point of sound wave interaction are influenced by the cumulative effect of all the waves that are

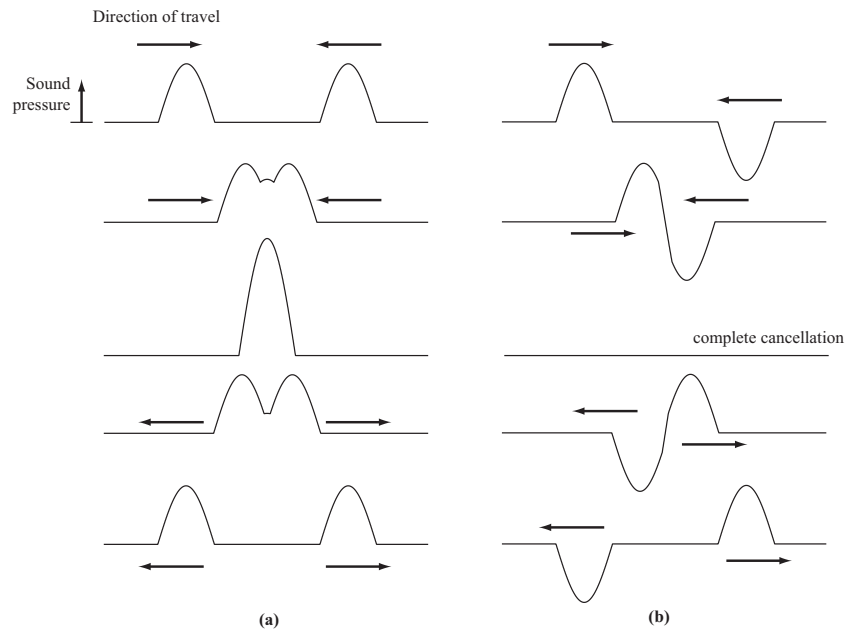


Figure 2.6: Examples of (a) constructive and (b) destructive wave interference, showing five snapshots at different points in time as two waves travel in opposite directions.

passing through that point. *Constructive* interference occurs when a compression in a sound wave interacts with compressions from other sound waves, or when a rarefaction in a sound wave interacts with rarefactions from other sound waves. Constructive interference results in the pressure amplitudes of the sound waves adding together at the point of interaction. Conversely, *destructive* interference occurs when a compression in a sound wave meets a rarefaction. The result of destructive interference is that the pressure amplitudes of the sound waves subtract at the point of interaction. Figure 2.5 shows examples of both constructive and destructive sound wave interference:

2.11 Diffraction of Sound

Sound waves travelling past a solid obstacle tend to bend around the object. The result is that a sound can be heard even if an object, such as a wall, obstructs the direct line between the listener and the sound source, and if there are no reflections from other walls in the space. Figure 2.7(a) shows the diffraction of a plane wave around the edge of a solid wall. Figure 2.7(b) illustrates the diffraction of a plane wave as it passes through a small gap in the wall. In Figure 2.7(a), the illustrated sound wave does not completely diffract around the corner of the object. The

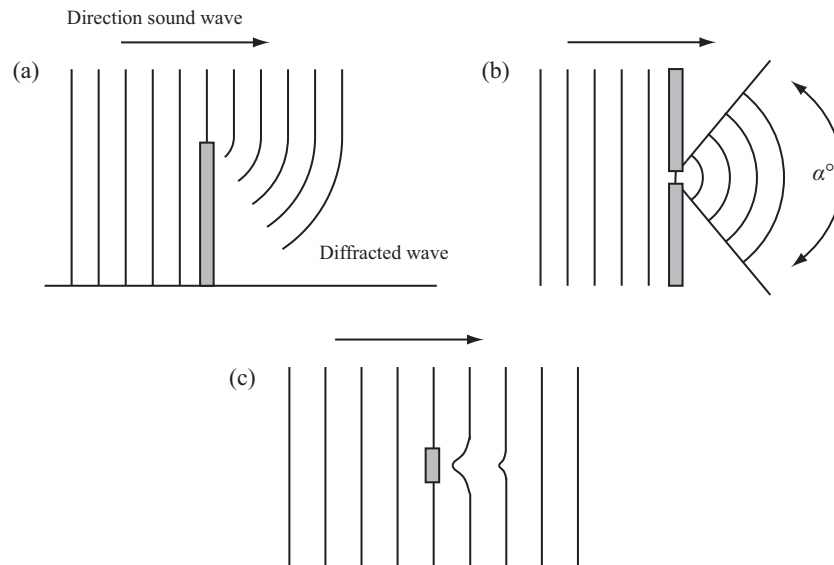


Figure 2.7: Illustration of Wave Diffraction (a) at the edge of a solid object, (b) through a gap in an object and (c) around the sides of an object.

amount of diffraction is related to the wavelength of the incident wave. Waves with longer wavelengths show higher diffractive tendencies than waves with shorter wavelengths. In a situation such as that described in Figure 2.7(b), the angle (α) by which the sound wave spreads as a result of the diffraction increases as the wavelength increases in relationship to the size of the gap, or if the size of the gap is decreased in relationship to the wavelength of the sound. Figure 2.7(c) shows how the effect of diffraction can cause sound waves to bend around an object where the size of the object is very small in comparison to the wavelength of the sound.

A number of mathematical techniques for predicting the effects of diffraction exist, given the dimensions of the solid object and the wavelength of the sound. The *Huygens-Fresnel* principle, for example, is commonly used to predict diffraction of plane waves incident on an aperture of arbitrary geometry [42].

2.12 Standing Waves and Room Modes

In an acoustic medium, a standing wave is a wave that is characterised by fixed points of minimum pressure fluctuation between fixed points of maximum fluctuation [31]. In other words it is a wave that appears to be stationary. If the medium itself remains in a constant position, standing waves can occur as a result of interference between two waves travelling in opposite directions. This situation

can occur when sound waves are enclosed in a space consisting of at least two acoustically reflective, parallel walls. If a sound wave reflects from one wall to the other and its wavelength is related to the distance between the walls then fixed concentrated points of constructive and destructive interference will be the result, forming a standing wave. Standing waves that occur in acoustic spaces are referred to as *room modes* and their corresponding frequencies as their *modal frequencies*. The relationship between the n th wavelength of a standing wave between two parallel boundaries λ and the distance between the boundaries L is given by (2.38), where $n = 1, 2, \dots \infty$.

$$\lambda = \frac{2L}{n} \quad (2.38)$$

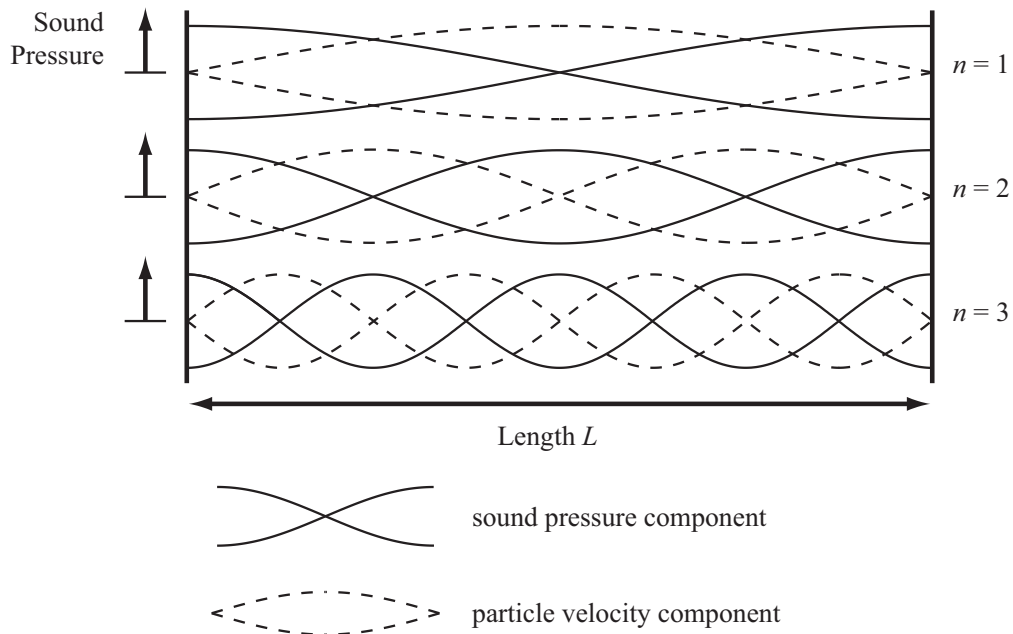


Figure 2.8: Pressure components of standing waves between two parallel reflective boundaries for $n = 1, 2$ and 3 .

It should be noted that for an ideal standing wave, sound pressure and particle velocity have a phase difference of $\pi/2$ radians. This situation is an example of a *reactive sound field* or *near field*, where there is no net flow of energy [43]. In the ideal case where sound propagates in free space with no reflection or interruption, and the distance from its source is large relative to its wavelength, sound pressure and particle velocity are in phase. This is known as an *active sound field* or *far field*, where energy flow exists [43].

Figure 2.8 illustrates the limits in pressure fluctuation that are found when sound waves of single frequencies reflect between two parallel, acoustically reflective boundaries for $n = 1, 2$ and 3 . In this case the particle velocity component of the sound waves are $\pi/2$ radians (90°) out of phase with the pressure component of the waves, and as such are zero at each boundary when standing waves are formed between rigid boundaries. The velocity component of the waves are marked in Figure 2.8 as dotted lines. In the context of room acoustics these standing waves occur between opposing surfaces, such as opposite walls or the floor and the ceiling, and are known as *axial* modes. Standing waves may also occur as a result of cyclic reflection paths between four or six surfaces in the room. These are known as *tangential* and *oblique* modes respectively. Figure 2.9 illustrates two simple examples of cyclic reflection paths.

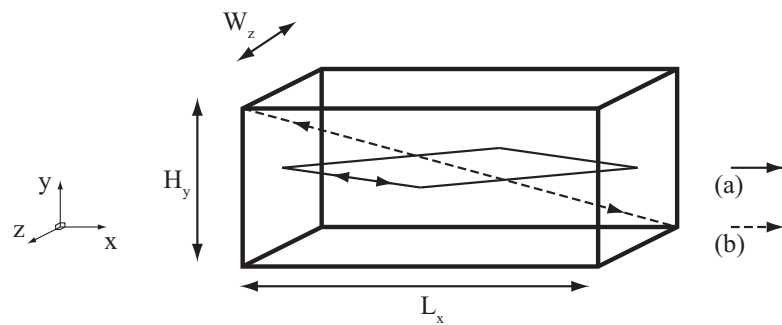


Figure 2.9: A simple cuboid shaped room showing examples of cyclic reflection paths that result in (a) a tangential and (b) an oblique room mode.

The modal frequencies of a simple cuboid shaped room with length L_x (m), width W_y (m) and height H_z (m), as shown in Figure 2.9, are calculated using (2.39), where c is the speed of wave propagation (in m/s). The terms x , y and z are integers that give the number of half wavelengths found in the standing wave between parallel surfaces along the x -axis, the y -axis or the z -axis respectively.

$$f_{xyz} = \frac{c}{2} \sqrt{\left(\frac{x}{L}\right)^2 + \left(\frac{y}{W}\right)^2 + \left(\frac{z}{H}\right)^2} \quad (2.39)$$

If only one of the terms x , y or z in the equation is non-zero, an axial modal frequency is calculated. For example, $f_{1,0,0}$ denotes the lowest axial modal frequency that is the result of a standing wave between the two opposing walls separated by the length L_x . If two of the terms are non-zero, a tangential modal frequency is calculated and

if all three of the terms are non-zero, an oblique modal frequency is calculated.

2.13 The Room Impulse Response

The *room impulse response* is the sound pressure experienced at a point or receiver in an enclosed space that results from the application of an impulse signal of sound pressure at another point in the space, or source. The ideal unit impulse signal, that is impossible to implement in a real system, is known as the *unit impulse function* or the *Dirac delta function*. An ideal unit impulse of sound pressure as a function of time $\delta(t)$ can be defined as:

$$p(t) = \begin{cases} \infty, & t = 0 \\ 0, & t \neq 0 \end{cases} \quad (2.40)$$

It must also satisfy the following identity:

$$\int_{-\infty}^{\infty} \delta(t) dt = 1 \quad (2.41)$$

The Fourier transform of the ideal impulse function (2.42) is a constant, showing that function is composed of all frequencies present in equal amplitude and phase. The impulse response therefore theoretically consists of information relating to how an enclosed space affects a sound source of any audible frequency for a specific location and receiver point. In (2.42), $\delta(f)$ is the Fourier transform of the ideal impulse function $\delta(t)$, i is the imaginary unit and e is the base of the natural logarithm.

$$\begin{aligned} \delta(f) &= \int_{-\infty}^{\infty} \delta(t) \cdot e^{-i2\pi ft} dt \\ &= e^{-i2\pi f0} \\ &= 1 \end{aligned} \quad (2.42)$$

As sound emanates from a source, it travels in all directions in the form of a spherical wave. There are therefore an infinite number of possible paths the sound can take before reaching a receiver. A room impulse response is typically made up of the *direct sound*, the *early reflections* and the *reverberant sound* [31]. The direct sound is the first sound to be experienced by the receiver after the impulse is applied, before any reflected sounds have time to reach it. Sound energy that subsequently reaches

the listener after a small number of reflections, usually from the major boundary surfaces within the space, makes up the early reflections. As sound continues to reach the receiver point after an increasing number of reflections, the time intervals between each subsequent reflection become increasingly smaller. The sound energy becomes weaker, due to absorption at the boundaries of the space, the effect of the inverse square law (2.32) and air absorption. This causes a tail at the end of the room impulse response, made up of a dense set of decaying reflections, known as the reverberant sound.

The reverberation time of a space is defined as the time it takes for the sound pressure of an impulse response to die away from its initial level (caused by the direct sound) by a defined amount. This is commonly chosen to be 60 dB and in this case the reverberation time is known as the *RT60*.

Chapter 3

Diffuse Reflection

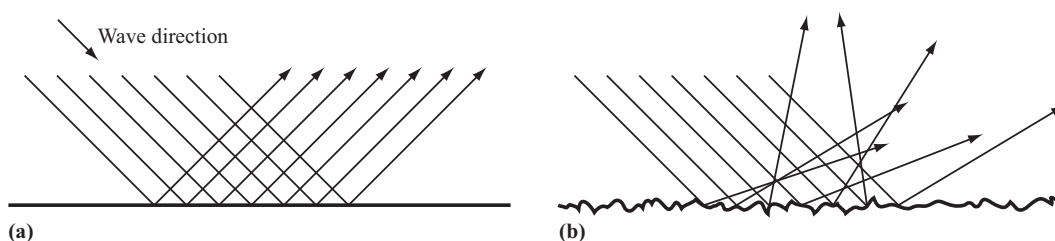


Figure 3.1: Illustration of (a) specular reflections and (b) diffuse reflections.

Specular reflections occur when sound waves reflect from a large surface that is flat and smooth, as illustrated in Figure 3.1(a). However if the surface is not flat or has geometric irregularities then diffuse reflection may occur, Figure 3.1(b). In order for a surface to be smooth, in this context, it must have irregularities that are minute in comparison to the wavelength of the incident sound [8]. As a result of diffuse reflections, sound energy is redistributed across a range of angles upon reflection, rather than being concentrated in the specular direction. If the sound energy is evenly distributed in every possible direction upon reflection, for a given angle of incidence, then this is known as *complete* diffusion.

Surfaces that cause diffuse reflections, also called diffusers, are a useful and important tool in the acoustic treatment of spaces [44].

3.1 Acoustic Diffusers

An acoustic diffuser is any surface that results in diffuse reflection of sound waves. For the purpose of acoustic modelling, it is useful to divide diffusers into two main

categories, referred to as *random rough* and *geometric* diffusers.

3.1.1 Random Rough Diffuser

This is an acoustically reflecting surface that consists of random irregularities that are sufficiently large to cause diffuse reflections. The scale of the irregularities determines the range of frequencies for which the effect of diffusion occurs. If the irregularities are very small in comparison to the wavelength of the incident sound wave, the resulting reflection is non-diffuse, as if from a smooth surface [8]. Owing to this, a frequency dependency is observed in the diffuse reflections caused by such a surface with higher frequencies diffused more effectively than lower frequencies, and with the cut-off frequency determined by the scale of the surface irregularities.

In an computer simulation of room acoustics, such as those described in Chapter 4, certain irregularities can be built into the model with relative ease, if their exact geometry is known and the number of aberrations is small enough that they can be programmed by hand. This method becomes problematic when the boundary is made up of a very large number of surface aberrations with complex non-repeating geometry, making it difficult to measure and reproduce. If this approach is used in the acoustic simulation of a room in order to predict its room impulse response, for example, a map of the roughness of every single diffuse surface would be required and this would be costly in effort and impractical to implement. It is therefore advantageous to approximate the diffuse behaviour of such surfaces using a statistical approach. This can be done either by approximating the shape of the surface and building the approximated shape into the model as described in [45,46, 47] or by approximating the diffuse characteristics of the surface by manipulating the reflected sound, examples of which can be seen in [48,16,49,30]. The choice of statistical approach is largely governed by the modelling paradigm in question.

3.1.2 Geometric Diffusers

Geometric diffusers are surfaces or objects that reflect sound but rather than consisting of random irregularities, they consist of a regular geometry. A geometric diffuser in an acoustic space can take the form of a cylindrical column for example, or a pyramidal extrusion at the surface. Other examples are illustrated in Figure 3.2. Even a finite plane surface causes some scattering, due to reflection and diffraction

effects at its edges.



Figure 3.2: Cross section of three simple geometric diffuser designs.

When modelling a geometric diffuser, for accuracy the shape of the diffuser is built into the model, rather than using a statistical approach. This approach requires that the shape and dimensions of the geometric diffuser are known, and that the irregularities are not too small or complicated for the particular modelling technique in use.

Schroeder Diffusers

With the aim of designing optimal acoustic diffusers, Schroeder proposed a class of diffuser known as the phase grating diffuser [50,10]. Schroeder diffusers offer a design of diffuser that is predictable and is now used commercially to provide sound diffusion in acoustic spaces such as concert halls or studios [51,44,52].

The basic Schroeder diffuser is designed to scatter sound in one dimension and consists of a surface made up by a sequence of depressions or wells separated by thin walls as shown in Figure 3.3. The depth of each well is determined by a mathematical sequence. The scattering effects caused by Schroeder diffusers designed with a range of different mathematical sequences are discussed in [44].

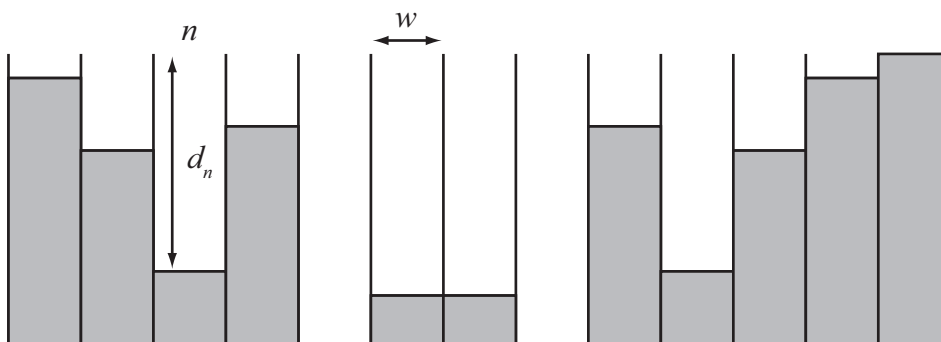


Figure 3.3: Cross section of a Quadratic Residue Schroeder diffuser with sequence length of 13.

The *maximum length sequence* diffuser, introduced in [50], consists of wells with two different depths (one usually being zero) which follow the pseudo-random binary maximum length sequence. The bandwidth of the diffuser is limited in this

case to one octave. The *quadratic residue* sequence [10, 53] is a common choice of sequence for the well depths and can theoretically be used to create diffusers that diffuse sound for any desired bandwidth.

Figure 3.3 illustrates an example of a *quadratic residue diffuser*, in which w is the width of the wells, d_n is the depth of the n th well in the sequence and the period length of the quadratic residue sequence is $N = 13$.

Quadratic Residue Diffuser Design

The width of the wells w is determined by the lower wavelength of the design bandwidth, λ_{min} as follows:

$$w = \frac{\lambda_{min}}{2} \quad (3.1)$$

Sound waves with wavelengths shorter than the lower wavelength, λ_{min} , can form standing waves between the walls of the diffuser wells, and the theory governing the diffuser design no longer holds. However diffuse reflection will still occur due to the geometric shape of the surface.

The quadratic residue sequence with period length denoted by the prime number N is determined by (3.2) where s_n is the n th number in the sequence and modulo denotes the least non-negative remainder after division by N .

$$s_n = n^2 \text{ modulo } N \quad (3.2)$$

As an example, for $N = 13$, the quadratic sequence starting at $n = 1$ would be as follows:

$$s_n = 1, 4, 9, 3, 12, 10, 10, 12, 3, 9, 4, 1, 0; 1, 4, 9 \dots \quad (3.3)$$

The depths of the wells are then determined using a design wavelength, λ_0 . The diffuser will work optimally at the design wavelength and at integer divisions of the design wavelength before λ_{min} is reached. Diffusion at higher wavelengths, by up to two octaves, are also observed however when compared to a flat plane surface [53, 54]. The depth of the n th well d_n is calculated as follows:

$$d_n = \frac{s_n \lambda_0}{2N} \quad (3.4)$$

Schroeder diffusers are a form of geometric diffuser, but are designed to give

optimally diffuse reflection within a specific bandwidth. They also have the advantage in that bandwidth for optimum diffusion can be determined using the simple design equations (3.1) and (3.4).

3.2 Measurement of Diffuse Reflections

Attempts to characterise and quantify the scattering of sound caused by a surface have resulted in the development of two different sets of coefficients, called *diffusion coefficients* and *scattering coefficients* [44]. Using two different approaches, both coefficients give a simplified description of the scattering behaviour of sound at the surface. For many diffuse surfaces, an exact description of the scattering unfortunately requires a large and unmanageable amount of data. For this reason the use of coefficients is an important factor when simulating surface diffusion in computer room acoustics models. The difference between the two coefficients lies in how this data is reduced.

The diffusion coefficient is a measure of how the surface scatters incident sound across the entire range of possible reflection angles. The scattering coefficient on the other hand is defined as the ratio of sound energy that is not reflected in the specular direction to the total amount of reflected energy.

3.2.1 The Diffusion Coefficient

The diffusion coefficient is defined, along with guidelines concerning its measurement, in the Audio Engineering Society (AES) information document for room acoustics and sound reinforcement systems entitled “Characterization and measurement of surface scattering uniformity” (AES-4id-2001) [14]. As the scattering effects of a surface may vary depending on the angle of incidence of the reflected sound, measurements are made for specific angles of incidence. The *directional* diffusion coefficient d_θ is the coefficient measured for the angle of incidence θ , relative to the normal of the surface under test. The mean of the directional diffusion coefficients for n angles of incidence, $\theta_1, \theta_2 \dots \theta_n$ give a diffusion coefficient for the surface denoted by $d_{\theta_1, \theta_2 \dots \theta_n}$. The *random incidence* diffusion coefficient d is calculated if the mean of the directional diffusion coefficients for a sufficiently representative set of angles of incidence is taken. In order to achieve

this condition, the angular separation between each of the source positions used in measurement must be no more than 10° [14].

The diffusion coefficient is calculated in each third-octave band, giving information about the frequency dependency of the diffusion model. The minimum value for a diffusion coefficient is 0, meaning that the reflected sound energy is found in only one direction, and the maximum is 1, which signifies complete diffusion.

Measurement and Geometry

In order to obtain diffusion coefficients for a surface, polar response information for the surface is required. A polar response in this context is the distribution of reflected sound energy across the range of possible angles for a given angle of incidence. Methods for obtaining the polar response of a diffusing surface both on a single 2-D plane of reflection and across the full hemisphere are outlined in [14]. The methods are readily applicable in wave and scattering approaches to computer room acoustic simulation, see section 4.3, with the advantage over real-world measurements that microphones and speakers can be implemented without having any physical presence and without any associated directivity or frequency response.

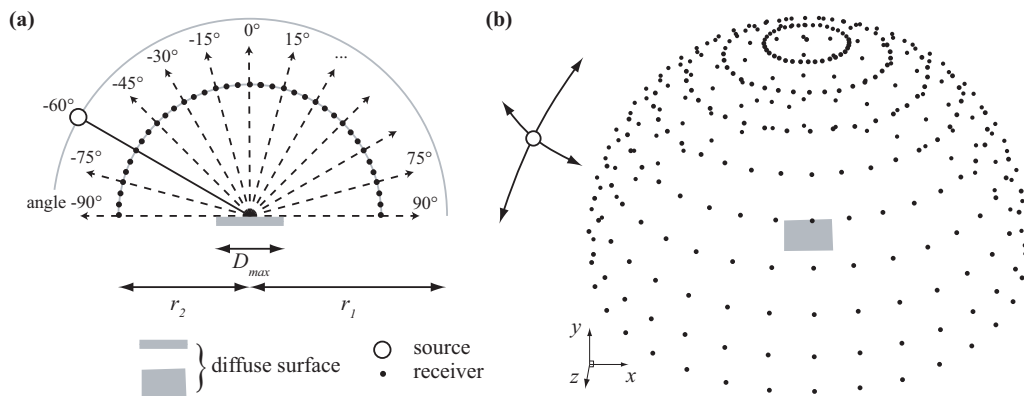


Figure 3.4: Diagram showing possible test geometry for obtaining (a) semicircular 2-D and (b) hemispherical 3-D polar responses, leading to diffusion coefficient measurement.

To obtain the polar response data for a surface, a speaker or source is used to produce sound energy which then causes a reflection from a sample of the surface with a chosen angle of incidence. Microphones or receivers are placed at various points around the face of the surface, equidistant from the centre of the face.

The source and receivers are either placed on a semicircle around the face of the surface in order to give a 2-D polar response, or on a hemisphere in order to give a 3-D polar response. Figures 3.4(a) and (b) show the positioning of the sources and receivers in relation to the surface under examination for 2-D and 3-D polar responses respectively.

According to [14] the maximum angular resolution of the receivers must be 5° in order to give valid results. Also, in order to get a sufficient set of directional diffusion coefficients to calculate the random incidence diffusion coefficient, the maximum angular resolution of the different source positions used must be 10° .

The test must ideally be placed in an anechoic space, so that readings are not compromised by unwanted sound reflections from other surfaces such as the walls, the floor and the ceiling. This can also be avoided by using a room that is sufficiently large in relation to the objects under consideration so that the recorded signals can be windowed in order to remove unwanted reflections.

The distances between source and receivers and the surface under test, as well as the dimensions of the surface are not explicitly defined in [14], however requirements are given that must be met in order to distinguish between *near-field* and *far-field* measurements. Far-field measurements are used to measure the amount of diffusion caused by the surface. Near-field measurements may be used to test the near-field diffusing effects of the surface; this is useful if testing a material under specific near-field conditions, and to test for effects such as focusing.

The ideal conditions in order for far-field measurements to be achieved are given by (3.5), where D_{max} is the largest dimension of the diffuser and λ is the wavelength, or shortest wavelength of sound considered in the test. r is defined by (3.6) where r_1 is the distance from the source position to the centre of the diffuse surface and r_2 is the distance from the receiver positions:

$$\begin{aligned} r &\gg D_{max} \\ \frac{r}{D_{max}} &\gg \frac{D_{max}}{\lambda} \end{aligned} \quad (3.5)$$

$$r = \frac{2r_1 r_2}{(r_1 + r_2)} \quad (3.6)$$

If true far-field conditions cannot be achieved, the minimum requirement is that

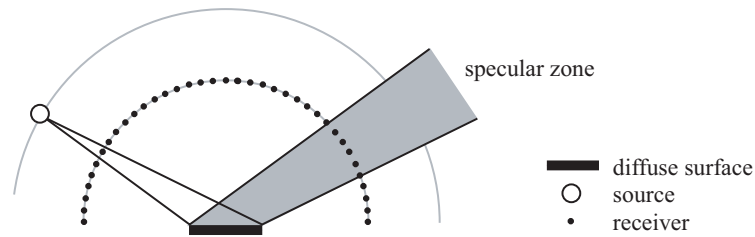


Figure 3.5: The specular zone of reflection.

80% of the receivers in the test are outside of the specular zone of reflection from the diffusing surface. It has been shown that if the number of receivers outside of the specular zone is less than 80%, then the results become invalid [14].

Calculation of the Diffusion Coefficient

In order to calculate the diffusion coefficient for each source position, impulse responses are obtained at each receiver position using the geometry described in the previous section, both with the test surface present, $h_1(t)$ and without, $h_2(t)$. In real world tests using a loudspeaker and microphones, a third set of impulse responses is required for each receiver position, where the diffusing surface is replaced by the loudspeaker and directed at each receiver position $h_3(t)$. This loudspeaker-microphone response is then taken into account using a process of deconvolution [14, 44]. This process also helps to reduce the undesirable effects of reflections and interference caused by equipment in the room, such as microphone stands or wires. Once the data is measured, the *diffuser impulse response* h_4 is calculated for each receiver using (3.7), where $F[\]$ is the Fast Fourier Transform and $F^{-1}[\]$ is the inverse Fast Fourier Transform.

$$h_4(t) = F^{-1} \left[\frac{F[h_1(t) - h_2(t)]}{F[h_3(t)]} \right] \quad (3.7)$$

In acoustic modelling approaches that use wave and scattering methods, signals can be directly applied and measured without the need to implement a physical object such as a microphone or speaker, and so measurement of the loudspeaker-microphone response is not necessary. In this case the diffuser impulse response can be calculated using the following:

$$h_4(t) = h_1(t) - h_2(t) \quad (3.8)$$

The diffuser impulse responses are also windowed so that reflections that are not caused by the test surface are removed from the signal.

Once the windowed diffuser impulse responses h_4 are obtained at each receiver for a fixed source position, their RMS pressure amplitude levels are calculated at each third-octave band of interest. These are then used to obtain the directional diffusion coefficient d_θ . In order to get a measure of the similarity of the pressure amplitude levels at each receiver, and therefore the spatial spread of reflected sound energy caused by the diffuser, an autocorrelation technique is preferred [55]. The following normalised circular autocorrelation function is employed to give R_j , where the receivers are numbered $\kappa = 0, 1 \dots (N - 1)$, and L_κ is the RMS level measured by the respective receiver. N is the total number of receivers used in the test:

$$R_j = \frac{\sum_{\kappa=0}^{N-1} 10^{L_\kappa/10} \cdot 10^{(L_{(\kappa+j) \bmod N})/10}}{\sum_{\kappa=0}^{N-1} (10^{L_\kappa/10})^2} \quad ; \quad j = 1, 2 \dots (N - 1) \quad (3.9)$$

The average is then taken to give a single figure diffusion coefficient $d_\theta = \bar{R}_j$. This process can be compacted into a single equation:

$$d_\theta = \frac{\left(\sum_{\kappa=0}^{N-1} 10^{L_\kappa/10} \right)^2 - \sum_{\kappa=0}^{N-1} (10^{L_\kappa/10})^2}{(N - 1) \sum_{\kappa=0}^{N-1} (10^{L_\kappa/10})^2} \quad (3.10)$$

The formulation (3.10) assumes that each receiver is representative of the same amount of sample area in the polar response. In the case of the single plane 2-D polar response, this is achieved by spreading the receivers evenly around the semicircle, as shown in Figure 3.4(a). Note however that the receivers at $\pm 90^\circ$ sample a representative area that is only half that sampled by the other receivers in this case. This can be ignored however, as the effect that this disparity has on the calculated diffusion coefficient is insignificant [44].

If the area sampled by the receivers is uneven, then the following equation must

be used instead, where Q_κ is proportional to the area sampled by receiver κ :

$$d_\theta = \frac{\left(\sum_{\kappa=0}^{N-1} Q_\kappa 10^{L_\kappa/10} \right)^2 - \sum_{\kappa=0}^{N-1} Q_\kappa (10^{L_\kappa/10})^2}{(N-1) \sum_{\kappa=0}^{N-1} Q_\kappa (10^{L_\kappa/10})^2} \quad (3.11)$$

For hemispherical measurements, used to give the full 3-D polar response, it is not so trivial to ensure that each receiver is sampling the same size of area on the hemisphere. The simplest way to measure across the hemisphere is to use equal angular spacing between the receivers in azimuth and elevation, although this results in an uneven size of area sampled by the receivers. Figure 3.6 shows what is meant by the angle of azimuth ϕ and the angle of elevation ω with respect to the test surface, where the angle of elevation is relative to the Normal.

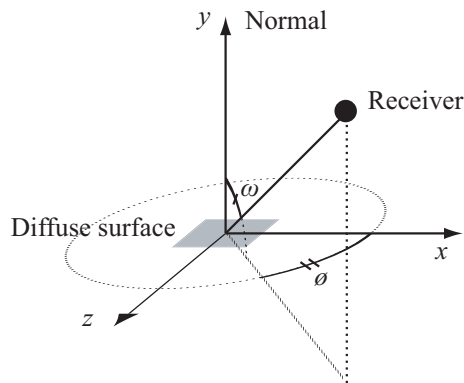


Figure 3.6: Diagram showing angles of azimuth ϕ and elevation ω of a receiver with respect to the test surface.

If receivers are placed on the hemisphere and are separated by equal angles in azimuth and elevation, the following equations can be used to give Q_κ , for each receiver point, where $\Delta\phi$ and $\Delta\omega$ are the angular separations between receivers in azimuth and elevation respectively. A_{min} is the smallest value of A_κ calculated for

all receivers.

$$A_{\kappa} = \frac{4\pi}{\Delta\phi} \sin^2\left(\frac{\Delta\omega}{4}\right) \quad \omega = 0^\circ \quad (3.12)$$

$$A_{\kappa} = 2 \sin(\omega) \sin\left(\frac{\Delta\omega}{2}\right) \quad \omega \neq 0^\circ, |\omega| \neq 90^\circ \quad (3.13)$$

$$A_{\kappa} = \sin\left(\frac{\Delta\omega}{2}\right) \quad |\omega| = 90^\circ \quad (3.14)$$

$$(3.15)$$

$$Q_{\kappa} = \frac{A_{\kappa}}{A_{min}} \quad (3.16)$$

Discussion

The nature of the measurement technique used in the calculation of the diffusion coefficient requires that a finite sample of the diffuse surface is used and this is problematic for two reasons. The first is that scattering effects will occur as a result of sound reflecting from the edges of the sample, with the result that even a plane specular reflecting surface will cause some scattering and therefore yield a diffusion coefficient that is greater than zero. It is therefore good practice, when considering diffusion coefficient results from a diffuse surface, to have at hand diffusion coefficients from a flat plane surface of the same dimensions and measured under exactly the same test conditions for comparison.

The second issue again is a result of the finite size of the test sample. If reflection from a plane surface of finite size is considered, then a cut-off frequency is observed above which the surface causes strongly specular reflection, when the wavelength of the sound is small relative to size of the surface. Below this cut-off frequency however, when the wavelength becomes larger relative to the size of the surface, diffraction effects begin to dominate and the reflected sound from the surface becomes attenuated and more diffuse [44]. Eventually, if the wavelength is very large compared to the surface, then no reflection will occur as the panel will have no effect on the sound wave. The effect on the reflected energy is similar to that of a hi-pass filter. The diffusion coefficient measurement technique is therefore only valid above this cut-off frequency. A method to calculate the cut-off frequency is proposed in [56] using a Fresnel integrals approximation. A similar attenuation of reflection strength below this cut-off frequency is observed when a diffuse surface is considered.

For a panel with width $2a$, where r_1 is the distance between the source and the panel centre at angle of incidence θ , r_2 is the distance between the receiver (preferably placed in the specular zone of reflection) and the panel centre and c is the speed of sound, the -3 dB cutoff frequency, f_{-3dB} of the reflected sound is given by (3.17). The equation assumes the panel is square in shape.

$$f_{-3dB} = \frac{c \left(\frac{2r_1 r_2}{r_1 + r_2} \right)}{8a^2 \cos^2(\theta)} \quad (3.17)$$

3.2.2 The Scattering Coefficient

The definition of the scattering coefficient and its real-world measurement are detailed in the International Organization for Standardization (ISO) document entitled "Acoustics - Sound-scattering properties of surfaces - Part 1: Measurement of the random-incidence scattering coefficient in a reverberation room" (ISO 17497-1:2004) [13] and in [57]. If sound reflects from a rough surface, a proportion of the reflected energy is found in the specular direction and the rest is scattered in a non-specular distribution. The scattering coefficient is defined as the ratio between this non-specular reflected sound energy and the total reflected sound energy.

Measurement

Considering the energies of reflection at a surface with an absorption coefficient α_s , normalised to reflection from a non-absorbing flat surface, the total energy of reflection, E_{total} , is given by:

$$E_{total} = 1 - \alpha_s \quad (3.18)$$

The non-specularly reflected energy E_{scat} and the specularly reflected energy E_{spec} can therefore be determined, given the scattering coefficient s :

$$E_{scat} = s(1 - \alpha_s), \quad E_{spec} = (1 - s)(1 - \alpha_s) \quad (3.19)$$

A new coefficient is defined for the purpose of the measurement procedure, known as the *apparent specular absorption coefficient*, α_{spec} . This is the apparent absorption observed in the specular direction only, which results from the absorption of the surface and the dispersion of energy to non-specular directions. Mathematically, it

is described in the following definition:

$$E_{spec} = (1 - s)(1 - \alpha_s) \equiv (1 - \alpha_{spec}) \quad (3.20)$$

From (3.20) it is possible to derive an expression for the scattering coefficient s in terms of the absorption coefficient of the surface α_s and its apparent specular absorption coefficient, α_{spec} :

$$s = \frac{\alpha_{spec} - \alpha_s}{1 - \alpha_s} \quad (3.21)$$

A method for measuring the random incidence scattering coefficient in the diffuse field, by acquiring the random incidence apparent specular absorption coefficient and the random incidence absorption coefficient of a sample of the diffuser or surface under test, is outlined in the ISO document [13] and in [57]. The test takes place inside a reverberation chamber. The diffuse surface is placed on a rotating turntable, and a sound source and receiver positioned above it, as shown in Figure 3.7. The surface must be circular in shape, otherwise the results will be overly contaminated by the scattering effect caused by reflection at its edges.

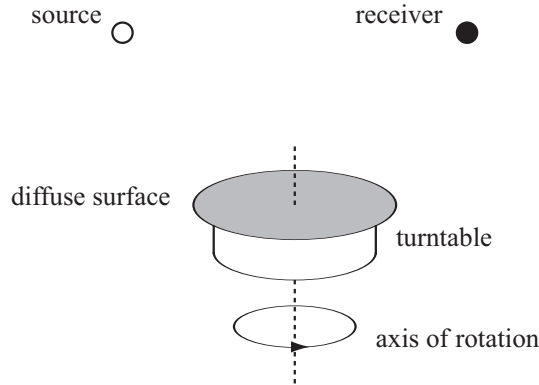


Figure 3.7: Diagram showing the test geometry used for measuring the scattering coefficient.

In order to measure the scattering coefficient, reverberation times must be measured under four different conditions using the standard procedure outlined in [58]. The first reverberation time T_1 is measured with the test sample not present and the turntable not rotating, the second T_2 is measured with the sample present and the turntable not rotating, the third T_3 is measured with the test sample not present and the turntable rotating and finally the fourth T_4 is measured with the test sample present and the turntable rotating. With the turntable rotating (T_3 and

T_4), multiple phase-locked impulse responses (typically 72 for one rotation [44]) are measured. The impulse responses are then averaged before the reverberation times are taken. The theory is built on the assumption that the components of the impulse response that result from scattering at the surface of the turntable are averaged out in the process, leaving only the impulse response that results from the specular reflection. T_1 and T_2 are calculated using impulse responses measured with the turntable not rotating, therefore only one impulse response is required each time as no averaging takes place. The result is impulse responses both consisting of the specular energy and the scattered energy (as it is not cancelled by averaging this time). The reverberation times T_1 and T_3 , taken in the absence of the test sample, are required in order to cancel out the effects of imperfections in the measurements such as those caused by a turntable that is not perfectly flat and circular [44].

The reverberation times are used to calculate both the random incidence absorption coefficient of the diffuser caused by specular and diffuse reflections, α_s and the apparent specular absorption coefficient, α_{spec} using (3.22) and (3.23). In the equations, V is the volume of the reverberation room, S is the area of the diffuser sample, c_q is the speed of sound in air and m_q is the energy attenuation coefficient of air during the measurement of the reverberation time T_q , where $q = 1, 2 \dots 4$.

$$\alpha_s = 55.3 \frac{V}{S} \left(\frac{1}{c_2 T_2} - \frac{1}{c_1 T_1} \right) - \frac{4V}{S} (m_2 - m_1) \quad (3.22)$$

$$\alpha_{spec} = 55.3 \frac{V}{S} \left(\frac{1}{c_4 T_4} - \frac{1}{c_3 T_3} \right) - \frac{4V}{S} (m_4 - m_3) \quad (3.23)$$

The random incidence scattering coefficient for the test sample is then calculated using (3.21).

Discussion

The nature of this method means that the random incidence scattering coefficient can be found without the need to repeat the measurement for multiple source positions, as is the case for the diffusion coefficient measurement. A similar test can be performed in a free-field environment, rather than in a reverberation chamber, as described in [59], which gives an indication as to the scattering effect of the surface at different angles of incidence. However owing to the requirement that the test sample

be rotated, true incidence dependent scattering coefficients are not determined in this way, but rather scattering coefficients that are measured at specific angles of elevation of the incident sound, but are still partly random incidence in terms of its angle of azimuth. This lack of distinction between different angles of azimuth also means, for example, that the scattering effect of diffusers that are designed to diffuse sound in only two dimensions cannot be measured in this way (either using the reverberation chamber method or the free field method).

The effect of scattering at the edges of the sample can, as in the case of the diffusion coefficient, colour the scattering coefficients measured using this technique and if the structural depth of the surface is too large then the results can even become invalid because of reflections caused by edge scattering [44, 60]. The limit of the structural depth h of the sample if it has a diameter d is given approximately by $h \leq d/16$, however even under this limit the measured scattering coefficient can be higher than it should be, as is evident when measured scattering coefficients are found to be greater than one [44].

3.2.3 Comparison of Diffusion and Scattering Coefficients

In summary, the diffusion coefficient is a measure of the uniformity of reflected sound energy from a diffuse surface across all angles of reflection, whereas the scattering coefficient is a measure of the fraction of reflected energy that is non-specular. It follows that the 2 coefficients will not necessarily correlate for certain diffuse materials. This is demonstrated by the very simple example illustrated in Figure 3.8(a), showing a hypothetical 2-D polar plot where the sound energy reflected from a surface is concentrated in one direction, but at a different angle to the specular angle of reflection. In this case the diffusion coefficient would be low, similar to that of a flat plane surface, as the energy is not spread across all angles of reflection. The scattering coefficient however would, by definition, be a high value as most of the reflected energy is non-specular. Figure 3.8(b) shows a hypothetical polar plot representing a diffuse surface that would yield both a high scattering coefficient and a high diffusion coefficient, because the energy is spread evenly across all angles of reflection.

A high scattering coefficient means only that the energy is moved from the direction of specular reflection, but does not give any indication of the quality of

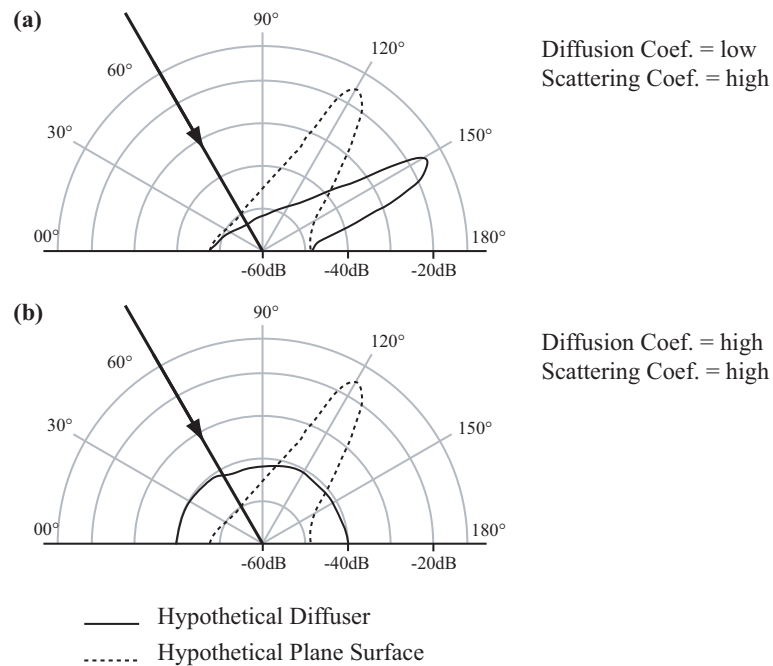


Figure 3.8: Hypothetical polar responses of a reflective surface that (a) yields a high scattering coefficient but a low diffusion coefficient and (b) yields both a high scattering coefficient and a high diffusion coefficient.

the diffuse reflection that results from the boundary. The diffusion coefficient on the other hand gives a more reliable indication as to the spread of energy caused by the diffuser, but does not give any indication as to whether or not the reflected energy is concentrated in the specular direction. Energy that is concentrated in non-specular directions upon reflection may occur if the surface has irregularities that are relatively large both compared to its size and to the wavelength of the sound, in particular if they are not random. A triangular or pyramid shaped geometric diffuser is a good example of this [44]. However in the case where the surface consists of random irregularities that are small compared to its size and the overall geometric shape of the surface appears flat if the small irregularities are ignored, then the reflected energy, if not completely diffuse, will still be concentrated to some extent in the specular direction.

Apart from a clear difference in the definition of the two coefficients, the method by which they are measured are also very different. Measurement for the diffusion coefficient requires preferably anechoic conditions and true far field measurements are difficult to acquire due to the large distances between source/microphones and the diffusing panel that are required. Measurement for the scattering coefficient can take place in a reverberation chamber but requires a strong and extremely level

rotating turntable that rotates at an accurate and consistent speed. It also requires that the test surface be perfectly circular in shape. Both techniques require accurate positioning of source and microphones. Diffusion coefficients can be measured for any angle of incidence, whereas using the measurement system described in section 3.2.2, only the random incidence scattering coefficient can be measured. The scattering coefficient measurement is therefore not useful in measuring the directional effect of diffusers that are designed to work in one plane of reflection or a limited number of planes, such as Schroeder diffusers as discussed in section 3.1.2. However if the random incidence diffusion coefficient is required, a far greater number of tests are needed than for the random incidence scattering coefficient measurement. Both measurement techniques also have problems caused by the finite size and scattering effects at the edges of the sample under measurement.

Prediction Techniques

One approach to obtaining diffusion and scattering coefficients is to predict the surface scattering using computer modelling techniques rather than by using real world measurements [44]. The most accurate computer model for the purpose of scattering prediction is the *boundary element method* (BEM) [44,61]. This approach is particularly suited to geometric diffusers and Schroeder diffusers, as their geometry and dimensions can be accurately mimicked in a computer model. Randomly rough surfaces, where the sizes of the irregularities are small relative to the diffuser under test can however be problematic as the surface geometry is difficult to accurately reproduce in a computer model.

Although successful attempts have been made to mimic the scattering coefficient measurement using the BEM [62], the work was proven to be costly both in time and effort because both a complex model and a very large number of measurements are required. Obtaining the polar response data necessary for the diffusion coefficient measurement is far more straight forward, and has shown to be accurate when compared to measured responses [44, 61, 63]. Owing to the nature of the BEM technique, large distances between source/receivers and the test surface are readily implemented, distances that would render real world measurements very difficult or even impossible, and so true far-field diffusion coefficient measurements can be obtained without any problem.

3.2.4 The Correlation Scattering Coefficient

A method to calculate a type of scattering coefficient, named the *correlation scattering coefficient* s_c , by correlating polar response data (see section 3.2.1) from a diffuse test surface and a reference flat surface is presented in [64] and [65]. For a single plane 2-D polar response, the correlation scattering coefficient is calculated using (3.24), where $p_{-1}(\kappa)$ is the complex amplitude at receiver κ (N receivers in total) measured for a diffuse surface and $p_{-0}(\kappa)$ is the complex amplitude at receiver κ measured for a flat specularly reflecting surface of the same proportions. $p_{-0}^*(\kappa)$ is the complex conjugate of $p_{-0}(\kappa)$. As with the 2-D polar responses described in 3.2.1, the angle between each consecutive receiver is constant.

$$p_{-1}(\kappa) = 1 - \frac{\left| \sum_{\kappa=0}^{N-1} p_{-1}(\kappa) \cdot p_{-0}^*(\kappa) \right|^2}{\sum_{\kappa=0}^{N-1} |p_{-1}(\kappa)|^2 \cdot \sum_{\kappa=0}^{N-1} |p_{-0}(\kappa)|^2} \quad (3.24)$$

In order to calculate the correlation scattering coefficient from a 3-D response, the angle of azimuth must also be considered in the calculation and a weighting factor must be introduced to account for the uneven areas sampled by each receiver point, unless the receivers are separated by equal solid angles. This process is described in detail in [65].

As it uses a very different approach to measurement than the scattering coefficient described in section 3.2.2 and in [13], the correlation coefficient does not always give the same results and the two coefficients cannot therefore be directly compared [44]. However it is consistent with the definition of the scattering coefficient as a measure of the fraction of reflected energy that is non-specular. An advantage to this method is that, so long as a flat surface with the same dimensions as the diffuser is used as the reference, the effect of diffraction and reflection caused by the diffuser edges rather than the diffuser itself are compensated for.

Chapter 4

Acoustical Modelling

There are currently three main approaches to modelling an acoustic space,. These approaches are referred to as *acoustic scale modelling*, *ray-based computer modelling*, also referred to as geometric acoustic modelling and *wave-based computer modelling*.

4.1 Acoustic Scale Modelling

Using this method, a physical scale model of the space under consideration must first be constructed. The acoustics of the model can then be measured and this information can then be scaled up to give the acoustical characteristics of the full sized room that is being modelled [7]. Wavelengths of the sound used in tests must be scaled for the model. For example, considering a room model at a scale of 1:10, measurements are carried out at frequencies ten times greater than the frequency range of interest for the full scale room. Surfaces in the room ideally have the same acoustical characteristics as the full size room, however if these characteristics are frequency dependent then their characteristic frequency dependency should be scaled up according to the scale of the model. For example in order to implement the frequency dependent absorption characteristics of a carpet in a scaled down model, a material must be chosen that ideally has identical absorption characteristics but that are shifted up in the frequency spectrum by the correct amount. This is often difficult to achieve in practice and the cost of producing materials that absorb sound according to a specified frequency dependency is high.

Expensive and sensitive measuring equipment is also required to accurately measure the acoustic properties of the modelled room. Appropriately small

loudspeakers are used to feed an audio signal into the space, which is then in turn recorded by microphones. These transducers must be small in order to fit into the space and to minimise the effect that they have on the acoustics of the space as a result of their physical structure. They must also be able to accurately produce and record sounds at the higher scaled frequencies required by the model. The frequency response of these transducers must also be taken into account in order to gain an accurate acoustic response for the space. It is possible to compensate for the transducer response by processing the impulse response that is obtained by the model, as described in [66].

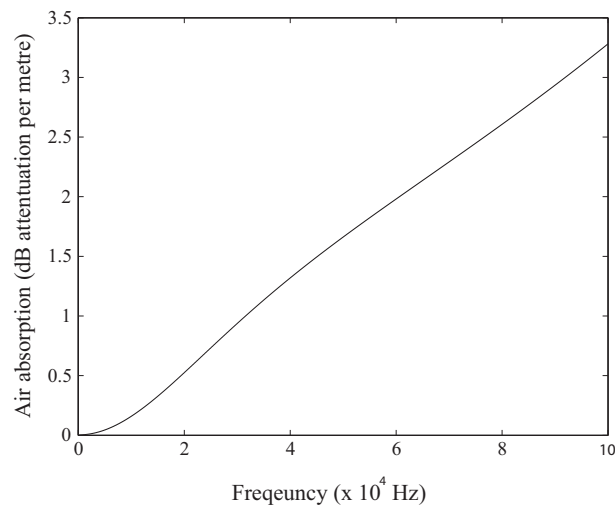


Figure 4.1: Graph showing calculated air absorption of sound in dB attenuation per metre in relationship to frequency, according to [39].

The advantage of this technique is that, although operating at a scaled up frequency that must later be compensated for, the sound propagation itself is real, with the result that the model is highly accurate. However, the frequency dependent nature of air absorption causes complications with acoustic scale models, as air absorption increases significantly with increasing frequency. According to the defined equations for calculating air absorption as specified in the International Organization for Standardization (ISO) document entitled “Acoustics – Attenuation of Sound During Propagation Outdoors – Part 1: Calculation of the Absorption of Sound by the Atmosphere.” (ISO 9613-1) [39], air absorption properties do not increase linearly with increasing frequency, particularly for frequencies up to about 20 kHz. Figure 4.1 gives air absorption in dB attenuation per metre plotted against frequency up to 100 kHz according to [39]. The absorption is calculated using

the standard air pressure at sea level, 101.325 kPa, an air temperature of 20°C and a relative air humidity of 50%. A solution to this problem is either to treat the air by reducing its humidity, or to replace it with nitrogen [7]. Another less expensive solution is to compensate for the error caused by excessive air absorption by processing the resulting measured impulse response [66].

4.2 Ray-based Computer Modelling

In this approach to room acoustics modelling, the shape and dimensions of the room are programmed into a computer, as well as information about the acoustical characteristics of the surfaces and the air. Sound waves are modelled as rays that travel in a straight line until they come into contact with a surface, upon which, unless a diffusion algorithm has been built into the model, they reflect specularly, according to Snell's law, and continue their journey. This technique is very similar in principle to the *ray-tracing* technique used to model light rays in geometrical optics.

In a ray-based model, the rays represent the wave-front of the sound wave. The rays begin their journey from a source, with a certain amount of sound energy attributed to each of them across a range of frequencies. This energy is attenuated as part of the overall model as the source signal propagates according to the inverse square law as described in section 2.8. Frequency dependent absorption upon reflection of different surfaces is implemented by attenuating the sound energy according to the absorption coefficient of the surface. Air absorption can also be implemented in the model by attenuating the sound energy associated to the ray according to the distance it has travelled.

The simplest ray-based model does not by its nature account for diffraction or interference effects. This model is therefore most effective in conditions where diffraction effects are at a minimum. Such conditions occur if surfaces in the modelled space are of dimensions that are large in comparison to the largest of the range of wavelengths of interest in the model, and also if the surfaces do not behave as diffusers. The result is that the model is limited in terms of accuracy to modelling high frequency sound propagation in large spaces with non-diffuse surfaces that are proportionally large.

The most commonly used techniques in ray-based acoustic modelling are the *image source method*, *ray-tracing* and *diverging beam-tracing*. The basic principles of these are described in the following sections. Methods to extend the models to approximate the effects of diffraction and diffuse surfaces in order to improve their accuracy are also discussed.

4.2.1 Image Source Method

Figure 4.2 shows a first order specular reflection, illustrating the source of the sound wave and its corresponding image source. The image source and the actual sound source are found equidistant to the surface edge, but on opposite sides. The actual source and the image source are connected by a straight line that runs perpendicular to the surface edge. Figure 4.3 illustrates examples of higher order image sources in a simple rectangular space. The order of the image source corresponds to the number of reflections within the space that are under consideration.

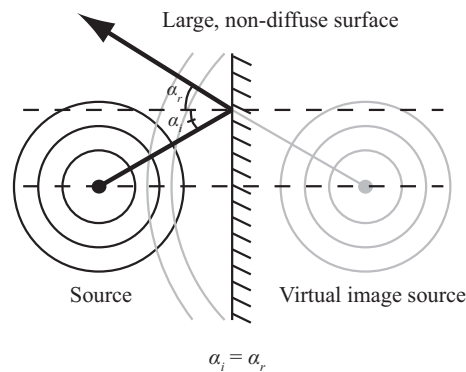


Figure 4.2: A first order specular reflection with its corresponding image source.

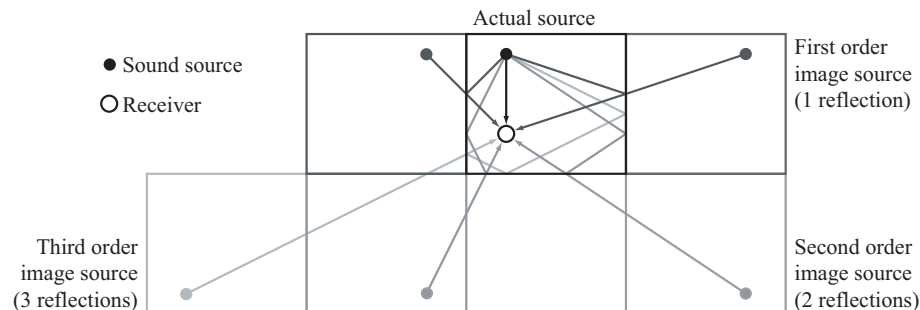


Figure 4.3: Diagram showing reflections of sound in a room and the corresponding image sources.

The image sources are considered as individual sound sources, from which

sound rays are emitted directly towards the receiver. The time that the sound ray takes to reach the receiver from the image source is determined by the distance between the image source and receiver. Attenuation is applied to the sound ray depending on the total distance travelled and also upon the frequency dependent absorption caused by reflection at relevant surfaces [67,17,68,69].

If a simple cuboid shaped room is considered where all the surfaces are reflective, such as the room illustrated in Figure 4.3, the number of image sources required increases exponentially with the order of reflections. Even in this simple case, it is clear that a great number of image sources are required to give a full impulse response where large numbers of reflections are considered. The number of image sources becomes even greater for more complex room shapes with a larger number of surfaces. In addition, *visibility checks* are required to test that image source is *visible* from the point of view of the receiver [70]. This is because some image sources become ineffective due to occlusion.

Edge Diffraction and Boundary Diffusion in the Image Source Method

Diffraction can be implemented as part of the image source model by introducing secondary sources at the edges of surfaces where the diffraction effect is expected. Paths can then be calculated between these sources and the receiver, as well as from the original source, therefore emulating diffraction effects [71]. The frequency dependent nature of the diffraction, based on the geometry of the surface and the angle of incidence of the sound, can be approximated in the model using a digital filter, the design of which is determined according to an approximate diffraction model [56,72].

Scattering at surfaces can also be approximated by generating a secondary source for each interaction with a diffusing surface. This approximation can be extended to generate a number of extra sources designed to create a blurred, diffuse image. The use of extra sources, known as *image source clouds* was originally proposed as a method for modelling diffuse reflection in the early development stages of the CATT-Acoustic computer program [9,73]. The incident angles and positions of the extra sources are designed to emulate the scattering of energy away from the specular direction. However, their introduction causes problems as the number of reflections becomes high (typically in the order of 10000) because the number

of sources is also high, resulting in a large increase in the computational power required by the model [74]. For this reason the model is impractical for modelling the later part of the impulse response.

Another approach to modelling diffuse reflection in the image source method is described in [75]. In this method, diffuse reflections are modelled simply by applying a special filter to the reflected sound that attenuates the signal and causes a smearing effect in the subsequent reflection. This model is extremely limited however, because the spread of energy away from the specular direction that is caused by diffuse reflection is not modelled at all. In other words the reflection is still completely specular but is simply filtered, and only the resulting smearing of the signal caused by diffuse reflection is taken into account.

4.2.2 Ray-Tracing

The basic principle behind ray-tracing techniques is in following or 'tracing' the paths of rays that are emitted from a source in a number of different directions within the modelled space [16,76]. In order to get most accurate results from the process, ideally an infinite number of rays are required in order to trace the path of sound in every possible direction from the source. In practice, a finite number are used, whose directions are evenly distributed across the desired directional range from the source. In the case of a point source, they would be distributed across the entire sphere of radiation from the source [16,77].

An approximation to the room impulse response of the space is achieved by recording the sound energy and arrival times of rays at a designated listening point, known as the *detector*. Typically the sound rays used in the process are infinitely small and so the detector must be implemented with sufficient dimensions in order for rays to actually come into contact with it, and not simply pass it by. The detector must detect the sound rays but at the same time must be transparent to them. If the detector is too large the results become distorted because the detector is struck by too many rays that should in fact be invisible to the source and the measured sound energy becomes inaccurate. A compromise must therefore be found when deciding the dimensions of the detector and this is an inherent source of inaccuracy for this method.

If a finite number of sound rays are considered diverging from a point source in

an open space, the distance between each ray increases. The area of physical space potentially capable of supporting sound propagation that is not taken into account by the model as the rays travel away from the source inevitably increases, no matter how many sound rays are considered. As a result of this, the accuracy of the ray representation decreases as the ray paths diverge. Clearly, the larger the number of rays used, the more accurate the results, but at greater computational expense.

The advantage of ray-tracing over other ray-based modelling techniques is that it is most suited to the possible extension of the model to include surface scattering effects.

Diffuse Reflection in the Ray-Tracing Method

Typically, surface scattering is modelled in the ray-tracing model using a statistical approach [28, 48, 16, 49]. Upon reflection, each ray is either reflected specularly, or its direction is moved away from the specular direction and is chosen according to a random probability function. If the reflection of rays at the surface are always determined by the random probability function, then the modelled surface is completely diffuse, its scattering coefficient is theoretically 1. For partially diffuse surfaces, the probability that the ray will reflect specularly or not is determined by a scattering coefficient assigned to the surface [49]. This process is described in the form of a flow-chart, Figure 4.4. For reference, the definition of Snell's law is given in section 2.9.

The random probability function, used to decide the direction of the reflected ray if it is not a specular reflection, determines how the sound energy is distributed upon reflection. The choice of this probability function when designing the model ideally should depend on the diffuse characteristics of the surface being modelled, however this is difficult to implement in practice. A common approach is to distribute the reflected energy according to Lambert's Cosine Law [28], a diffusion model with roots in optical ray-tracing. The law states that the amount of reflected energy found at a particular direction from the point of reflection at the surface is proportional to the cosine of the angle between the direction of the reflected energy and the normal of the surface, irrespective of the incident angle of the wave. Measured polar responses from diffuse surfaces however show that this assumed independence between energy distribution and angle of incidence is inaccurate in most cases

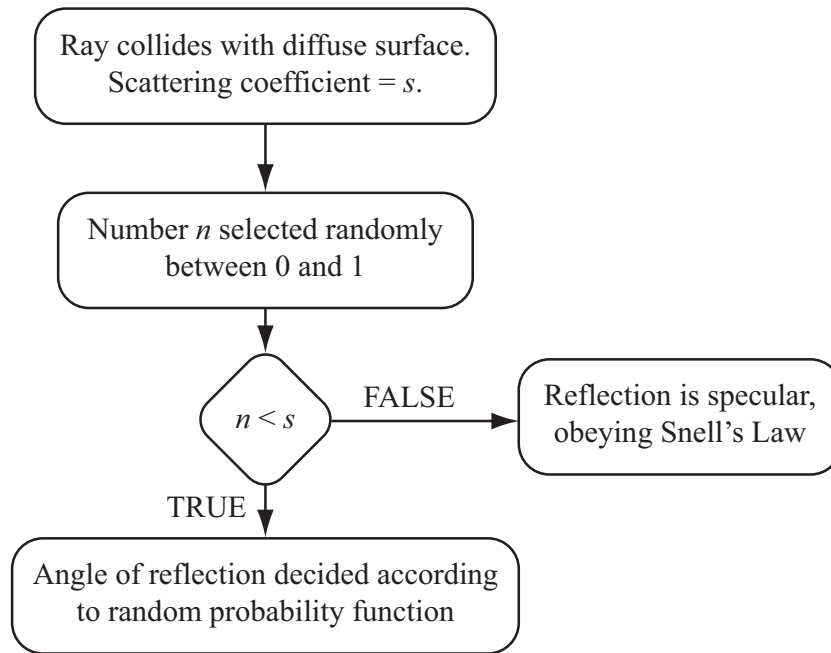


Figure 4.4: Flow chart describing a technique for implementing diffuse reflection in the ray-tracing model.

[47,44]. Accuracy could be improved by implementing probability functions that are designed to give energy distribution based on recent work and data acquired in measuring or predicting the diffuse characteristics of surfaces, as described in Chapter 3.

The surface scattering method can be further improved if each ray generates a number of new rays upon contact with a diffuse surface. The strength and direction of the new rays are also determined by a distribution function, however this approach greatly increases the computational expense of the ray-tracing model, particularly in cases where a relatively large number of surface are diffuse and a large number of reflections are considered [74].

In order to model frequency dependent diffuse reflections, the process is repeated at different frequency bands and the scattering coefficient is adjusted accordingly for each repeated simulation [74]. A method to provide frequency dependent surface scattering that eliminates the need to repeat the simulation for different frequency bands is suggested in [49], however this method results in statistical error that requires further computational effort to correct.

The basic scattering model described here only gives an approximate model for surface scattering and in reality results in diffuse reflections that are inaccurate

compared to measured or predicted scattering responses. This inaccuracy is particularly true when considering only a small number of reflections and particularly affects the early reflections of a room impulse response. The result of the model is to give early reflections that are not smeared as a result of the diffuse reflection, but are the same strength, or even stronger, and with incorrect timing. The method is improved with increasing numbers of rays, because the representative sound power of each ray is decreased [9].

Despite the errors of the model, its implementation has been found to significantly improve the overall performance of the model, in particular the determination of decay curves in the later part of the impulse response, when compared to room impulse responses measured in the real world [25,78,79,26].

Extending the Ray-Tracing Method to Model Diffraction

The issue of modelling diffraction in the ray-tracing method is both important and non-trivial, owing to the complex nature of sound diffraction which is heavily dependent on frequency, the boundary dimensions and angle of incidence. Existing approaches are typically based on mathematical models designed to predict the diffraction properties of a boundary for an incident sound. The most common method is equivalent to the technique described previously for the image source method. Diffraction is modelled by introducing a secondary sound source at the corners of objects or protruding sections of the boundary in the modelled space. The frequency dependent nature of the diffraction impulse response is determined using a mathematical approximation [56,80]. This can either be taken into account using multiple passes for different frequency bands, or using a digital filter implementation, with an impulse response designed to match the diffraction impulse response [72].

4.2.3 Approximate Beam-Tracing

Sound propagation in a beam-tracing technique is described by a number of diverging beams travelling away from a source, as opposed to the ray-tracing technique where the rays that are infinitely small [81]. In this case the detector can be any size, because the beams cover all possible angles of radiation. In the basic beam-tracing model, when the beams come into contact with the detector,

their path is traced according to the reflection history of their central point. This is sometimes referred to as an *approximate* beam-tracing model. The original beam-tracing methods use conical shaped beams, however pyramidal beams are advantageous because they remove the necessity for the beams to overlap in order to cover the entire sphere of radiation [81], as illustrated in Figure 4.5. This avoids problems in the model caused by multiple detections of the same path being traced by different beams.

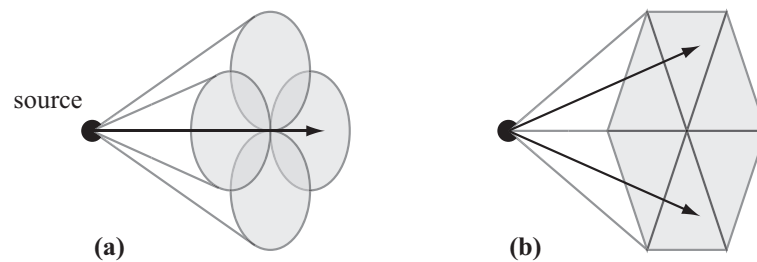


Figure 4.5: Illustration of (a) conical and (b) pyramidal diverging beams radiating from source.

The main advantage of this approach is that it is relatively cheap computationally, however as the length of each beam increases along with the number of reflections, the area covered by the front of the beam also increases. This causes problems as, in the basic model, the beams' reflection histories are calculated by following their central points, and the larger beam-fronts are far more likely to come into contact with more than one surface. This is the reason such models are given the title *approximate* beam-tracing.

As an enhancement to the basic model, if a beam comes into contact with a surface edge, or if it comes into contact with more than one surface or wall at the same time, the beams can be split, so that the new beams that result can move in different directions, thus reducing error [82,83]. Diffraction effects are approximated by the introduction of new sources at the edges of objects [84,85], a similar technique to that used for the image source technique.

Diffuse Reflection in the Approximate Beam-Tracing Method

A technique for implementing diffuse reflections in an approximate cone tracing model is outlined in [74]. In this method, each diffusing surface is divided up into square shaped areas that cover the entire surface. The basic principle behind

the method is that each area acts as a detector that records the history of beam reflection and the reflection timing for that particular part of the surface. They can also act as sources, and this is how the diffuse reflections are modelled. A number of simulations, or passes are then performed. In the first simulation, only the specular component of the reflection is modelled at each boundary and only the main source is considered. The reflection history is recorded at each section of each diffuse surface. On the second pass, a second response is measured in which each section of diffuse surface now acts as a source, triggered by the reflection history recorded at the previous pass. This response is added to the first response, so that the response caused by specular reflection and the response caused by first-order diffuse reflection are now considered. At the same time, the reflection history at each area of diffuse surface is again recorded, to be used in the next pass. The process then repeats itself until an adequately high-order of diffuse reflection is accounted for.

Evidently, in order to approximate diffuse reflection for a sufficient number of reflections, a large number of simulations would be required, greatly adding to the computational cost. This is a particular problem if the room to be modelled is large and the surfaces are highly reflecting, resulting in a long reverberation tail. The approach can be made more efficient if the incident angle at each reflection is ignored and the direction of reflected energy is modelled according to Lambert's law, as described in section 4.2.2. This is because information about the incident angle of each reflection need not be recorded and dealt with accordingly on the next pass. However this approach is based on an inaccurate representation of diffuse reflection. Conversely, angle dependent diffusion algorithms can be implemented readily if this incident angle information is recorded, and if sections of the diffuse surface act as more complex sources, thus increasing accuracy but also the associated computational load of the model.

Another approach for modelling diffuse reflection, also designed to model diffraction, as an extension to the pyramid-tracing model is described in [86]. This method works by using extra receivers in virtual positions. The reflected energy is split into *diffuse energy*, which is recorded by all receivers adjacent to the surface, and the specular component, which is only recorded by those receivers found in the path of the reflected pyramid ray. This method is only applicable for first

reflections however, and to model higher order reflections the author suggests a similar method for modelling diffusion as that described earlier for the ray-tracing technique.

4.2.4 The Room Acoustic Rendering Equation

An integral equation known as the *room acoustic rendering equation* is introduced in [27] which offers a general approach to ray-based room acoustic modelling techniques. The techniques described previously in this section can be seen as special cases of this general model. One possible solution for the room acoustic rendering equation is termed the *acoustic radiance transfer method* [27], which is the equivalent to the *progressive radiosity solution* to the rendering equation used in the field of computer graphics [87]. Diffuse reflection is dealt with efficiently in this model by considering each reflection as a finite number of discrete sections of a hemisphere facing into the room. Diffusion is then controlled at the point of reflection by selectively distributing the reflected energy amongst these discrete components.

Although the model allows for the emulation of diffuse reflection with great efficiency, there are possible sources of error. Firstly, the issue of diffraction has not yet been considered in this approach. The discretization in the direction of reflected energy at boundaries is also a potential issue, particularly if the resolution used is low.

4.2.5 Hybrid Models

Hybrid models can be used to create room impulse responses by exploiting advantages of different approaches to ray-based acoustic modelling. An example of a hybrid model is to mix the image source method with the ray-tracing method [88]. The image source method is used to compute the early part of the room impulse response, providing accurate early reflections where a relatively low number of image sources are required. The tail of the response can then be calculated using ray-tracing, which is far less computationally expensive than the image source method for calculating high order reflections, but less exact. Another example, which combines the image source method with the beam-tracing technique, again using the image source method to give an accurate early response, is presented in [89].

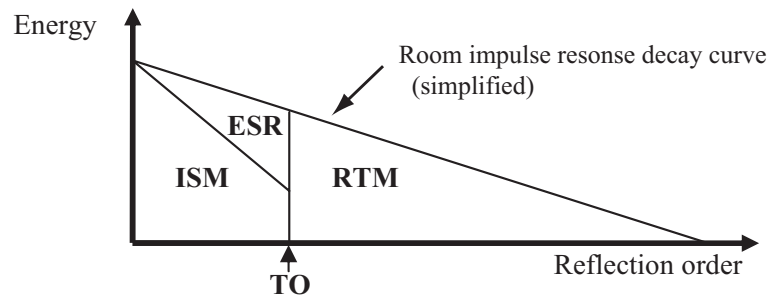


Figure 4.6: Simplified diagram showing the hybrid ray-based approach used in ODEON, from [80].

In the computer program ODEON, currently at version 9.0 [90] the early reflections of a room impulse response are modelled using a hybrid combination of the image source method and the ray-tracing method, with the influence of the image source model (**ISM**) decreasing and the influence of the ray-tracing model, known as the early scattering rays (**ESR**), increasing with time. After a certain temporal point in the calculated impulse response, known as the optimal reflection order (abbreviated to **TO**), the later part of the room impulse response is calculated using only a ray-tracing model, known as the late ray-tracing model (**RTM**). This hybrid process is summarised in Figure 4.6.

The benefit of such a hybrid approach when boundary diffusion is considered, is that different diffusion approaches can be implemented. For example, with a computer model that uses the image source method for the earliest reflections and ray-tracing for the later reflections, image source clouds [9, 73] offer a reasonably accurate solution to modelling diffuse reflection for the earliest part, but become impractical for high order reflections due to the exponentially increasing computation requirements. For the latter ray-traced part of the room impulse response, a simple Lambertian approach for diffuse surface modelling can be used, which is often computationally very efficient when compared to other models, but less accurate [28, 48, 16, 49].

4.2.6 Discussion

A significant advantage of ray-based implementations over other competing computer modelling techniques is that the computational requirements are much less and the algorithms are relatively fast. The disadvantage of this approach is the inherent inaccuracies caused by the over-simplification of sound-wave propagation.

These inaccuracies must be compensated for by using intelligent algorithms, but a perfect solution has yet to be found to the problem of modelling diffraction and boundary scattering effects.

The importance of the implementation of boundary scattering in ray-based models is widely acknowledged. Evidence of the improvement is given in the first *International Round Robin on Room Acoustical Computer Simulations* [78] where the most reliable results for ray-based computer models were given by those programs that included the effects of wave scattering. The improvements to the ray-based approach brought about by the introduction of boundary scattering is further investigated in [25,9,91]. Although attempts to model surface scattering in ray-based models have improved their performance, none so far offer an entirely satisfactory solution and the resulting modelled reflection is over-simplified.

Generally, ray-based computer models simulate diffusion by dividing reflected energy between the specular part and the diffuse part. This general approach means that the scattering coefficient is a highly suited representation for diffuse reflection in these models. Indeed, the scattering coefficient was first developed with geometric ray-based computer models in mind, rather than as a method to measure surface scattering. This explains the difficulty in using the scattering coefficient as a measurement for real diffuse surfaces. Currently, computer programs designed to model acoustics such as ODEON [92] and CATT [93] generally use the ray-tracing based diffusing method described earlier (section 4.2.2) where the probability of a ray reflecting diffusely is decided by the scattering coefficient.

4.3 Wave-based Computer Modelling

Wave-based acoustic models are based on solutions to the wave equation for the room system under consideration. They have the advantage over geometrical room acoustic modelling techniques in that they inherently model complex acoustical phenomena such as diffraction and wave interference.

The wave-based approaches to modelling acoustic systems are divided into two main types called *Frequency Domain* or *Element* methods and *Time Domain* methods.

4.3.1 Element Methods

Element based methods offer one approach, where the modelled space is discretised into a number of smaller sub-domains. The *Finite Element Method* (FEM) works by dividing the *domain* itself into a number of *subregions*. The *Boundary Element Method* (BEM) on the other hand involves dividing the domain *boundaries* in the domain into a mesh of discrete sections.

Finite Element Methods

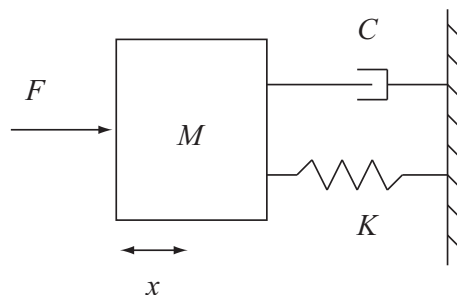


Figure 4.7: A mechanical system with a single degree of freedom, after [94].

A good description of the Finite Element Method is outlined in [94]. More in-depth description and discussion can be found in [95,96]. In the simple mechanical system illustrated in Figure 4.7 a body with mass M is coupled to a fixed point by a perfect spring with stiffness K and its motion is damped by a damping element C . In this system the mass only has one degree of freedom, in other words it can only move in two directions. If an external force F is applied to the mass, the equation of motion can be expressed using (4.1), where x is the position of the mass along its axis

of freedom and \dot{x} and \ddot{x} are the first and second time derivatives of x respectively.

$$F = M\ddot{x} + C\dot{x} + Kx \quad (4.1)$$

If F and C are set to zero, the natural frequency of vibration for this system is found. If sinusoidal motion is assumed for the system, with angular frequency ω , as described by (4.2)

$$x = |x|e^{j\omega t} \quad (4.2)$$

then the equation of motion can be expressed as:

$$(K - \omega^2 M)x = 0 \quad (4.3)$$

A similar formulation can be derived from the general wave equation (2.12), which can be expressed as follows, where $\xi(\bar{x}, t)$ denotes the pressure at time t at the point whose position vector is \bar{x} :

$$\nabla^2 \xi(\bar{x}, t) - \frac{1}{c^2} \frac{\partial^2 \xi(\bar{x}, t)}{\partial t^2} = 0 \quad (4.4)$$

Considering the case where acoustic propagation is simple-harmonic and separating the variables \bar{x} and t , the acoustic pressure is given by the following:

$$\xi(\bar{x}, t) = \xi(\bar{x})e^{(-j\omega t)} \quad (4.5)$$

Substituting (4.5) into (4.4) gives a single frequency time-independent form of the wave equation, known as the Helmholtz equation (4.6), where $k = \omega/c$ is a positive constant known as the wave number [97].

$$(k^2 + \nabla^2)\xi(\bar{x}) = 0 \quad (4.6)$$

Considering again the mechanical system described by Figure 4.7, a more complicated system can be considered with multiple elements, and therefore multiple values for F, M, K and C . Using the finite element method, a mechanical system is spatially divided into discrete *finite elements* which interact with each other. Each finite element acts as a simple mechanical system and the moving

elements are called *nodes*. The system as a whole is now described as number of simultaneous equations, which can be represented in matrix form. (4.1) and (4.3) therefore become:

$$\mathbf{F} = \mathbf{M}\ddot{x} + \mathbf{C}\dot{x} + \mathbf{K}x \quad (4.7)$$

and

$$(\mathbf{K} - \omega_n^2 \mathbf{M})[x] = 0 \quad (4.8)$$

The n th harmonic frequency ω_n for the system can be obtained using (4.8). For an acoustic system, the nodes have one degree of freedom which represents the sound pressure in the model. In order to obtain a full description of the acoustic system at a specific frequency, the number of required nodes and the complexity of the system increases as frequency increases. It was also found in [94] that non-uniform distribution of nodes in the mesh improved the performance of the model when considering natural harmonic frequencies, or modal frequencies, because the nodes are less likely to be positioned in the zero pressure area of standing waves.

Boundary Element Methods

Boundary Element Methods (BEM) provide an alternative approach to solving the Helmholtz equation governing an acoustic field (4.6), however rather than being applied to the problem directly, as with the FEM, it is applied to a reformulation known as the *Helmholtz-Kirchhoff integral equation* or the *boundary integral equation* [44, 98]. As a result, it is possible to subdivide the boundary into a number of elements, each with its own boundary integral equation, and to express the system using a boundary element matrix formulation, (4.9), where \mathbf{P} and \mathbf{V} are pressure and velocity on the boundary respectively [99]. \mathbf{H} and \mathbf{G} are influence coefficient matrices for the boundary integral equations [99].

$$\mathbf{HP} = \mathbf{GV} \quad (4.9)$$

By solving the simultaneous boundary integral equations, it is possible to calculate acoustic variables at all the node points on the boundary and in turn the sound pressure and velocity can be calculated at points of interest inside the space by applying the boundary integral equation also at these points [99]. A detailed

description of the BEM as applied to acoustics, specifically for predicting the reflection of sound from acoustic diffusers is presented in [44].

Discussion

The advantage of element methods in acoustic modelling, is their ability to model complicated domain shapes and boundary structures with relative ease, as there is no requirement for mesh uniformity, and mesh density and shape can be adapted where necessary [94]. The models are able to produce highly accurate results, however as the frequency of the modelled sound increases, the minimum density of the meshes used in the process must also be increased, and so the computational requirements greatly increase. This is because in order to avoid excessive error, a minimum number of elements must be used for each wavelength [97]. Similarly, as the size of the room is increased, the size of mesh must also be increased. The models are also dependent on a multi-pass approach for individual frequency considerations, resulting in a requirement of many mesh simulations in order to build a room impulse response that covers a satisfactory frequency range. The methods are therefore limited to modelling only small enclosures at low frequencies [7, 100].

The choice between BEM or FEM depends on the nature of the acoustic space to be modelled. The advantage of the BEM is that the modelling of open space, unlike with the FEM, needs no special consideration. The modelling of unbounded space using the FEM however is a problem and must be solved using special techniques that again add to the computational cost and complexity of the model, such as the use of an *absorbing boundary condition* that does not allow scattered waves to reflect at the FEM boundary [97].

Although limited in the general case of modelling room acoustics, the BEM method is particularly suited to the application of scattering prediction of diffuse boundaries, and despite requiring much human input and therefore being prone to human error, gives very accurate predictions provided the shape, dimensions and acoustic properties of the scattering surface are known [61, 44]. Methods for implementing diffuse surfaces that are based on statistical models, in order to model and predict the effects of random roughness, are discussed in [65].

4.3.2 Finite Difference Time Domain Methods

The *Finite Difference Time Domain* (FDTD) method was first introduced in 1966 to model the movement of electrical and magnetic fields using a finite difference approximation of Maxwell's equations [101].

A similar approach can be taken to model the propagation of sound by using finite difference approximations for both time and space derivatives of the wave equation (2.12) [102]. This was initially used as a method for synthesizing musical sounds but has also been used in room acoustics applications [103, 104]. Such systems are referred to as FDTD models.

The most common method to discretize the wave equation in time and space is by use of the central difference finite difference approximation of the partial derivatives. For an arbitrary continuous function with a single variable $f(x)$, the first derivative, $df(x)/dx$ which can also be described as the gradient of its tangent, can be defined as follows:

$$\frac{df(x)}{dx} = \lim_{\Delta x \rightarrow 0} \frac{f(x + \Delta x/2) - f(x - \Delta x/2)}{\Delta x} \quad (4.10)$$

This equation is exact as Δx tends to zero, however in a finite difference scheme, Δx is a finite value and (4.10) becomes a finite difference approximation, known as the central difference approximation:

$$\frac{df(x)}{dx} \approx \frac{f(x + \Delta x/2) - f(x - \Delta x/2)}{\Delta x} \quad (4.11)$$

By iterating the difference approximations, a finite difference approximation for the second-order partial derivative can be formulated:

$$\frac{d^2f(x)}{dx^2} \approx \frac{f(x + \Delta x) - 2f(x) + f(x - \Delta x)}{\Delta x^2} \quad (4.12)$$

This method can also be applied to functions with more than one variable. For example, the spatial and temporal partial derivatives of the one dimensional wave equation (2.14) can be approximated respectively by the following finite difference formulations, where $u(x, t)$ is a function of variables representing time, t and location in 1-D, x :

$$\frac{\partial^2 u(x, t)}{\partial x^2} \approx \frac{u(x + \Delta x, t) - 2u(x, t) + u(x - \Delta x, t)}{\Delta x^2} \quad (4.13)$$

$$\frac{\partial^2 u(x, t)}{\partial t^2} \approx \frac{u(x, t + \Delta t) - 2u(x, t) + u(x, t - \Delta t)}{\Delta t^2} \quad (4.14)$$

By substituting these approximations in (2.14) and by setting the propagation speed, $c = \frac{\Delta x}{\Delta t}$ the following finite difference equation for the system can be calculated:

$$u(x, t + \Delta t) = u(x + \Delta x, t) + u(x - \Delta x, t) - u(x, t - \Delta t) \quad (4.15)$$

For convenience, an index notation for space, $k = x/\Delta x$ and time, $n = t/\Delta t$ can be substituted in (4.15):

$$u(k, n + 1) = u(k + 1, n) + u(k - 1, n) - u(k, n - 1) \quad (4.16)$$

It can be seen in (4.16) that for each time step, n , a new sample value for wave displacement, $u(k, n + 1)$ can be computed as the sum of its spatial neighbours, $u(k + 1, n)$ and $u(k - 1, n)$ minus the value at the same point in space but one time step earlier, $u(k, n - 1)$. A similar approach can be used to discretize the wave equation in 2-D and 3-D space.

Spatial sampling points are usually arranged in a Cartesian grid across the space that is being modelled. An important consideration in FDTD models, as with other Digital Signal Processing systems, is the sampling rate. The finite difference approximation becomes more accurate as spatial sampling distances and periods become smaller, as described in (4.10). By increasing the density of the grid, the sampling rate of the grid is increased, thus allowing the accurate propagation of higher frequencies. The relationship between the density of the mesh and the sampling rate, f_s Hz in an N -Dimensional mesh is described by (4.17), where c is the speed of wave propagation and d is the distance between two neighbouring junctions [105]. This equation is derived from the *Courant condition* for the finite difference time domain algorithm [106]. The Courant condition is a stability condition that dictates the minimum sampling rate of the mesh for the system to be convergent, in other words so that the results produced are not unacceptably inaccurate.

$$f_s = \frac{c\sqrt{N}}{d} \quad (4.17)$$

The sample rate of the grid dictates the highest frequency of the propagating waves that are modelled in a FDTD system. However, as the sample rate increases, so

does the processing cost, both in terms of computations per second and memory. For example, for a sampling rate of 44.1 kHz (the standard CD sampling rate) in a standard 2-D finite difference mesh (arranged in a rectangular Cartesian grid), and with wave propagation speed, c , being 343 ms^{-1} , then the distance between neighbouring junctions should be set at 0.011 m to 2 significant digits. In a FDTD mesh 4.4 m wide by 6.0 m long, the number spatial sampling points required would be in the region of 218,000 [107].

A limitation of 2-D and 3-D FDTD systems is *dispersion* error. This results in an inconsistency in the velocity of wave propagation that is dependant on both its frequency and direction of travel [108, 109]. This does not agree with the wave equation in its pure form, which is non-dispersive. The dispersion error can be reduced within the desired frequency range by increasing the sampling rate so that it is higher than the sampling rate required according to (4.17). Again, this increases the computational cost of the system. Analysis of the dispersion error for finite difference schemes can be carried out using *Von Neumann* analysis [108, 102]. The dispersion characteristics of a system will depend upon the choice of sampling grid topology as investigated in [20, 107] and this, as well as methods to reduce the error, is discussed in more detail in section 4.4.4.

As they are time domain models, FDTD models have the advantage over element methods that they can be used to predict acoustic propagation over a range of frequencies (limited by the sampling rate of the grid) in one simulation. However the spacing and density of the grid in FDTD models is fixed and so the grid cannot be adapted to accurately model complex boundary geometry, as it can be with element based methods.

The *Digital Waveguide Mesh* (DWM) is a different implementation of a FDTD solution to the wave equation described here. Its implementation and its relation to other FDTD methods is described in detail in section 4.4.

4.4 The Digital Waveguide Mesh

The Digital Waveguide Mesh is derived (DWM) from the 1-D digital waveguide used extensively for physical modelling synthesis. It was first proposed as a synthesis technique suitable for modelling 2-D and 3-D objects for audio applications [5, 6, 23, 110, 111]. It has also been applied to the modelling of room acoustics using both 2-D, 3-D structures [18, 19, 20, 21] and even structures of higher dimensions [22].

The Digital Waveguide Mesh consists of discrete time bi-directional delay lines, or digital waveguides, that are connected together by scattering junctions, or nodes, which are arranged to form two and three dimensional structures, making up a grid of spatial and temporal sampling points.

4.4.1 The One Dimensional Digital Waveguide

The theory of the one dimensional digital waveguide stems from d'Alembert's solution of the one dimensional wave equation (4.18). The derivation of the d'Alembert's solution is given in Appendix A.1.

$$\xi(t, x) = \xi^+(t - x/c) + \xi^-(t + x/c) \quad (4.18)$$

A discrete time formulation of this solution (4.19) describes wave displacement at time intervals nT and at discrete sampling points in one dimensional space mX . As in (2.15), ξ^+ and ξ^- are functions representing the displacement of waves travelling in the positive and negative x directions respectively and are band-limited to half the sampling rate of the system, and c is the speed of the waves. n and m are integers representing the time-step and sample point respectively, T is the time between each time-step and $X = cT$ is the distance between each sample point (the distance travelled by sound in one time-step):

$$\begin{aligned} \xi(nT, mX) &= \xi^+(nT - mX/c) + \xi^-(nT + mX/c) \\ &= \xi^+((n - m)T) + \xi^-((n + m)T) \end{aligned} \quad (4.19)$$

This discrete time formulation can be implemented using bi-directional delay lines as illustrated in Figure 4.8. In this system, two independent signals propagate in

opposite directions. The sum of these signals can be obtained at each sampling instant, giving the wave displacement at a discrete point in time and space. The sampling points are separated by unit delay elements, marked z^{-1} in Figure 4.8, the term used for a unit delay in the z -domain representation of a discrete signal.

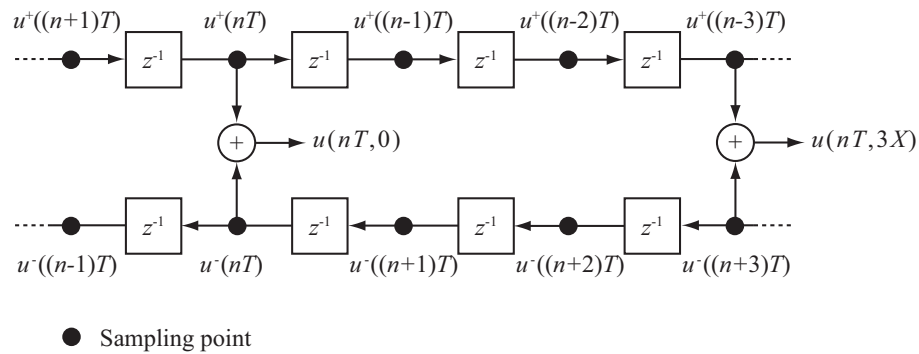


Figure 4.8: Discrete time implementation of lossless 1-D wave propagation, observed at the spatial sampling points $x = 0$ and $x = 3X$.

Figure 4.8 shows a section of a digital waveguide implementation of the 1-D wave equation. This can be used, for example, to model wave propagation in an ideal lossless string and is exact at the sampling instants in time and space.

4.4.2 The Scattering Junction

Any number of digital waveguide elements, each with an arbitrary impedance, can be connected together by means of a *scattering junction*. In the lossless case, signals that arrive at a scattering junction are scattered amongst its connected waveguides in such a way that energy and power is conserved. The preservation of energy and continuity at the junction in terms of sound pressure and particle velocity is analogous to Kirchoff's laws of power conservation that apply to voltage and current in an electrical circuit. Waveguide elements are arranged into network structures using scattering junctions, and such structures are known generally as *digital waveguide networks* (DWNs). DWNs have been used to simulate artificial reverberation effects [112, 113]. By arranging N -port scattering junctions in a regularly arranged and equally spaced grid however, and by connecting neighbouring scattering junctions using unit delay waveguide elements, it is possible to form 2D and 3D structures within which wave propagation is simulated. The scattering junctions act as both spatial and temporal sampling points and such a network of scattering junctions is known as a *Digital Waveguide Mesh* (DWM).

The Scattering Equations

Figure 4.9 shows a scattering junction J connected to N neighbouring junctions, $i = 1, 2 \dots N$, using unit delay waveguide elements. The sound pressure in each waveguide is represented by p_i , the particle velocity by v_i and the acoustic impedance in the waveguide by Z_i , where $Z_i = p_i/v_i$. The incoming signal to junction J along the waveguide from the connecting junction i is represented by $p_{J,i}^+$. Similarly, $p_{J,i}^-$ represents the outgoing signal from junction J along the waveguide connecting it to the opposing junction labelled i .

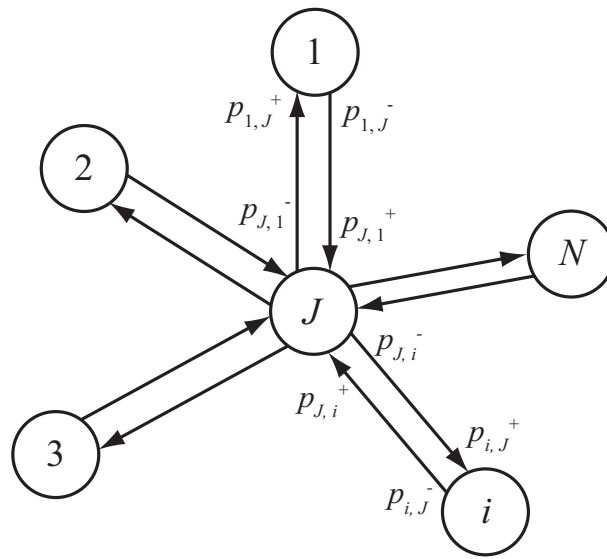


Figure 4.9: A general scattering junction J with N connected waveguides for $i = 1, 2 \dots N$, after [107].

The sound pressure of a propagating wave signal is defined as the sum of the travelling wave components within the waveguide, (4.19). Therefore the sound pressure at a junction J is equal to the sum of the input and output of the waveguide element connected to the neighbouring junction i :

$$p_{J,i} = p_{J,i}^+ + p_{J,i}^- \quad (4.20)$$

As the waveguides are equivalent to bi-directional unit-delay lines, the input to scattering junction J at time index n , $p_{J,i}^+(n)$, is equal to the output from neighbouring junction i into the connecting waveguide at the previous time step, $p_{i,J}^-(n-1)$.

By applying an appropriate linear transformation, as described in [6], [116] and [117], an equivalent formulation can be derived in terms of junction pressure values only:

$$p_J = \frac{2 \sum_{i=1}^N \frac{p_i}{Z_i} \cdot z^{-1}}{\sum_{i=1}^N \frac{1}{Z_i}} - p_J \cdot z^{-2} \quad (4.24)$$

A direct derivation of this expression, (4.24), from a finite difference time domain formulation of the 2-D implementation of the wave equation, for the specific case of the 4 port scattering junction, is given in [107]. An alternative derivation, for the more general N -port scattering junction case, based on Kirchoff's continuity laws, is presented in [115]. Digital waveguide meshes built using this alternative implementation are termed *K-models* or *K-DWMs* [115]. The K is a reference to the Kirchoff type physical variables used in this modelling type, analogous to those used in Kirchoff's integral solution of Maxwell's equations. A general K-DWM lossless scattering junction J with N neighbours is shown in the form of a digital signal functional block diagram in Figure 4.11, again where $Y_i = 1/Z_i$ is the admittance of the waveguide connecting junction J with the neighbouring junction i .

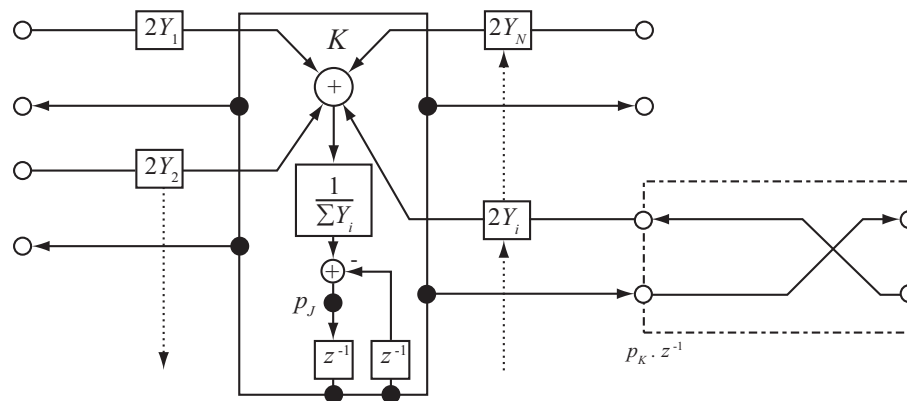


Figure 4.11: A digital signal functional block diagram representation of a K-model scattering junction K with N connected waveguides for $i = 1, 2, \dots, N$, after [3].

4.4.3 Comparison of K-Modelling and W-Modelling and Mixed Modelling

In the case of 2-D and 3-D meshes, the K-modelling approach offers greater computational efficiency over the W-modelling approach, as it requires less memory

than W-modelling. From (4.23), it can be seen that for any dimensionality, and for any number of connecting waveguides, K-modelling (in its basic form) requires that the pressure value of each junction is stored, as well as the value of each junction at the previous time step, with a total number of two memory positions required for each junction. W-modelling, however, requires that the input or output pressure values at each waveguide connected to a junction is stored at any one time, therefore the number of memory positions required for each junction is equal to the number of connecting waveguides to that junction. It can also be seen from Figures 4.10 and 4.11 that at each time step and at each junction, an extra addition is required in the signal processing algorithm in the W-modelling case when compared to the K-modelling case, meaning that for the K-modelling approach, less operations per junction are required than for the W-modelling case.

An advantage of the W-modelling approach however is that it allows for the use of scattering based boundary termination options. Owing to the ability to process signals as they travel in and out of junctions, coupled with the memoryless nature of the scattering equations in the W-modelling method, DSP techniques such as filtering [118] are easier to implement with assured stability, when compared with the K-modelling case.

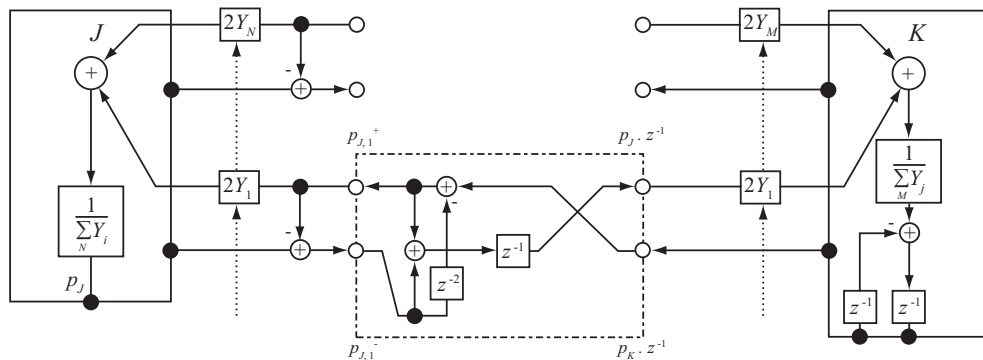


Figure 4.12: A digital signal functional block diagram representation of a W-model scattering junction J interfaced with a K-model scattering junction K using a KW-pipe, after [3].

It is possible to combine both the K-DWM and W-DWM approaches by interfacing them using the KW-pipe technique, as discussed in [117]. This results in the formulation of a 2-D hybrid DWM [115, 117]. Figure 4.12 is a signal processing diagram showing a KW-pipe connecting an M -port K-DWM junction to an N -port W-DWM junction, after [3].

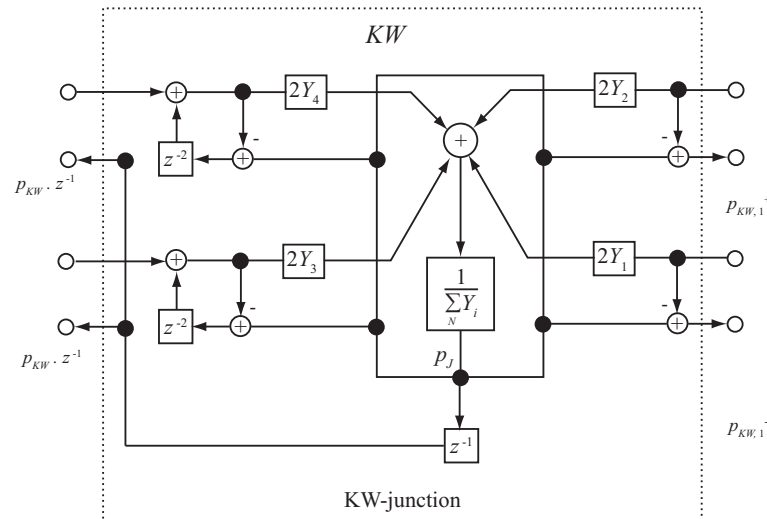


Figure 4.13: A digital signal functional block diagram representation of a KW-junction KW with two K-model ports and two W-model ports, after [119].

In [119] a different approach to KW-conversion is introduced, named the KW-junction, which offers a computational improvement if multiple KW-pipes are attached to a W-model scattering junction, because the output variable that is passed to the attached K-model scattering junctions is only calculated once at each sampling instance, rather than being calculated separately for each port as is the case when the KW-pipe is used. Figure 4.13 presents a signal processing diagram showing a KW-junction. The KW-junction consists of both K-model ports and W-model ports. The example shown in this diagram consists of two K-model ports and two W-model type ports, but a limitless number of extra ports of either type can be added, along with their respective admittances.

4.4.4 Mesh Topology

The choice of mesh *topology* determines the way by which scattering junctions are uniformly arranged in a DWM, as well as the number of connecting waveguides (neighbouring junctions) that each scattering junction has. Different mesh topologies can be used to model wave propagation in the same physical structure. For instance a 2-D space can be modelled using either a *rectilinear* mesh or a *triangular* mesh, diagrams of which can be seen in Figure 4.14(a) and 4.14(b) respectively. In the rectilinear mesh, the non-boundary, or *air*-junctions each have 4 connecting waveguides, as opposed to the air-junctions in the triangular mesh which have 6 connecting waveguides. These are the most commonly used DWM topologies for

2-D structures and their characteristics are studied and compared in detail in [120].

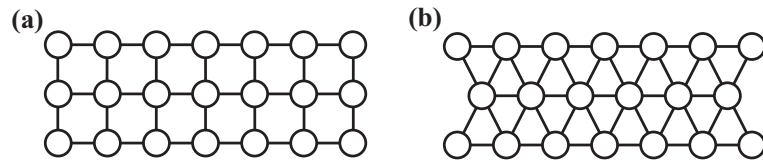


Figure 4.14: (a) A 4-port 2-D rectilinear mesh structure and (b) a 6-port 2-D triangular mesh structure.

Commonly used examples of 3-D mesh topologies are the rectilinear [104], 3-D tetrahedral [111, 121], 3-D dodecahedral (cubic close packing) [122] and octahedral mesh structures, as illustrated in Figure 4.15(a)-(d) [3]:

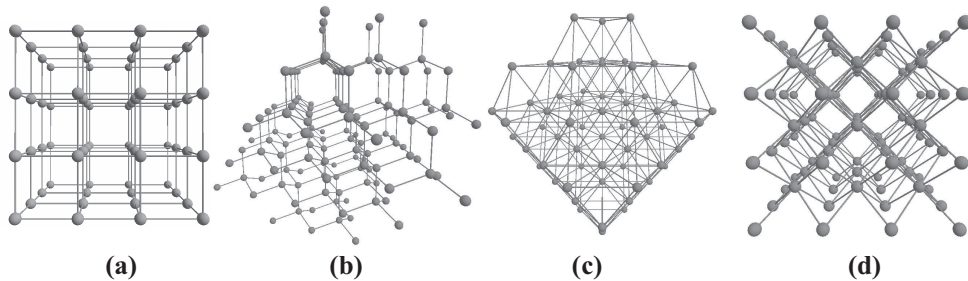


Figure 4.15: (a) 6-port 3-D rectilinear, (b) 4-port 3-D tetrahedral, (c) 12-port 3-D dodecahedral (CCP) and (d) 8-port 3-D octahedral mesh structures, from [3].

The Interpolated Mesh

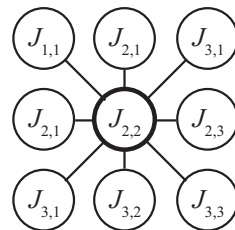


Figure 4.16: Diagram showing a junction in a 2-D rectilinear DWM with its 8 neighbours.

Dispersion error is an inherent error in FDTD solutions and the DWM, and is discussed in more detail in section 4.4.6. Interpolated meshes have been successfully implemented in both 2-D and 3-D rectilinear DWM structures and have been shown to dramatically reduce this error [123, 124]. Considering the 2-D rectilinear mesh, each junction is connected by a unit delay element to 4 neighbouring junctions. In the interpolated 2-D rectilinear mesh, a single unit delay element is also inserted

between the diagonally positioned neighbours to the junctions. For each junction, these diagonal delay elements do not reach the diagonal neighbours as their distance is greater than that of the axial neighbours, and so values at their end points are interpolated using a technique described in [125]. (4.25) is a point-spreading function which describes the pressure at a central junction $p_{2,2}$ at sampling instance n . $p_{l,k}$ are the pressure values of the central junction and both its axial and diagonal neighbours and $h_{l,k}$ is a weighting factor for each junction [126]. The labelling system for each junction is described by Figure 4.16.

$$p_{2,2}(n) = \frac{1}{4} \sum_{l=1}^3 \sum_{k=1}^3 h_{l,k} p_{l,k}(n-1) - p_c(n-2) \quad (4.25)$$

The weighting factors can either be determined using bilinear interpolation [126] or quadratic interpolation [127]. An alternative approach however, is to select the weighting factors using a trial and error approach so that weighting values are selected in such a way that an optimal reduction of dispersion error is achieved [127]. The process can also be extended for the 3-D rectilinear mesh, as detailed in [124,128].

4.4.5 Sampling Rate

The sampling frequency, f_{update} , of a DWM with D dimensions is given by (4.26), where c is the speed of sound and x is the spatial distance between mesh junctions [105]. In the same way as the sampling frequency is determined in a FDTD grid, this is dictated by the Courant condition [106].

$$f_{update} = \frac{c \sqrt{D}}{x} \quad (4.26)$$

Figure 4.17 shows a section of a 2-D rectilinear mesh decomposed into two *sub-grids*, with one composed of white junctions and the other of grey junctions. In the 2-D rectilinear mesh topology there can be only an odd or an even number of delay units connecting two junctions together within the mesh and not both. The result of this is that signals propagating in one sub-grid are completely independent of signals propagating in the other sub-grid at a particular time-step, and that

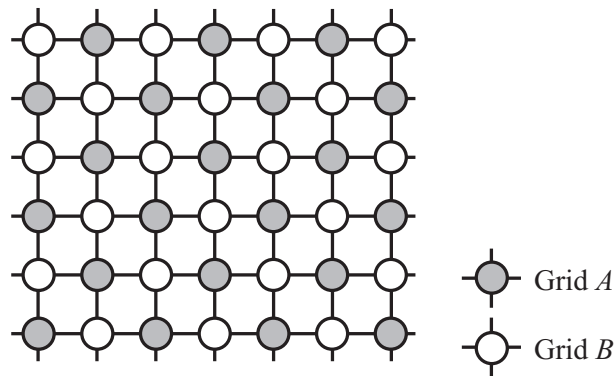


Figure 4.17: Decomposition of the 2-D rectilinear mesh into sub-grids.

these mutually exclusive sets of signals alternate from one sub-grid to the other with each consecutive time-step [129]. A consequence of this is that the resulting output from the mesh is limited to a quarter of the mesh sampling rate, f_{update} . This *chessboard* effect is also observed in the 3-D rectilinear mesh, the tetrahedral mesh, the octahedral mesh and any mesh topology in which the path between two junctions can be made up only of either an odd number or an even number of delay units. As a result of this, the maximum limit of $0.25 \times f_{update}$ can be used as a benchmark figure for other mesh topologies [23,111].

If a DWM can be decomposed into two independent signals operating in alternative grids in this way, only one set of signals needs to be considered in mesh simulation. It therefore follows that the number of calculations required for each time step and the total number of memory locations required for a simulation can be halved. This is known as the *chessboard technique*.

The scattering equations in the chessboard technique are formulated in exactly the same way, but the calculations are only applied to those junctions that make up one sub-grid at alternate simulation time-steps. For example, if the junctions are split into two sub-grids (see Figure 4.17), labelled sub-grid *A* and sub-grid *B*, then at the first time step out of every consecutive pair of time steps, scattering equations are applied to inputs only at the junctions that make up sub-grid *A*. At the second of every two time-steps, the outputs of the junctions from sub-grid *A* become the inputs of the junctions that make up sub-grid *B* and the scattering equations need only be applied to this second set of junctions. The outputs of the junctions of sub-grid *B* are then passed to the inputs of the sub-grid *A* junctions and the process continues in a 2-step cycle [129].

4.4.6 Dispersion

Owing to the non-isotropic nature of the DWM in 2-D and 3-D, the velocity of the propagating wave is dependent upon both its frequency and direction of travel, leading to wave propagation errors and a mistuning of the expected resonant modes. This is known as *dispersion* error. The degree of dispersion error is highly dependent upon mesh topology and has been investigated in [18], [111] and [130]. Von Neumann analysis is used to measure the dispersive characteristics of different mesh topologies and dispersion is quantified by a *dispersion factor*, k_d [102] (4.27). The dispersion factor in an N -dimensional mesh is defined in (4.27) as a function of an N -dimensional vector, $\underline{\beta}$. The norm of the vector $\underline{\beta}$ defines the *spatial angular frequency* in the mesh and the direction specifies direction of wave travel. The dispersion factor is the ratio the actual wave propagation speed in the mesh, $c'(\underline{\beta})$ to the propagation speed in a dispersionless, isotropic ideal medium, c :

$$k_d(\underline{\beta}) = \frac{c'(\underline{\beta})}{c} \quad (4.27)$$

The spatial angular frequency vector $\underline{\beta}$ is related to the *spatial frequency* vector $\underline{\xi}$ as follows:

$$\underline{\beta} = 2\pi\underline{\xi} \quad (4.28)$$

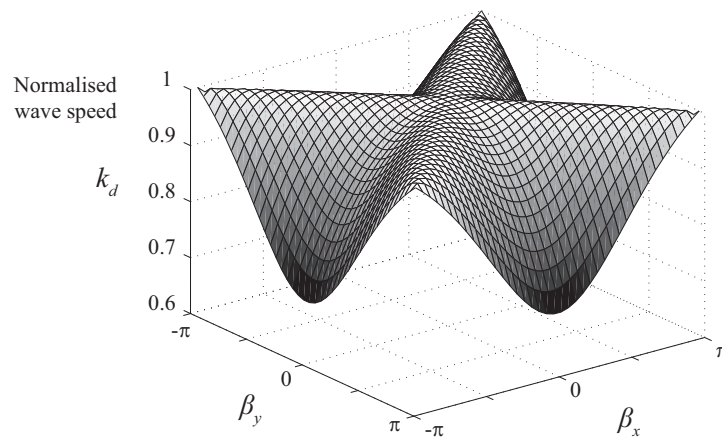


Figure 4.18: Dispersion factor k_d in the 2-D rectilinear mesh.

Figures 4.18 and 4.19 plot the calculated dispersion factor k_d for the 2-D rectilinear and triangular meshes respectively. In the diagrams β_x and β_y are the x

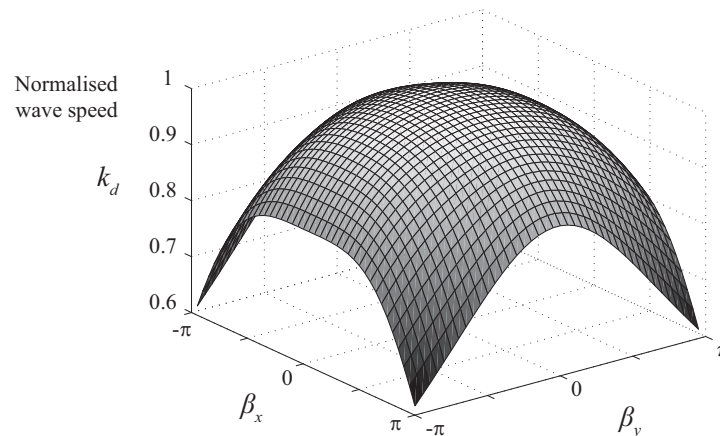


Figure 4.19: Dispersion factor k_d in the 2-D triangular mesh.

and y components of the vector $\underline{\beta}$. In the rectilinear mesh, there is no dispersion error for waves travelling in the diagonal direction, 45° relative to the waveguides in the mesh. However the error increases for other directions, with maximum error for waves travelling along the direction of the waveguides themselves. In the non-diagonal direction of wave travel, the dispersion factor drops considerably as the spatial angular frequency increases. Dispersion error in the triangular mesh (Figure 4.19) shows relatively far less dependency on the direction of wave travel, such that dispersion is substantially reduced to a function of frequency only. Also, as spatial angular frequency increases from zero (the centre of the graphs) the maximum dispersion error increases at a faster rate in the rectangular mesh for low frequencies.

The interpolated rectilinear DWM structure provides similarly directionally independent dispersion error to the triangular mesh, although dispersion is still a function of frequency [123, 131, 132]. The computational cost of the interpolated mesh is great however, introducing nine extra multiplications for each junction in the mesh at every time-step in the 2-D rectilinear case. Further improvements can be achieved with *frequency warping* techniques [123, 124]. This reduces the frequency dependency of the dispersion error in the DWM by post-processing the output of the mesh. Another approach to reduce the frequency dependency is to over-sample the mesh. The triangular mesh however offers the most efficient solution when a balance between acceptable dispersion levels and directional dependency and computational cost is required in the 2-D DWM [107, 120, 133].

The dispersion in 3-D Digital Waveguide Mesh structures is presented in [130]. It is shown that in order to achieve a maximum dispersion error of 22.8% or less by oversampling the mesh, the tetrahedral DWM topology is the most efficient mesh in terms of computation power. Dispersion in the dodecehedral (CCP) mesh however, has the lowest directional dependence [130, 133] and is therefore best suited for frequency warping post-production techniques [123]. Frequency warping has also been applied to the 3-D interpolated rectilinear DWM structure, although again at a relatively high computational expense [124].

4.4.7 Boundary Termination

1-D Boundary Termination

Considering a 1-D waveguide string, in the simplest case the boundary condition is derived using a boundary junction B connected to a single *dummy* junction D as shown in Figure 4.20 [107].

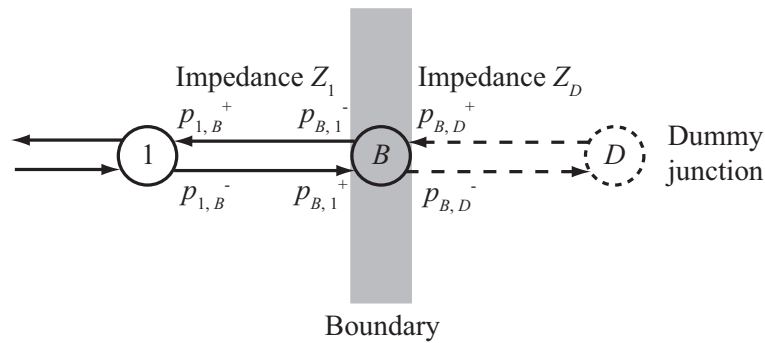


Figure 4.20: Simple termination of a 1-D waveguide string.

The dummy junction acts only to absorb energy from the system upon reflection at junction B and its output is forced to zero, therefore $p_{B,D}^+ = 0$. In this case the characteristic impedance in the waveguide connecting the boundary junction to the dummy junction is Z_D and the impedance in the waveguide connecting the boundary junction to the rest of the string is Z_1 . The boundary absorbing condition is controlled by a reflection coefficient r , defined as:

$$r = \frac{Z_D - Z_1}{Z_D + Z_1} \quad (4.29)$$

Rearranging (4.29) gives:

$$Z_D = \left(\frac{1+r}{1-r} \right) Z_1 \quad (4.30)$$

From (4.23) and given that $p_{B,D}^+ = 0$, the sound pressure at the boundary junction p_B is:

$$p_B = \frac{2 \frac{p_{B,1}^+}{Z_1}}{\frac{1}{Z_1} + \frac{1}{Z_D}} \quad (4.31)$$

Substituting (4.30) into (4.31) gives:

$$P_B = (1+r)p_{B,1}^+ \quad (4.32)$$

Setting $r = 1$ ($Z_D = \infty$) results in total reflection at the boundary and the phase of incoming waves is preserved, effectively modelling a clamped boundary. Setting $r = -1$ ($Z_D = 0$) results in total phase inverting reflection at the boundary, modelling a free boundary (like the edge of an unclamped vibrating rod for example). Values of r set between these two extremes result in partial absorption at the boundary, with positive values resulting in phase preservation and negative values resulting in phase reversal. Total absorption is achieved at the boundary by setting $r = 0$. The assumption of total absorption is perfectly valid for a 1-D waveguide string only. For waveguide meshes with higher dimensions however, total absorption is very difficult to achieve in reality [107].

Multi-dimensional N -port Boundary Termination

For the multi-dimensional DWM case, boundaries are terminated in the simplest case using an N -port boundary junction with an extra dummy junction, as illustrated in Figure 4.21. It should be noted that the connection to the dummy junction is not counted as one of the N boundary ports. The number of waveguide connections to the boundary junction in a multi-dimensional DWM depends on the topology of the mesh. For each mesh topology there are a number of different possible types of boundary junctions depending on the position of the boundary junction within the structure. In the 2-D triangular mesh for example, there are 18 different boundary junction types possible with the number of connecting waveguides ranging from 1 to 5 [107].

Like with the 1-D case, the output from the dummy junction is always zero,

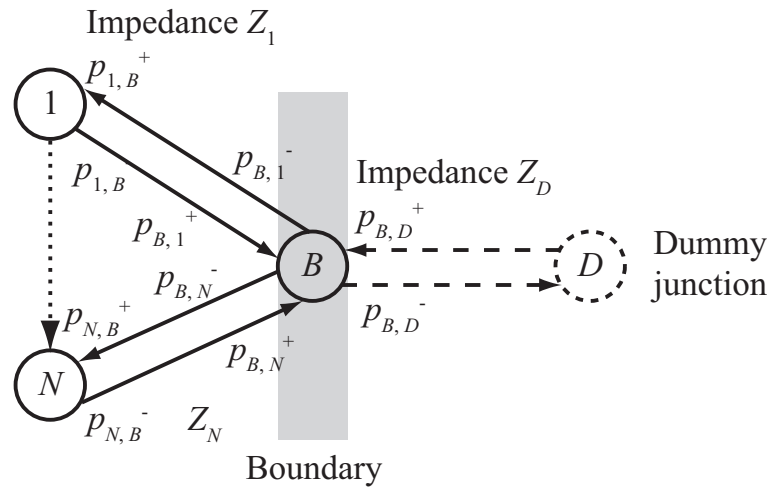


Figure 4.21: Simple termination of a DWM at an N -port boundary junction.

therefore $p_{B,D}^+ = 0$. The scattering equation (4.23) becomes:

$$p_B = \frac{2 \sum_{i=1}^N \frac{p_{B,i}^+}{Z_i}}{\sum_{i=1}^N \frac{1}{Z_i} + \frac{1}{Z_D}} \quad (4.33)$$

For a DWM used to model an homogeneous medium such as air, the characteristic impedance in all connecting waveguides (Z_1 to Z_N but not Z_D) are the same, i.e. $Z_1 = Z_2 = \dots = Z_N$. In this case, substituting (4.30) into (4.33) gives an expression for the pressure at the N -port boundary junction B in terms of the boundary reflection coefficient r :

$$p_B = \frac{2 \sum_{i=1}^N p_{B,i}^+}{N + \left(\frac{1-r}{1+r}\right)} \quad (4.34)$$

The simple boundary implementation is effective in the case of total reflection, however total absorption is not observed when r is set to zero at the boundaries of multi-dimensional DWM structures, except in specific cases. For example the 2-D rectilinear mesh boundary shows total absorption when $r = 0$ if the incident sound is a plane wave approaching the boundary with an incident angle of $\pm 45^\circ$, however this is not the case for other angles of incidence. In order to give anechoic behaviour the impedance at the boundary must be matched to the impedance of the mesh itself. For multi-dimensional DWMs however, waves that interact with the

boundary at non-normal angles of incidence do not see an exact impedance match for the case when $r = 0$, or $Z_1 = Z_N = Z_D$. For this reason a relatively small level of reflection is observed, particularly at high frequencies [104,134].

Advanced Boundary Conditions

Methods to implement improved anechoic boundaries in the DWM are presented in [135] and [136]. The most effective approach however is the *Perfectly Matched Layer* (PML) [137,138,139]. It consists of a lossy layer at the perimeter of the domain which is truncated by a *perfect electric conductor* (PEC), used to terminate the finite difference mesh. Although not completely perfect, PML boundaries have been implemented with reflection coefficients of below -60dB for electromagnetic wave modelling. Unfortunately, in order to implement a PML boundary, both pressure and particle velocity components of sound must be explicitly considered by the model, which is not the case for the FDTD models described in this thesis.

In order to achieve frequency dependent absorption, the simplest approach is to attach filters to each boundary junction [140,119]. The transfer functions of the digital filters must correspond to the desired reflection factors [140], however when designing filters, care must be taken to avoid introducing too much delay, which would cause modal frequencies to be out of tune. With the basic approach, the boundary filters are blind to the angle of incidence of incoming waves as they interact with the boundary, however it may be possible, for example, to implement filters with transfer functions that adjust according to angle of incidence, by observing the pressure variable history at neighbouring junctions to the boundary. Typically, filters are designed with the assumption that the angle of incidence of incoming waves, θ_i (see Figure 2.5), is a specific value, usually zero. It is shown in [114] that this assumption results in boundary conditions that are dependent on angle of incidence, but not in the same way that a real absorbing boundary is dependent on angle of incidence.

A filter design that accepts the angle of incidence θ_I as a parameter is also introduced in [114], and the effects of altering this parameter on the boundary behaviour are studied.

In [141], an approach is described that introduces 1st-order digital waveguide filters at the boundary of the mesh. Here, the issue of the application of the filters to

multi-port boundary junctions is explicitly considered, suggesting that some degree of directional dependency can be built into the model.

Another technique, as well as a method to measure the boundary absorption, is described in [142] in which the aim is to improve upon the inconsistency between multi-dimensional DWM structures and the 1-D Digital Waveguide case that is observed when the reflection coefficient r is set to be less than 1 or greater than -1. This is done by considering the junctions in the adjacent layers to the boundary junctions in the scattering calculations and has shown significant improvement under test. The technique is further developed in the 2-D DWM structure [143] and is also applied to the 3-D DWM in [144].

Smooth Boundaries

The stepped grid-like structure of a DWM can potentially introduce error at terminating boundaries, particularly when the associated update frequency is low. This error is caused by the desired boundary shape in the model being overly distorted by the inherent discretisation. Special filters with fractional delay times [125], referred to as *rimguides*, can be used at the boundaries of the mesh in order to model the boundary location more accurately [145], as illustrated in Figure 4.22. However these are inherently frequency dependent and this property must therefore be considered in their design and use [133].

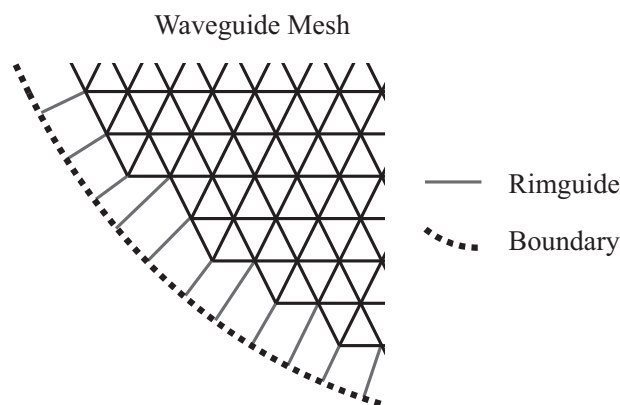


Figure 4.22: Modelling a smooth, curved boundary using rimguides, after [145]

4.4.8 Diffuse Reflection in Digital Waveguide Mesh

Quadratic Residue Diffuser Implementation

A method to implement a highly diffuse boundary based on the quadratic residue diffuser design, as discussed in section 3.1.2, is introduced in [29]. The diffuser wells are simulated using 1-D strings of scattering junctions connected to the boundaries of the mesh, as described in Figure 4.23 for a 2-D mesh. The depths of these wells, which are determined by the number of junctions in the string, correspond to the depths of the wells in real quadratic residue diffusers, determined according to the design equations given in section 3.1.2. In this basic model, the widths of the wells are not taken into account because the wells are only modelled using simple 1-D waveguide strings.

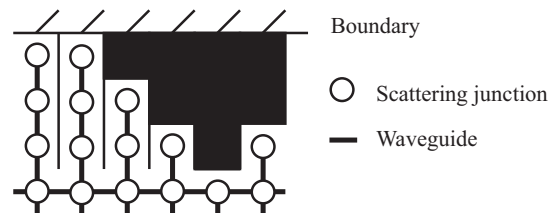


Figure 4.23: Modelling diffuser wells at the boundary of a 2-D Digital Waveguide Mesh

Such a model has been shown to simulate highly diffusive surfaces very well, however in order to model surfaces with relatively small amounts of diffusion, a different approach is required. The method limits the amount of control over the diffusivity of the surface and also causes complications if other boundary characteristics are to be modelled, such as frequency dependent absorption. The model is described in more detail in Chapter 5, as well as an extension of the model to implement diffuser wells with varying widths.

Diffusion Modelling using Circulant Matrices

A different, statistical approach to modelling diffusion uses *circulant* matrices to randomly vary the angle of incident waves prior to reflection [30]. The diffusivity of the boundary can be controlled using this method, and the system is lossless and stable. However an error is introduced that is dependent on the angle of incidence of the reflected waves. This model, and its associated error is reviewed in detail in

Chapter 5. A method to avoid this error is also introduced and an observation of the effects of this modification is presented.

When compared to the quadratic residue method, the circulant matrix techniques described in [30] and Chapter 5 offer a far higher degree of controllability of the amount of diffusion at the boundary, and also have the advantage that they do not alter the physical make-up of the boundary in any way. Both approaches presented here however are potentially useful models, being fundamentally different in their nature. The optimal selection therefore depends on the desired scattering characteristics of the modelled boundary.

Chapter 5

Diffuse Reflection in the Digital Waveguide Mesh

5.1 Introduction

Two main approaches exist for modelling diffuse reflection in a room acoustics simulation. The first is to intricately build each individual boundary irregularity directly into the model. For convenience this approach is referred to here as *physical mapping*. Large boundary irregularities can be modelled in this way with relative ease. However this method becomes problematic when the roughness of the actual real boundary is relatively small scale and complex, making it difficult to measure and reproduce. If this is applied to a model of a room in order to predict its room impulse response, for example, a map of the roughness of every single diffuse boundary would be required and this would be costly in effort and impractical to implement. This method is useful however, if the surface irregularities are very simple, or if the surface shape is periodic, like the geometric diffusers described in section 3.1.2. An example of this approach in the DWM is the implementation of a quadratic residue diffuser, introduced in section 4.4.8. This method is expanded and analysed in detail in this chapter.

The second method, referred to here as *statistical diffusion modelling* is to approximate the diffuse behaviour of the boundary in a more general way using a statistical approach. Such a model should ideally be adjustable so that the diffusive effects of the simulated boundaries can be optimized to match those of a wide

range of real, irregularly shaped boundaries as closely as possible. The match can be verified using scattering or diffusion coefficient data for example, as described in section 3.2. This approach is best suited for modelling complex random rough surfaces as described in section 3.1.1. An example of this approach in the DWM is the diffusion model using circulant matrices, introduced in section 4.4.8. This technique is described in detail in this chapter.

5.2 Physical Mapping

5.2.1 Quadratic Residue Diffuser

A quadratic residue diffuser is implemented in the DWM using unconnected 1-D strings of scattering junctions connected to the boundaries of the mesh, as described in [29] and in section 4.4.8. The design equations for a quadratic residue diffuser, given in section 3.1.2, state that the width of the wells w determines the lower wavelength of the design bandwidth λ_{min} as follows:

$$w = \frac{\lambda_{min}}{2} \quad (5.1)$$

The lower wavelength of the design bandwidth λ_{min} is increased by increasing the widths of the wells. It should be noted however that some scattering will still occur for smaller wavelengths owing to the geometric shape of the surface. For the quadratic residue diffuse implementation described in [29], the width of the wells is only one spatial sampling interval x , which is determined from the sampling frequency of the mesh f_{update} , the number of dimensions of the mesh D and the speed of sound in the mesh c according to (4.26). Rearranging (4.26) for x gives:

$$x = \frac{c\sqrt{D}}{f_{update}} \quad (5.2)$$

As an example, if the speed of sound in the mesh c is 343 ms^{-1} and the update frequency f_{update} is 44.1 kHz , then the spatial sampling distance x is 0.0110 m in a 2-D DWM.

The well depths are determined by the design wavelength λ_0 , according to (3.4) and the diffuser will work optimally at the design wavelength and at integer

divisions of the design wavelength before λ_{min} is reached. By dividing (3.4) by (5.2), the depth of the n th well in the sequence in number of spatial sampling intervals (the number of junctions that make up the length of each string), x_n , is obtained, as follows:

$$x_n = \frac{s_n \lambda_0}{2N} \frac{f_{update}}{c \sqrt{D}} \quad (5.3)$$

Figure 5.1(a) shows a section of boundary from a DWM with triangular topology with a simple quadratic residue diffuser implemented (sequence length $N = 11$), where the width, w , of the wells is given by x . Figure 5.1(b) shows a section of a quadratic residue diffuser implementation with the same sequence length, but this time the width of the wells is doubled, by using 2-D strips of junctions, arranged in a rectangular topology, rather than the 1-D strings, as illustrated in Figure 5.1. The width, w , of the wells in this case is given by $2 \times x$.

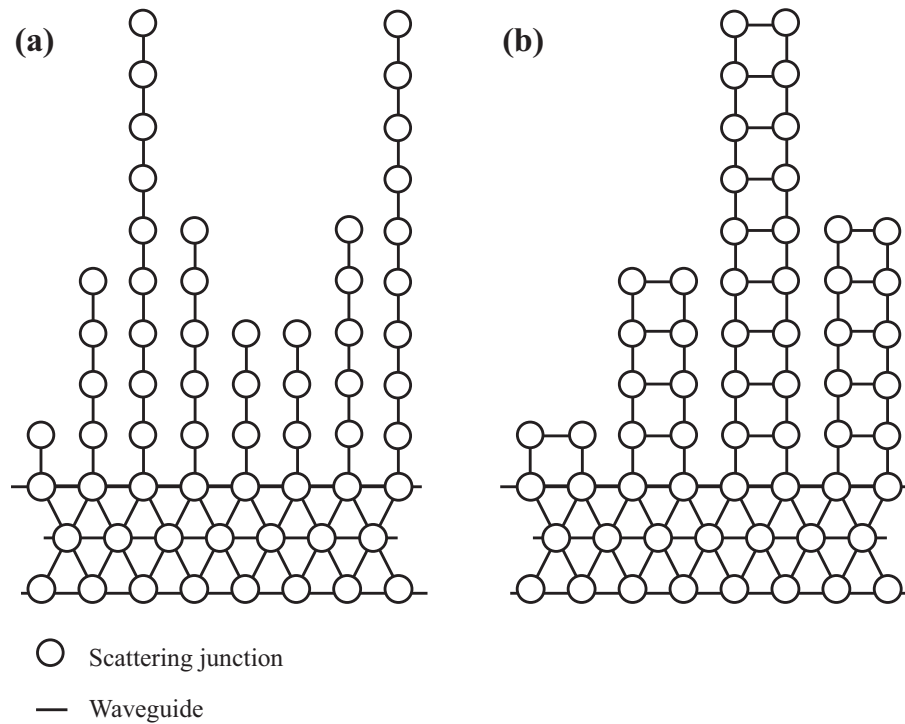


Figure 5.1: Quadratic residue diffuser implementation in a triangular DWM with well widths (a) $w = x$ and (b) $w = 2 \times x$.

The diffuser implementations illustrated in Figure 5.1 show only the particular case where the boundary of the mesh is exactly parallel to the horizontal waveguides within the mesh itself. Figure 5.2 shows a method for applying the quadratic residue implementation to a more irregular boundary in a 2-D DWM with triangular topology.

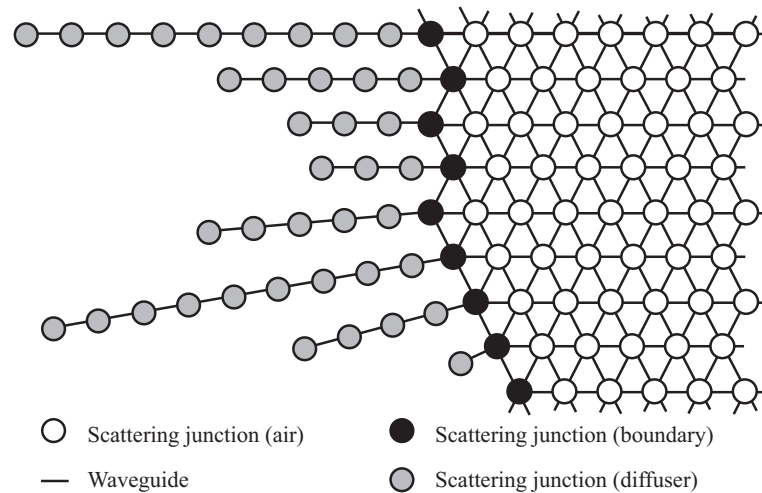


Figure 5.2: Quadratic residue diffuser implementation in a triangular DWM applied to an irregular boundary.



Figure 5.3: 3-D diagram of a simple Schroeder diffuser with cross section.

In the 3-D domain, the simplest quadratic residue diffuser designs result in scattering sound in directions limited to 2 dimensions only, as they are simply extrusions of the 2-D well pattern, as illustrated in Figure 5.3. In order to implement the quadratic residue diffuser model for use in the 3-D DWM, the strings of junctions that make up the wells in 2-D, as illustrated in Figure 5.1, could potentially be extruded by applying them to the mesh boundaries in repeating and connected layers, such that the physical shape of a 3 dimensional quadratic residue diffuser is modelled. Schroeder diffuser designs that apply scattering to sound travelling in more than 2 dimensions are detailed in [44] and could also be modelled at the boundaries of a 3-D DWM.

In [29], the well depths in the diffuser are deliberately chosen to be exact integer multiples of the spatial sampling interval of the mesh. It may however be desirable to model well depths that do not fit this criteria. If this is the case, the well depths can

either be rounded to the nearest integer multiple of the spatial sampling interval, or the other option is to use fractional delay filters, as described in [125]. Such filters are inherently frequency dependent however. A study of the use of a number of fractional delay filters, also known as *rimguides*, and their frequency dependency is presented in [133].

5.2.2 Large Scale Boundary Irregularities

As well as emulating Schroeder diffuser designs at the boundaries of the DWM, it is also possible to model irregularities that are relatively large in comparison to the boundary size, by building them directly into the model. The mesh boundary, with its fixed sampling points in space, is shaped to best fit the desired boundary mapping. The best approach is therefore to use a mesh with sufficient density (corresponding to its update frequency) such that the boundary irregularities are modelled accurately.

5.3 Statistical Diffusion Modelling

5.3.1 Random Roughness

The problem of wave scattering from random rough surfaces is an extensive area of research in the study of electromagnetic waves [146, 147]. One method of scattering prediction involves the generation of 1-D or 2-D rough surfaces based on a mathematical process whose arguments include parameters like rms height and correlation length for example [146]. A similar random generation process can be used to generate a boundary map for the DWM. This is illustrated in Figure 5.4, in which a one-dimensional Gaussian surface is used as a boundary map for part of a 2-D DWM. Processes for random boundary generation, such as the Gaussian surface, are detailed in [146].

Modelling of random rough surfaces requires a knowledge of the statistical properties of the rough surface that is being modelled. This information is not easily acquired for naturally occurring rough surfaces. In addition, the detail of the surface is limited by the density of the mesh, with the result that only relatively large scale random irregularities can be modelled in this way.

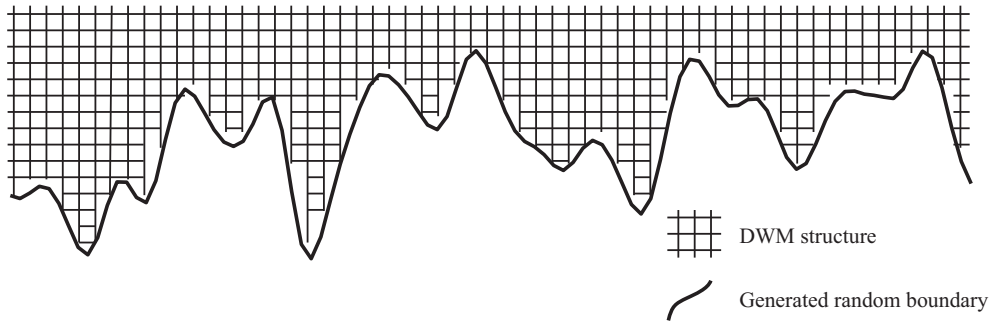


Figure 5.4: Section of a DWM structure with a randomly generated boundary mapping.

5.3.2 A Diffusion Model Using Circulant Matrices

Incoming signals to a scattering junction, $p_{j,i}^+$, in a W-DWM, are processed at each time step according to the scattering equations described in section 4.4.2, resulting in new outgoing signals that are received by the neighbouring junctions at the next time step. These signals can be considered as vectors representing a travelling wavefront. These vectors have directions, \hat{p}_i that are equal to the directions of the connected waveguides. Provided that the vectors evenly span a circle, their directions can be calculated as follows:

$$\hat{p}_i = \begin{bmatrix} \cos\left((i-1)\frac{2\pi}{M}\right) \\ \sin\left((i-1)\frac{2\pi}{M}\right) \end{bmatrix} \quad (5.4)$$

where $i = 1, 2, \dots, M$, equal to the number of connecting waveguides at the scattering junction.

The magnitudes of the vectors are given by the incoming signal values, $p_{j,i}^+$. Therefore the direction ϕ of the wavefront at the junction p_j is:

$$\phi = \angle \left(\sum_{i=1}^N p_{j,i}^+ \hat{p}_i \right) \quad (5.5)$$

It is possible to redistribute these signals so that the direction of travel, ϕ of the wave at that particular junction is altered by an arbitrary angle, φ . Care must be taken however to ensure that signal power and strength are conserved and that the

model remains stable. The altered direction of the wave, ϕ' is therefore:

$$\phi' = \phi + \varphi \quad (5.6)$$

One approach for modelling boundary diffusion in the DWM, introduced in [30] is to multiply the incoming signals, or vector magnitudes at a boundary by circulant matrices in such a way that the resultant directions of the travelling waves, ϕ' are randomly altered at each boundary junction just before they are reflected.

A circulant matrix is a square matrix where each row vector is cyclically shifted by one element to the right relative to the preceding row vector. Circulant matrices have been previously used in the field of audio signal processing, although in a different way, providing a special class of *Feedback Delay Networks* (FDNs) [148, 149, 150]. FDNs are used in the design of digital reverberation effects based on delay lines interconnected in a feedback loop. The feedback signals are processed using a matrix known as the *feedback matrix*. It is important that such systems show stability and this is controlled by the design of the feedback matrix. It is also useful to be able to provide lossless prototypes as a starting point in the FDN design [150]. One approach that can be used in the design of the FDN is to use a circulant matrix, which can be made both stable and lossless by positioning the associated eigenvalues on the unit circle [151]. The positions of the eigenvalues can then be used to control the distribution of the resonant peaks and other properties of the resulting artificial reverb tail [152]. It should be noted that the goal of FDNs however, is to provide reverberation for a sound as a perceptual effect, rather than accurately modelling a sound propagation in an acoustic system, which is the goal according to [30].

In this application the circulant matrix in the DWM is used to rotate the direction ϕ of the travelling waves at each boundary junction, by a different angle at each time step. The design and implementation of the circulant matrices is detailed in section 5.3.3. If this angle φ is varied using an appropriate random function, the energy of the propagating sound waves is effectively diffused as it travels through the boundary junctions. The greater the range of angles by which the propagating wavefronts are rotated, the greater the spread of energy upon reflection. Note that for any angle of incidence, this spread of energy will focus around the specular angle of reflection provided that the mean of the applied random function is zero

degrees.

Rotation Error

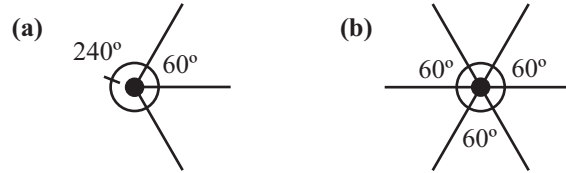


Figure 5.5: (a) A 3-port boundary junction and (b) a 6-port junction with connecting waveguides.

Connecting waveguides at the boundary junctions of a 2-D DWM are generally not distributed uniformly around the junction meaning that they are not all separated by equal angles. An example of this is illustrated in the diagram of a 3-port boundary junction from a 2-D triangular mesh shown in Figure 5.5(a). Similarly, the case also exists where a boundary junction is connected to only 1 neighbour, and hence there is no possibility for any rotation of an incoming signal.

The nature of the circulant matrix transformation technique means that it is only consistent and without error if the connecting waveguides are uniformly distributed around the junction within the DWM, an example of which is shown in Figure 5.5(b). Hence, due to a non-uniform distribution of connecting waveguides at a boundary junction, inconsistencies will occur when the incoming signals are manipulated by the circulant matrices. This is referred to as *rotation error* and analysis shows [30] that there is a complex non-linear mapping between the intended (ideal) angle of rotation and the actual (real) angle of rotation that is dependent on two factors. The first is the amount of rotation that is applied in the ideal case and the second is the angle of approach of the incoming waves. The effects of this discrepancy become less extreme as the number of waveguides connected to a boundary junction increases. This implies that there are non-uniform distribution inconsistencies in this proposed DWM diffusion model, as different types of boundary junctions exhibit different diffusive characteristics. The error becomes particularly apparent when modelling boundaries with low diffusivity, as small angles of rotation will tend to be distorted into large angles.

Figures 5.6(a), (b) and (c), from [30], show the effect of the rotation error on boundary junctions in a 2-D mesh of triangular topology, where φ_r is the desired

rotation angle and θ_i is the original angle of incidence of the reflected wave at the boundary junction in question. The rotation error is defined as the difference between the desired angle of incidence of the reflected wave after rotation and the actual angle of incidence of the reflected wave after rotation.

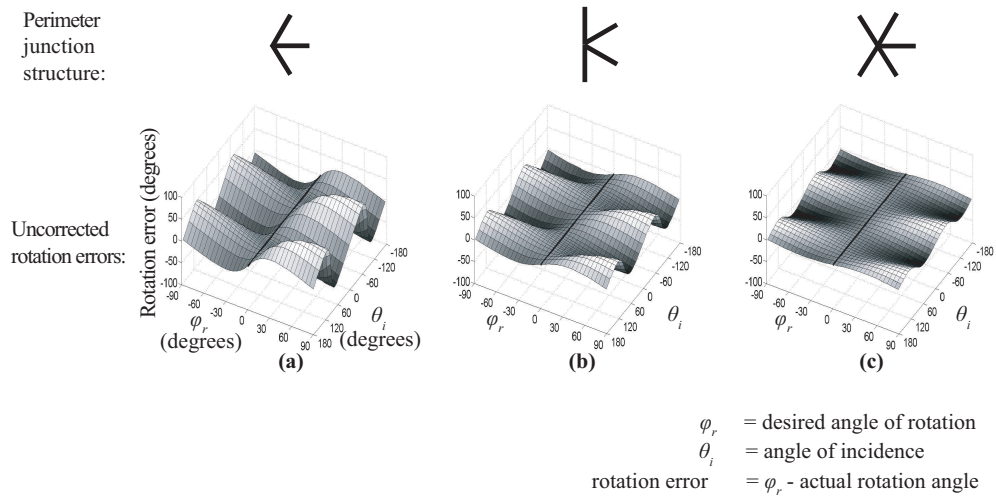


Figure 5.6: Plots of the rotation error for different perimeter junction structures, from [30]

Implementation in the 2-D Triangular DWM

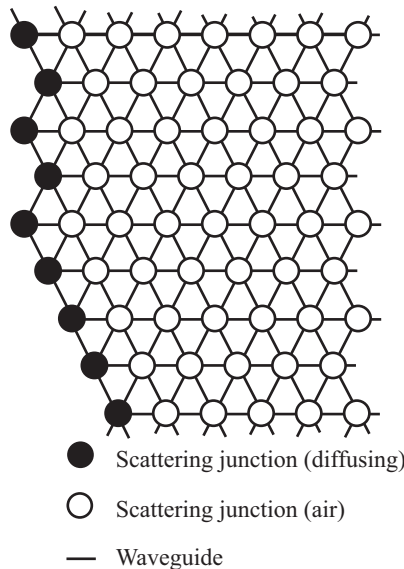


Figure 5.7: A section of a DWM showing the *diffusing* junctions on the mesh boundary.

In the method of modelling diffusion using circulant matrices described in [30], the rotations are applied to boundary junctions in a 2-D DWM of triangular topology,

like those highlighted in the section of DWM illustrated in, for example, Figure 5.7. Such junctions are connected to their neighbouring junctions using waveguides that are not evenly distributed in a circle around them, and there are fewer connecting waveguides to a boundary junction than there are to a 6-port air-junction. Boundary junctions to which the rotations are applied in a 2-D triangular DWM consist of either 2, 3, 4 or 5 connecting waveguides, as illustrated in Figures 5.8(a), (b), (c) and (d) respectively. The junction structures illustrated in Figures 5.8(a), (b), (c) and (d) are the most common boundary junction structures in terms of the relative angles of connecting waveguides, although they may be rotated depending on their position on the boundary of the mesh. In rare cases, other structures are found in a 2-D triangular DWM, such as the 2-port junction illustrated in Figure 5.8(e). It should be noted that for clarity that other configurations than those described in Figure 5.8 are possible.

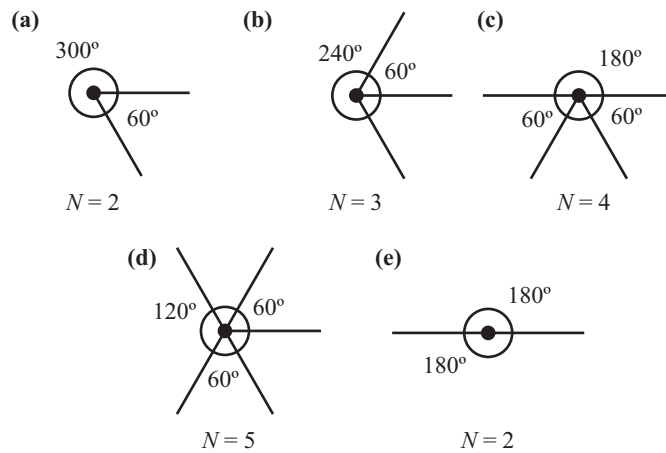


Figure 5.8: (a) 2-port, (b) 3-port, (c) 4-port, (d) 5-port and (e) 2-port scattering junctions from a 2-D triangular DWM with connecting waveguides

The direction of wave travel, ϕ at an N -port air-junction in a 2-D DWM can be rotated by an angle φ if the incoming signals are multiplied with a circulant matrix, \mathbf{A} , whose coefficients can be calculated using the set of eigenvalues X , described by (5.7)-(5.10), where N is the number of connecting waveguides to junction. To achieve rotation, the eigenvalues are arranged symmetrically and are distributed along the unit circle, resulting in signal conservation and stability, as described in [30]. A detailed study of circulant matrices and their associated eigenvalues is given in [153].

$N=2$:

$$X = \begin{bmatrix} e^{j\varphi_r} & e^{-j\varphi_r} \end{bmatrix} \quad (5.7)$$

$N=3$:

$$X = \begin{bmatrix} 1 & e^{j\varphi_r} & e^{-j\varphi_r} \end{bmatrix} \quad (5.8)$$

$N=4$:

$$X = \begin{bmatrix} 1 & e^{j\varphi_r} & -1 & e^{-j\varphi_r} \end{bmatrix} \quad (5.9)$$

$N=5$:

$$X = \begin{bmatrix} 1 & e^{j\varphi_r} & e^{j2\varphi_r} & e^{-j2\varphi_r} & e^{-j\varphi_r} \end{bmatrix} \quad (5.10)$$

An inverse discrete Fourier transform, performed on these eigenvalues, yields N real numbers that sequentially make up the first row of coefficients, $x_0 \dots x_{N-1}$, in the circulant matrix, \mathbf{A} . The coefficients in subsequent rows can be calculated as follows:

$$\mathbf{A} = \begin{bmatrix} x_0 & x_1 & \dots & x_{N-1} \\ x_{N-1} & x_0 & \dots & x_{N-2} \\ \dots & \dots & \dots & \dots \\ x_1 & \dots & x_{N-1} & x_0 \end{bmatrix} \quad (5.11)$$

The resultant direction of the wavefront at the N -port junction, ϕ (defined in (5.5)) is rotated by the angle φ by multiplying the matrix A with the incoming signals p_{ji}^+ to produce a new set of incoming signals, p'_{ji}^+ (5.12). This process is illustrated for a 5-port air-junction in Figure 5.9.

$$\mathbf{A} \begin{bmatrix} p_{j,0}^+ \\ p_{j,1}^+ \\ \vdots \\ p_{j,N-1}^+ \end{bmatrix} = \begin{bmatrix} p'_{j,0}^+ \\ p'_{j,1}^+ \\ \vdots \\ p'_{j,N-1}^+ \end{bmatrix} \quad (5.12)$$

The new incoming signals at the diffusing junctions, p'_{ji}^+ , are subsequently used in the scattering equations (4.20), (4.21) and (4.23) and the simulation continues until the next time step when the next set of incoming signals at each junction are determined and the rotation process described here repeats itself.

Diffusion is simulated by randomly altering the amount of rotation, φ , of the incoming signals at each of the chosen diffusing junctions at each sample time

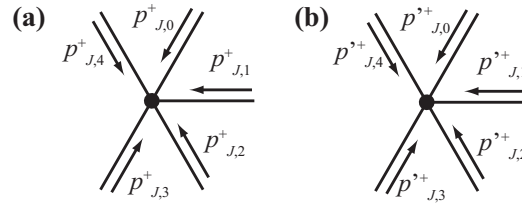


Figure 5.9: Incoming signals at a 5-port diffusing junction J (a) before rotation and (b) after rotation. The resulting incoming signals, $p_{J,i}^{\prime+}$ are then used in the scattering equations rather than the original signals, $p_{J,i}^+$.

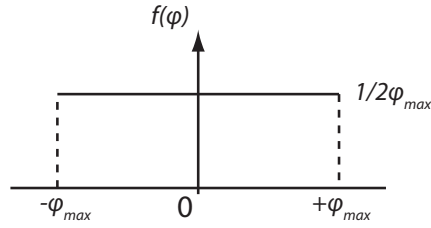


Figure 5.10: Probability density function of the uniform distribution used in the diffuse boundary model.

step, before the scattering equations are calculated. The rotation is applied to the boundary junctions if the original model as described in [30] is employed. A different angle of rotation is randomly chosen for each junction and at each time step, according to a *probability distribution*. The amount of diffusion that is modelled can be controlled by limiting the algorithm to a range of angles. For instance, to simulate a relatively smooth wall the maximum random angle that can be selected is set to ± 5 degrees. Greater diffusivity can be achieved by increasing this angle. In the diffusion model implementation used in this thesis, the rotation angle φ is selected at random according to a uniform probability distribution function $f(\varphi)$ given by (5.13) and illustrated by Figure 5.10, with the result that the rotation angle is limited to $\pm\varphi_{max}$ degrees and the mean of the distribution is zero. Analysis has shown that the use of a fixed rotation angle for each junction, rather than selecting new angles, at each time step, results in a much less effective boundary diffusion model, however this is also an option that could be investigated further.

$$f(\varphi) = \begin{cases} \frac{1}{2\varphi_{max}} & \text{for } -\varphi_{max} \leq \varphi \leq +\varphi_{max} \\ 0 & \text{for } \varphi < -\varphi_{max} \text{ or } \varphi > +\varphi_{max} \end{cases} \quad (5.13)$$

To conveniently distinguish this method of modelling diffuse boundaries from

other methods, it is referred to subsequently as the *diffusing boundary* model.

5.3.3 The Diffusing Layer Model

The Diffusing Layer

Rotation error occurs when the circulant matrix transformation technique is applied to boundary junctions in the DWM. However, if the same method is applied to a standard N -port air-junction then the error is eliminated because the connecting waveguides are uniformly distributed, being separated by equal angles. In the case of a 2-D triangular DWM such junctions have six connecting waveguides, separated by angles of sixty degrees, as shown in 5.5(b). This is the ideal case for the circulant matrix rotation technique as the connecting junctions are evenly distributed around the junction and hence there is no rotation error. Therefore by applying these rotations at air-junctions *adjacent* to the boundary, rather than the boundary junctions themselves, it is possible to achieve diffusion without inherent rotation error.

As a result of this *diffusing layer* technique, waves that approach the boundary are usually rotated twice. Once as they approach the boundary and a second time as they travel away from it after being reflected. This can be compensated for by halving the required rotation angles at the junctions adjacent to the boundary. Undesirable effects may occur, however, when large rotation angles are applied because waves may be rotated more than twice or even just once, depending on the angle of approach and the amount of rotation that is applied.

Implementation in the 2-D Triangular DWM

For the *diffusing layer* model, the circulant matrix operations are applied to 6-port ($N = 6$) air-junctions adjacent to the boundary junctions, like those highlighted in the section of DWM illustrated in Figure 5.7. In this case the eigenvalues used in the construction of the circulant matrix are described by (5.14).

$$X = \begin{bmatrix} 1 & e^{j\varphi} & e^{j2\varphi} & -1 & e^{-j2\varphi} & e^{-j\varphi} \end{bmatrix} \quad (5.14)$$

An inverse discrete Fourier transform, performed on these eigenvalues, yields 6 real numbers that sequentially make up the first row of coefficients, $x_0 \dots x_5$, in

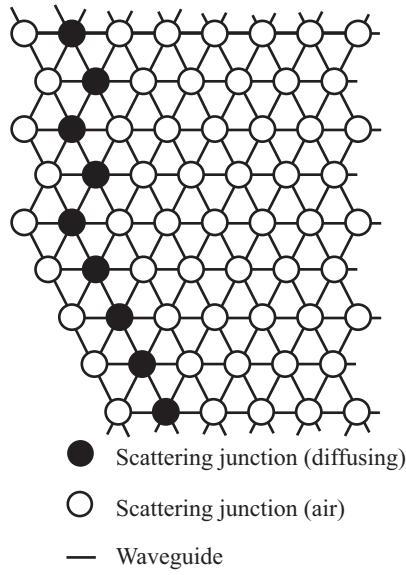


Figure 5.11: A section of a DWM showing the *diffusing* junctions in the diffusing layer model.

the circulant matrix, \mathbf{A} . The coefficients in subsequent rows can be calculated as follows:

$$\mathbf{A} = \begin{bmatrix} x_0 & x_1 & \dots & x_5 \\ x_5 & x_0 & \dots & x_4 \\ \dots & \dots & \dots & \dots \\ x_1 & \dots & x_5 & x_0 \end{bmatrix} \quad (5.15)$$

The resultant direction of the wavefront at the 6-port air-junction, ϕ (defined in (5.5)) is rotated by the angle φ by multiplying the matrix A with the incoming signals $p_{J,i}^+$ to produce a new set of incoming signals, $p'_{J,i}^+$ (5.16). This process is illustrated for a 6-port air-junction in Figure 5.12.

$$\mathbf{A} \begin{bmatrix} p_{J,0}^+ \\ p_{J,1}^+ \\ \vdots \\ p_{J,5}^+ \end{bmatrix} = \begin{bmatrix} p'_{J,0}^+ \\ p'_{J,1}^+ \\ \vdots \\ p'_{J,5}^+ \end{bmatrix} \quad (5.16)$$

As for the circulant matrix diffusing model described in section 5.3.2 the new incoming signals at the diffusing junctions, $p'_{J,i}^+$, are subsequently used in the scattering equations (4.20), (4.21) and (4.23) and the simulation continues until the next time step when the next set of incoming signals at each junction are determined

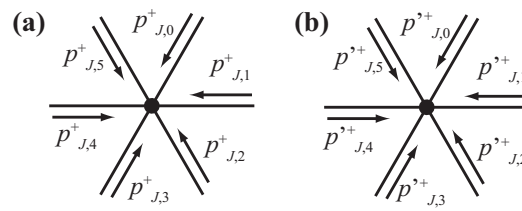


Figure 5.12: Incoming signals at a 6-port diffusing junction J (a) before rotation and (b) after rotation. The resulting incoming signals, $p_{J,i}^{\prime+}$ are then used in the scattering equations rather than the original signals, $p_{J,i}^+$.

and the rotation process described here repeats itself.

Diffusion is simulated by randomly altering the amount of rotation, φ , of the incoming signals at each of the chosen diffusing junctions at each sample time step, before the scattering equations are calculated. In this case the rotation is applied to the junctions found adjacent to the boundary junctions, as illustrated in Figure 5.11. Again a different angle of rotation is randomly chosen for each junction and at each time step, according to a *probability distribution* as detailed in section 5.3.2.

Implementation for Other DWM Topologies and Other Considerations

For other 2-D DWM topologies, diffusion can be implemented using the same principles detailed in the previous section. The diffusing layer model works by performing individual actions to individual junctions either on the boundary or adjacent to the boundary. Because the choice of topology determines the exact positions of junctions in the modelled space and their density even if the same update frequency is used, there will be some effect of topology on the scattering characteristics of the model and this must be investigated. In a similar way, the effect of the mesh update frequency on the diffusion models must be investigated. This is because the greater the update frequency, the more densely populated the scattering junctions in the modelled space, and therefore the more junctions to which the rotations are applied to for a certain length of boundary.

Extending the technique to model surface diffusion in the 3-D DWM requires a 3-D rotation of wave direction at the junctions, and further work is required to achieve this. A method to extend the model for the 3-D rectilinear mesh is presented here however. In this case, six connecting waveguides at a 6-port air-junction can be considered as three sets of four connecting waveguides, found on three different

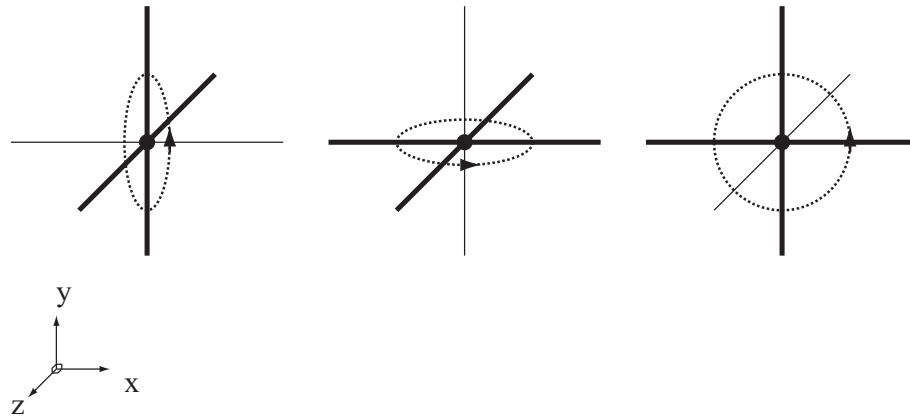


Figure 5.13: Rotation of wave direction in a 6-port air-junction in the 3-D rectilinear DWM.

planes. This is illustrated in Figure 5.13 where it can be seen that each of the three planes divide each other at a perpendicular angle, such that for the first plane x is constant, for the second plane y is constant and for the third plane z is constant. It is also the case that for each of the three sets of four waveguides the remaining two waveguides are perpendicular to the plane in which the four waveguides are found. For the rectilinear case, it is therefore possible to model 3-D diffusion by applying the 2-D matrix operations to either of these three sets of waveguides (chosen at random according to a uniform probability function), where $N = 4$, with a different random angle of rotation determined for each rotation. Considering Figure 5.13, the direction of wave travel is therefore rotated around the x axis, the y axis and the z axis. It is even possible using this method to selectively implement diffuse reflection on one or two of the three planes, by only applying rotations to the relative signals at each junction.

The aim of the diffusing layer technique is to provide a statistical method to implement boundary diffusion without altering the physical make-up of the DWM. The diffusivity of the boundary can also be controlled by altering the probability function used in the random selection of rotation angles, and the model is lossless. In order to be most effective, the technique must have the ability to model the scattering effects of surface irregularities that are too intricate to be modelled by altering the shape of the mesh itself, but also to model the scattering effects of larger surface irregularities as well if required. The effects of the model are investigated in detail in Chapter 6.

Chapter 6

Characterisation of Diffuse Boundary Models in the DWM

6.1 Introduction

A number of different approaches to modelling diffuse reflections in a DWM have been discussed in the previous chapter. It is important however to measure the diffusion characteristics of these approaches in order to test that they work correctly, to measure and record their effects in as much detail as possible, and also to compare their diffusion characteristics to real diffuse surfaces.

In section 6.3 a test is described that is designed to measure the diffusion coefficients of diffusion models in the 2-D DWM, in accordance with the procedure described in section 3.2.1 and [14]. For each boundary the test is performed using a DWM with triangular topology and an update frequency of 44.1 kHz. The results from the tests, including the measured diffusion coefficients, are then presented and discussed. Diffusion coefficient data is obtained for the following boundary implementations:

- A flat plane boundary (section 6.4.1)
- Diffusing objects made up of simple geometry (section 6.4.2)
- Quadratic residue diffuser implementations (section 6.4.3)
- The *diffusing boundary* model (section 6.4.4)
- The *diffusing layer* models (section 6.4.5)

For each boundary implementation, the reflection coefficient r is 1, so that no boundary absorption is modelled. For the diffusing layer model, diffusion coefficients are also measured for the model extended to two and three layers. Also, a number of extra test are performed for the diffusing layer model, in order to investigate how the model behaves at different sample rates and how the diffusing characteristics of the model differ when implemented in a 2-D DWM with rectilinear topology (section 6.4.5).

In section 6.5 the diffusion characteristics of the diffusing boundary and diffusing layer models are further investigated and compared using a modal analysis technique. In section 6.6 the effect of the diffusing layer model on early reflections in the DWM is investigated and in section 6.7, a simple test is described and used to investigate the effect of the diffusing boundary and diffusing layer models on boundary absorption. Section 6.8 describes another way to investigate the behaviour of the diffusing layer model, based on measuring its effect on the diffuseness of the modelled space and its reverberation time. This technique is used to investigate the implementation of the diffusing layer model both in the 2-D triangular DWM and also the 3-D rectilinear DWM. Finally section 6.9 details an investigation into the computational load of adding a diffusing layer model to a DWM system.

During the simulations that follow in which the diffusing boundary and diffusing layer models are implemented, the angle of rotation is selected at random according to a uniform probability function (5.13), limited to a specified range of angles by altering the maximum angle of the probability function φ_{max} . The mean of the function always remains constant at zero.

The following section describes how the mesh excitation is implemented in the simulations used to produce the results in this thesis.

6.2 Mesh Excitation

The signal used to excite the DWM in the following simulations is created by applying a 20th order low-pass Finite Impulse Response filter to the dirac unit impulse function [154]. The filter is designed with a relative cut-off frequency of 0.25 (f/f_{update}). Figure 6.1 shows the resulting signal that is actually used both in

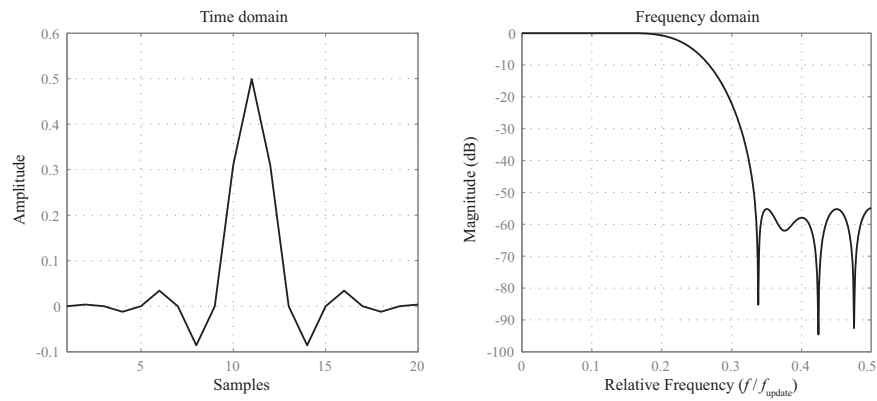


Figure 6.1: Graphs showing the low-pass filtered impulse used as the excitation signal.

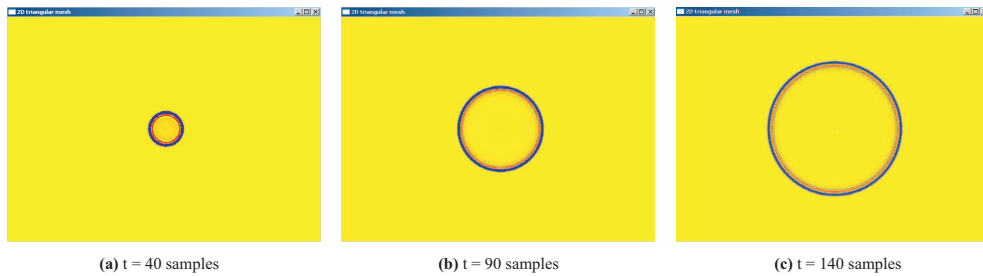


Figure 6.2: Screen shots showing excitation and wave propagation in a 2-D DWM of triangular topology.

the time and frequency domains.

The excitation is applied directly to an input junction by adding the signal to the incoming pressure values at that junction until the excitation signal has finished. Taking (4.23) and assuming that all waveguide impedances are equal at the input junction gives the following:

$$p_J = \frac{2}{N} \sum_{i=1}^N p_{J,i}^+ \quad (6.1)$$

The excitation signal, $x(t)$, is added to the incoming signals, $p_{J,i}^+$, from the connecting waveguides with the result that the scattering equation for the input junction becomes (6.2) and all other scattering equations are implemented as normal.

$$p_J = \frac{2}{N} \sum_{i=1}^N \left(p_{J,i}^+ + \frac{x(t)}{2} \right) \quad (6.2)$$

Figure 6.2 shows the movement of sound waves in a 2-D DWM of triangular topology with an update frequency, f_{update} , of 44.1 kHz, after being excited with the

impulse signal shown in Figure 6.1. The images are produced at time $t = 40, 90$ and 140 samples after the first application of the excitation signal.

6.3 Diffusion Coefficient Measurement in the 2-D DWM

6.3.1 Test Set-up and Geometry

In order to measure the diffusion coefficients for the surface scattering models across a range of incident angles, a test is prepared using the method for obtaining the diffusion coefficient on a single 2-D plane, described in section 3.2.1 and illustrated in Figure 3.4(a). The surface diffusion model is implemented at one edge of a rectangular block placed in the centre of the mesh. In each test, a low-pass filtered impulse is applied to the mesh as the source, which is located at a range of incident angles, from -80° to $+80^\circ$. The impulse is applied at a distance of 8 m from the centre of the diffuse boundary in each simulation. Receivers are placed in a semicircle so that each receiver is at a distance of 5 m from the centre of the diffuse boundary. An angular resolution of 5° is used, with the total number of receivers therefore being 37 , running from -90° to $+90^\circ$ with respect to the norm of the diffuse boundary. The geometry used in each test is illustrated in Figure 6.3. The tail end of the output signal at each receiver is windowed using half of a Hann function [155]. This avoids any abrupt truncation at the end of the signal which can cause errors in the frequency response calculated for the system.

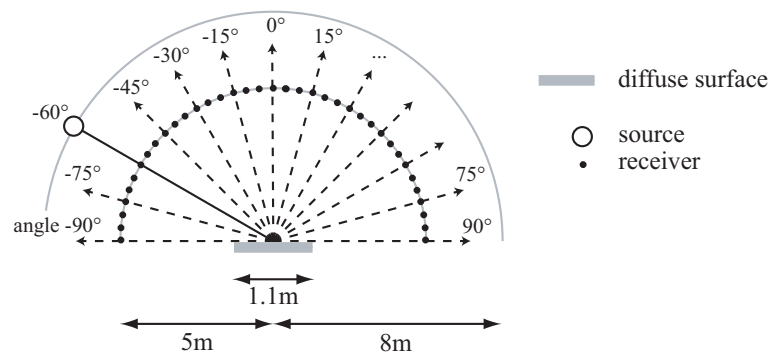


Figure 6.3: Diagram showing the set-up used for the diffusion testing leading to the measurement of the diffusion coefficient in the 2D DWM.

Each simulation is run for sufficient time to allow the propagating signal to travel from the source to the boundary sample under test and then to subsequently reflect and propagate to the receivers. The DWMs used in the tests are sufficiently

large that waves reflecting from the perimeter boundaries do not interfere with the results. In order to obtain the *diffuser impulse response* of the test boundary at each receiver position and for each source position, an impulse response is measured in an empty mesh, so that the direct responses from source to receiver can be removed according to (3.8).

6.4 Results and Discussion

The diffusion coefficient test described in the previous section is applied to a series of different test boundary implementations, resulting in a large quantity of data. The data is represented here using a number of different approaches so that the scattering effects of the different test boundaries can be studied and compared efficiently. All results are provided on the CD-ROM accompanying this thesis, should further analysis be required. A guide to all files found on the CD-ROM is provided in Appendix C. The techniques used to represent the data are described in detail in the following section, where the measured diffuser impulse responses from a plane surface are used. Inspection of the diffuser impulse responses reveals in some cases a rising and falling in signal amplitude with respect to time. This amplitude variation is explained in many cases by diffraction effects caused by the finite length of the diffuse boundary segment. Figure B.3 shows a selection of screen shots taken during a diffusion coefficient measurement simulation for a flat plane boundary where diffraction effects are clearly visible at the corners of the diffuser. Some diffusers used in the diffusion coefficient measurements, such as the quadratic residue diffusers, also have complex geometry, which again will contribute to this variation in amplitude.

6.4.1 Plane Boundary

A flat plane boundary, with no diffusion model applied, is implemented as the test boundary in the form of a thin rectangular block with width 1.10 m and height 0.0381 m. Figure 6.4 shows a frequency analysis of the diffuser impulse responses of the flat plane boundary for the measured angles of incidence from -80° to 80° in the form of spectrograms. For each of the 37 receiver angles, the diffuser impulse response is zero-padded and a 4096-point FFT is applied. The results are presented

using an x -axis relative frequency scale up to a quarter of the sampling rate. The sampling rate of the mesh, f_{update} is set at 44.1 kHz.

Patterns of constructive and destructive interference are evident in the frequency analysis of the diffuser impulse responses for the flat plane boundary case. For each angle of incidence, the amplitude of the reflected energy diminishes in the low frequency region due to the wavelength of the incident sound wave being large when compared to the width of the diffusing object, as discussed in section 3.2.1. According to (3.17), the width of the object, 1.1 m, implies that an incident sound wave will not be reflected effectively below 872 Hz (a relative frequency value of 0.0198 if $f_{update} = 44.1$ kHz). It is important to note that the energy in this low frequency region is not lost as a result of the diffusion model, but rather is not reflected due to the finite size of the test sample.

Figure 6.5 shows the data represented using polar plots. The data is given for the measured angles of incidence -60° , -30° and 0° . The graphs show the RMS levels of the diffuser impulse responses computed at 6 different third octave bands with centre frequencies at 1 kHz, 1.6 kHz, 2.5 kHz, 4 kHz, 6.3 kHz and 10 kHz. These frequencies are chosen so that the scattering effect of the boundary can be observed over a range of frequencies. It can again be seen that the amount of energy that is reflected diminishes at lower frequencies, below 2 kHz. For higher frequencies and for angles of incidence greater than 30° or less than -30° , particularly in the 6.3 kHz and 10 kHz third octave frequency bands, the graphs show that some reflection is caused by edges of the finite test boundary.

The auto-correlation of the measurements taken at each receiver for a specific angle of incidence gives the corresponding directional diffusion coefficient as detailed in section 3.2.1. Figure 6.6 and Table 6.1 show directional diffusion coefficients measured from the flat plane surface for angles of incidence running from -80° to 0° . The diffusion coefficients in these graphs are calculated using the RMS levels at each third octave frequency with central frequencies running from 1 kHz to 10 kHz. The graph and table show that the directional diffusion coefficients measured for the plane flat surface are low but not zero. This demonstrates the scattering effects of a finite boundary, owing to diffraction effects and also reflections from the side of the test boundary. This is also explained by the size of the test boundary in relationship with its distance from the source and receivers. Unless

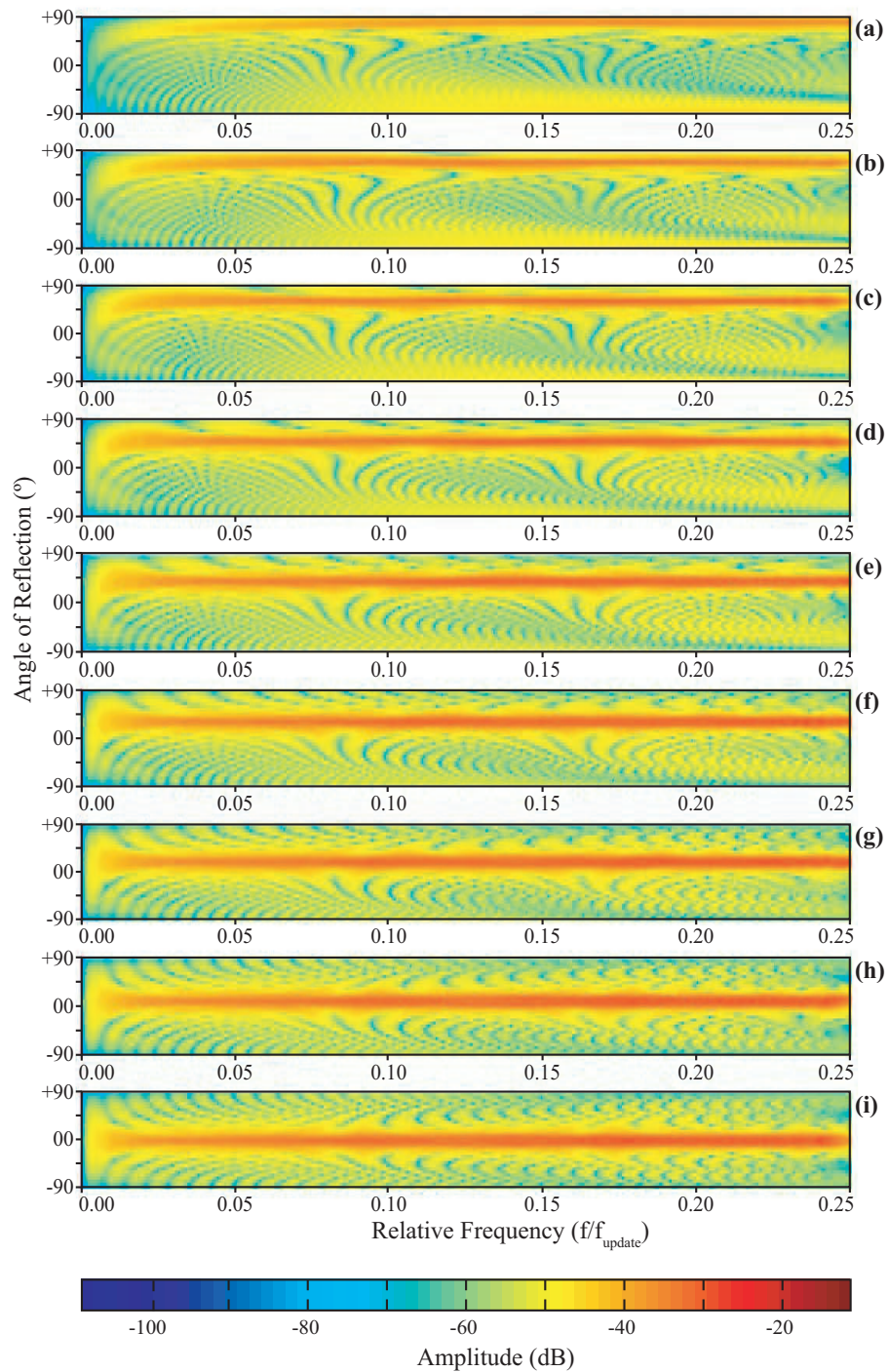


Figure 6.4: Spectrograms showing reflection magnitude of a flat plane boundary varying with angle of reflection across the semicircular range of receivers for incident angles (a) -80° , (b) -70° , (c) -60° , (d) -50° , (e) -40° , (f) -30° , (g) -20° , (h) -10° and (i) 0° .

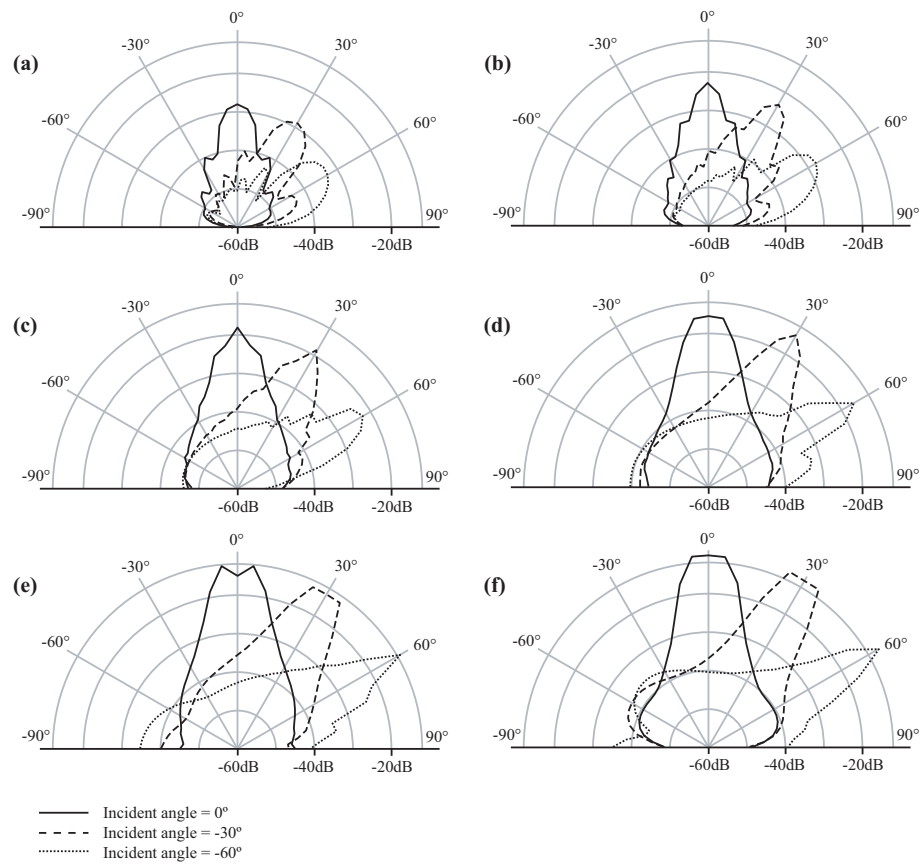


Figure 6.5: Polar responses showing scattering of reflected sound energy from a flat plane surface for incident angles -60° , -30° and 0° in (a) 1 kHz, (b) 1.6 kHz, (c) 2.5 kHz, (d) 4 kHz, (e) 6.3 kHz and (f) 10 kHz third octave bands.

the test boundary is sufficiently small, and the distance from source to receivers is sufficiently large in comparison, the specular zone of reflection from the boundary will encompass more than one receiver, and so a non-zero diffusion coefficient will result even from a plane flat surface. Such conditions, if the size of the test sample is to remain at 1.1 m, require the implementation of a very large DWM and is impractical at this point. If the sample is made smaller, the effective lower cut-off frequency of the reflected energy increases according to (3.17) and the test becomes invalid.

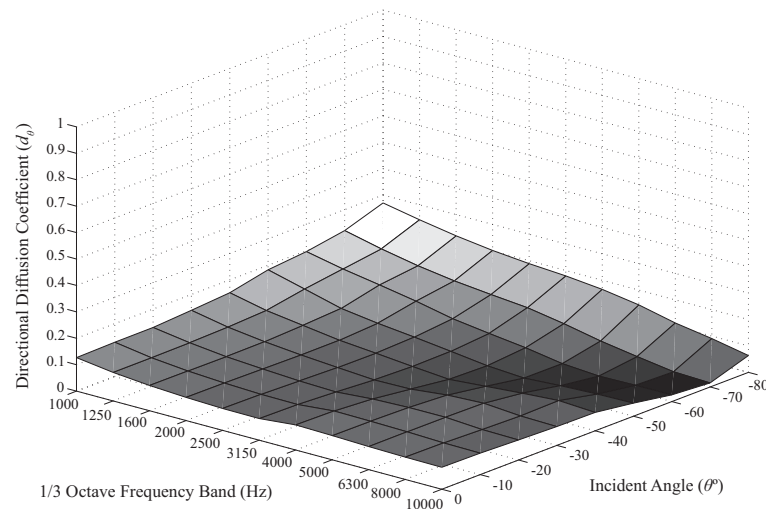


Figure 6.6: Graph showing directional diffusion coefficients measured from a flat plane boundary in third octave bands from 1 kHz to 10 kHz.

Incident Angle (°)	1/3 Octave Band (kHz)										
	1.00	1.25	1.60	2.00	2.50	3.15	4.00	5.00	6.30	8.00	10.00
-80	0.265	0.236	0.210	0.189	0.174	0.162	0.147	0.127	0.108	0.091	0.066
-70	0.220	0.188	0.161	0.140	0.125	0.112	0.089	0.063	0.041	0.020	0.016
-60	0.196	0.168	0.145	0.120	0.091	0.072	0.055	0.032	0.022	0.025	0.026
-50	0.183	0.147	0.111	0.092	0.076	0.060	0.042	0.033	0.041	0.047	0.049
-40	0.151	0.121	0.102	0.083	0.071	0.058	0.046	0.057	0.068	0.077	0.069
-30	0.140	0.113	0.095	0.082	0.072	0.062	0.065	0.079	0.085	0.074	0.071
-20	0.130	0.110	0.094	0.085	0.076	0.072	0.082	0.087	0.088	0.078	0.076
-10	0.130	0.108	0.095	0.087	0.081	0.080	0.092	0.091	0.088	0.083	0.081
0	0.127	0.108	0.096	0.088	0.083	0.082	0.095	0.092	0.087	0.084	0.084
Random Incidence:	0.174	0.147	0.125	0.108	0.095	0.084	0.078	0.072	0.069	0.063	0.058

Table 6.1: Table showing Directional Diffusion Coefficients and Random Incidence Diffusion Coefficients measured from a flat plane boundary.

Once sufficient directional diffusion coefficients are collected then the random incidence diffusion coefficient is determined by calculating their mean [14]. The random incidence diffusion coefficient data for the flat plane surface is given in the bottom row of Table 6.1. The information is also represented in the form of a line

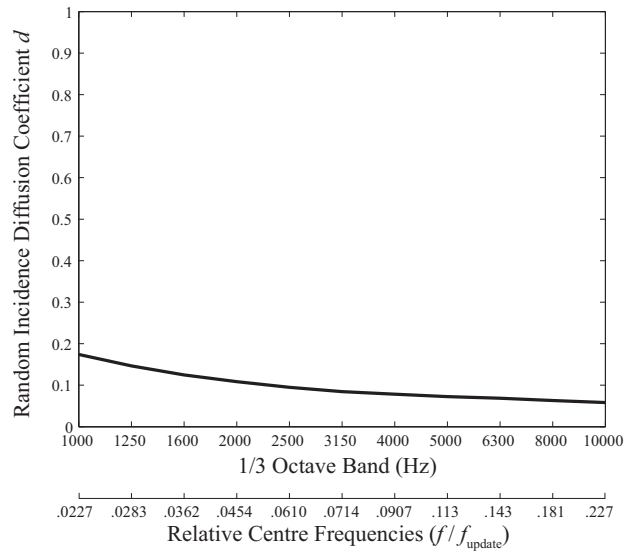


Figure 6.7: Graph showing random incidence diffusion coefficients measured from a flat plane boundary in third octave bands from 1 kHz to 10 kHz.

graph in Figure 6.7. The graph shows a slight increase in diffusion coefficient from 0.058 at the 10 kHz third octave frequency band to 0.174 at the 1 kHz third octave frequency band. This is explained by the reflected energy being diminished at the lower frequencies due to the finite size of the panel, resulting in the energy found in the specular zone of reflection being diminished, as can be seen in the polar plots given in Figure 6.5. This attenuation of energy, alongside the effect of diffraction, results in an attenuation of the difference between energy found in the specular direction and energy found in the non-specular direction, which in turn results in a higher value yielded by the auto-correlation function used in the calculation of the diffusion coefficient.

The data presented here, obtained from diffusion coefficient measurements for a flat plane boundary, is important as it must be taken into account when considering diffusion coefficient measurements for other boundaries, provided the test geometry and conditions are exactly the same. Therefore in the subsequent presentation of results in this thesis, random incidence diffusion coefficient data measured for other diffuse boundaries is given alongside random incidence diffusion coefficient data measured for the flat plane boundary under the same conditions.

6.4.2 Simple Geometric Diffusing Objects

A selection of diffusing objects with simple geometrical shapes are implemented and the results of the diffusion coefficient measurements presented. The geometric objects provide a useful way to test the validity of this method, as the results can easily be compared to results measured using other methods for predicting scattering at boundaries, such as the BEM technique. The results can also be compared to results measured using ray-based modelling techniques, using the same test geometry and diffuser shape.

Triangular Object

An object is implemented in the shape of an isosceles triangle. Two of its angles are 30° , the other 120° and its base is 1.1 m in length. The triangular object is placed such that the base of length 1.1 m is facing away from the receivers, as illustrated in Figure 6.8. The test geometry used is the same as that used for the flat plane boundary, described in section 6.3.1.

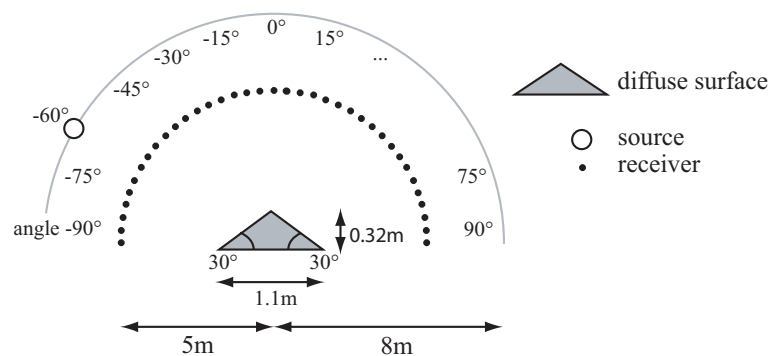


Figure 6.8: Diagram of a triangular shaped diffusing object

Incident Angle ($^\circ$)	1/3 Octave Band (kHz)										
	1.00	1.25	1.60	2.00	2.50	3.15	4.00	5.00	6.30	8.00	10.00
-80	0.119	0.094	0.072	0.055	0.045	0.045	0.068	0.130	0.134	0.123	0.263
-70	0.080	0.069	0.086	0.198	0.194	0.132	0.180	0.269	0.297	0.400	0.404
-60	0.197	0.372	0.268	0.181	0.282	0.284	0.263	0.234	0.225	0.304	0.492
-50	0.366	0.244	0.226	0.209	0.176	0.142	0.109	0.098	0.084	0.111	0.192
-40	0.276	0.236	0.205	0.162	0.141	0.113	0.090	0.083	0.063	0.087	0.096
-30	0.242	0.220	0.170	0.152	0.136	0.121	0.112	0.115	0.094	0.093	0.083
-20	0.258	0.178	0.152	0.125	0.110	0.099	0.093	0.109	0.106	0.118	0.133
-10	0.284	0.222	0.155	0.116	0.096	0.082	0.069	0.075	0.088	0.083	0.186
0	0.465	0.381	0.310	0.252	0.217	0.202	0.162	0.125	0.181	0.209	0.383
Random Incidence:	0.242	0.215	0.175	0.156	0.152	0.131	0.125	0.138	0.139	0.168	0.240

Table 6.2: Table showing Directional Diffusion Coefficients and Random Incidence Diffusion Coefficients measured from a triangular shaped diffuser.

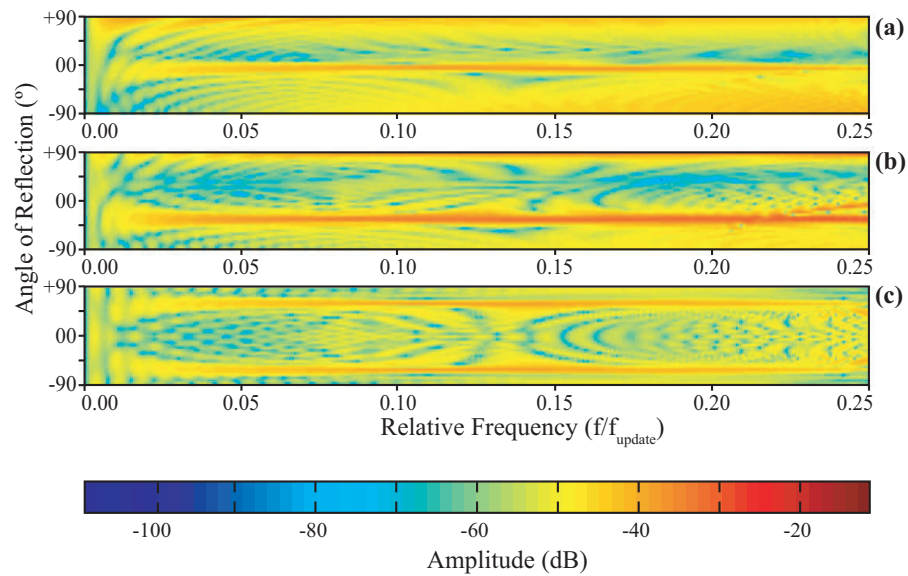


Figure 6.9: Spectrograms showing reflection magnitude of a triangular object varying with angle of reflection across the semicircular range of receivers for incident angles (a) -60° , (b) -30° , (c) 0° .

For this test the spectrograms showing the recorded reflection magnitude, Figure 6.9, and the polar response graphs, Figure 6.10, demonstrate that the propagating sound waves reflect from the diffuser shape in a manner that is predicted according to Snell's law (section 2.9). For example, in the case of normal incidence (Figure 6.9(c)) the reflected energy is largely concentrated at reflection angles -60° and $+60^\circ$ as a result of the incident sound wave reflecting from the front two sides of the triangular diffuser. Figure 6.10(g) shows the frequency independent polar response measured using the ODEON ray-tracing software, with an identical diffuser shape and the same test conditions applied. The difference in the ray-tracing prediction from the DWM simulations is accounted for by the absence of wave diffraction in the applied ray-tracing model, however the direction of concentrated energy in both models is the same.

Table 6.2 shows the resulting frequency dependent directional diffusion coefficients and random incidence diffusion coefficients from the test. The random incidence diffusion coefficients are also shown in Figure 6.11 with random incidence diffusion coefficients from a flat plane boundary for comparison. The diffusion coefficients measured for this diffuser shape remain low, despite the fact that the spectrograms and polar response graphs show that the reflected sound energy is largely scattered away from the specular direction. This is because although the

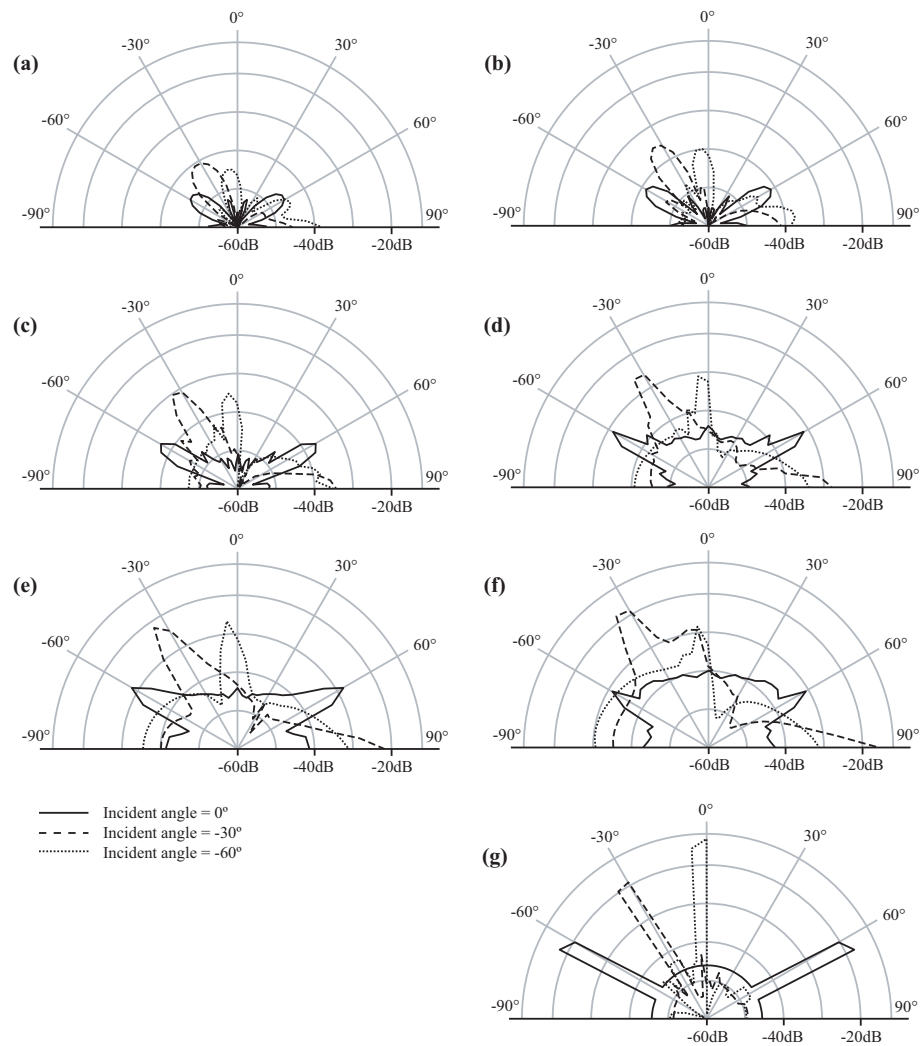


Figure 6.10: Polar responses showing scattering of reflected sound energy from a triangular shaped diffuser for incident angles -60° , -30° and 0° in (a) 1 kHz, (b) 1.6 kHz, (c) 2.5 kHz, (d) 4 kHz, (e) 6.3 kHz and (f) 10 kHz third octave bands, with (g) a frequency independent prediction from ray-tracing simulation.

reflected energy is scattered, it remains concentrated in one or two reflection angles (depending on the angle of incidence). By way of contrast, the scattering coefficient for this diffuser shape would be relatively high compared to that of a flat plane boundary, as discussed in section 3.2.3.

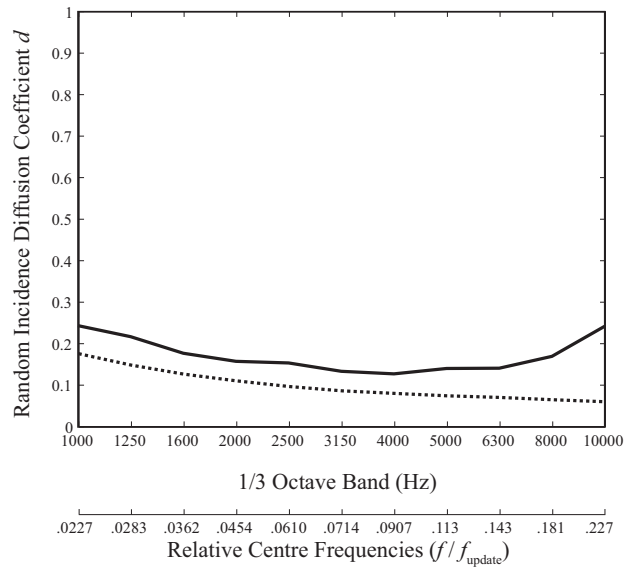


Figure 6.11: Graph showing random incidence diffusion coefficients measured from a triangular shaped diffuser in third octave bands from 1 kHz to 10 kHz.

Semicircular Object

A semicircular object with a diameter of 1.1 m is implemented. For the diffusion coefficient measurements, the object is placed such that the curved side is facing the receivers and flat side of the semicircle is positioned in line with the receivers found at $+90^\circ$ and -90° , as illustrated in Figure 6.12. Again the test geometry is the same as that used for the flat plane boundary.

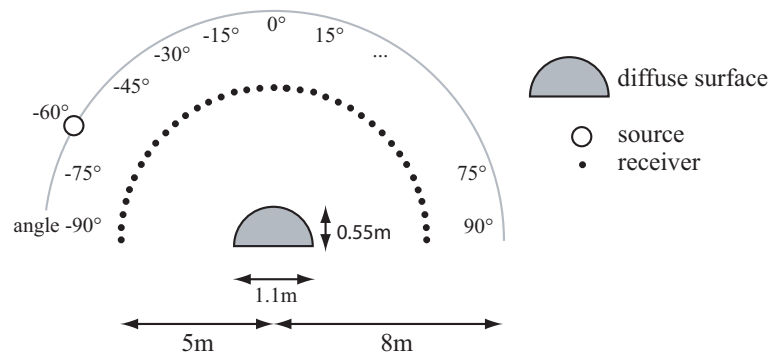


Figure 6.12: Diagram of a semicircular diffusing object.

The resulting spectrograms and polar responses, Figures 6.13 and 6.14 respectively, from the semicircular diffuser show a significant spread of reflected energy away from the specular direction across all frequencies when compared with the flat plane boundary case. Diffusion coefficient data however, as shown in

Table 6.3 and Figure 6.15, implies that this spread of energy reaches a peak in the 4 kHz third octave band and then reduces as the frequency increases. A possible further experiment is to implement a full circle as the diffuse surface rather than a semi-circle. A full circle should theoretically show diffusion characteristics to a semi-circle, owing to the both the effects of diffraction and the increase in the reflection of wave energy from the diffuser's sides.

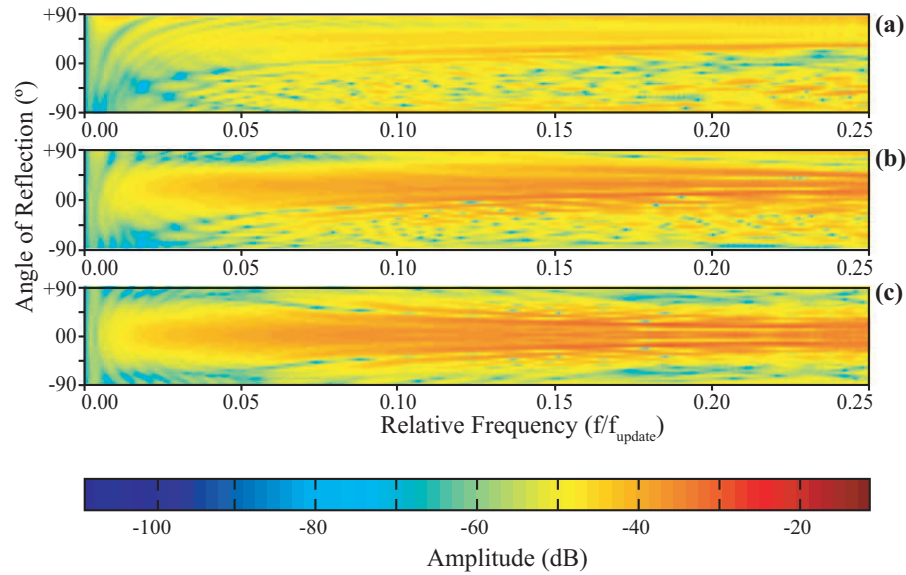


Figure 6.13: Spectrograms showing reflection magnitude of a semicircular object varying with angle of reflection across the semicircular range of receivers for incident angles (a) -60° , (b) -30° , (c) 0° .

Incident Angle ($^\circ$)	1/3 Octave Band (kHz)										
	1.00	1.25	1.60	2.00	2.50	3.15	4.00	5.00	6.30	8.00	10.00
-80	0.077	0.060	0.047	0.040	0.040	0.056	0.076	0.067	0.050	0.061	0.075
-70	0.097	0.180	0.339	0.252	0.205	0.467	0.435	0.543	0.488	0.443	0.555
-60	0.597	0.472	0.521	0.714	0.736	0.807	0.824	0.735	0.619	0.507	0.500
-50	0.564	0.524	0.533	0.539	0.607	0.631	0.638	0.558	0.436	0.369	0.334
-40	0.482	0.464	0.456	0.465	0.493	0.521	0.526	0.466	0.383	0.309	0.377
-30	0.456	0.441	0.426	0.423	0.427	0.484	0.499	0.455	0.391	0.252	0.337
-20	0.447	0.427	0.410	0.404	0.416	0.474	0.485	0.440	0.384	0.235	0.274
-10	0.442	0.422	0.413	0.411	0.416	0.427	0.462	0.459	0.374	0.223	0.260
0	0.435	0.422	0.421	0.414	0.409	0.414	0.462	0.463	0.372	0.220	0.262
Random Incidence:	0.398	0.377	0.395	0.406	0.417	0.479	0.491	0.465	0.389	0.295	0.334

Table 6.3: Table showing directional diffusion coefficients and random incidence diffusion coefficients measured from a semi-circular shaped diffuser.

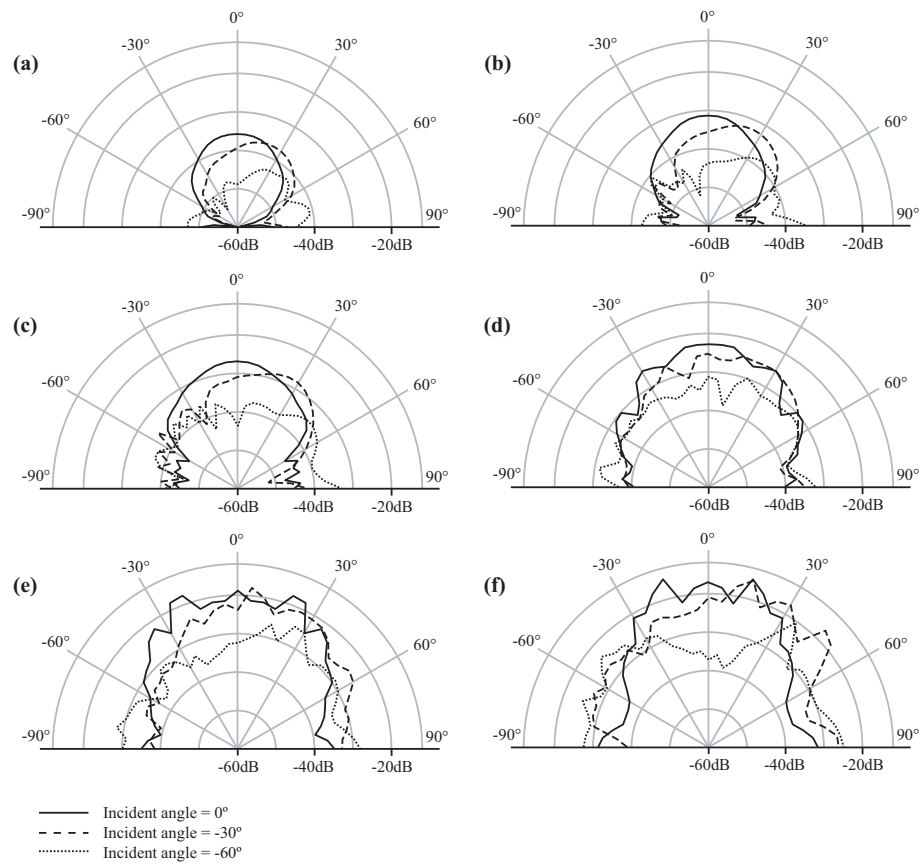


Figure 6.14: Polar responses showing scattering of reflected sound energy from semi-circular shaped diffuser for incident angles -60° , -30° and 0° in (a) 1 kHz, (b) 1.6 kHz, (c) 2.5 kHz, (d) 4 kHz, (e) 6.3 kHz and (f) 10 kHz third octave bands.

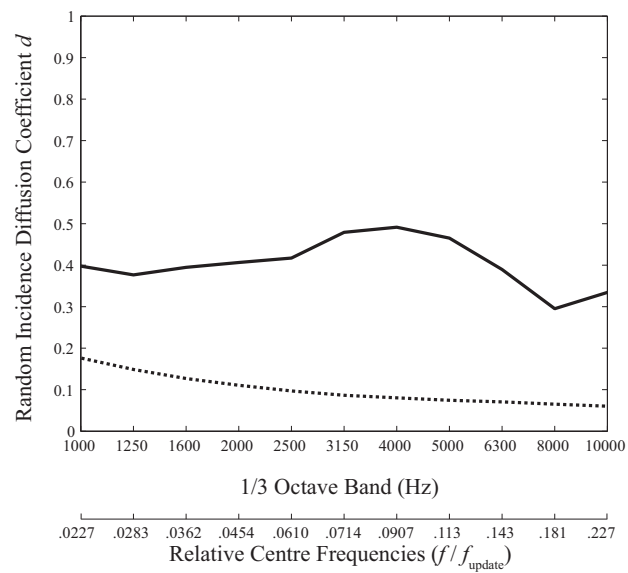


Figure 6.15: Graph showing random incidence diffusion coefficients measured from a semi-circular shaped diffuser in third octave bands from 1 kHz to 10 kHz.

6.4.3 Quadratic Residue Diffuser

A quadratic residue diffuser is implemented as the test surface for the diffusion coefficient tests, using the design described in section 5.2.1. In previous work, the scattering effects of such a model are analysed empirically using a visualisation of a DWM at different stages of wave propagation [29]. A single polar plot is also given, showing the scattering levels for a half-plane wave normal to the boundary for all frequencies. The information for the polar plot given in [29] is obtained using a slightly different technique to that used here. A half-plane wave is used as the source and the diffuser is implemented at the mesh boundary, with receivers placed along a line parallel to the boundary [29]. The analysis in [29] clearly demonstrates the scattering ability of the model, however a more detailed analysis of its scattering properties are presented here and different implementations of the model, as discussed in section 5.2.1 are tested and compared.

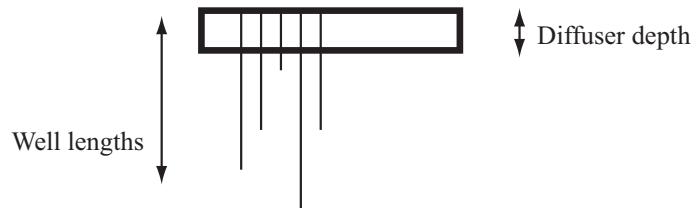


Figure 6.16: Illustration showing the lengths of the modelled quadratic diffuser wells in comparison with apparent depth of the diffuser object as used in the diffusion coefficient measurement.

In each test, a triangular DWM is used. Using the plane boundary model used in section 6.4.1 as a starting point, the quadratic residue diffuser is implemented by attaching 1-D columns, or strings, of junctions to its edge. The strings of junctions are attached using the approach illustrated in Figure 5.1. Using this method of implementation, the depth of the diffuser, based on the orientation of its sides and back, is kept the same as the depth of the plane surface used in section 6.4.1, however the depths of most of the wells are actually greater than the depth of the diffuser when observed from behind or from the side. This situation, illustrated in Figure 6.16, would be impossible to implement in the real world, as the depth of the diffuser must be at least as great as the depth of the deepest well. This ability of the DWM to model physically impossible space is advantageous in this case, because by keeping the apparent depth of the diffuser, as seen from its back and its sides, to a minimum, the effects of edge diffraction and reflection at the edges of

the boundary, which serve to interfere with the polar response, are also kept to a minimum.

For each quadratic residue diffuser implementation, a mesh update frequency, f_{update} of 44.1 kHz is used, and the width of the diffuser is 1.1 m (100 junctions). The quadratic residue sequence is repeated for the required number of times such that it is implemented across the entire receiver-facing edge of the diffuser.

Quadratic Diffuser Model Q-A

For the first quadratic residue implementation, the quadratic residue sequence length $N = 17$ is used. A design wavelength λ_0 of 0.264 m is chosen, with the result that the depth of the n th well in spatial sampling intervals x_n (i.e. the number of junctions) is equal to the integer value of the n th number in the quadratic residue sequence, s_n (5.3). The design wavelength λ_0 is equivalent to a frequency f_0 of 1.297 kHz, or a relative frequency f/f_{update} of 0.0294. The lower wavelength of the design bandwidth is $\lambda_{min} = 0.0220$ m, such that the width of each well, w is 0.0110 m, equating to 1 spatial sampling distance x (one junction). The lower wavelength λ_{min} corresponds to an upper frequency of 15.6 kHz, or a relative frequency f/f_{update} of 0.354, well above the upper frequency limit of measurement. This implementation is referred to as **Q-A**. In order that the quadratic residue model is implemented across the entire face of the diffusing object, the sequence of wells is repeated five full times, with a partial repetition of the sequence added in order to give the required diffuser width of 1.1 m. The partial repetition of the sequence consists of the first 15 wells in the sequence only.

Frequency analysis of the diffuser impulse responses, shown in Figure 6.17, indicates a general increase in signal scattering as frequency increases. However, from about 684 Hz and upwards, patterns of diffusion in the reflected energy become apparent. Schroeder diffusers theoretically diffuse the reflected sound energy optimally at the design frequency, f_0 , and at integer multiples of the design frequency. Frequency bands of high boundary diffusivity are apparent in the frequency analysis that demonstrate optimal diffusion frequency bands in the actual model, however it is not possible with this data to fully measure their consistency with the frequency bands of optimal diffusion as predicted by the design theory [44]. Further analysis is required to test for this effect, where the boundary diffusivity is

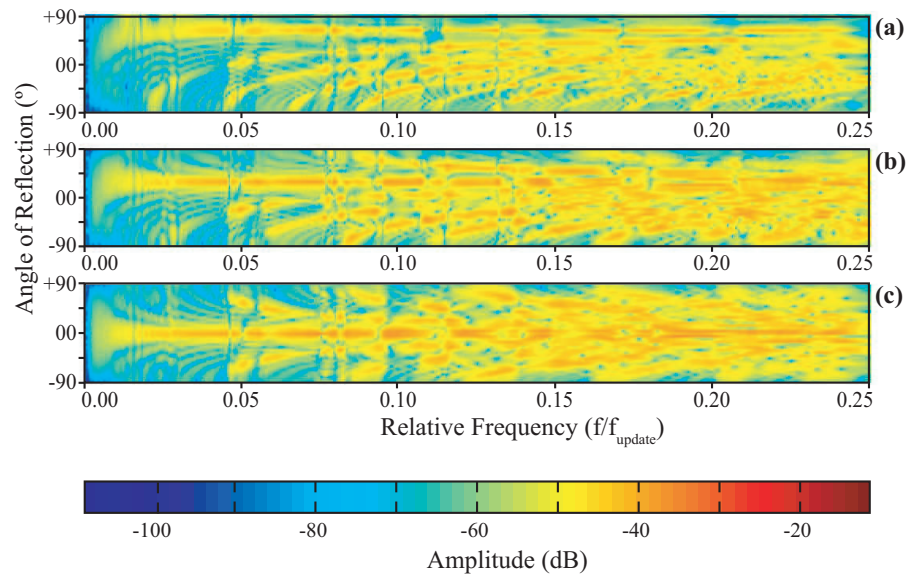


Figure 6.17: Spectrograms showing reflection magnitude of the quadratic diffuser model **Q-A** varying with angle of reflection across the semicircular range of receivers for incident angles (a) -60° , (b) -30° , (c) 0° .

measured only for a narrow frequency band.

The reason for the general increase in diffusion as frequency increases is most likely because of the scattering caused by the irregular geometry of the boundary, rather than the optimum scattering effect that is predicted by the theory which governs the diffuser design. Scattering caused by the geometry of the scattering object increases as the wavelength of the sound approaches a length that is comparable to, or even smaller than, the size of the irregularities of the diffusing object.

In addition to the narrow frequency bands at which the diffuser causes maximum scattering, critical frequencies occur at Nf_0 and at integer multiples of this frequency, where the scattering of the quadratic residue diffuser is effectively like that of a plane surface [44]. For the diffuser model **Q-A** however, the lowest of these frequencies is at 15.6 kHz, a relative frequency of 0.354, which is greater than the measurement limit of 0.25. This phenomena is therefore not observed in the results.

The polar response graphs, Figure 6.18, and resulting diffusion coefficients, Table 6.4 and Figure 6.19, again show a general increase in scattering as frequency is increased. There are two explanations for this. The first is, as stated before, that the scattering caused by the general complexity of the boundary is greater at

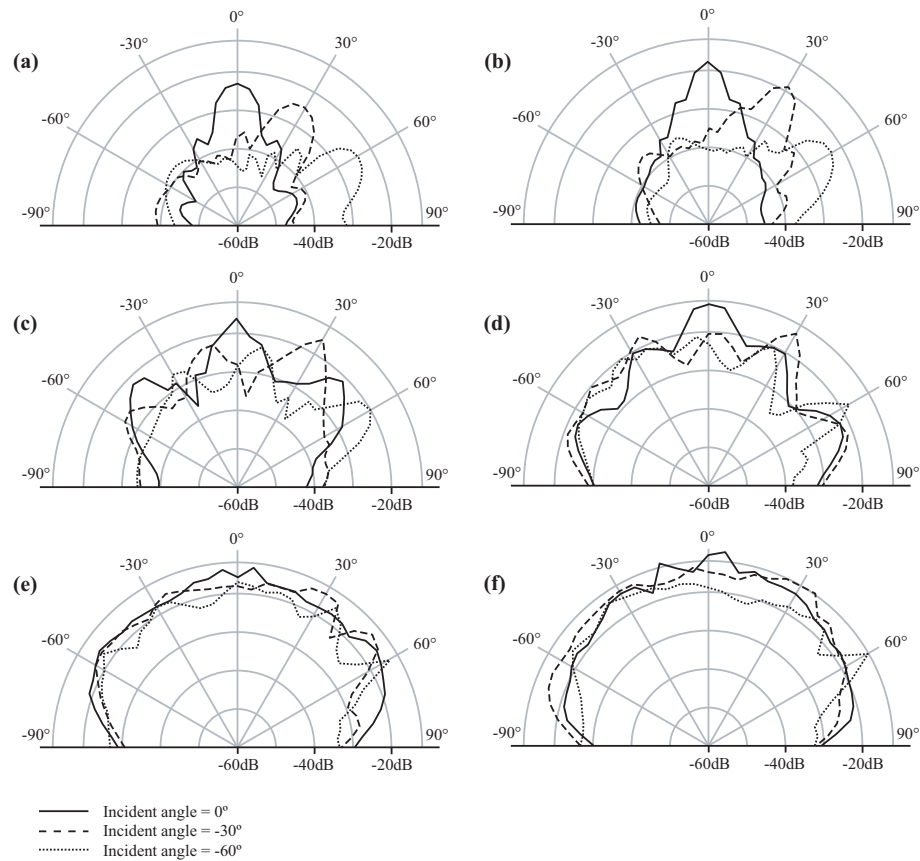


Figure 6.18: Polar responses showing scattering of reflected sound energy from quadratic diffuser model **Q-A** for incident angles -60° , -30° and 0° in (a) 1 kHz, (b) 1.6 kHz, (c) 2.5 kHz, (d) 4 kHz, (e) 6.3 kHz and (f) 10 kHz third octave bands.

Incident Angle ($^\circ$)	1/3 Octave Band (kHz)										
	1.00	1.25	1.60	2.00	2.50	3.15	4.00	5.00	6.30	8.00	10.00
-80	0.594	0.334	0.261	0.364	0.402	0.503	0.638	0.598	0.624	0.529	0.332
-70	0.614	0.370	0.194	0.382	0.445	0.441	0.635	0.582	0.607	0.526	0.423
-60	0.450	0.354	0.167	0.293	0.289	0.298	0.555	0.478	0.551	0.504	0.542
-50	0.313	0.255	0.121	0.234	0.220	0.209	0.415	0.435	0.566	0.705	0.686
-40	0.223	0.230	0.111	0.177	0.194	0.179	0.383	0.476	0.607	0.634	0.696
-30	0.160	0.188	0.103	0.166	0.186	0.181	0.456	0.518	0.607	0.669	0.654
-20	0.135	0.144	0.100	0.166	0.167	0.225	0.386	0.510	0.592	0.484	0.558
-10	0.130	0.130	0.097	0.175	0.251	0.238	0.305	0.634	0.609	0.467	0.528
0	0.126	0.131	0.095	0.169	0.260	0.130	0.256	0.454	0.710	0.521	0.458
Random Incidence:	0.315	0.244	0.141	0.240	0.269	0.275	0.459	0.525	0.602	0.562	0.547

Table 6.4: Table showing directional diffusion coefficients and random incidence diffusion coefficients measured from the quadratic diffuser model **Q-A**.

higher frequencies. The second is that the third octave bands are on a logarithmic scale, meaning that as the centre frequency of the third octave band increases with each subsequent third octave band, the range of frequencies covered by the band increases. Owing to the fact that the quadratic diffuser residue works optimally at the design frequency (1.297 kHz) and at integer multiples of this design frequency, a greater number of optimal frequency points are found in each third octave band

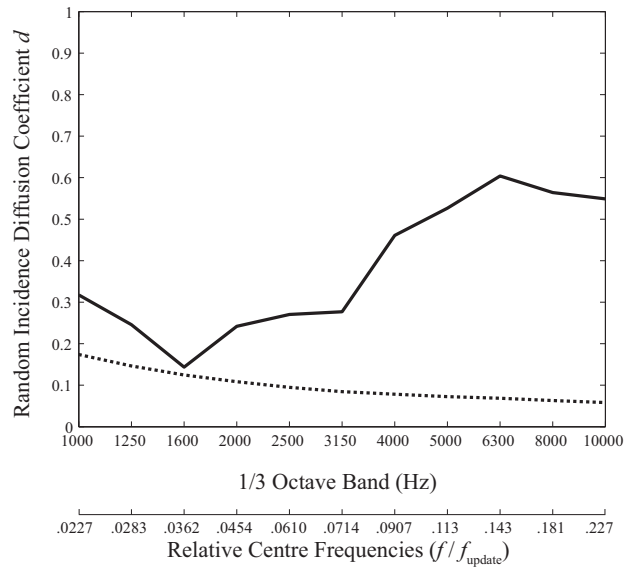


Figure 6.19: Graph showing random incidence diffusion coefficients measured from the quadratic diffuser model **Q-A** in third octave bands from 1 kHz to 10 kHz.

as the centre frequency increases, and hence the overall amount of diffusion caused by the design of the diffuser itself, rather than its complex shape, also increases.

The random incidence diffusion coefficient, Table 6.4 and Figure 6.19 shows a drop at the third octave band with centre frequency 1.6 kHz. The coefficient reaches a minimum value here of 0.141, only 0.016 (12.8%) greater than the random incidence coefficient of a flat plane surface, 0.125, measured at the same third octave band. The most likely reason for this is that the third octave frequency band does not include, nor is it close to, any of the multiples of the lower design frequency f_0 . The nearest multiples are found at 1.297 kHz and 2.594 kHz. Additionally at this low frequency, the scattering effect of the diffuser caused by the complexity of the model is also low.

Quadratic Diffuser Model Q-B

For this case, a quadratic residue sequence length $N = 17$ is again used and the lower wavelength of the design bandwidth λ_0 is 0.0220 m, such that the width of each well w is 0.0110 m (one spatial sampling distance). A design wavelength λ_0 of 0.529 m is chosen, so that the depth of the n th well in the quadratic residue sequence in spatial sampling intervals, x_n , is equal to twice the integer value of the n th number in the quadratic residue sequence. In other words, for quadratic residue diffuser **Q-B** the depth of the diffuser wells is doubled in comparison to model **Q-A**. The design wavelength λ_0 is equivalent to a frequency f_0 of 649 Hz, a relative frequency of 0.0147, equal to half of the design frequency of model **Q-A**. The sequence of wells is again repeated 5 full times, with the addition of a partial repetition, consisting of the first 15 wells in the sequence.

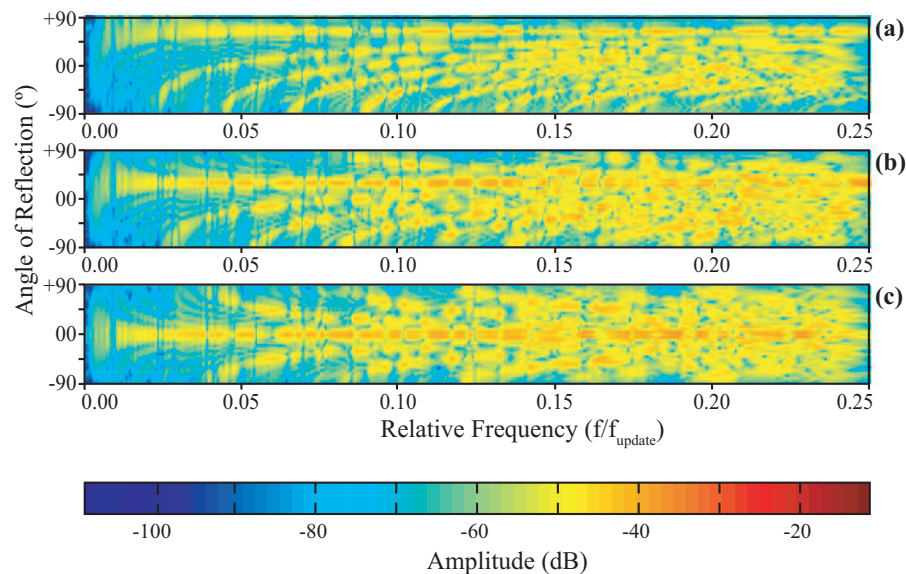


Figure 6.20: Spectrograms showing reflection magnitude of the quadratic diffuser model **Q-B** varying with angle of reflection across the semicircular range of receivers for incident angles (a) -60° , (b) -30° , (c) 0° .

Frequency analysis of the diffuser impulse responses, shown in Figure 6.20, again indicate a general increase in signal scattering as frequency increases. Again, disturbances in this general pattern occur across the entire measurement spectrum. This time, the disturbances start from a lowest frequency of about 419 Hz, a relative frequency of 0.0950. The distribution of the disturbances appears to be denser than the distribution in the previous model. This behaviour is expected because the

design frequency f_0 of the quadratic residue diffuser **Q-B** is half that of **Q-A**, and the theoretical optimal diffusion frequencies, existing at integer multiples of the design frequency, are uniformly distributed across the frequency spectrum with twice the density.

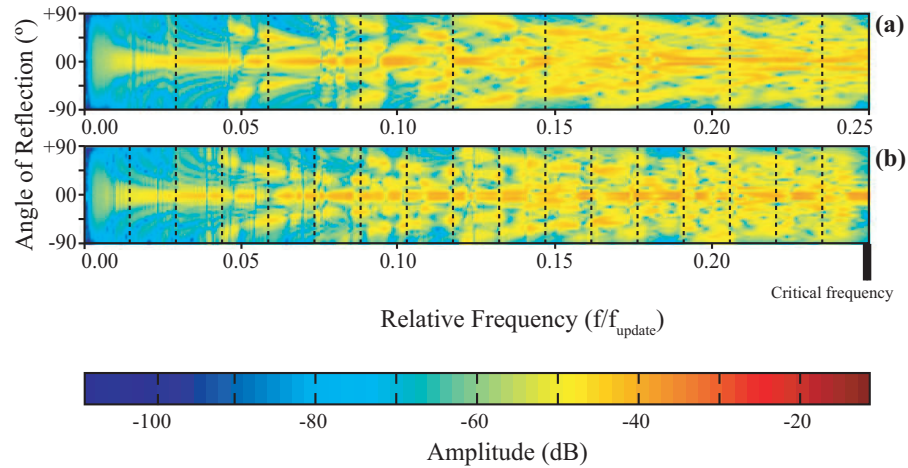


Figure 6.21: Spectrograms showing reflection magnitude of the quadratic diffuser models (a)**Q-A** and (b)**Q-B** across the semicircular range of receivers for the 0° angle of incidence, with theoretical optimal diffusion frequencies marked using dotted lines.

Figure 6.21 shows the reflection magnitude spectrograms for the 0° angle of incidence only for both (a) model **Q-A** and (b) model **Q-B**. In each spectrogram, the frequencies at which the models theoretically demonstrate optimal diffusion, according to the design theory, are marked using vertical dotted lines.

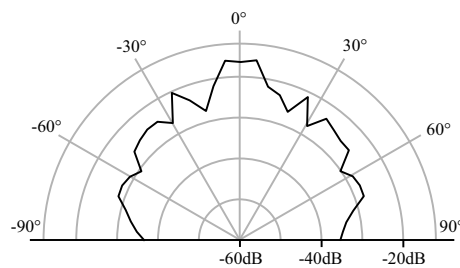


Figure 6.22: Polar response showing scattering of reflected sound energy from quadratic diffuser model **Q-B** for normal incidence at the frequency 11.025 kHz.

According to the design theory, the so-called critical frequencies (the frequencies at which the model exhibits specular behaviour) occur at Nf_0 and at integer multiples of this frequency. At these frequencies the theoretical scattering of the quadratic residue diffuser is effectively like that of a plane surface [44]. For the

diffuser model **Q-B** the lowest of these frequencies is at 11.025 kHz, a relative frequency of 0.25. This frequency is marked on the spectrogram in Figure 6.21(b) by a thick black vertical line positioned underneath the frequency axis. The expected behaviour is not completely apparent from the spectrogram, largely due to increased scattering of reflected waves at high frequencies caused by the complex shape of the diffuser.

Figure 6.22 is a polar response showing scattering caused by the quadratic diffuser **Q-B** for the specific frequency of 11.025 kHz. The response was created by exciting the mesh using a 11.025 kHz pure tone that repeats for 11 cycles and is windowed using a Hann function [155]. The polar response yields a diffusion coefficient of 0.405, indicating that the diffuser is not effectively behaving like a plane surface at this frequency, as the design theory predicts. One reason for this discrepancy may be the fact that in order to have the correct width, the implemented diffuser is not made up of 3 complete repeating quadratic residue sequences, but rather 2 and 15/17 sequences. Another reason may lie in errors caused by the assumption of using 1-D strings of junctions to model wells that should theoretically be 2-D.

Incident Angle (°)	1/3 Octave Band (kHz)										
	1.00	1.25	1.60	2.00	2.50	3.15	4.00	5.00	6.30	8.00	10.00
-80	0.392	0.350	0.334	0.403	0.394	0.470	0.541	0.418	0.616	0.488	0.215
-70	0.467	0.424	0.305	0.420	0.433	0.579	0.668	0.363	0.618	0.512	0.266
-60	0.418	0.425	0.219	0.285	0.282	0.446	0.641	0.247	0.491	0.544	0.481
-50	0.311	0.329	0.163	0.191	0.241	0.339	0.501	0.205	0.447	0.614	0.647
-40	0.220	0.299	0.148	0.152	0.240	0.267	0.324	0.261	0.543	0.726	0.626
-30	0.156	0.233	0.139	0.142	0.231	0.192	0.342	0.308	0.557	0.635	0.501
-20	0.136	0.153	0.135	0.141	0.219	0.234	0.300	0.305	0.571	0.481	0.470
-10	0.132	0.128	0.128	0.154	0.321	0.226	0.287	0.325	0.550	0.408	0.517
0	0.130	0.131	0.120	0.203	0.319	0.163	0.313	0.316	0.494	0.395	0.461
Random Incidence:	0.270	0.283	0.192	0.234	0.296	0.333	0.442	0.305	0.546	0.542	0.465

Table 6.5: Table showing directional diffusion coefficients and random incidence diffusion coefficients measured from the quadratic diffuser model **Q-B**.

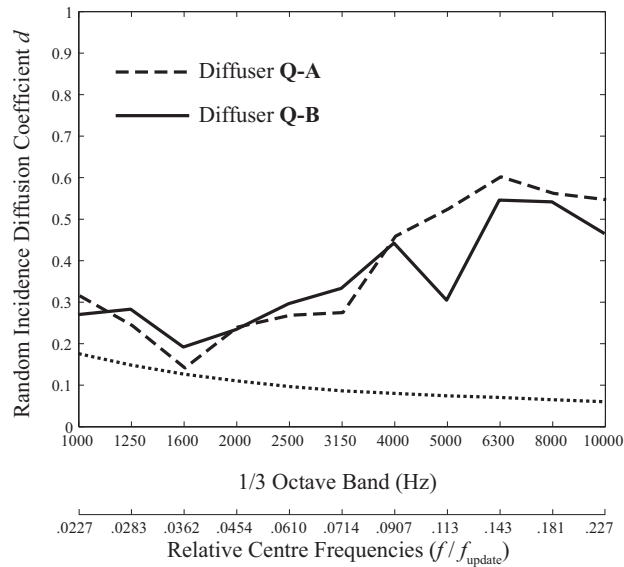


Figure 6.23: Graph showing random incidence diffusion coefficients measured from the quadratic diffuser models **Q-A** and **Q-B** in third octave bands from 1 kHz to 10 kHz.

6.4.4 The Diffusing Boundary Diffusion Model

The *diffusing boundary* diffusion model, described in section 5.3.2, is implemented at one edge of a rectangular block, exactly the same in shape as the rectangular block used to implement the flat plane boundary in section 6.4.1. The diffusion coefficient measurements are made with the same test geometry as used in the other tests described so far. All boundaries of the rectangular panel are defined as totally reflective.

The circulant matrix diffusion model is tested for seven different levels of diffusivity, theoretically analogous to seven acoustically reflective materials with different diffusive properties. The materials are modelled using a uniform probability function to select the random angles of rotation, with maximum rotation angles of 0° , $\pm 15^\circ$, $\pm 30^\circ$, $\pm 45^\circ$, $\pm 60^\circ$, $\pm 75^\circ$ and $\pm 90^\circ$. For later reference, these are labelled **CM00**, **CM15**, **CM30**, **CM45**, **CM60**, **CM75** and **CM90** respectively. The **CM** refers to the circulant matrix model and the number that follows this prefix refers to the maximum rotation angle used in the model. Theoretically the higher the maximum angle in the random function used to control the diffusion, the greater the diffusivity of the material. The first model, **CM00**, is effectively a plane boundary model and results should theoretically be identical to the results measured from the

plane boundary model in section 6.4.1. This is confirmed by comparing the random incidence diffusion coefficients measured for the model **CM00** (found in the first column of diffusion coefficients in Table 6.6) with the random incidence diffusion coefficients measured for the plane surface model (found in the final row of Table 6.1), which are identical in each third octave band.

Figures 6.24 and 6.25 show a frequency analysis of the diffuser impulse responses for angles of incidence -30° and 0° respectively in the form of spectrograms. In each figure, the angle of incidence is constant and the results are displayed for each of the range of diffusive materials modelled with the circulant matrix technique.

The patterns of constructive and destructive interference, evident in the plane surface models and simple geometric models, are not observed when the diffuse models are used, as the spectrum becomes more noise-like. It is clear from the spectrograms that as the maximum angle is increased for the uniform random distribution function, the energy observed at the angle of specular reflection (30° in Figure 6.24 and 0° in Figure 6.25) reduces, and the total energy observed at other angles increases.

The data is also presented using polar plots, Figures 6.26, 6.27 and 6.28. This time the data is given for angles of incidence -60° , -30° and 0° respectively. The graphs show the RMS levels of the diffuser impulse responses computed for third octave bands with centre frequencies 1 kHz, 2 kHz, 4 kHz and 8 kHz.

Figure 6.29 shows directional diffusion coefficients for each boundary model for angles of incidence running from -80° to 0° . The diffusion coefficients in these graphs are calculated using the RMS levels of the diffuser impulse responses at four different third octave bands with centre frequencies equal to those chosen for the polar responses (Figures 6.26, 6.27 and 6.28).

The graphs in Figure 6.29 show a rise in diffusion coefficient across all angles of incidence as the maximum rotation angle used in the diffusion model increases, although for angles of incidence of -60° and above this rise in diffusion coefficient is very slight in the lower three third octave bands. At 1 kHz, the diffusion coefficients rise from 0.174 on average across the range of incident angles for the diffusion model **CM00**, to just 0.227 on average for **CM90**. At 8 kHz however, this average of diffusion coefficients rises from 0.063 for the diffusion model **CM00** to 0.536 for **CM90**. Further tests show that increasing the maximum rotation angle further than

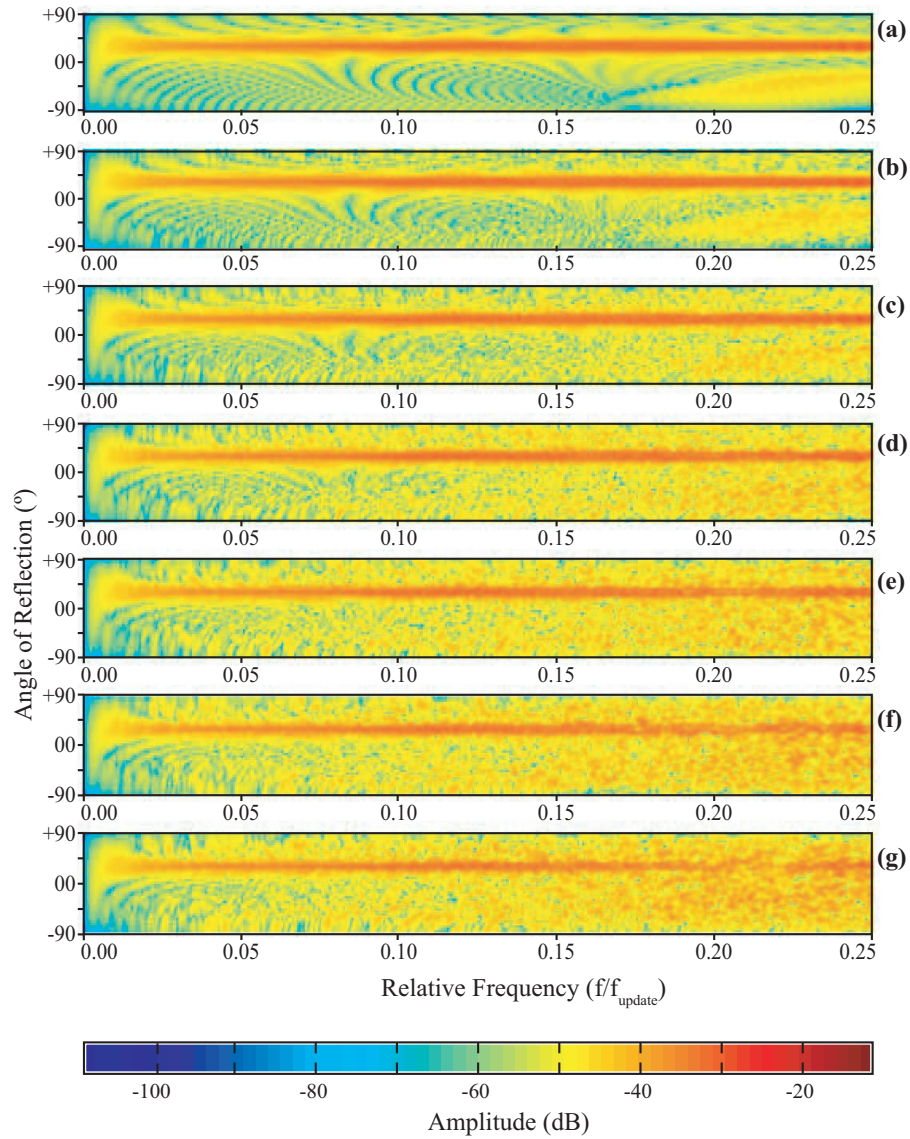


Figure 6.24: Spectrograms showing reflection magnitude for -30° incidence, varying with angle of reflection across the semicircular range of receivers with (a) CM00, (b) CM15, (c) CM30, (d) CM45, (e) CM60, (f) CM75 and (g) CM90.

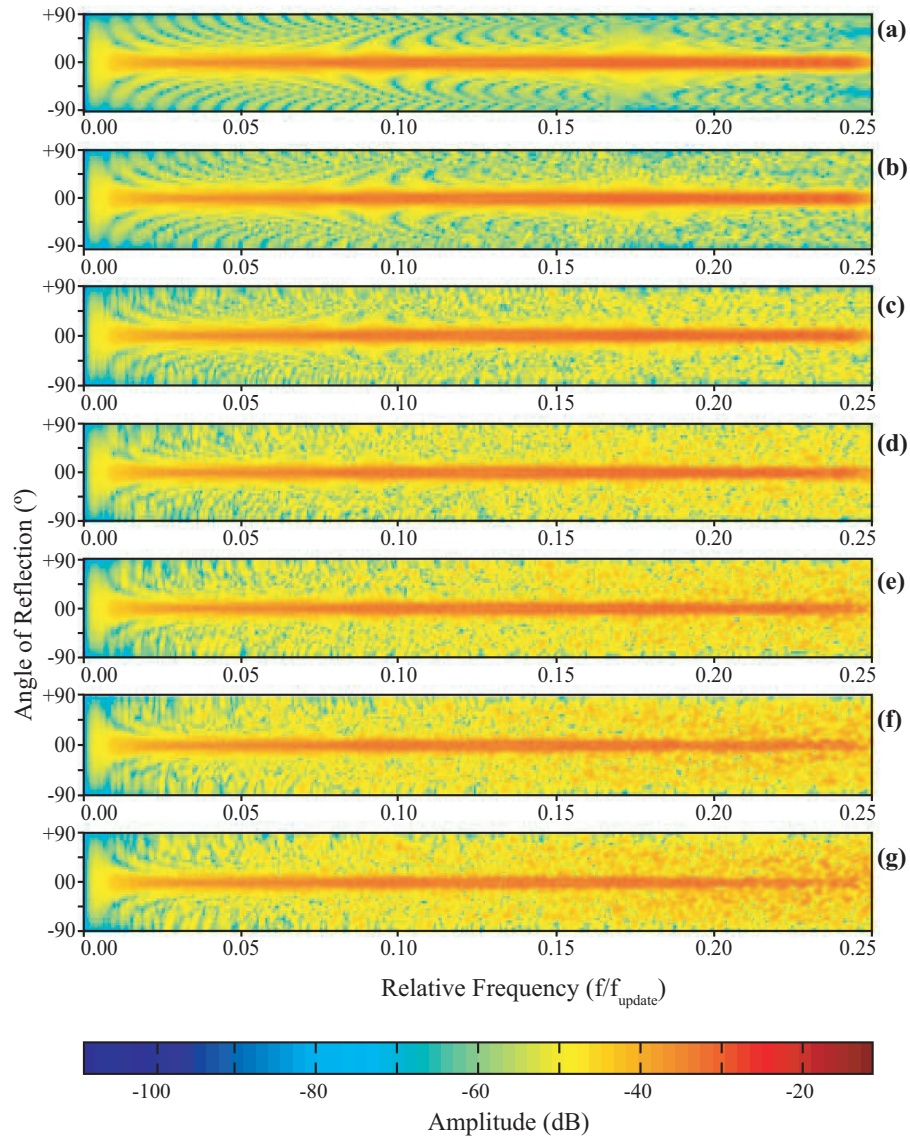


Figure 6.25: Spectrograms showing reflection magnitude for 0° incidence, varying with angle of reflection across the semicircular range of receivers with (a) CM00, (b) CM15, (c) CM30, (d) CM45, (e) CM60, (f) CM75 and (g) CM90.

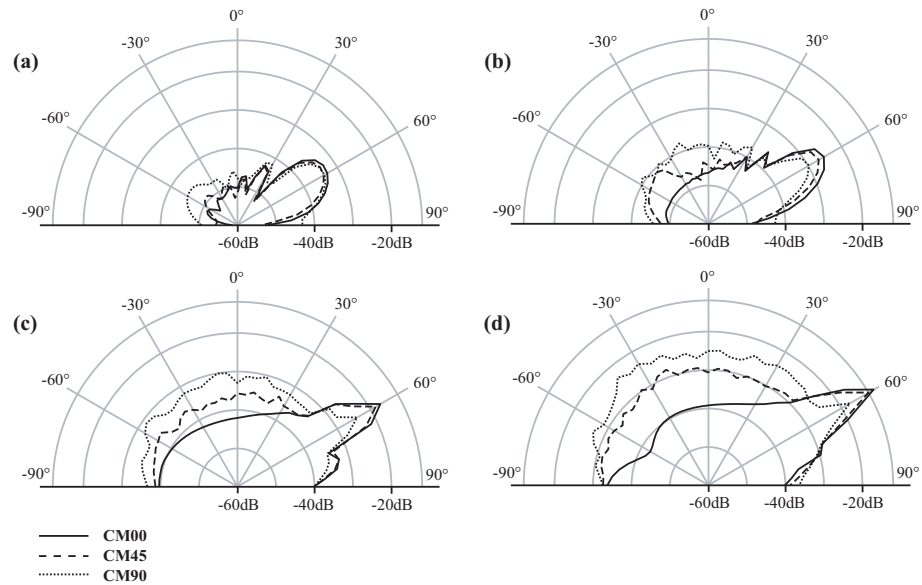


Figure 6.26: Polar responses showing scattering of reflected sound energy from diffuser models **CM00**, **CM45** and **CM90** for incident angle -60° in (a) 1 kHz, (b) 2 kHz, (c) 4 kHz and (d) 8 kHz third octave bands.

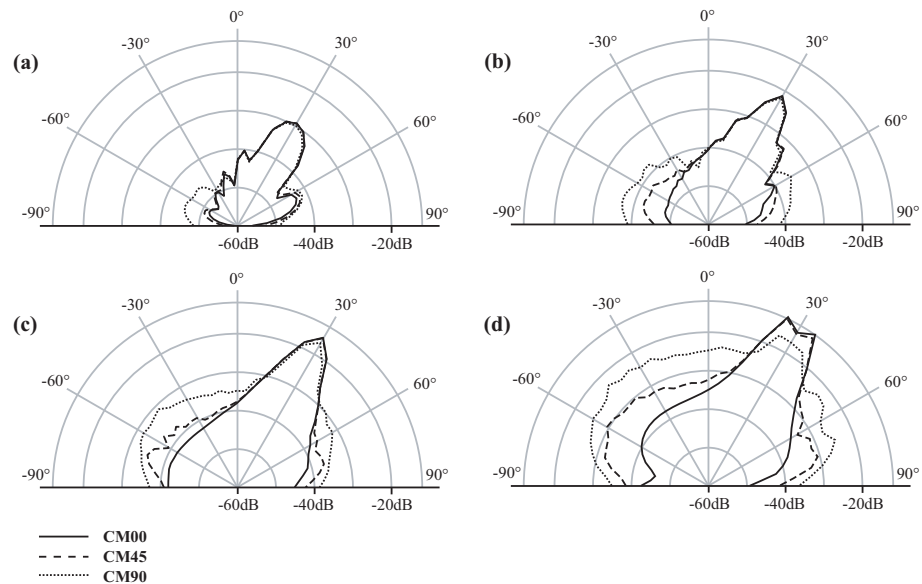


Figure 6.27: Polar responses showing scattering of reflected sound energy from diffuser models **CM00**, **CM45** and **CM90** for incident angle -30° in (a) 1 kHz, (b) 2 kHz, (c) 4 kHz and (d) 8 kHz third octave bands.

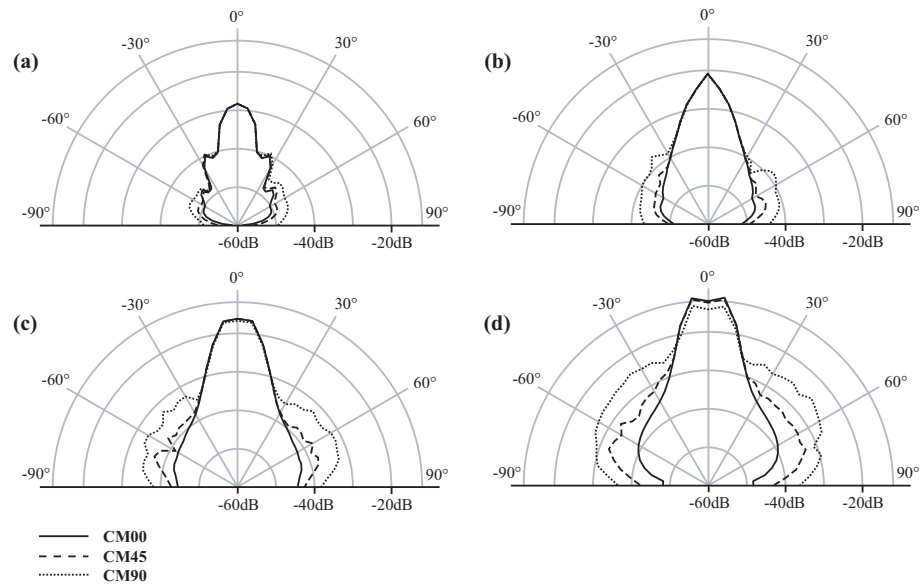


Figure 6.28: Polar responses showing scattering of reflected sound energy from diffuser models **CM00**, **CM45** and **CM90** for incident angle 0° in (a) 1 kHz, (b) 2 kHz, (c) 4 kHz and (d) 8 kHz third octave bands.

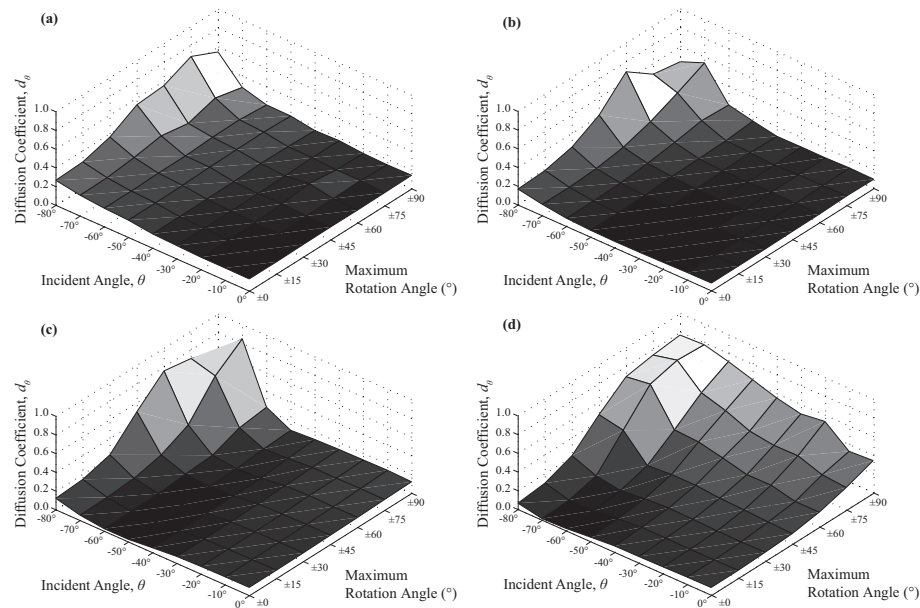


Figure 6.29: Graphs showing directional diffusion coefficients for the modelled boundaries **CM00**-**CM90** in (a) 1 kHz, (b) 2 kHz, (c) 4 kHz and (d) 8 kHz third octave bands.

$\pm 90^\circ$ to values as high as $\pm 120^\circ$ does not cause any significant rise in the measured diffusion coefficient for any frequency band.

For very shallow incident angles (-80° and -70°), the measured diffusion coefficient is high in comparison with measured diffusion coefficients for incident angles between -60° and 0° , particularly for maximum rotation angles $\pm 45^\circ$ and

greater. Inconsistencies at shallow angles may be caused by reflections of sound waves from the edge of the strip of diffusing material as well as diffraction effects, which are seen to have an effect on the diffusion coefficient measurements for the flat plane surface (section 6.4.1), however this does not fully explain the discrepancy in this case, which is far greater. The difference is likely to be caused by the fact that changing the angle of incidence alters the way in which the incident sound waves and the diffusing boundary panel interact, although the exact reason is unclear and will be the subject of further work. One theory is that at the shallow angles, the amount of sound wave energy that interacts with the boundary is less than for other angles, but because the boundary is the same length, this smaller amount of energy interacts with the same amount of diffusing material. The proportion of energy that is scattered to total energy reflected is therefore higher for shallow angles than the proportion of scattered-to-reflected energy that is observed at angles of incidence closer to the normal. In future work it must be determined whether this inconsistency is consistent with the behaviour of real randomly rough diffuse surfaces.

1/3 Octave Band(kHz)	Modelled Boundary Diffusion Coefficients						
	CM00	CM15	CM30	CM45	CM60	CM75	CM90
1.00	0.174	0.177	0.195	0.226	0.232	0.258	0.227
1.25	0.147	0.150	0.173	0.186	0.227	0.224	0.239
1.60	0.125	0.128	0.142	0.170	0.212	0.208	0.213
2.00	0.108	0.111	0.126	0.176	0.216	0.217	0.225
2.50	0.095	0.098	0.113	0.145	0.201	0.202	0.215
3.15	0.084	0.088	0.106	0.153	0.198	0.216	0.212
4.00	0.078	0.082	0.098	0.143	0.197	0.220	0.253
5.00	0.072	0.077	0.093	0.142	0.197	0.255	0.281
6.30	0.069	0.075	0.101	0.154	0.246	0.306	0.344
8.00	0.063	0.074	0.101	0.169	0.284	0.424	0.536
10.00	0.058	0.070	0.108	0.214	0.357	0.474	0.585

Table 6.6: Table showing random incidence diffusion coefficients for the 7 boundary models **CM00-CM90**.

Table 6.6 shows the calculated random incidence diffusion coefficients for seven modelled diffusing boundaries **CM00-CM90**. The diffusion coefficients are given for the third octave bands with central frequencies running from 1 kHz to 10 kHz. These results are also displayed in the form of a 3-D graph, Figure 6.30.

The random incidence diffusion coefficient data shows that although the diffusion model has an effect in all the measured third octave frequency bands, it becomes more effective as the frequency of the incident sound wave increases from the 5 kHz third octave band upwards. Sound waves in the 8 kHz and 10 kHz third

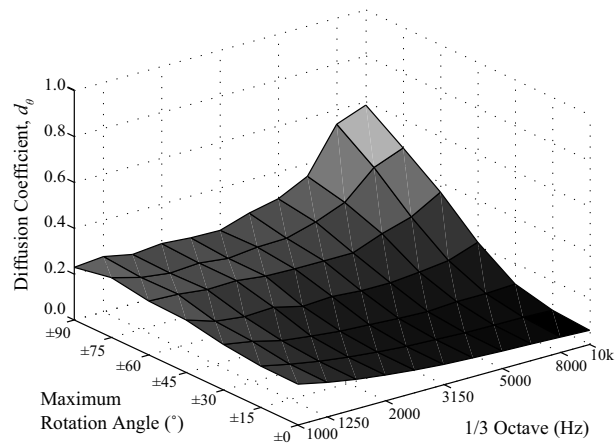


Figure 6.30: Random incidence diffusion coefficients for the 7 boundary models **CM00-CM90**.

octave frequency bands are diffused most effectively by the model. The diffusive effect of the model increases as the maximum rotation angle that can be selected by the uniform probability function is increased. In the 10 kHz third octave band for example, the measured random incidence diffusion coefficient increases from 0.058 for the plane boundary model (**CM00** to 0.585 for the **CM90** model, an increase of 909%. In the 8 kHz third octave band the random incidence diffusion coefficient increases from 0.063 for the **CM00** model to 0.536 for the **CM90** (751%). The increase is relatively smaller at lower frequencies bands however. For example in the 2.5 kHz third octave band, the random incidence diffusion coefficient increases from 0.095 to 0.215, a relative increase of 126%.

6.4.5 The Diffusing Layer Model

Single layer

The diffusing layer model, as described in section 5.3.3, is implemented on one edge of a rectangular block, again exactly the same shape to the rectangular block used to implement the flat plane boundary in section 6.4.1, and all other subsequent tests. The diffusion coefficient measurements are also made with the same test geometry as that used in these other tests. All boundaries of the rectangular panel are totally reflective.

The results from the single diffusing layer model are presented in the same format as for the previous diffusion model. The diffusing layer diffusion model is tested for seven different levels of diffusivity. The materials are modelled using a uniform probability function to select the random angles of rotation, with maximum rotation angles of 0° , $\pm 15^\circ$, $\pm 30^\circ$, $\pm 45^\circ$, $\pm 60^\circ$, $\pm 75^\circ$ and $\pm 90^\circ$. For the single diffusing layer model, these are labelled **DL00**, **DL15**, **DL30**, **DL45**, **DL60**, **DL75** and **DL90** respectively. The prefix, **DL**, this time refers to the *diffusing layer* approach of the model and the number that follows again refers to the maximum rotation angle used in the model. Theoretically, the higher the maximum angle in the random function used to control the diffusion, the greater the diffusivity of the material. **DL00** is effectively a plane boundary model and results are identical to the results measured from the plane boundary model in section 6.4.1. This is confirmed by comparing the random incidence diffusion coefficients measured for the model **DL00** (found in the first column of diffusion coefficients in Table 6.7) with the random incidence diffusion coefficients measured for the plane surface model (found in the final row of Table 6.1), which are identical in each third octave band.

The spectrograms (Figures 6.31 and 6.32) again show that as the maximum angle is increased for the uniform random distribution function used in the model, the energy observed at the angle of specular reflection (30° in Figure 6.31 and 0° in Figure 6.32) reduces, and the total energy observed at other angles increases. This effect is more evident for the diffusing layer model however than for the diffusing boundary model presented in the previous section, particularly for greater maximum rotation angles.

As with the diffusing boundary model, the directional diffusion coefficients,

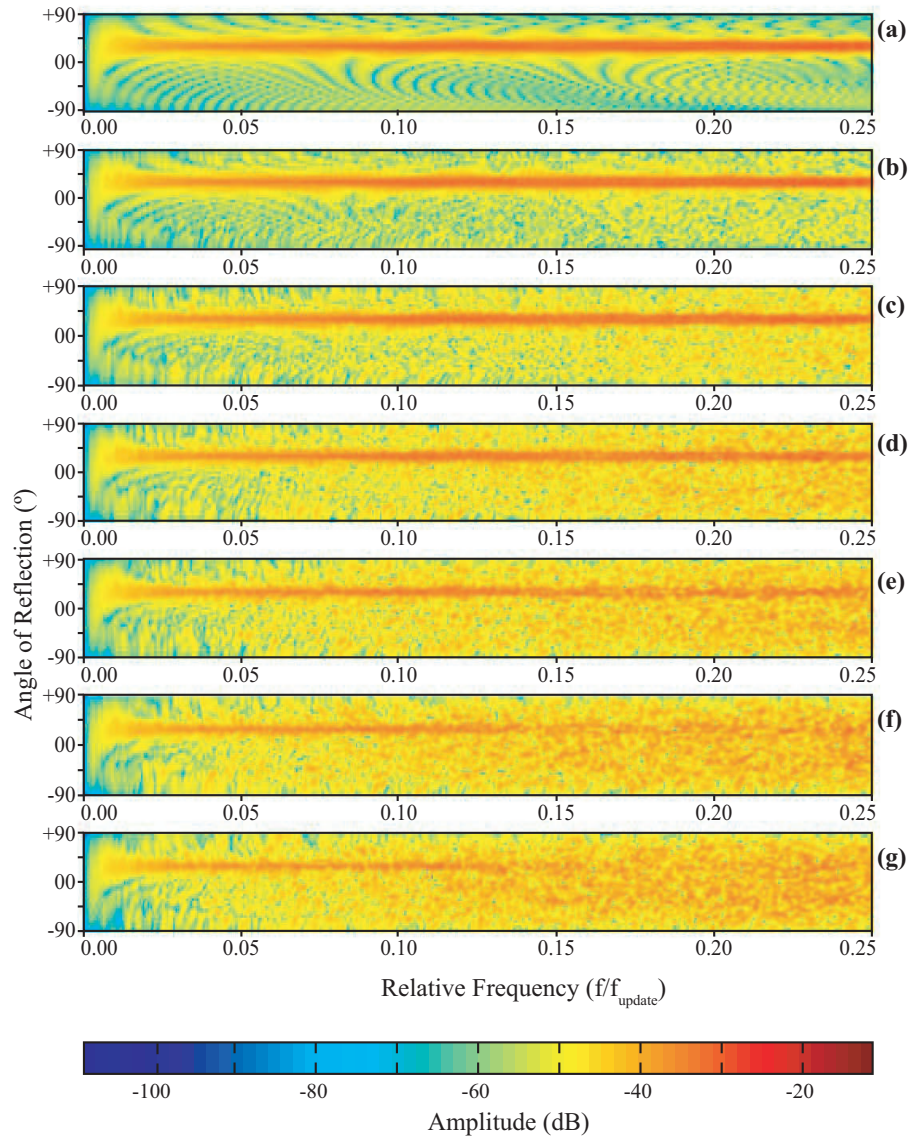


Figure 6.31: Spectrograms showing reflection magnitude for -30° incidence, varying with angle of reflection across the semicircular range of receivers with (a) DL00, (b) DL15, (c) DL30, (d) DL45, (e) DL60, (f) DL75 and (g) DL90.

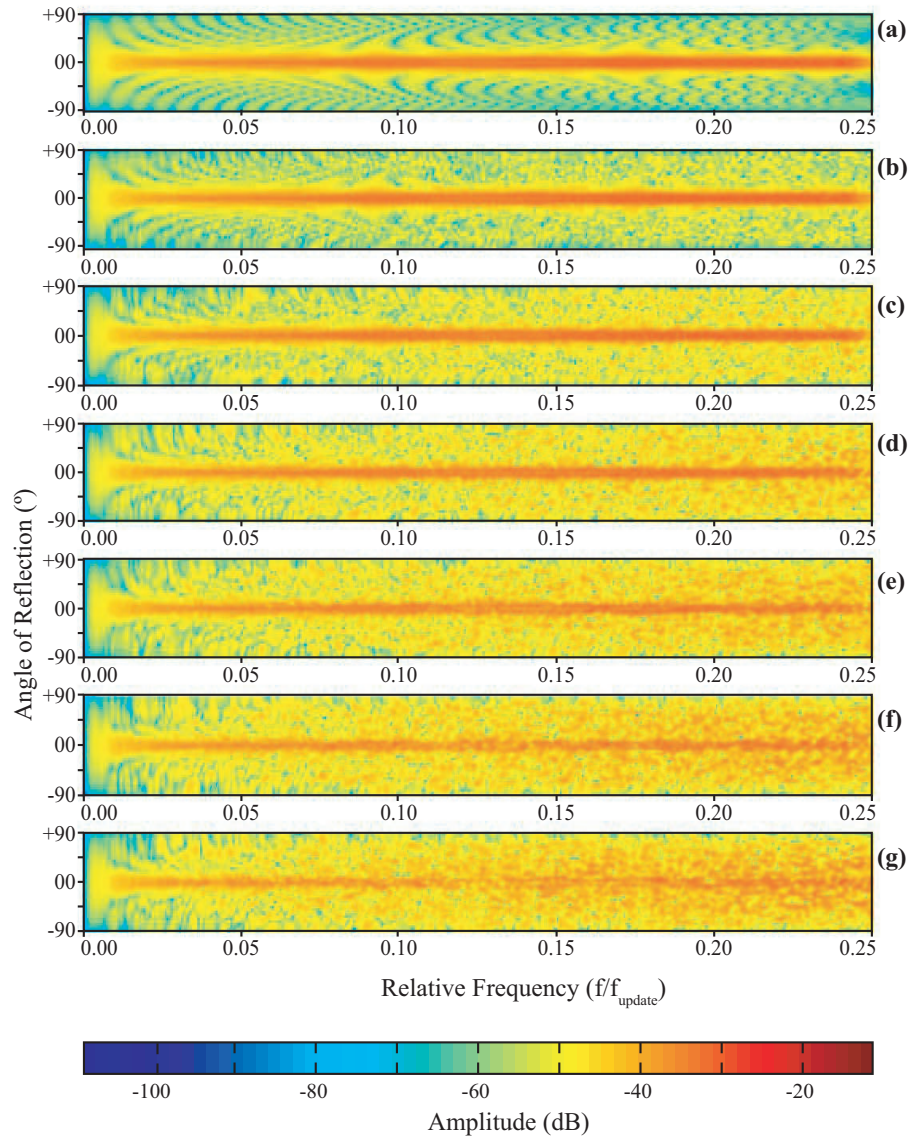


Figure 6.32: Spectrograms showing reflection magnitude for 0° incidence, varying with angle of reflection across the semicircular range of receivers with (a) DL00, (b) DL15, (c) DL30, (d) DL45, (e) DL60, (f) DL75 and (g) DL90.

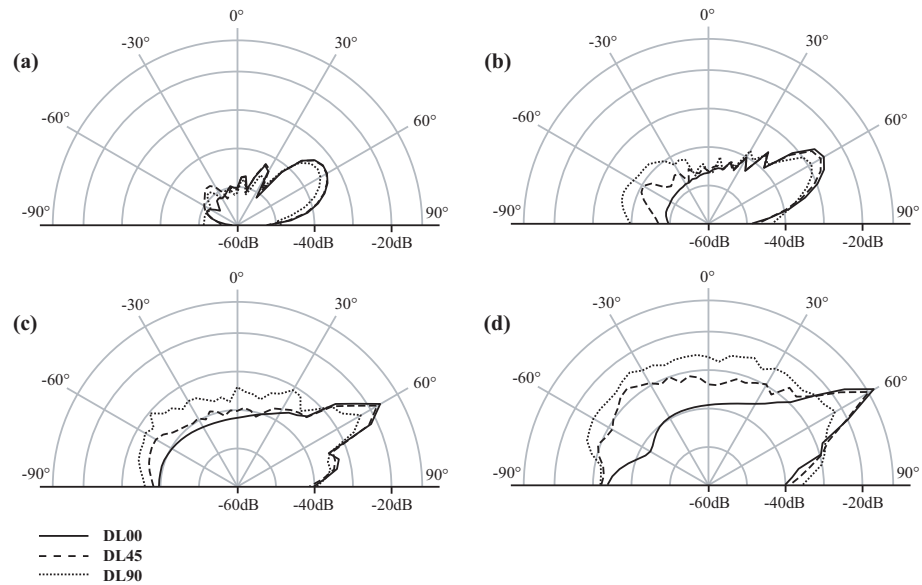


Figure 6.33: Polar responses showing scattering of reflected sound energy from diffuser models DL00, DL45 and DL90 for incident angle -60° in (a) 1 kHz, (b) 2 kHz, (c) 4 kHz and (d) 8 kHz third octave bands.

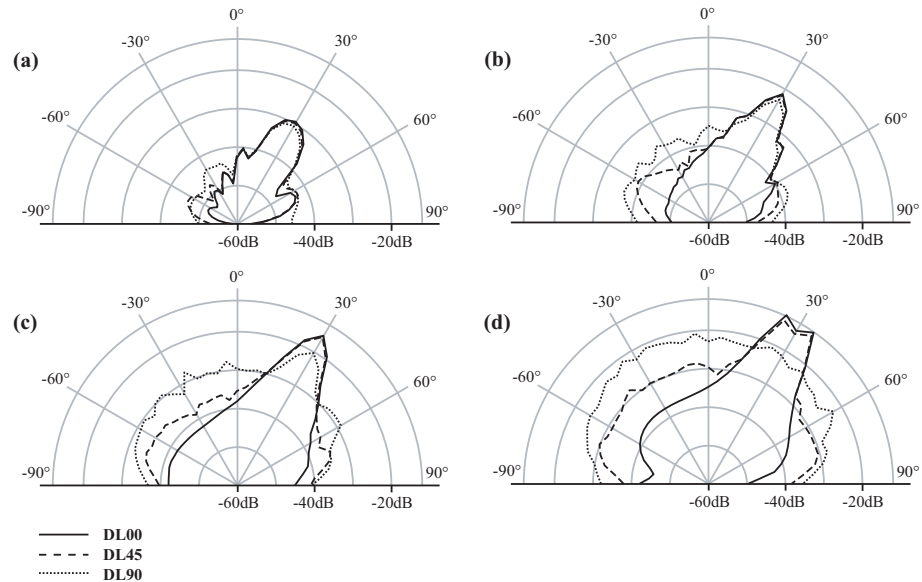


Figure 6.34: Polar responses showing scattering of reflected sound energy from diffuser models DL00, DL45 and DL90 for incident angle -30° in (a) 1 kHz, (b) 2 kHz, (c) 4 kHz and (d) 8 kHz third octave bands.

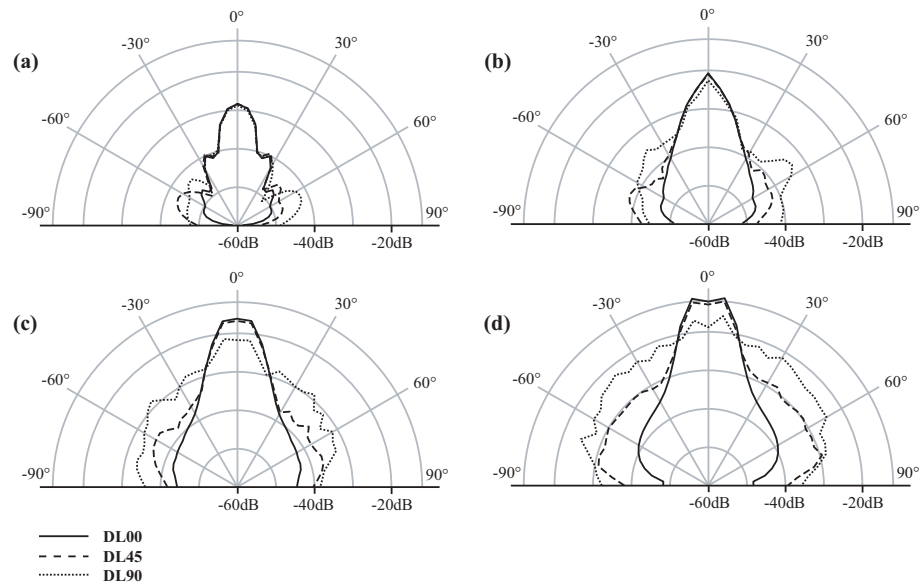


Figure 6.35: Polar responses showing scattering of reflected sound energy from diffuser models **DL00**, **DL45** and **DL90** for incident angle 0° in (a) 1 kHz, (b) 2 kHz, (c) 4 kHz and (d) 8 kHz third octave bands.

displayed in Figure 6.36, show a rise in diffusion coefficient across all angles of incidence as the maximum rotation angle used in the diffusion model increases, although for angles of incidence of -60° and above this rise in diffusion coefficient is very slight in the lower three third octave bands. At 1 kHz, the diffusion coefficients rise from 0.174 on average across the range of incident angles for the diffusion model **DL00**, to just 0.244 on average for **DL90**. At 8 kHz however, this average of diffusion coefficients rises from 0.063 for the diffusion model **DL00** to 0.615 for **DL90**. Further tests again show that increasing the maximum rotation angle further than $\pm 90^\circ$ to values as high as $\pm 120^\circ$ does not cause any significant rise in the measured diffusion coefficient for any frequency band.

Similarly to the diffusing boundary case discussed in the previous section, the measured diffusion coefficients for shallow incident angles (-80° and -70°), are high in comparison with measured diffusion coefficients for incident angles between -60° and 0° , particularly for maximum rotation angles $\pm 45^\circ$ and greater. This inconsistency is discussed in the previous section.

The random incidence diffusion coefficient data, Table 6.7 and Figure 6.37, again shows that the diffusion model becomes more effective as the frequency of the incident sound wave increases. The sound waves in the 8 kHz and 10 kHz third octave frequency bands are diffused most effectively by the model. The diffusive

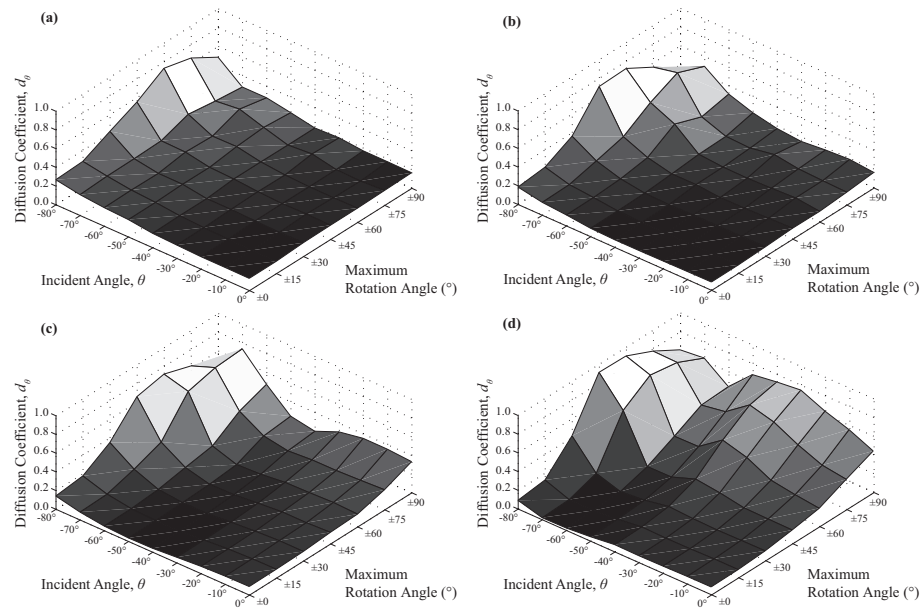


Figure 6.36: Graphs showing directional diffusion coefficients for the modelled boundaries DL00-DL90 in (a) 1 kHz, (b) 2 kHz, (c) 4 kHz and (d) 8 kHz third octave bands.

1/3 Octave Band(kHz)	Modelled Boundary Diffusion Coefficients						
	DL00	DL15	DL30	DL45	DL60	DL75	DL90
1.00	0.174	0.180	0.203	0.232	0.267	0.274	0.244
1.25	0.147	0.153	0.181	0.223	0.264	0.289	0.240
1.60	0.125	0.132	0.161	0.223	0.258	0.271	0.258
2.00	0.108	0.115	0.150	0.216	0.275	0.276	0.263
2.50	0.095	0.101	0.129	0.208	0.263	0.274	0.314
3.15	0.084	0.091	0.129	0.207	0.265	0.315	0.325
4.00	0.078	0.086	0.125	0.192	0.267	0.333	0.393
5.00	0.072	0.080	0.124	0.209	0.305	0.387	0.444
6.30	0.069	0.077	0.124	0.226	0.351	0.504	0.573
8.00	0.063	0.072	0.134	0.305	0.436	0.546	0.615
10.00	0.058	0.071	0.189	0.418	0.581	0.618	0.614

Table 6.7: Table showing random incidence diffusion coefficients for the 7 boundary models DL00-DL90.

effect of the model increases as the maximum rotation angle that can be selected by the uniform probability function is increased. It is also apparent that the effective cut-off frequency of the diffusion model reduces as the maximum rotation angle increases.

The random incidence diffusion coefficient data also shows that the diffusion model becomes more effective as the frequency of the incident sound wave increases. This is particularly true from the 3.15 kHz third octave band upwards. Sound waves in the 6.3 kHz, 8 kHz and 10 kHz third octave frequency bands are diffused most effectively by the model. The diffusive effect of model increases as the maximum rotation angle that can be selected by the uniform probability function is increased.

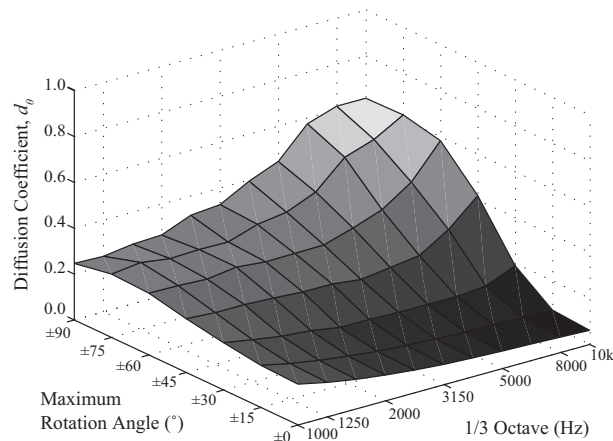


Figure 6.37: Random incidence diffusion coefficients for the 7 boundary models DL00-DL90.

In the 10 kHz third octave band for example, the measured random incidence diffusion coefficient increases from 0.058 for the plane boundary model (**DL00**) to 0.614 for the **DL90** model, a relative increase of 959%. In the 8 kHz third octave band the random incidence diffusion coefficient increases from 0.063 for the **DL00** model to 0.615 for the **DL90** model (an increase of 876%). In the 2.5 kHz third octave band, where the diffusion model is not so effective according to these results, the random incidence diffusion coefficient increases from 0.095 to 0.314, a relative increase of 231%.

In general, the diffusion model is more effective across all frequencies when compared to the diffusing boundary model (**CM00-CM90**) described in the previous sections. This is particularly true at frequencies found in the measured third octave bands with centre frequencies less than the 8 kHz. The models are compared further in section 6.5.

Considering the data in the 8 kHz third octave band only, a peak of 0.615 is observed when the maximum angle of the diffusion model is set to $\pm 90^\circ$. In the 10 kHz third octave band, where the diffusion model is more effective according to these results, a diffusion coefficient of 0.618 is obtained when the maximum rotation angle of the diffusion model is set to $\pm 75^\circ$. As the maximum rotation angle is increased, the measured random incidence diffusion coefficient in the 10 kHz third octave band decreases by a very small amount to 0.614 for maximum rotation angle $\pm 90^\circ$. This behaviour indicates an upper threshold in the model at about 0.618, beyond which the random incidence diffusion coefficients do not increase.

Multiple Diffusing layers

1/3 Octave Band(kHz)	Modelled Boundary Diffusion Coefficients						
	DDL00	DDL15	DDL30	DDL45	DDL60	DDL75	DDL90
1.00	0.174	0.202	0.241	0.309	0.293	0.298	0.319
1.25	0.147	0.164	0.235	0.293	0.307	0.349	0.310
1.60	0.125	0.142	0.224	0.258	0.334	0.319	0.382
2.00	0.108	0.127	0.206	0.281	0.343	0.401	0.440
2.50	0.095	0.112	0.219	0.302	0.382	0.477	0.497
3.15	0.084	0.106	0.191	0.284	0.413	0.507	0.574
4.00	0.078	0.100	0.196	0.312	0.439	0.599	0.636
5.00	0.072	0.090	0.194	0.329	0.485	0.615	0.672
6.30	0.069	0.087	0.210	0.366	0.579	0.631	0.679
8.00	0.063	0.084	0.239	0.459	0.614	0.685	0.649
10.00	0.058	0.095	0.336	0.654	0.731	0.701	0.654

Table 6.8: Table showing random incidence diffusion coefficients for the 7 boundary models DDL00-DDL90.

1/3 Octave Band(kHz)	Modelled Boundary Diffusion Coefficients						
	TDL00	TDL15	TDL30	TDL45	TDL60	TDL75	TDL90
1.00	0.174	0.188	0.317	0.343	0.353	0.435	0.439
1.25	0.147	0.177	0.269	0.332	0.374	0.400	0.466
1.60	0.125	0.148	0.284	0.344	0.438	0.495	0.560
2.00	0.108	0.138	0.252	0.373	0.479	0.529	0.615
2.50	0.095	0.130	0.266	0.396	0.508	0.630	0.636
3.15	0.084	0.118	0.259	0.403	0.540	0.667	0.671
4.00	0.078	0.110	0.244	0.387	0.608	0.682	0.701
5.00	0.072	0.103	0.235	0.426	0.629	0.670	0.696
6.30	0.069	0.097	0.237	0.474	0.652	0.689	0.676
8.00	0.063	0.104	0.283	0.588	0.703	0.711	0.679
10.00	0.058	0.128	0.458	0.731	0.733	0.700	0.662

Table 6.9: Table showing random incidence diffusion coefficients for the 7 boundary models TDL00-TDL90.

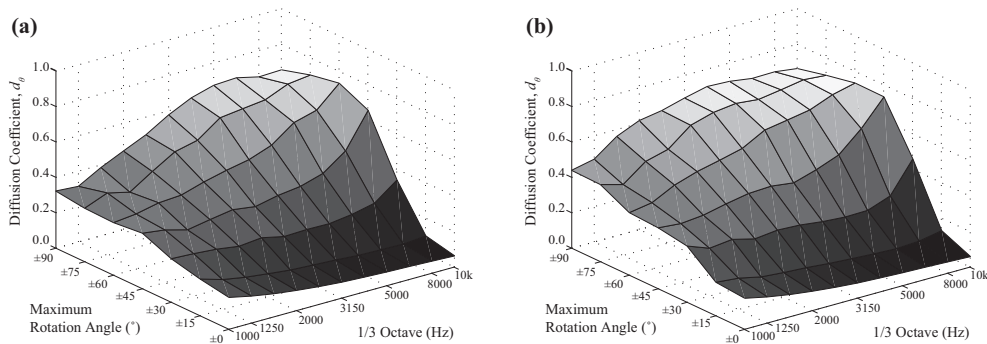


Figure 6.38: Random incidence diffusion coefficients for the boundary models (a) DDL00-DDL90 and (b) TDDL00-TDDL90.

Tables 6.8 and 6.9 show frequency dependent random incidence diffusion coefficient data for adapted versions of the diffusing layer model. The test conditions in these cases are identical to those applied to the diffusing boundary and diffusing layer models in the previous sections, however two and three layers, respectively, of diffusing junctions adjacent to the receiver-facing boundary of the

rectangular block are implemented rather than just one. The different diffusing materials modelled with two diffusing layers are labelled **DDL00-DDL90** where the prefix **DDL** refers to the *double* diffusing layer used in the model and the number following refers to the maximum angle of rotation that can be selected by the uniform probability function. Similarly the diffusing materials modelled with three diffusing layers are labelled **TDL00-TDL90**, where the prefix **TDL** refers to the *triple* diffusing layer used in the model. The results are also presented in the form of 3-D graphs in Figures 6.38(a) and 6.38(c) for the two layer and the three layer model respectively.

It is observed that such an adaptation to the original diffusing layer model has a significant effect on the frequency dependency of the diffusion model. The effective cut-off frequency of the diffusion model is reduced as the number of layers is increased. For the cases where the maximum angle of rotation is $\pm 90^\circ$, for instance, the cut-off frequency of the diffusion model is reduced from about 4 kHz for the single diffusing layer model (**DL90**), to 3.15 kHz for the double layer model (**DDL90**) and finally to 2 kHz for the triple layer model (**TDL90**). Again an upper limit is observed in the measured random incidence diffusion coefficient data for both adapted versions of the model, but with the threshold slightly greater than the single layer case, at 0.731 for the double layer model and 0.733 for the triple layer model, compared with the apparent upper threshold of 0.618 for the single layer model.

Effect of Sample Rate on Diffusing Layer Model Behaviour

The diffusing boundary and diffusing layer models consist of signal manipulations that are performed at mesh sampling points both in space (at mesh junctions) and in time. This implies that the behaviour of each model is dependent on the mesh update frequency f_{update} . In order to examine this dependency, diffusion coefficients are measured for the diffusing layer model with mesh update frequencies 22.05 kHz (half the sampling rate used in previous models) and 33.075 kHz. For each test, the geometry is the same as that used in previous sections, such that the measurements of the diffuser (1.1 m in length) and all other relative distances are the same. The diffusing layer model is applied in exactly the same way for each test, and for each model a range of materials are examined with maximum rotation angles 0° , $\pm 15^\circ$, $\pm 30^\circ$, $\pm 45^\circ$, $\pm 60^\circ$, $\pm 75^\circ$ and $\pm 90^\circ$. For the mesh with sampling frequency 22.05 kHz, the materials are labelled **HRDL00-HRDL90** for convenience. The prefix **HRDL** stands for *half resolution diffusing layer*, because the update frequency of the mesh in this test is half of that used in previous tests. For the mesh with update frequency 33.075 kHz, the materials are labelled **TRDL00-TRDL90**, where the prefix **TRDL** stands for *three-quarter resolution diffusing layer*, in reference to the update frequency of the mesh this time being three-quarters of the update frequency used in previous tests (44.1 kHz).

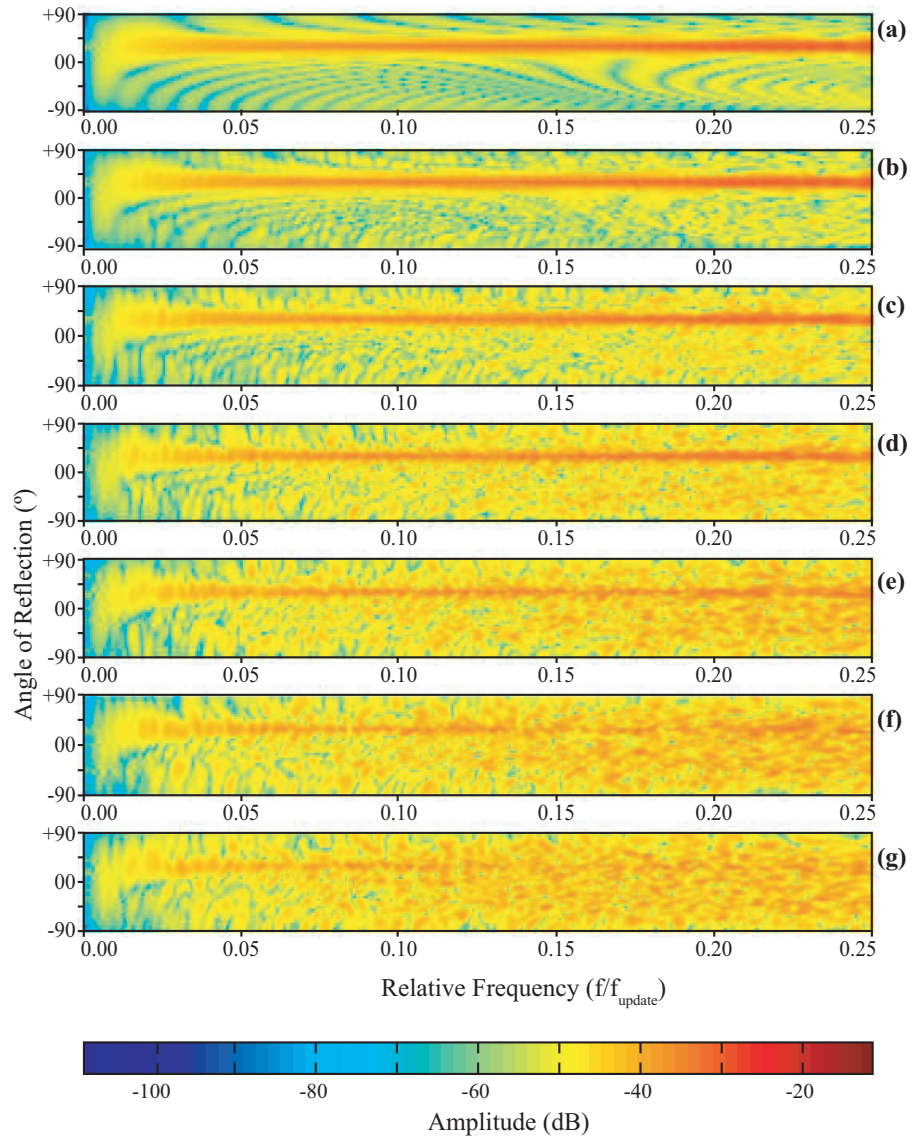


Figure 6.39: Spectrograms showing reflection magnitude for -30° incidence, varying with angle of reflection across the semicircular range of receivers with (a) HRDL00, (b) HRDL15, (c) HRDL30, (d) HRDL45, (e) HRDL60, (f) HRDL75 and (g) HRDL90 for sample rate 22050Hz.

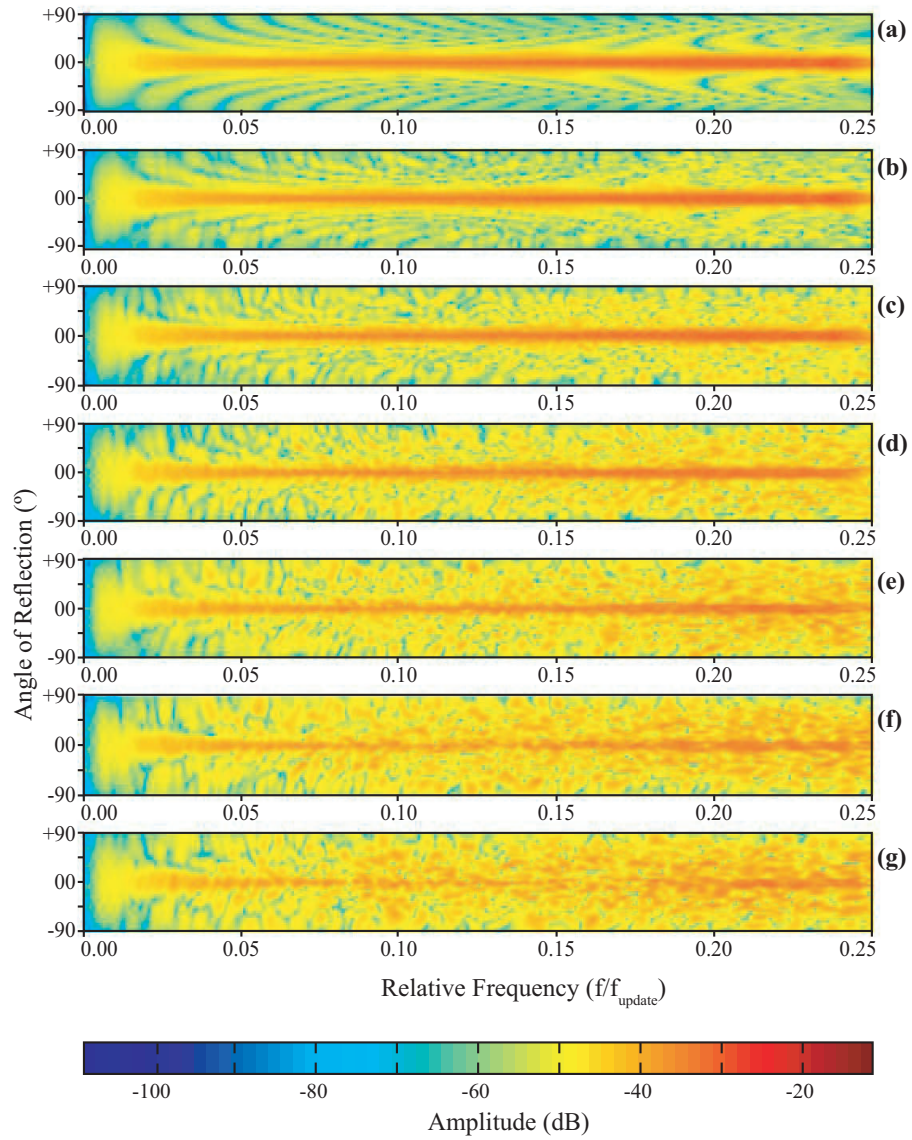


Figure 6.40: Spectrograms showing reflection magnitude for 0° incidence, varying with angle of reflection across the semicircular range of receivers with (a) HRDL00, (b) HRDL15, (c) HRDL30, (d) HRDL45, (e) HRDL60, (f) HRDL75 and (g) HRDL90 for sample rate 22050Hz.

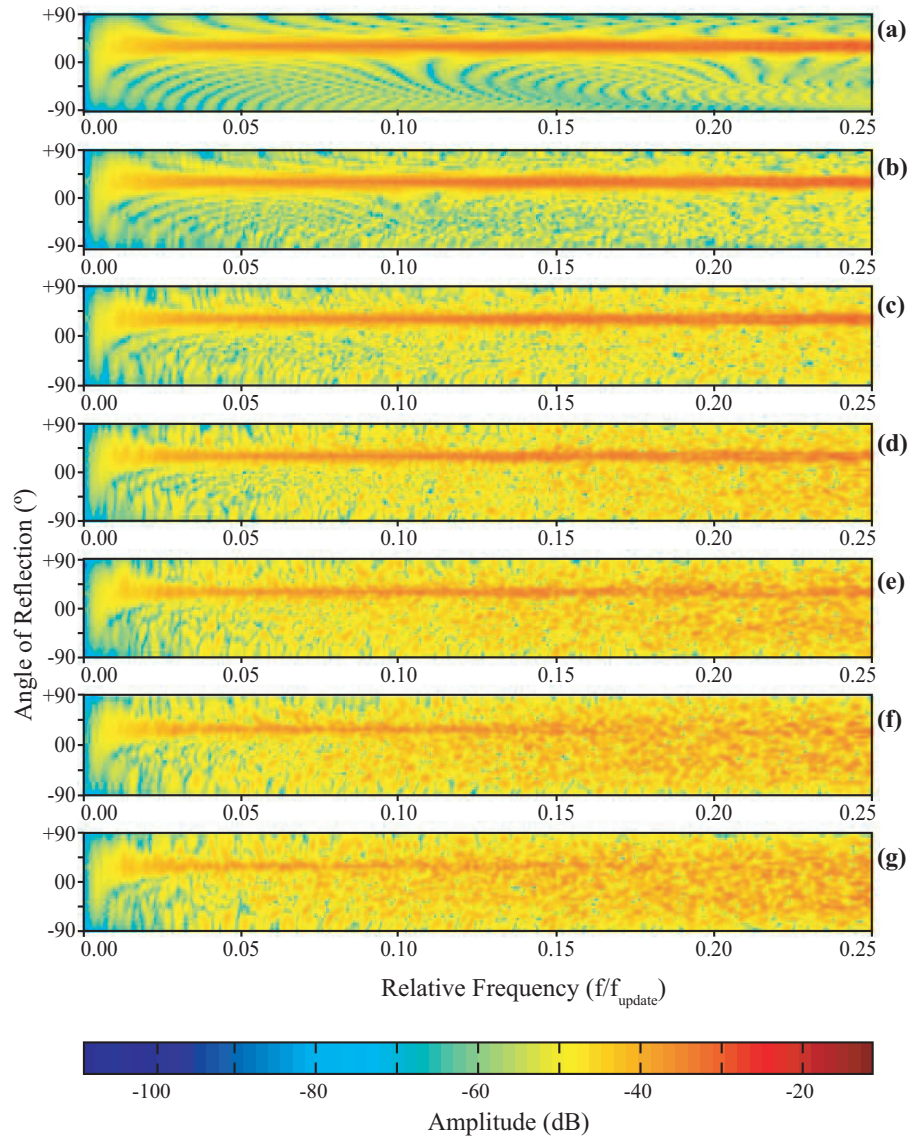


Figure 6.41: Spectrograms showing reflection magnitude for -30° incidence, varying with angle of reflection across the semicircular range of receivers with (a) TRDL00, (b) TRDL15, (c) TRDL30, (d) TRDL45, (e) TRDL60, (f) TRDL75 and (g) TRDL90 for sample rate 33075Hz.

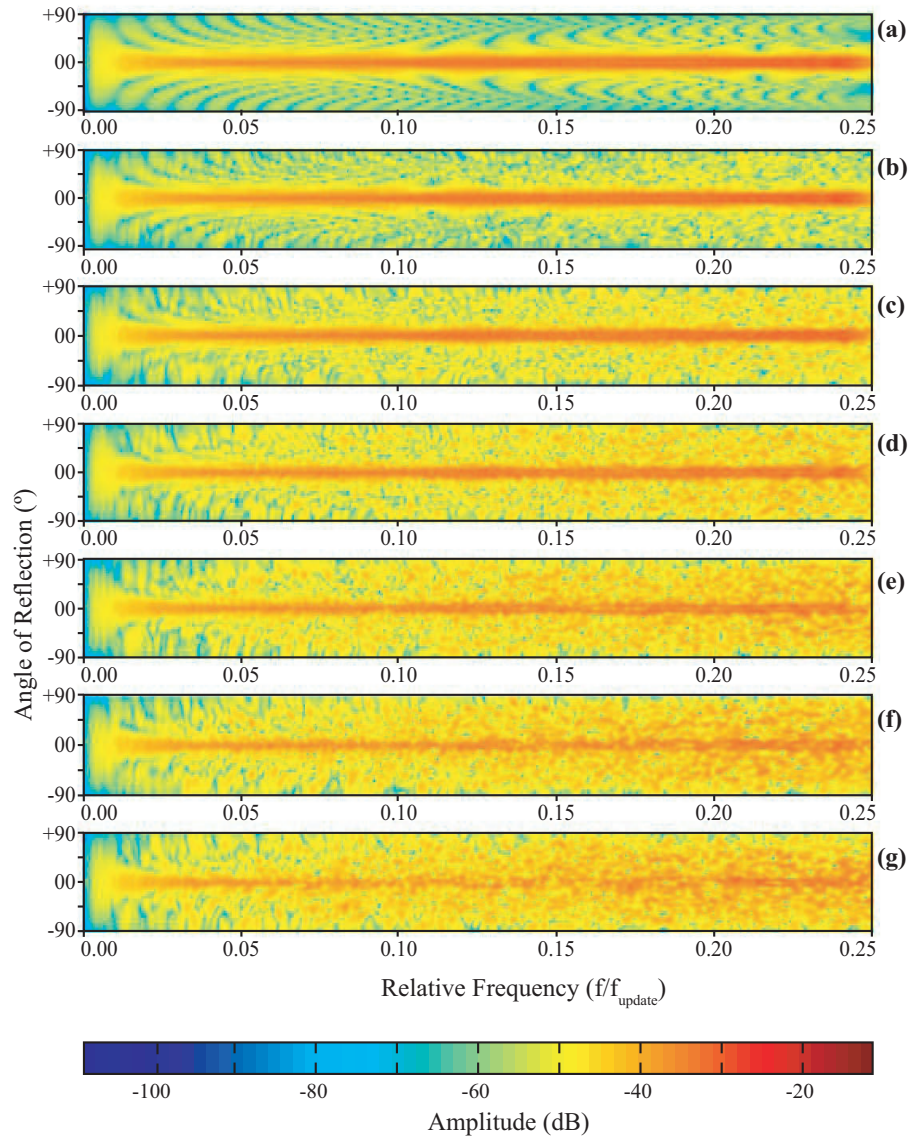


Figure 6.42: Spectrograms showing reflection magnitude for 0° incidence, varying with angle of reflection across the semicircular range of receivers with (a) TRDL00, (b) TRDL15, (c) TRDL30, (d) TRDL45, (e) TRDL60, (f) TRDL75 and (g) TRDL90 for sample rate 33075Hz.

1/3 Octave Band(kHz)	Modelled Boundary Diffusion Coefficients						
	HRDL00	HRDL15	HRDL30	HRDL45	HRDL60	HRDL75	HRDL90
1	0.197	0.204	0.234	0.327	0.414	0.433	0.492
1.25	0.174	0.184	0.224	0.327	0.395	0.448	0.475
1.6	0.153	0.165	0.225	0.297	0.385	0.423	0.500
2	0.130	0.144	0.200	0.281	0.381	0.490	0.580
2.5	0.106	0.117	0.170	0.291	0.400	0.493	0.618
3.15	0.088	0.099	0.167	0.279	0.393	0.554	0.681
4	0.081	0.090	0.151	0.289	0.436	0.608	0.671
5	0.077	0.089	0.162	0.329	0.537	0.602	0.597

Table 6.10: Table showing random incidence diffusion coefficients for the 7 boundary models **HRDL00-HRDL90**.

1/3 Octave Band(kHz)	Modelled Boundary Diffusion Coefficients						
	TRDL00	TRDL15	TRDL30	TRDL45	TRDL60	TRDL75	TRDL90
1	0.176	0.189	0.224	0.245	0.290	0.323	0.322
1.25	0.151	0.161	0.205	0.287	0.298	0.319	0.352
1.6	0.131	0.138	0.178	0.242	0.313	0.331	0.365
2	0.115	0.122	0.170	0.247	0.312	0.340	0.390
2.5	0.101	0.111	0.149	0.240	0.310	0.377	0.430
3.15	0.087	0.097	0.145	0.227	0.333	0.409	0.498
4	0.078	0.087	0.134	0.231	0.366	0.435	0.560
5	0.073	0.083	0.144	0.266	0.400	0.554	0.640
6.3	0.070	0.080	0.153	0.304	0.472	0.611	0.669
8	0.063	0.078	0.197	0.443	0.598	0.644	0.626

Table 6.11: Table showing random incidence diffusion coefficients for the 7 boundary models **TRDL00-TRDL90**.

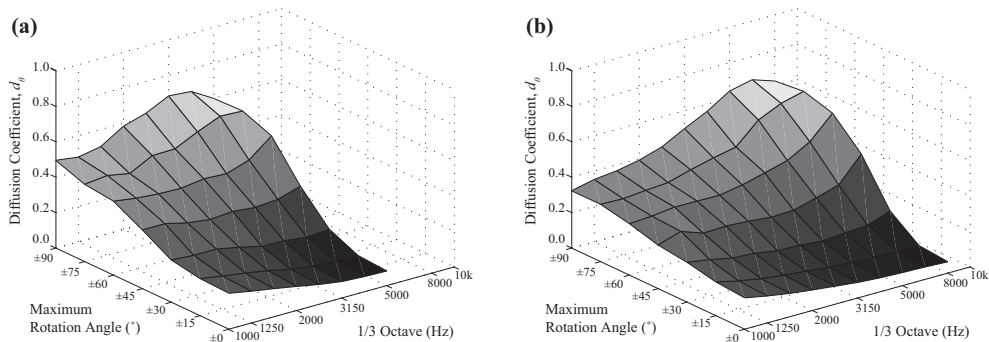


Figure 6.43: Random incidence diffusion coefficients for the boundary models (a) **HRL00-HRL90** and (b) **TRDL00-TRDL90**.

The spectrograms, Figures 6.39-6.42, with frequency represented in relative terms to the sample rate (f/f_{update}), show that the scattering of the models demonstrate very similar frequency dependent behaviour when considered in relation to the update frequency of the mesh. In other words, the frequency dependency of the model is scaled linearly in proportion to the update frequency of the mesh. This observation is supported by the random incidence diffusion coefficient data (Tables 6.10 and 6.11 and Figures 6.43(a) and 6.43(b)). For the case where the maximum rotation angle of the model is $\pm 90^\circ$, the **HRDL** model

has a lower cut-off point for maximum diffusion, the point at which the diffusion coefficients start to slope down at lower frequencies, in the 3.15 kHz third octave band. For model **TRDL** on the other hand, this lower cut-off frequency is in the 5 kHz third octave band. Finally for the original diffusing layer model, model **DL**, the lower cut-off frequency is found in the 8 kHz third octave band (Figure 6.37).

The measured diffusion coefficients in the lower third octave bands (1 kHz to 2.5 kHz) rise significantly as the update frequency of the mesh is decreased, even though the maximum rotation angle used in the models remains constant. For example, in the 1 kHz third octave band, with a maximum rotation angle of $\pm 90^\circ$, a diffusion coefficient of 0.492 is measured for the **HRDL90** model. This is an increase of 102% in comparison to the diffusion coefficient of 0.244, measured in the same third octave band for the **DL90** model which is implemented in a mesh with twice the update frequency. For the **TRDL90** model, a diffusion coefficient of 0.322 is measured in the 10 kHz third octave band, an increase of 32% in comparison with the diffusion coefficient measured for the **DL90** model.

The significant increase in diffusion coefficients observed in these models, which results from decreasing the update frequency rate of the mesh, indicates a strong dependency of the diffusing layer model on the mesh update frequency. This is a consequence of the approach used in the model, where incident waves are rotated at a different angle which is selected both for every individual time-step and also for each individual spatial sampling instance at a selection of junctions found close to the boundary. The behaviour does however indicate a consistent relationship between diffusion coefficient data and mesh update frequency which must be considered in the future development of the diffusing layer model.

The Diffusing Layer Model in the 2-D Rectilinear DWM

The diffusion coefficient test is repeated with the same test geometry as described in previous tests and by Figure 6.3, however a DWM with rectilinear topology is now used instead of a DWM with triangular topology. The diffusing layer model is implemented by applying rotations to a layer of junctions adjacent to the diffusing boundary. The update frequency f_{update} used in this implementation is 44.1 kHz. A range of materials are tested and the same maximum rotations are applied across the range of 0° , $\pm 15^\circ$, $\pm 30^\circ$, $\pm 45^\circ$, $\pm 60^\circ$, $\pm 75^\circ$ and $\pm 90^\circ$. For reference, the materials modelled in the 2-D rectilinear DWM are labelled **RDL00**, **RDL15**, **RDL30**, **RDL45**, **RDL60**, **RDL75** and **RDL90** respectively.

1/3 Octave Band(kHz)	Modelled Boundary Diffusion Coefficients						
	RDL00	RDL15	RDL30	RDL45	RDL60	RDL75	RDL90
1	0.177	0.184	0.200	0.231	0.246	0.248	0.234
1.25	0.148	0.152	0.184	0.227	0.243	0.232	0.248
1.6	0.125	0.131	0.158	0.222	0.262	0.224	0.252
2	0.106	0.110	0.133	0.188	0.234	0.222	0.230
2.5	0.088	0.093	0.117	0.159	0.263	0.254	0.257
3.15	0.074	0.079	0.098	0.148	0.249	0.259	0.293
4	0.070	0.074	0.090	0.143	0.244	0.299	0.378
5	0.071	0.076	0.094	0.139	0.251	0.352	0.464
6.3	0.073	0.078	0.099	0.153	0.259	0.417	0.519
8	0.071	0.076	0.096	0.143	0.235	0.367	0.501

Table 6.12: Table showing random incidence diffusion coefficients for the 7 boundary models RDL00-RDL90.

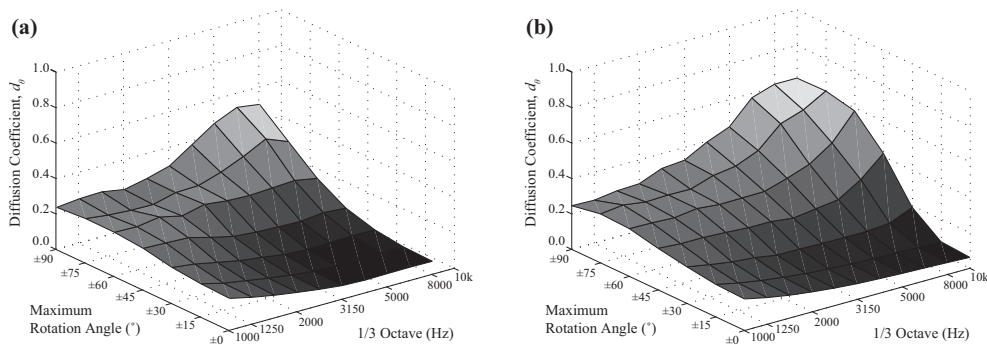


Figure 6.44: Random incidence diffusion coefficients for the boundary models (a) RDL00-RDL90 and (b) DL00-DL90 for comparison.

The results in these tests are only valid up to the 8 kHz third octave band, owing to limitations of the rectilinear mesh topology at higher frequencies [130, 107].

For further comparison between the behaviour of the diffusing layer model in the triangular topology and in the rectilinear topology, Figure 6.45 shows the averages of the absolute value of the difference between the measured diffusion

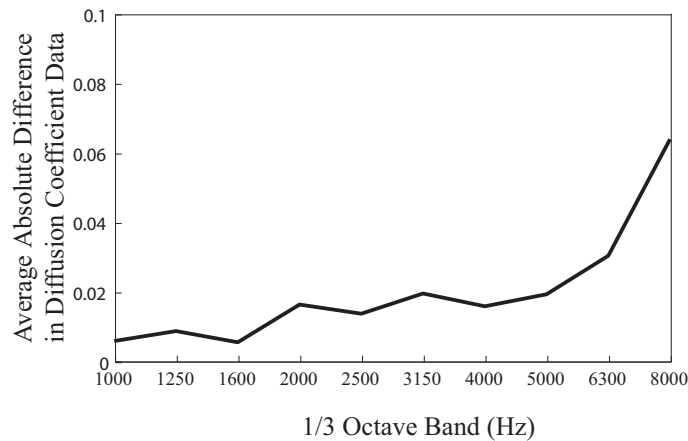


Figure 6.45: Graph Showing the average of the absolute values of the differences between the measured diffusion coefficients in boundary models **RDL00-RDL90** and **DL00-DL90** for each third octave band.

coefficients for each third octave band. The results show a relatively close match for measured diffusion coefficients in the DWM compared to those measured in the triangular topology from the lowest third octave band (1 kHz) to the 5 kHz third octave band, with the average absolute difference in diffusion coefficients not exceeding a value of 0.0197. For example, the diffusion coefficient in the 1.25 kHz third octave band rises from 0.148 for the **RDL00** model to 0.248 for the **RDL90** model, an increase of 68%, in comparison to the rise of 63% measured for the diffusing layer models in the triangular mesh, **DL00** and **DL90**, in the same third octave band. At the 5 kHz third octave band a rise in diffusion coefficient from 0.071 for the **RDL00** model to 0.464 for the **RDL90** model is observed, a relative increase of 554%, which is slightly greater than the increase of 517% measured in the triangular mesh from model **DL00** to model **DL90** in the same third octave band. For higher third octave bands, the rise in diffusion coefficients from the **RDL00** model to the **RDL90** becomes smaller in comparison to the rise in diffusion coefficients measured from the triangular mesh models **DL00** to **DL90** in the corresponding third octave bands, and the average absolute value of the difference in diffusion coefficient data increases. For example in the 8 kHz third octave band, the rectilinear mesh models show an increase of 556% from the diffusion coefficient measured for the **RDL00** model to that measured for the **RDL90** model. This a much smaller increase in comparison to the rise of 876% increase in diffusion coefficients measured in the triangular mesh models, from the **DL00** model to the **DL90** model.

6.4.6 Mesh Orientation

An important consideration for the diffusion coefficient measurements in the DWM is the orientation of the mesh with respect to the geometry and boundaries in the model. This orientation determines the angle of the waveguides that connect each neighbouring junction in relation to the edges of the diffuser. Figure 6.46 shows the orientation of the DWM in all diffusion coefficient measurement procedures executed in this thesis for both the triangular and rectilinear topologies. Owing to the non-isotropic dispersion characteristics of the DWM, and also to the dependence of some diffusion models on the number of connecting waveguides at the boundary junctions (particularly the diffusing boundary), the mesh orientation may have an effect on the diffusing behaviour of a boundary and this should be investigated further in future work.

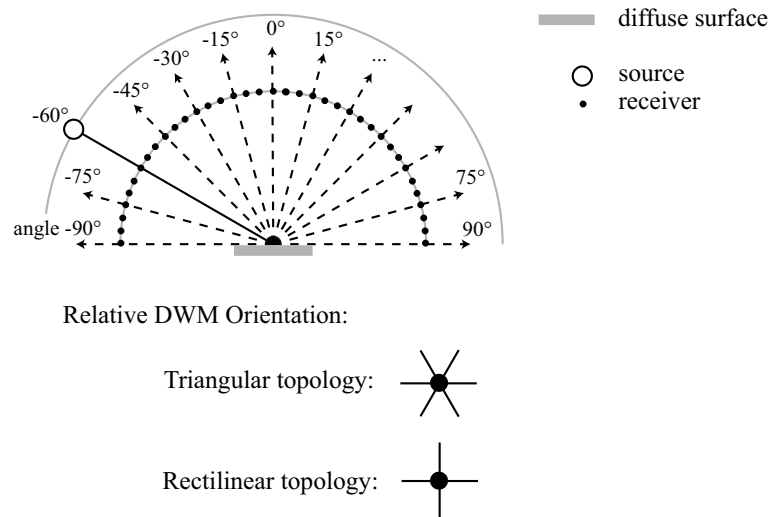


Figure 6.46: Diagram of the set-up used for the diffusion testing in the 2-D DWM showing the orientation of the mesh both for the triangular and rectilinear topologies.

6.5 Modal Analysis of Diffusion Models in a 2-D Lossless DWM

In order to further test and compare the diffusing layer method, described in section 5.3.3, with the diffusing boundary method, described in section 5.3.2, two identical structures are defined. In one structure, labelled **Model DL**, the *diffusing layer* model is implemented at the boundaries and in the other structure, labelled **Model CM**, the *diffusing boundary* method is implemented at the boundaries. For the diffusing layer model, **Model DL**, the rotations are applied at a single layer of junctions adjacent to the diffusing boundaries.

The two structures are rectangular in shape, and the 2-D triangular DWM is used. The length of each structure is 1.91m and the width 1.10m, and f_{update} is set at 44.1 kHz, giving an inter-nodal distance, x , of 0.0110 m according to (4.17). Ten consecutive simulations, each lasting 4 seconds, are performed on each mesh, each with an increasing level of diffusivity implemented at every boundary. At the start of each simulation, the meshes are excited with a low-pass filtered impulse applied near a corner and the outputs are obtained at a junction at the opposite corner. The maximum angle used in the probability function is 0° in the first simulation, where effectively no diffusion model is applied. This maximum diffusion angle increases at each simulation by $\pm 5^\circ$ until the final test when it reaches a maximum of $\pm 90^\circ$.

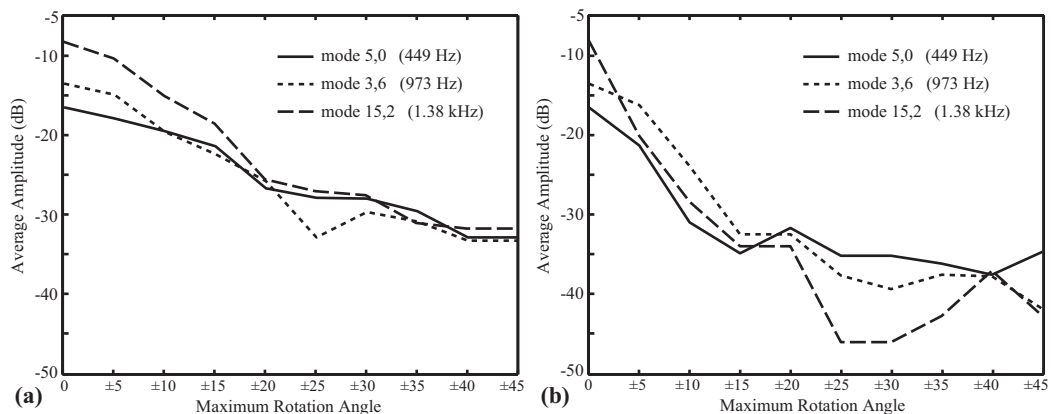


Figure 6.47: Graphs showing the average amplitudes of the outputs from (a) **Model DL** and (b) **Model CM** at 3 modal frequencies for each 4 second simulation.

In order to compare the effects of the simulated boundary scattering in the two models, three modal frequencies (449 Hz, 973 Hz and 1.38 kHz) are arbitrarily selected for analysis. These theoretical frequency values have been calculated using

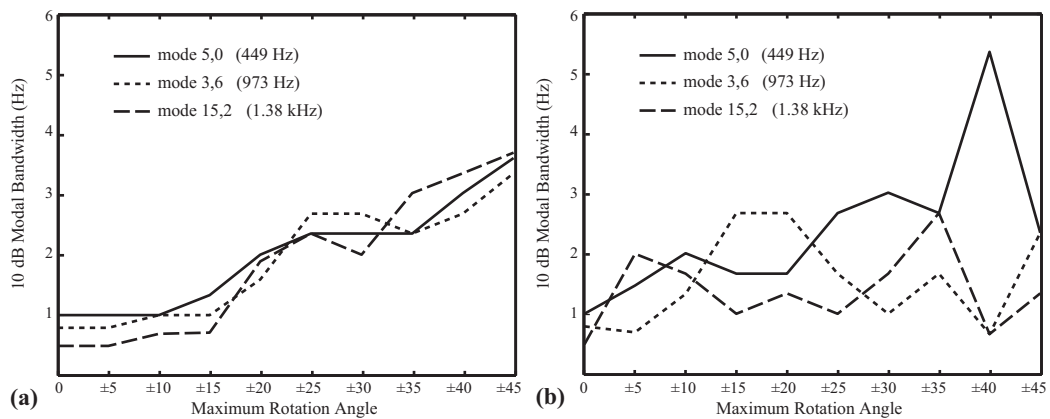


Figure 6.48: Graphs showing the 10dB modal bandwidths of the outputs from (a) **Model DL** and (b) **Model CM** at 3 modal frequencies for each 4 second simulation.

(2.39). The dispersion error which causes a dependence of wave propagation speed in the mesh on frequency and direction of travel (see section 4.4.6) has also been taken into account in the calculation of these modal frequencies. In order to achieve this the wave propagation speed in a DWM with triangular topology is assumed to be independent of the direction of travel up to a relative frequency of 0.25. The same function to describe the dispersion error is therefore assumed for all directions of wave travel within the mesh. The average dispersion over 1000 directions evenly distributed around the circle is taken in order to achieve this function. This directionally independent function, describing the wave speed in the mesh in terms of frequency, is then used to calculate the accurate theoretical modal frequencies that result from the DWM models used in the simulation.

Increased boundary scattering at the boundaries results in the average amplitudes of the output being diminished at modal frequencies. As well as this, the bandwidth of energy found at the modal frequencies increases as energy is spread away from the modal frequencies [12]. The average amplitude at each of these three modal frequencies, for each simulation, in both **Model DL** and **Model CM** is shown in Figure 6.47. 10 dB modal bandwidths for the same three modal frequencies are shown in Figure 6.48.

6.5.1 Discussion

When the diffusion algorithm is limited by a maximum angle of just 5° , the attenuation in average amplitude observed in **Model CM** is 4.8 dB at the modal frequency of 559 Hz, 2.7 dB at 973 Hz and 12.0 dB at 1.38 kHz. The attenuation in

average amplitude at the same modal frequencies shows more consistency in **Model DL**, with attenuations of 2.0 dB, 2.0 dB and 2.1 dB observed at 559 Hz, 973 Hz and 1.38 kHz. As the limit of the angles is increased, the observed diffusivity of **Model CM** appears to fluctuate to varying degrees at different modal frequencies. Some fluctuation is also observed in **Model DL** but to a lesser extent and the diffusivity at the boundaries increases consistently.

This difference in consistency of the two models can be observed at other modal frequencies and is evidence that the rotation error, even when corrected, has a significant effect on the diffusion model. The mesh structure is rectangular in shape and owing to the nature of its implementation and the triangular topology of the mesh, the boundary junctions found along the length of the structure differ to the boundary junctions located along its width in terms of their number of connecting waveguides. The inconsistencies observed between different modal frequencies in **Model CM** are a result of the errors introduced when rotations are applied to boundary junctions with differing numbers of connecting waveguides, as discussed in section 5.3.2. These inconsistencies are also explained by the fact that rotation error is dependent on the angle of incidence of the waves. This dependency is described by Figure 5.6 of section 5.3.2. This is a factor because the angle of incidence of reflections of a standing wave within the structure vary depending on its cyclic path. The sharp increase in amplitude levels at modal frequencies in **Model CM** for relatively small angles of rotation in comparison with **Model DL** is again a result of the rotation error because small angles of rotation are distorted into large angles, as discussed in section 5.3.2. The results show that using the diffusing layer method described in section 5.3.3, a more controlled and consistent diffusion model can be achieved. This is particularly true for small ranges of diffusion angles.

The improved diffusion exhibited by this new method can be explained by the elimination of the rotation error, implying that small rotation angles are no longer translated into larger angles. This has a clear advantage when modelling boundaries with low diffusivity, commonly found in real world materials.

6.6 Early Reflection Testing in a 2-D DWM

The early reflections are the stronger, more distinct and widely spaced reflections that are found at the beginning of the impulse response. They are typically found in the first 100ms, although this is dependent on the volume of the space and the geometrical arrangement of the source, receiver and boundaries. The early reflections help the listener to determine source location and information about the geometry of the space itself [31]. Diffusivity at the boundaries of the room will have some effect on the early reflections. Generally, small scale boundary diffusion results in a slight diminution in the strength of the early reflections as well as some smearing as the energy distribution in the space is spread out more evenly. However the overall geometry of the room is not changed, therefore the early reflections should not be any different in the respect of timing and their dominance is preserved [9].

In order to test that the diffusing layer implementation behaves correctly and does not result in inaccurate early reflections being produced by the room model, a simple 2-D DWM structure is defined with triangular topology. The structure is again rectangular in shape, the dimensions of which are 8m by 6m. Again f_{update} is set at 44.1 kHz, giving an inter-nodal distance, x , of 0.0110 m. Three simulations are performed, each with a length of 3000 samples, or 0.068 seconds. Impulse responses are obtained for each simulation by exciting the mesh with a low-pass filtered impulse (see section 6.2) near one corner and outputs are generated from a junction near the opposite corner. In each simulation the diffusing layer is applied at the boundaries of the structure, with the limited range of rotation angles set to 0° in the first simulation, 45° in the second simulation and 90° in the third. Using the same naming system as that used in previous sections, these boundary models are referred to as **DL00**, **DL45** and **DL90** respectively.

Figure 6.49 shows the early part of the impulse responses obtained using the simulation. The signals have been low-pass filtered at a quarter of the sampling rate, as the DWM typically is limited to giving valid results in this bandwidth only as described in section 4.4.5. It can be seen that in each test the peaks in pressure amplitude caused by early reflections are largely preserved but become slightly attenuated as the range of rotation angles in the diffusion model is increased. For

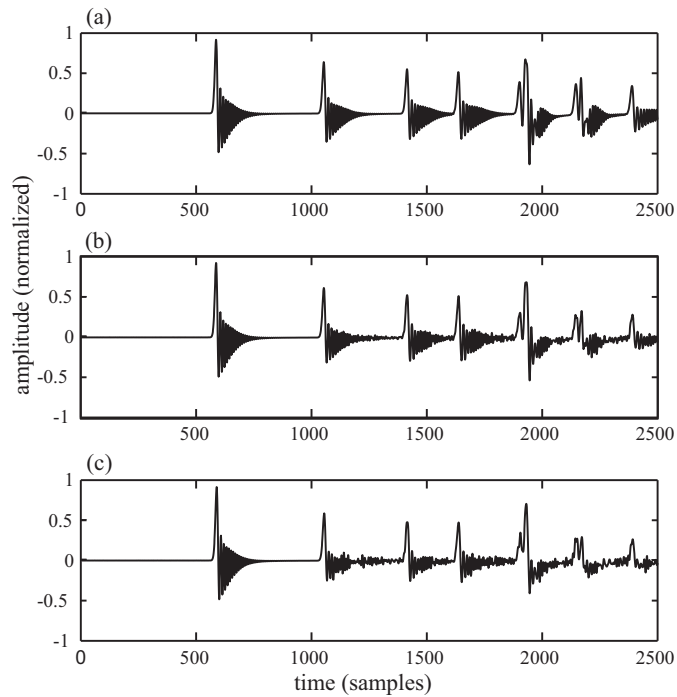


Figure 6.49: Graphs showing early part of impulse responses for room simulations with boundary diffusion models (a) DL00, (b) DL45 and (c) DL90 implemented at each boundary.

instance the second peak, which is the first first-order reflection to reach the receiver, is attenuated as a result of the 45° diffusion implementation by just 4.95% and by 5.41% when the maximum diffusion rotation angle is set to 90° . Likewise, the third peak (the second first-order reflection) is reduced by 5.30% when the maximum rotation angle is set to 45° and by 6.50% when it is set to 90° .

6.7 Effect of Diffusion Models on Boundary Absorption

The diffusing boundary and diffusing layer models allow for the simultaneous application of frequency dependent absorption filters at the boundary junctions of the Digital Waveguide Mesh, because signals can still be processed after the circulant matrix transformation is applied. In the diffusing layer case, the boundary junctions are not involved in the diffusion process, and so further processing can be applied without any hindrance. The nature of these diffusing models however means that the energy of incident sound waves at a boundary is scattered at the point of reflection. This potentially alters the way in which incident waves interact with the boundary filters when the diffusion model is implemented. The greater the range of rotation angles used in the boundary scattering model, the greater the scattering of the sound wave energy and the greater this potential effect, with the possibility that some energy is scattered away from the incident direction completely and therefore does not interact with the boundary filter at all.

In order to test the effect of the diffusion models on boundary absorption filtering, a rectangular shaped DWM of triangular topology is constructed with a length of 3.81m and a width of 3.3m. The update frequency of the mesh f_{update} is 44.1 kHz. For both tests, a series of 7 simulations are then performed and in each simulation the diffusing method under test is implemented at all boundaries of the structure. Specific maximum rotation angles in the diffusing method of $\pm 0^\circ$, $\pm 15^\circ$, $\pm 30^\circ$, $\pm 45^\circ$, $\pm 60^\circ$, $\pm 75^\circ$ and $\pm 90^\circ$ are used for each subsequent simulation. The boundaries are terminated with simple N -port terminations, as described in section 4.4.7. This termination is chosen because it results in absorption at all frequencies of interest and does not introduce any unnecessary delay at the boundary that may effect the results.

In every simulation, 20 impulse responses are obtained simultaneously by exciting the mesh with a low-pass filtered impulse near one corner and generating outputs from junctions at random points elsewhere in the mesh. Although the output junctions are initially chosen at random, the same locations for the output junctions are then used in each subsequent simulation. From these impulse responses, average RT_{60} values are calculated at octave bands according to [156]. It is important to note at this stage that the measured RT_{60} times at low frequency

octave bands are not completely reliable due to the low number of modal frequencies found in these regions and this will have an effect on all subsequent results involving low frequency RT_{60} calculations. However for low frequency regions the results are considered important, as some observation can be made about the effects of the diffusion models, by comparing the results with those obtained for the case where no diffusion is implemented in the same octave band.

The test is repeated 4 times, and for convenience the tests are labelled Test A, Test B, Test C and Test D. In Test A and Test B, the diffusing boundary model is applied at the mesh boundaries and the reflection coefficient of all boundaries r is set at 0.3 for Test A and 0.5 for Test B. In Test C and Test D the diffusing layer model is applied at the mesh boundaries and the reflection coefficient of all boundaries r is set to be 0.3 for Test C and 0.5 for Test D.

Octave Band(Hz)	RT_{60} Times (seconds)						
	CM00	CM15	CM30	CM45	CM60	CM75	CM90
63	0.131	0.133	0.133	0.131	0.133	0.137	0.132
125	0.104	0.105	0.107	0.105	0.105	0.112	0.110
250	0.103	0.105	0.107	0.108	0.106	0.109	0.106
500	0.116	0.117	0.122	0.122	0.123	0.121	0.123
1000	0.128	0.130	0.138	0.144	0.148	0.150	0.153
2000	0.126	0.128	0.137	0.153	0.164	0.171	0.180
4000	0.132	0.137	0.151	0.175	0.203	0.231	0.255
8000	0.164	0.254	0.316	0.366	0.401	0.457	0.501

Table 6.13: Table showing measured RT_{60} times of a DWM structure at different octave bands for the 7 boundary models **CM00-CM90** with boundary reflection coefficient $r = 0.3$ (Test A).

Octave Band(Hz)	RT_{60} Times (seconds)						
	CM00	CM15	CM30	CM45	CM60	CM75	CM90
63	0.169	0.168	0.170	0.171	0.176	0.174	0.172
125	0.168	0.163	0.175	0.162	0.164	0.170	0.165
250	0.158	0.159	0.156	0.153	0.150	0.153	0.154
500	0.166	0.172	0.180	0.185	0.180	0.174	0.175
1000	0.189	0.195	0.212	0.222	0.227	0.229	0.227
2000	0.198	0.206	0.230	0.246	0.259	0.265	0.273
4000	0.201	0.212	0.245	0.278	0.305	0.334	0.365
8000	0.254	0.347	0.421	0.453	0.491	0.529	0.565

Table 6.14: Table showing measured RT_{60} times of a DWM structure at different octave bands for the 7 boundary models **CM00-CM90** with boundary reflection coefficient $r = 0.5$ (Test B).

Octave Band(Hz)	RT_{60} Times (seconds)						
	DL00	DL15	DL30	DL45	DL60	DL75	DL90
63	0.131	0.132	0.142	0.135	0.157	0.177	0.208
125	0.104	0.107	0.111	0.119	0.120	0.150	0.182
250	0.103	0.109	0.107	0.116	0.117	0.137	0.158
500	0.116	0.118	0.125	0.136	0.147	0.160	0.173
1000	0.128	0.132	0.139	0.157	0.178	0.209	0.249
2000	0.126	0.130	0.142	0.176	0.231	0.293	0.348
4000	0.132	0.140	0.164	0.249	0.344	0.428	0.483
8000	0.164	0.239	0.312	0.422	0.513	0.577	0.615

Table 6.15: Table showing measured RT_{60} times of a DWM structure at different octave bands for the 7 boundary models **DL00-DL90** with boundary reflection coefficient $r = 0.3$ (Test C).

Octave Band(Hz)	RT_{60} Times (seconds)						
	DL00	DL15	DL30	DL45	DL60	DL75	DL90
63	0.169	0.179	0.180	0.183	0.186	0.205	0.258
125	0.168	0.164	0.158	0.174	0.180	0.193	0.194
250	0.158	0.161	0.163	0.163	0.165	0.180	0.185
500	0.166	0.174	0.185	0.195	0.209	0.224	0.246
1000	0.189	0.195	0.206	0.229	0.260	0.296	0.321
2000	0.198	0.204	0.218	0.257	0.331	0.400	0.451
4000	0.201	0.210	0.243	0.344	0.449	0.522	0.574
8000	0.254	0.328	0.378	0.492	0.568	0.621	0.658

Table 6.16: Table showing measured RT_{60} times of a DWM structure at different octave bands for the 7 boundary models **DL00-DL90** with boundary reflection coefficient $r = 0.5$ (Test D).

Tables 6.13 and 6.14 show the RT_{60} times measured for the diffusing boundary model with $r = 0.3$ and $r = 0.5$ respectively (Test A and Test B). Tables 6.15 and 6.16 show the results for the diffusing layer model again with $r = 0.3$ and $r = 0.5$ respectively (Test C and Test D). The results are also displayed for all tests in the graphs shown in Figure 6.50.

The results show that the general pattern for the RT_{60} times is to increase for both diffusion models as the maximum rotation angles used in the models are increased. This trend indicates that the effect of the boundary absorption filters is attenuated as the maximum rotation angle increases. In both models this effect is dependent on frequency, with the frequency dependent characteristics closely matching those observed in the diffusion coefficient measurements for the same models. The effect becomes greater at higher frequencies for both models. The apparent cut-off of the effect is lower for the tests with the diffusing layer model (Test C and Test D). For the case where $r = 0.3$ for example (Test A and Test C), the RT_{60} times measured at the 500 Hz octave band rises from 0.116 seconds (for no diffusion at the boundaries) to 0.123 seconds (model **CM90**) in Test A, an increase of just 6% whereas at the 8 kHz octave band, the RT_{60} times increase from 0.164 seconds to 0.501 seconds ,

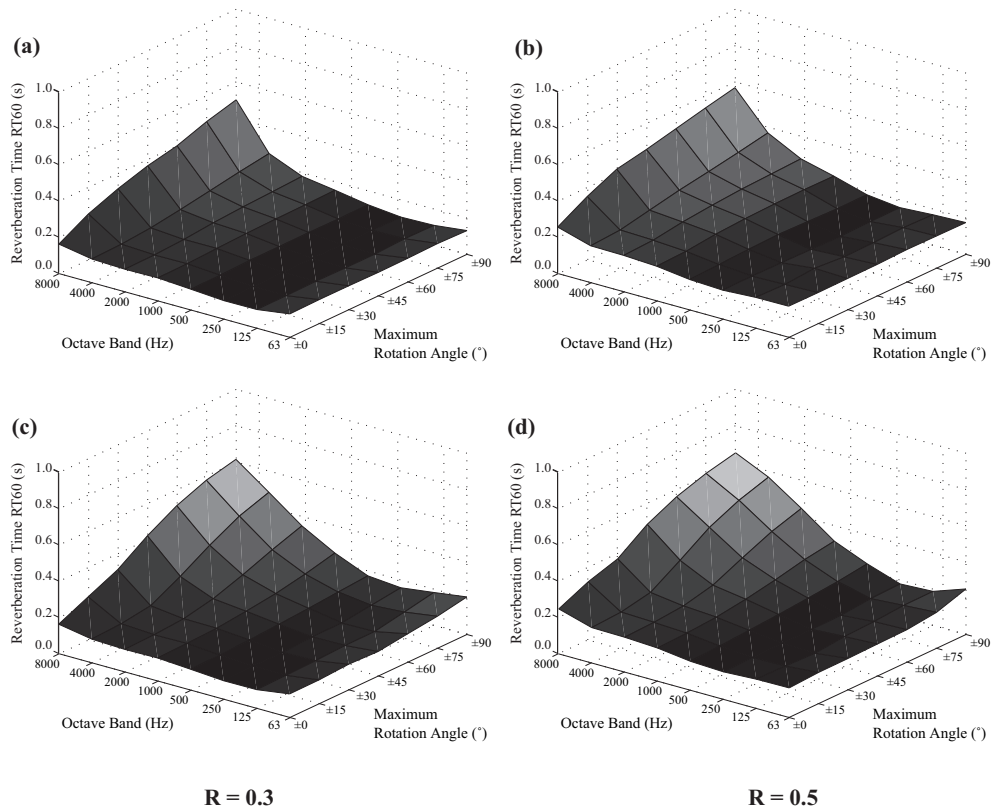


Figure 6.50: Graphs showing RT_{60} times of a DWM structure for boundary models (a) CM00-CM90 with $r = 0.3$ (Test A), (b) CM00-CM90 with $r = 0.5$ (Test B), (c) DL00-DL90 with $r = 0.3$ (Test C) and (d) DL00-DL90 with $r = 0.5$ (Test D).

an increase of 205%. For the diffusing layer case, Test C, the RT_{60} times rise from 0.116 seconds to 0.173 seconds (model DL90) in the 500 Hz octave band, an increase of 49%, whereas in the 8 kHz octave band the rise is from 0.164 seconds to 0.615 seconds, an increase of 275%.

The relative increases in RT_{60} times also show a dependence on the reflection coefficient applied at the boundaries, r . For example in the 8 kHz octave band, the RT_{60} times for the diffusing boundary and diffusing layer models (Test A and Test C) increase by 205% and 275% respectively when the reflection coefficient at the boundaries $r = 0.3$. However for a higher reflection coefficient $r = 0.5$, the increase for each of the two models is lower at 122% for the diffusing boundary model (Test B) and 159% for the diffusing layer model (Test D).

Other factors must be considered that affect the RT_{60} times given in these results. A major factor is the spread of energy away from the modal frequencies and the predicted shortening effect this has on the decay times at these frequencies [12]. The next section explores how this effect causes a decrease in RT_{60} if the diffusion and

absorption models are implemented only in certain selected boundaries.

The tests presented serve as evidence that the diffusion models do have an effect on boundary absorption models, and the nature of this effect to some extent, however they do not quantify the effect in any way. The results might change dramatically if the size of the DWMs used in the tests are changed for example. A more detailed and extensive study is therefore required to fully understand this effect and this is the subject of future work. Once this is achieved then any erroneous increase in reverberation times caused by the increase in rotation angle of the diffuse boundary model can potentially be compensated for by increasing the absorption coefficient of the modelled boundary using low-pass filters.

6.8 An Investigation of Diffusion Based on Room Diffuseness

6.8.1 The 2-D Triangular Mesh

Section 6.7 describes tests that are designed to investigate the effect of diffusion models on boundary absorption by measuring their effect on the reverberation characteristics of a room. By altering the model slightly, a similar test is designed to investigate the diffuse behaviour of the models.

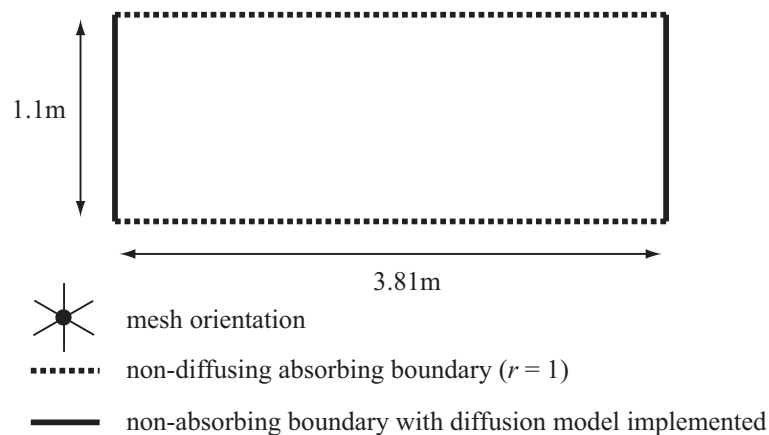


Figure 6.51: Diagram of DWM with alternating absorbent walls and diffusing walls.

Figure 6.51 shows a rectangular shaped mesh with a length of 3.81 m and width 1.1 m. With no diffusion model applied along the width-wise boundaries of the wall, the space is highly non-diffuse and strong standing waves occur along the mesh

length when it is excited with an impulse. By applying diffusion to these boundaries, sound energy that reflects from one end to another, hence forming standing waves, is scattered onto the absorbing boundaries, resulting in an overall decrease in the reverberation time of the system. If a diffuse boundary model is implemented in this system which scatters all reflected energy into the non-specular direction, i.e. a boundary with a scattering coefficient of 1, then it is possible to measure a lowest possible limit of such a system on the reverberation time. The system can then be used to measure the scattering coefficient of an arbitrary diffusing boundary by measuring where the measured reverberation time for the boundary falls between a minimum value, which equates to a scattering coefficient of 1, and a maximum value, which equates to a scattering coefficient of 0 and then scaling the actual scattering coefficient of the boundary accordingly [44]. A problem is that such an optimal diffuse boundary has not yet been implemented in a DWM model. Also the theory works on the assumption that a flat specular surface has a scattering coefficient of 0 and that the scattering coefficient can be linearly scaled to the measured reverberation time of the system.

Although there are issues to this approach when used as a method to quantify the diffusivity of a boundary, it may be a useful approach to compare the diffuse characteristics of materials, or to investigate its diffusion properties in cases where the implementation of the scattering coefficient or diffusion coefficient test set-ups, as described in Chapter 3, is impractical for certain reasons.

Octave Band(Hz)	RT_{60} Times						
	DL00	DL15	DL30	DL45	DL60	DL75	DL90
63	0.131	0.151	0.131	0.133	0.133	0.131	0.130
125	0.085	0.218	0.121	0.095	0.090	0.089	0.089
250	0.084	0.282	0.158	0.113	0.097	0.093	0.094
500	0.094	0.291	0.209	0.137	0.128	0.118	0.111
1000	0.219	0.330	0.278	0.230	0.213	0.199	0.188
2000	0.735	0.721	0.561	0.414	0.313	0.256	0.229
4000	1.002	0.912	0.638	0.380	0.281	0.295	0.338
8000	0.983	0.957	0.652	0.404	0.419	0.460	0.509

Table 6.17: Table showing RT_{60} times of the DWM structure described by Figure 6.51 with boundary models **DL00-DL90** implemented at the diffusing boundaries and reflection coefficient $r = 0.3$ applied at the absorbing boundaries.

Table 6.17 and Figure 6.52 show the resulting RT_{60} times of the DWM structure described by Figure 6.51 with a reflection coefficient $r = 0.3$ applied at the two opposing absorbing boundaries using the N -port terminations described in section 4.4.7. Note that the maximum rotation angle axis in Figure 6.52 has been flipped

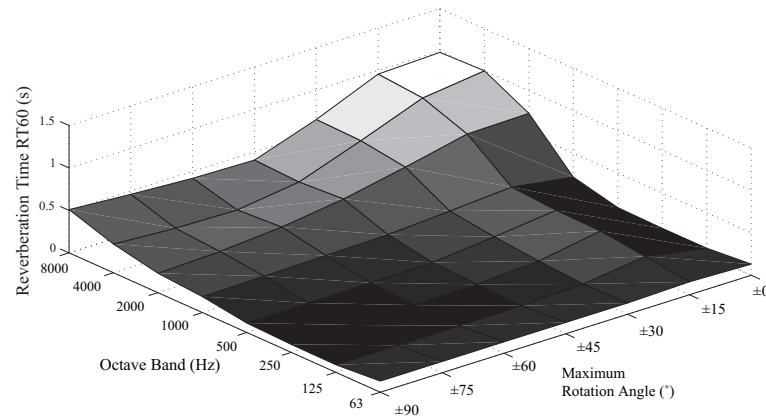


Figure 6.52: Graph showing RT_{60} times of the DWM structure described by Figure 6.51 with boundary models **DL00-DL90** implemented at the diffusing boundaries and reflection coefficient $r = 0.3$ applied at the absorbing boundaries.

in comparison to previous graphs, in order that the data can be seen more clearly. A 2-D mesh with a triangular topology is used, with an update frequency $f_{update} = 44.1$ kHz. In a similar approach to the tests used in the previous section, a series of 7 simulations are run with the boundary models **DL00**, **DL15**, **DL30**, **DL45**, **DL60**, **DL75** and **DL90** implemented at the two opposing diffusing boundaries in each subsequent simulation. In every simulation, 20 impulse responses are obtained simultaneously by exciting the mesh with a low-pass filtered impulse near one corner and generating outputs from junctions at random points elsewhere in the mesh. The average RT_{60} values are then calculated at octave bands according to [156].

The results show that applying diffusion to width-wise boundaries (see Figure 6.52) causes a general decrease in reverberation time in the octave bands with centre frequencies 2 kHz, 4 kHz and 8 kHz. In the 2 kHz octave band the RT_{60} time decreases from a maximum value of 0.735 seconds with the **DL00** boundary implementation to a minimum of 0.229 seconds with the **DL90** boundary implementation, a decrease of 69%. In the 4 kHz octave band, the RT_{60} time decreases from a maximum value of 1.002 seconds with the **DL00** boundary implementation to a minimum value of 0.281 seconds, this time with the **DL60** boundary implementation, before rising by a small percentage for each of the next two boundary diffusion implementations. The decrease from the maximum RT_{60} time to the smallest value in this octave band is 72%. Finally, in the 8 kHz octave band a decrease of 59% occurs from a maximum value of 0.983 seconds for the

DL00 boundary implementation to a minimum value of 0.404 seconds with the **DL45** boundary diffusion model. Again the RT_{60} times rise by a small percentage at a time with each boundary diffusion model after this minimum has been reached. In the lower frequency bands, the general trend in each band is for the RT_{60} times to rise to a peak with the **DL15** diffusion model implemented at the two width-wise boundaries, and then decrease slightly as the maximum diffusion angle used in the diffusion model increases.

It should be noted that the higher RT_{60} times measured at the higher frequencies, particularly for the **DL00** diffusion model implementation, are caused by a greater concentration of modal frequencies found within these bands. The inconsistencies observed in the results may indicate inconsistencies in the model, or may be a result of the complex nature and behaviour of sound waves in such a system when scattering is introduced. Further work is required in order to determine what should be seen in the results. In general however, increasing the boundary diffusion at the width-wise boundaries will cause a decrease in reverberation time, and the diffusion models behave as predicted according to these tests. The apparent cut-off frequency of the diffusion model shown in these tests corresponds to that observed in the diffusion coefficient measurements for the diffusing layer models.

6.8.2 The 3-D Rectilinear Mesh

Section 5.3.3 describes a method to implement the diffusing layer boundary model in a 3-D DWM with rectilinear topology. Theoretically, it is possible to carry out diffusion coefficient measurements for this diffusion model by applying the tests described in section 3.2.1 and [14], much like the diffusion coefficient measurements carried out earlier in this chapter for diffusion models in the 2-D DWM. Such a test requires a relatively large amount of computer processing power and memory by today's standards and so such measurements have not yet been performed. For example, in order to perform the measurement for diffusion coefficient data of a modelled diffuse boundary in a 3-D DWM with a distance of 8 m between the source and the central point of the diffuse boundary sample, and assuming that it is possible to model perfectly anechoic boundaries, a mesh with a volume of at least 2048 cubic metres is required. If a mesh with rectilinear topology and an update frequency of 44.1 kHz is used, then the simulation would require the

implementation of a mesh with 6.17×10^{10} junctions. If the chessboard technique is used (see section 4.4.5), the number of junctions stored in the memory is half this value, however the implementation of such a model requires advanced computing techniques and much time, and is therefore beyond the scope of this thesis and the subject of future work.

In order to implement and test the diffusion model using an empirical approach however, a similar test to that described in the previous section for the 2-D DWM is performed.

A cuboid shaped 3-D DWM is constructed with a square shaped cross section. The topology of the DWM is rectilinear. The update frequency of the mesh f_{update} is 44.1 kHz, resulting in an inter-nodal distance of, x , of 0.0135 m. The length of the cuboid is 4.02 m and both its width and height are 0.673 m. The diffusing layer diffusion model is applied at the two opposing surfaces of the cuboid at either end along its length, and the reflection coefficient r at these surfaces is 1. All other surfaces of the DWM are flat with no diffusion model applied, and with a reflection coefficient $r = 0.8$. Figure 6.53 shows the movement of sound waves in the DWM, after being excited near one corner, at earlier stages of the simulation. The boundaries of the mesh are made invisible and waves are represented using a colour scale. The diffusing layers, applied to junctions at either end of the mesh, are coloured black. Note that in order to show the wave propagation more clearly, the diagrams are created by exciting the mesh with a simple pure tone rather than a low-passed impulse signal that is used in the test simulations.

A series of 7 simulations are run with the maximum rotation angle of the diffusing model set to ± 0 , ± 15 , ± 30 , ± 45 , ± 60 , ± 75 and ± 90 in each subsequent simulation. These modelled surfaces are labelled **3DDL00**, **3DDL15**, **3DDL30**, **3DDL45**, **3DDL60**, **3DDL75** and **3DDL90**. In every simulation, 20 impulse responses are obtained simultaneously by exciting the mesh with a low-pass filtered impulse near one corner and generating outputs from junctions at random points elsewhere in the mesh. The average RT_{60} values are then calculated at octave bands according to [156].

The results show a relatively small change in RT_{60} times of the DWM, as the maximum rotation angle in the diffusing layer model increases, for octave bands with central frequencies 2 kHz and below. The RT_{60} times in these octave bands

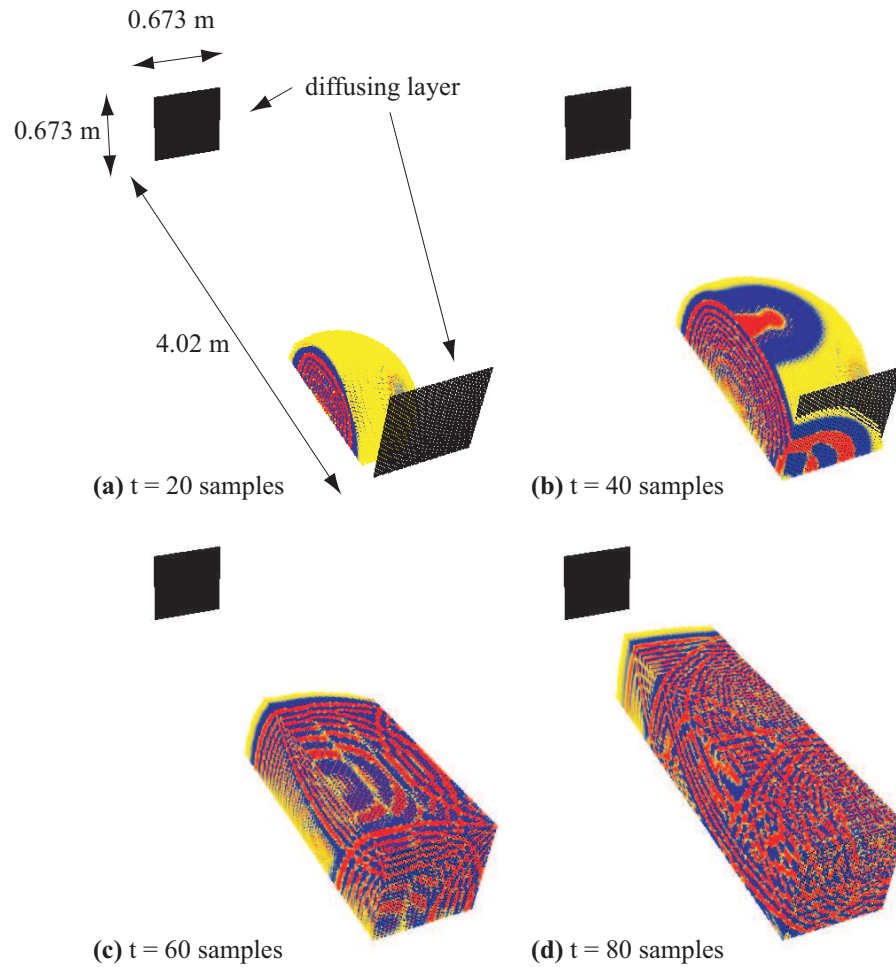


Figure 6.53: Wave propagation in a cuboid shaped 3-D DWM.

Octave Band(Hz)	RT_{60} Times						
	3DDL00	3DDL15	3DDL30	3DDL45	3DDL60	3DDL75	3DDL90
63	0.145	0.145	0.145	0.145	0.145	0.143	0.145
125	0.116	0.119	0.118	0.116	0.116	0.112	0.115
250	0.107	0.126	0.112	0.125	0.110	0.108	0.108
500	0.098	0.123	0.124	0.117	0.120	0.114	0.112
1000	0.099	0.137	0.139	0.151	0.134	0.128	0.129
2000	0.147	0.164	0.152	0.158	0.143	0.142	0.144
4000	0.422	0.365	0.267	0.208	0.157	0.151	0.155

Table 6.18: Table showing RT_{60} times of the DWM structure described by Figure 6.53 with boundary models 3DDL00-3DDL90 implemented at the diffusing boundaries and reflection coefficient $r = 0.8$ applied at the absorbing boundaries.

do not show a general rise or fall as the maximum rotation angle is increased, but instead show small fluctuation. For example in the 500 Hz octave band, the measured RT_{60} times increase from 0.098 seconds for the 3DDL00 model to a highest value of 0.124 seconds for the 3DDL30 model before fluctuating slightly and eventually falling to 0.112 seconds with the 3DDL90 diffusion model. In the

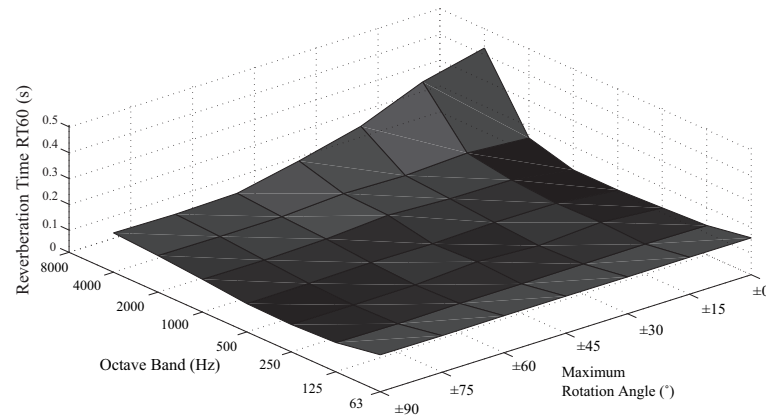


Figure 6.54: Graph showing RT_{60} times of the DWM structure described by Figure 6.53 with boundary models **3DDL00-3DDL90** implemented at the diffusing boundaries and reflection coefficient $r = 0.8$ applied at the absorbing boundaries.

4 kHz octave band however, a decrease in RT_{60} time from 0.422 seconds for the **3DDL00** model to 0.155 seconds for the **3DDL90** model is observed, a decrease of 63%, indicating that the diffusion model works most effectively in this octave band.

Again, the higher RT_{60} times recorded at the 4 kHz octave band are a result of the greater concentration of modal frequencies found within this band in comparison with lower frequency bands. With the length of model being 2.2 m, the lowest modal frequency caused is 127 Hz. This explains why very little change in the RT_{60} times is observed in the octave bands with central frequencies 63 Hz and 125 Hz, because the concentration of modal frequencies is very low in these regions, making the tests invalid.

6.9 Computational Analysis of the Diffusing Layer Model in the 2-D DWM

In order to test the added computational load that results from the diffusion layer boundary model, a simple rectangular DWM structure with length 1.91 m and width 1.10 m is constructed. The update frequency of the mesh f_{update} is 44.1 kHz. The boundaries of the mesh are totally reflective so no energy is lost during simulation. An impulse is applied to the mesh and the processing time taken to perform a 2 second simulation is measured. The memory used by the computer DWM implementation is also measured. The test is performed first with the diffusing layer model applied at all boundaries (with maximum angle set to $\pm 45^\circ$ and then

again with no diffusing layer model applied at all. The total number of scattering junctions in the structure (for both tests) is 20201 junctions. The number of scattering junctions used for the diffusing model in the first test is 590, 2.92% of the total amount.

The results show that when the diffusing layer model is implemented at all boundaries in the DWM, the increase in memory usage in this case is negligible (13,772 kb measured for both simulations). The execution time of the simulation without the diffusing layer implementation is 1472.44 seconds. However the total computation time for the same system with the diffusing layer implemented is slightly longer by 7.48 seconds (1479.92 seconds), an increase of only 0.508%.

6.10 Auditory Demonstration

6.10.1 Test Description

Auditory Examples in the 2-D Digital Waveguide Mesh

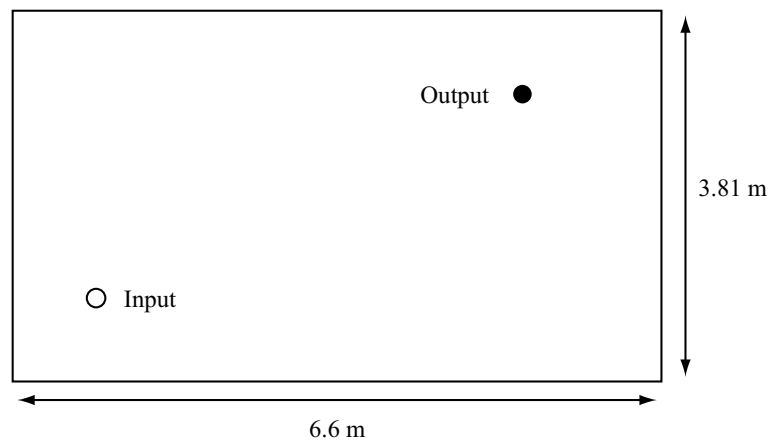


Figure 6.55: Diagram showing the mesh geometry used to create the 2-D auditory examples.

A 2-D DWM structure, rectangular in shape and with a triangular mesh topology, is used to create a series of impulse responses designed to demonstrate the auditory effect of the diffusing layer model implementations. The structure has a length of 7 m and a width of 4 m and the update frequency of the mesh is 44.1 kHz. The dimensions and geometry of the mesh are illustrated in Figure 6.55. The diffusing layer diffusion model is applied at all boundaries of the structure and a reflection coefficient r is also applied at all boundaries. Two sets of tests are performed. The

first is designed to investigate the auditory effect of the diffusing layer model on the impulse response with a relatively high reflection coefficient ($r = 0.95$) and the second is designed to investigate the auditory effect of the diffusion model with a relative low coefficient ($r = 0.4$). In each set of tests seven impulse responses are obtained, with different implementations of the diffusing layer model applied at the boundaries. In order to be consistent with previous tests, the diffusing layer boundary model implementations are named **DL00**, **DL15**, **DL30**, **DL45**, **DL60**, **DL75** and **DL90**. In each test an impulse response is created by applying a low-pass filtered impulse near one corner of the mesh and taking an output from a point near the opposite corner.

Auditory Examples in the 3-D Digital Waveguide Mesh

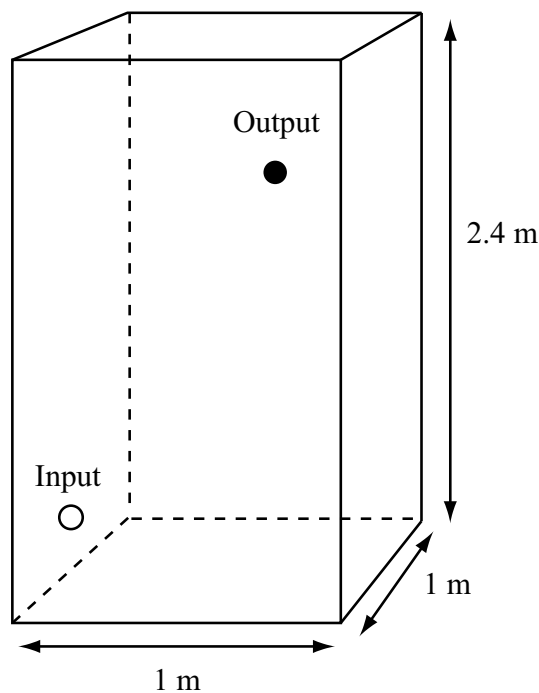


Figure 6.56: Diagram showing the mesh geometry used to create the 3-D auditory examples.

A 3-D DWM structure in the shape of a cuboid and with a rectilinear mesh topology is used to create a series of impulse responses designed to demonstrate the auditory effect of the diffusing layer model implementations, this time in a 3-D mesh. The structure has a length of 1 m, a width of 1 m and a height of 2.4 m (similar in proportions to a shower unit for example). Again the update frequency of the

mesh is 44.1 kHz. The diffusing layer diffusion model is applied at all boundaries of the structure and a reflection coefficient r is also applied at all boundaries. As for the case of the 2-D mesh in the previous section, two sets of tests are performed. In each set of tests seven impulse responses are obtained, with different implementations of the diffusing layer model applied at the boundaries. In order to be consistent with previous tests, the diffusing layer boundary model implementations are named **3DDL00**, **3DDL15**, **3DDL30**, **3DDL45**, **3DDL60**, **3DDL75** and **3DDL90**. In each test an impulse response is created by applying a low-pass filtered impulse near one corner of the mesh and taking an output from a point near the opposite corner.

6.10.2 Discussion

All impulse responses described here are provided on the CD-ROM accompanying this thesis. A description of the file names and the directory structure of the CD-ROM is found in Appendix C. The impulse responses are also used to process a selection of auditory samples, recorded in anechoic conditions, using the technique of convolution [157]. This process effectively places the source sound within the modelled space hence adding a reverberant effect to the original samples, so that the influence of the diffusion models can be heard on real and familiar sounds. A vocal speech recording, a piano recording, an electronically synthesised musical sequence and a recorded sequence played on an electronic drum kit are used as the original samples, all recorded in anechoic conditions. On the included CD-ROM, these sounds are referred to as *Speech*, *Piano*, *Synth* and *DrumKit* respectively.

The auditory evidence for the diffusion model implementations are made very clear by these examples. The comb filter effect caused by strong modal frequencies is significantly reduced as modelled diffusion increases and the impulse responses generally sound more noise-like, as energy concentrated at the modal frequencies increasingly escapes into other non-modal frequencies. The effect on the recorded sounds is also very clear, and a more natural and rich reverberant sound is heard as soon as the diffusion model is applied. The reverberation heard with the diffusion model present appears more natural because strong modal frequencies in a room are rarely heard in the real world. Exceptions for this may occur however in enclosed spaces where the surfaces are highly reflective and specular, like a tiled shower unit for example. The tests show that the diffusing layer models in both the 2-D

and 3-D DWM not only have a clearly audible effect, but also serve to improve the perceptual quality of the room response, by removing some of the unrealistic and unnatural elements largely caused by the lack of complexity and fine detail in the shape of the mesh in comparison to real world situations.

Chapter 7

Summary and Conclusions

An account of current methods for simulating diffuse boundaries in room acoustic modelling systems has been presented, including a detailed overview of current methods for simulating diffuse boundaries in the digital waveguide mesh. A new method for modelling diffuse boundaries with controllable boundary scattering based on a statistical approach, referred to as the *diffusing layer* method, has also been presented. The implementation of this boundary diffusion method is described for 2-D DWM structures with both triangular and rectilinear topologies, as well as for 3-D DWM structures with rectilinear topologies.

A number of different approaches have been proposed to investigate and characterise the boundary diffusion models presented in this thesis. This is an important problem because their behaviour must be well understood in order to make full use of the methods with the goal of accurate simulation of real acoustic boundaries in mind.

7.1 Diffusion Coefficient Measurements

In order to analyse the diffuse characteristics of diffuse boundary implementations, a standard technique is chosen which gives a frequency dependent measure of surface scattering of incident waves upon reflection. The data is quantified in the form of coefficients called *diffusion coefficients* [14]. This approach has the benefit that standard tests designed for diffusing boundaries in the real world can be directly applied to modelled diffusing boundaries in the DWM. Diffusion coefficients can also be achieved using highly accurate modelling techniques, designed specifically

for this application [44]. This approach should not be confused with another approach to characterising boundary scattering, where data is quantified in the form of *scattering coefficients* [13]. The scattering coefficient is less appropriate for DWM diffusing boundaries, as testing conditions are difficult to achieve, both for real world diffusing boundaries, and diffusing boundaries modelled in the DWM. The scattering coefficient was developed with diffuse boundary implementations for ray-based acoustical modelling approaches in mind, and differences between the two types of coefficient have been explored in this thesis.

The specific test geometry described in this thesis are based on guidelines outlined in [14] and result in diffusion coefficient results that are valid for frequencies above 872 Hz. Information regarding the scattering properties of the models at lower frequencies can be acquired by increasing the length of the boundary sample under test, as well as increasing the relative distances between the boundary and the source and receivers. Using this geometry, diffusion coefficients have been measured for a number of modelled diffusers. The results of the tests have been displayed not only in the form of diffusion coefficient data, but also using polar response graphs and spectrograms in order to give a rich insight into the behaviour of the diffusing models. Diffusion coefficient tests have been implemented only in 2-D DWM structures, however the tests can be extended for 3-D models by following guidelines outlined in Chapter 3.

Firstly, diffusion coefficients have been measured for a simple flat plane boundary of finite length, implemented in a 2-D triangular DWM with an update frequency of 44.1 kHz. The limited length of the diffuser was required to achieve useful results, as outlined in [14]. The measured diffusion coefficients show that the finite flat boundary indeed shows some degree of boundary scattering. This is an important test to carry out, as measured diffusion coefficients for a flat plane boundary must be used as a reference when considering measured diffusion coefficients for other boundary types under exactly the same testing conditions [14].

Diffusion coefficient measurements have also been carried out on two diffusers consisting of very simple shapes, designed to demonstrate the effectiveness and validity of the diffusion coefficient approach. Again, the objects were implemented in a 2-D triangular DWM with an update frequency of 44.1 kHz. The first of these two diffusers is a simple triangular object. The results show that the measured

diffusion coefficients can indicate a low level of boundary scattering, despite the fact that most of the reflected energy is not found in the specular zone of reflection. This is an issue related to the nature of the diffusion coefficient itself rather than a problem with the model, and has been discussed in more detail in Chapter 3. The second diffuser consisted of a semicircular object, and the results show a significant spread of reflected energy away from the specular direction across all measured frequencies, as would be expected.

In addition, diffusion coefficients have been measured for two different quadratic residue diffuser implementations, based on the approach initially proposed in [29], although the model was adapted in this thesis to be implemented in a 2-D triangular DWM system, again with an update frequency of 44.1 kHz. The results show a high level of boundary scattering exhibited by these models, however a detailed frequency analysis of the diffuser response reveals patterns in the scattering characteristics which disagree somewhat with the behaviour that is predicted by the design equations for the models, and the diffusion coefficient data is not consistent across all frequencies.

Diffusion coefficient measurements were then carried out on a range of boundaries implemented using a technique for modelling diffuse boundaries in the 2-D DWM based on a statistical approach, referred to in this thesis as the *diffusing boundary* method. Again a 2-D triangular DWM is used with an update frequency of 44.1 kHz. This method was originally proposed in [30]. Results have shown that for a sampling frequency of 44.1 kHz, this model is most effective for frequencies over 6.3 kHz. The results indicate that the model is suitable for modelling small-scale, random irregularities with maximum sizes of between 3 cm and 6 cm.

Finally diffusion coefficient measurements have been carried out on a range of boundaries implemented using the *diffusing layer* method, which offers a similar approach to the *diffusing boundary* method but which has been designed in such a way that an inherent error found in the design theory of the *diffusing boundary* technique is removed. The results show that this method results in a more dynamic control over the modelled boundary diffusion under the same test conditions, with the maximum diffusion coefficient value measured for this model being greater by 7%. For a sampling frequency of 44.1 kHz and using a DWM of triangular topology, this model is most effective for frequencies over 5 kHz, indicating that the model

is suitable for modelling small-scale, random irregularities with maximum sizes of between 3 cm and 8 cm. It has also been shown that by adapting the model so that more than one single diffusing layer is applied, the model becomes effective for frequencies lower than 4 kHz and the diffusion bandwidth of the model can be increased.

In order to study the effect of the mesh update frequency on the diffusing layer approach, diffusion coefficient measurements have been performed on implementations of the diffusing models at sampling frequencies of both 22.05 kHz and 33.075 kHz. The results show that the frequency dependent diffuse characteristics of the model are dependent on the update frequency of the mesh. For the case where the update frequency of the mesh is 22.05 kHz, the model is most effective for frequencies above 2 kHz, and for the case where the update frequency of the mesh is 33.075 kHz, the model is most effective above 4 kHz. The results indicate that the lower cut-off frequency of the diffusion bandwidth of the model decreases as the sample rate decreases. A useful subject for future work would be to create a detailed bank of diffusion coefficient measurement data using single, double and triple layer diffusion models implemented at a range of commonly used update frequencies (for example 22.04 kHz, 44.1 kHz and 88.2 kHz). This data could then be used as a reference when choosing the particular diffusing layer implementation that matches the diffuse reflection characteristics that are desired in the model. The change in diffusion effect of the model with the mesh update frequency would therefore be taken into consideration.

The diffusing layer model has also been implemented in a rectilinear 2-D mesh with a sampling rate of 44.1 kHz and the results have been presented and directly compared with the results obtained using the triangular 2-D mesh with the same update frequency. The results show a close match in diffusion coefficient data between the two models, although differences are most apparent at frequencies above 6.3 kHz.

7.2 Further Investigation

7.2.1 Modal Analysis

A modal analysis technique designed to measure the diffusion characteristics of diffusers by measuring their effect on the impulse response of an acoustic system at the modal frequencies has been described and applied to both the diffusing boundary and diffusing layer models. Both models are implemented in identical DWM structures of triangular topology and with update frequencies of 44.1 kHz. When subject to this analysis, the diffusing layer approach displays greater consistency in terms of its effect on the modal frequencies of the DWM structure over the range of frequencies. This difference in consistency between the two models can be explained by the error found in the design theory of the diffusing boundary approach.

7.2.2 Early Reflection Testing

Analysis of the effect of the diffusing layer model on the early reflections of an impulse response, measured in a 2-D DWM, show that their timing is not effected. The energy found in the resulting early reflections is also slightly reduced as a result of the diffuse reflections, which is in agreement with what would be expected [9].

7.2.3 Effect on Boundary Absorption

A concern for the diffusing boundary and diffusing layer techniques is the potential effect that the models have on the implementation of boundary absorption in the DWM. Tests have been designed to investigate this issue and have been carried out on a range of diffusion models implemented using a 2-D triangular DWM with an update frequency of 44.1 kHz. The results show a potential attenuation in the effectiveness of the boundary absorption implementations that increases with the modelled diffusion for the diffusing layer and diffusing boundary techniques. The validity of these tests is questionable however, and further work is required to fully investigate this.

7.3 An Alternative Investigation into Boundary Diffusion

When placed in an acoustic system, diffusing boundaries exhibit a number of *macroscopic* effects which are made evident when impulse responses of the system are obtained. Evidence of this, for example, is made clear by the use of diffusing surfaces to alter the acoustical characteristics of a concert hall or music studio for aesthetic reasons. Examples of the use of professional diffusing panels in concert halls include the Carnegie Hall in New York, USA and the Fritz Philips Muziekcentrum in Eindhoven, the Netherlands [158]. In the absence of standard measurement and characterisation procedures for these macroscopic effects, a simple test has been designed to characterise the diffusive effect of diffusion models based on their effect on the reverberation characteristics of a simple room. Results are measured for the diffusing layer model, implemented in the 2-D digital waveguide mesh, and show a pattern of frequency dependency in the model that is in close agreement with that indicated by the diffusion coefficient measurements. The test has also been applied to the diffusing layer model implemented in the 3-D digital waveguide mesh of rectilinear topology and with an update frequency of 44.1 kHz, and the results indicate that this implementation of the diffusing layer approach is most effective in the 4 kHz third octave band.

7.4 Audio Demonstration

A very clear demonstration of the effect of the implementation of diffusing layer models in both the 2-D triangular DWM and the 3-D rectilinear DWM has also been provided, where the quality of the reverberant sound is significantly altered, and the comb filter effect caused by strong modal frequencies is significantly reduced, resulting in a more natural reverberant sound.

7.5 Conclusion

The study of diffuse acoustic boundaries is a highly active area of research in the general field of acoustics, and much of the work in this thesis has only been made possible thanks to recent developments. For example, the AES Information Document describing the diffusion coefficient was first published as recently as 2001.

The importance of the accurate modelling of diffusing boundaries in room acoustic modelling is widely accepted, however publication related to this issue in the Digital Waveguide Mesh has so far been limited. Part of the aim of this thesis has been to further the development of previous work and bring it together, and at the same time to work towards a standard analysis technique for measuring and quantifying the diffuse effect of boundary diffusion models in the DWM, and also to expose any issues that were brought to light during the process. In particular, problems were found when attempts were made to measure the *macroscopic* effect of diffuse boundary models on room acoustic attributes such as reverberation time, which are important considerations when the aim is to design a model that accurately reflects the behaviour of diffuse boundaries in the real world. These aims have been met with the successful implementation of a number of tests, and a selection of boundary diffusion models have been analysed in detail and their diffusive effects, as well as potential issues, have been explored. Results have been presented in a consistent format so different diffusion models can be directly compared.

A particular focus for the diffusing boundary testing and measurements has been a new diffuse boundary model, the *diffusing layer*, and this has been described in detail in this thesis. The aim of this approach is to provide a statistical method to implement boundary diffusion and such a model is required for certain reasons, which have been previously explained, relating to the complexity of the small-scale surface roughness found in everyday real world boundaries. The results show that this is a successful and effective model, but also reveal certain problems that need to be accounted for. This model has been implemented in the 2-D triangular DWM, the 2-D rectilinear DWM and also the 3-D rectilinear DWM and has been shown to require a relatively small amount of computational resources during simulation in comparison to that required by the entire DWM.

7.6 Future Work

The diffusion coefficient provides a useful and concise method to characterise the diffuse effects of diffuse boundary models. The models presented in this thesis are designed using a range of approaches, however their behaviour is difficult to accurately predict. For this reason, a useful approach in future work is in the

acquisition of diffusion coefficient data for a range of different diffusing boundary models including those presented in this thesis and diffusing boundary models that are designed and implemented in later work. This collection of data can then be used as a reference when implementing diffuse boundaries in DWM acoustic models. In this way the diffuse boundary with the associated diffusion coefficient data that best reflects the diffusion coefficient data of the intended surface to be modelled can be employed. The diffusing layer model and its variants have been shown to give a wide range of diffusing characteristics according to measured diffusion coefficient data and it is hoped that they can be used to model a wide range of real world surfaces in the future.

An important issue not considered in detail in this thesis and that needs to be further investigated is the effect of the orientation of the DWM with respect to the diffusing boundary. This can be achieved by performing repeated diffusion coefficient measurements using the same test geometry, but rotating the mesh orientation for each test.

The information and theory required to extend the diffusion coefficient tests to the 3-D digital waveguide mesh has been provided in this thesis and an important next step is to implement these tests. Given time, and the constant increase in computer technology, the implementation of large 3-D DWM structures is an increasing possibility and the importance of diffuse boundaries in such models needs to be considered. Implementation of diffusion models and tests for the acquisition of diffusion coefficient data in 3-D DWM structures is therefore an essential requirement in future research.

A further goal is to better explore and understand the effect of the diffusing boundary and diffusing layer models on boundary absorption, for example by implementing the models in a specific boundary absorption test scenario such as that described in [142]. Once a better understanding is achieved, the next step is to compensate for any undesirable effects, for example by the use of appropriate filters.

In general terms the goal of future research is to concentrate on the implementation of a further selection of new and improved diffuse boundary models in the DWM which employ a wide range of techniques depending on the type of boundary they are designed to model. It is hoped that alongside the current improvements

in the understanding of diffusing boundaries and their importance in the field of acoustics, the issue of modelling diffuse boundaries in the DWM can ultimately be successfully resolved, and that this will greatly enhance the use of the DWM approach as an accurate acoustical modelling tool.

Appendix A

Mathematical Derivation

A.1 The d'Alambert Solution of the 1-D Wave Equation

The one-dimensional wave equation is given as follows:

$$\frac{\partial^2 \xi(x, t)}{\partial t^2} = c^2 \frac{\partial^2 \xi(x, t)}{\partial x^2} \quad (\text{A.1})$$

In order to achieve the d'Alambert's Solution to the one-dimensional wave equation, two new variables $\zeta = t - x/c$ and $\eta = t + x/c$ are introduced, such that:

$$\xi(x, t) = \xi(\zeta, \eta) = \xi(\zeta(x, t), \eta(x, t)) \quad (\text{A.2})$$

Applying the chain rule, the partial derivatives of the function ξ in terms of x and t are expressed in terms of ζ and η as follows:

$$\begin{aligned} \frac{\partial \xi}{\partial x} &= \frac{\partial \zeta}{\partial x} \frac{\partial \xi}{\partial \zeta} + \frac{\partial \eta}{\partial x} \frac{\partial \xi}{\partial \eta} \\ &= \frac{\partial \xi}{\partial \zeta} + \frac{\partial \xi}{\partial \eta} \end{aligned} \quad (\text{A.3})$$

$$\begin{aligned} \frac{\partial \xi}{\partial t} &= \frac{\partial \zeta}{\partial t} \frac{\partial \xi}{\partial \zeta} + \frac{\partial \eta}{\partial t} \frac{\partial \xi}{\partial \eta} \\ &= -c \frac{\partial \xi}{\partial \zeta} + c \frac{\partial \xi}{\partial \eta} \end{aligned} \quad (\text{A.4})$$

The second order derivatives are calculated as follows:

$$\begin{aligned}
 \frac{\partial^2 \xi}{\partial x^2} &= \frac{\partial}{\partial x} \left(\frac{\partial \xi}{\partial x} \right) \\
 &= \frac{\partial \zeta}{\partial x} \frac{\partial}{\partial \zeta} \left(\frac{\partial \xi}{\partial x} \right) + \frac{\partial \eta}{\partial x} \frac{\partial}{\partial \eta} \left(\frac{\partial \xi}{\partial x} \right) \\
 &= \frac{\partial}{\partial \zeta} \left(\frac{\partial \xi}{\partial \zeta} + \frac{\partial \xi}{\partial \eta} \right) + \frac{\partial}{\partial \eta} \left(\frac{\partial \xi}{\partial \zeta} + \frac{\partial \xi}{\partial \eta} \right) \\
 &= \frac{\partial^2 \xi}{\partial \zeta^2} + 2 \frac{\partial^2 \xi}{\partial \zeta \partial \eta} + \frac{\partial^2 \xi}{\partial \eta^2}
 \end{aligned} \tag{A.5}$$

$$\begin{aligned}
 \frac{\partial^2 \xi}{\partial t^2} &= \frac{\partial}{\partial t} \left(\frac{\partial \xi}{\partial t} \right) \\
 &= \frac{\partial \zeta}{\partial t} \frac{\partial}{\partial \zeta} \left(\frac{\partial \xi}{\partial t} \right) + \frac{\partial \eta}{\partial t} \frac{\partial}{\partial \eta} \left(\frac{\partial \xi}{\partial t} \right) \\
 &= \frac{\partial}{\partial \zeta} \left(-c \frac{\partial \xi}{\partial \zeta} + c \frac{\partial \xi}{\partial \eta} \right) + \frac{\partial}{\partial \eta} \left(-c \frac{\partial \xi}{\partial \zeta} + c \frac{\partial \xi}{\partial \eta} \right) \\
 &= c^2 \frac{\partial^2 \xi}{\partial \zeta^2} - 2c^2 \frac{\partial^2 \xi}{\partial \zeta \partial \eta} + c^2 \frac{\partial^2 \xi}{\partial \eta^2}
 \end{aligned} \tag{A.6}$$

Substituting (A.5) and (A.6) into the one-dimensional wave equation (A.1) gives:

$$\frac{\partial^2 \xi}{\partial \zeta^2} - 2 \frac{\partial^2 \xi}{\partial \zeta \partial \eta} + \frac{\partial^2 \xi}{\partial \eta^2} = \frac{\partial^2 \xi}{\partial \zeta^2} + 2 \frac{\partial^2 \xi}{\partial \zeta \partial \eta} + \frac{\partial^2 \xi}{\partial \eta^2} \tag{A.7}$$

Rearranging (A.7) gives:

$$\frac{\partial^2 \xi}{\partial \zeta \partial \eta} = 0 \tag{A.8}$$

Integrating the partial differential equation (A.8) first with respect to ζ and then with respect to η gives the following general solution, where f and g are arbitrary functions of ζ and η respectively:

$$\xi(\zeta, \eta) = f(\zeta) + g(\eta) \tag{A.9}$$

Expressing ζ and η in terms of x , c and t gives:

$$\xi(x, t) = \xi^+(x - ct) + \xi^-(x + ct) \tag{A.10}$$

In this equation, ξ^+ and ξ^- are arbitrary functions representing waves travelling in positive and negative directions, respectively, along the x axis.

Appendix B

Software Implementation

Figure B.1 describes the core of the software used to create all results in this thesis.

A description of each method follows.

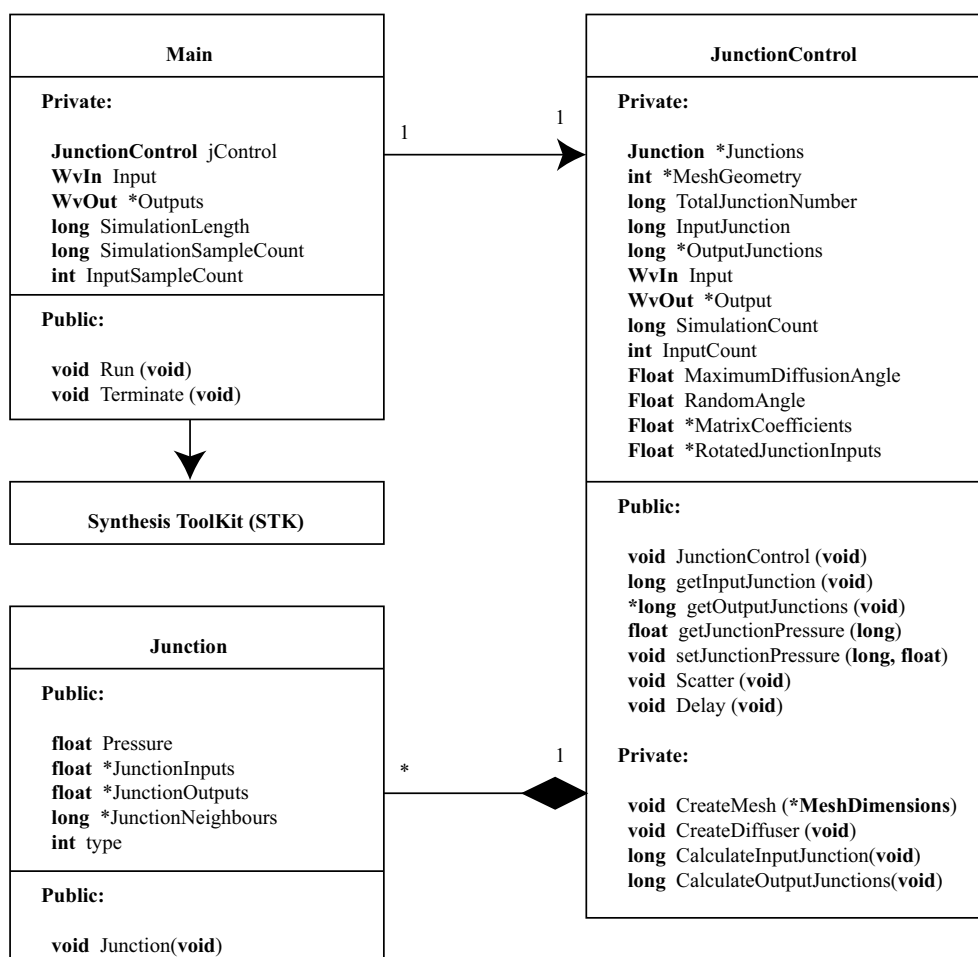


Figure B.1: A class diagram describing the core of the software used to create all results in this thesis.

B.1 Class Description

B.1.1 Main Class

This class controls the simulation. **WvIn** and **WvOut** are member classes of the **Synthesis ToolKit (STK)** open source library for audio signal processing and algorithmic synthesis [159]. The **WvIn** class is used to read a pre-prepared impulse sample in a Microsoft WAV format and convert it to data of type **float**. The **WvOut** class is used to convert float data to a number of output files in Microsoft WAV format which are then used for analysis.

void Run(void)

The Run method consists of a loop that continues until the simulation length is reached. In each loop, the *scatter* and *delay* methods from an instance of the **JunctionControl** class are called. Other methods are called to send or receive sample data from the **JunctionControl** instance.

void Terminate(void)

This method is used to terminate the program, to delete class instances and to finalise the wave output data file. It is called when the program is terminated by the user, or when the simulation has finished.

B.1.2 JunctionControl Class

The **JunctionControl** class controls the initial creation of the mesh by creating and controlling multiple instances of the class **Junction**. Each instance of **Junction** represents a DWM junction and is assigned a position in the mesh in relation to neighbouring junctions. This class also controls the scattering process at each junction according to the three scattering equations (4.20), (4.21) and (4.23). Prior to compiling and running the program, the private methods are edited accordingly, depending on the specific test requirements.

void JunctionControl(void)

The constructor method is used to create the mesh structure, a diffuser object if required and the necessary number of instances of the **Junction** class by calling the private methods *CreateMesh*, *CreateDiffuser*, *CalculateInputJunctions* and *CalculateOutputJunctions*. Junctions are indexed by numerical value and their locations in virtual space are mapped here. These private methods are adjusted and tested before the program is run, depending on the specific test that is being performed. Integer values relating to the specific junctions that are assigned as inputs and outputs are also determined here.

long getInputJunction(void)

This method is used to return the numerical value relating to the junction which is used to inject an excitation into the mesh.

***long getOutputJunctions(void)**

Returns a pointer to an array of numerical index values relating to the junctions which are used to determine an output from the mesh.

long getJunctionPressure(long)

Returns the current Pressure value of a specified junction, determined by its index value.

void setJunctionPressure(long, float)

Takes a value and adds it to the current Pressure value of a specified junction.

void Scatter(void)

Implement scattering equations (4.20) and (4.23) at all junctions.

void Delay(void)

Implement scattering equation (4.21) at all junctions.

void CreateMesh(*MeshGeometry)

Takes a list of values relating to the required geometry of the mesh and creates an array of the class **Junction**. Initial values for each junction are set here.

void CreateDiffuser(void)

Places a diffuser object in the DWM. This method is for the diffusion coefficient measurements specifically and is only called if required. The shape and type of diffuser is defined here. Junction values can be overridden by this method.

void CalculateInputJunction(void)

Determines the value relating to the junction which will be used to excite the mesh.

void CalculateOutputJunctions(void)

Determines the value relating to the junctions which will be used to create signal outputs from the mesh.

B.1.3 Junction Class

Each instance of this class represents a junction in the DWM. The data that is held is the current Pressure value, a list of input pressure values, a list of output pressure values a corresponding to the instances of the same class that are direct neighbours of the junction and finally an integer corresponding to the junction *type*. The type integer is used to set whether the junction is a boundary junction, a normal non-boundary junction, a diffusing junction, an input junction or an output junction.

void Junction(void)

The constructor method simply creates an instance of the class and sets all values to a default of zero.

B.2 Software Testing

Before each simulation, a number of tests are carried out in order to ensure that the model has been correctly implemented:

- Each model used for testing is run over 12,000 samples both with and without diffusion models applied with output points positioned at random locations. These outputs are analysed in order to check that the early reflections are correctly timed and that the observed modal frequencies are equal to calculated modal frequencies for the system. Figure B.2 shows an example low frequency analysis of a test output from the 2-D DWM system used to measure diffusion coefficients for a flat plane boundary. The mesh in this case has a width of 19.05 m and a length of 22.00 m and is constructed from a triangular topology. Theoretical modal frequencies have been calculated, with dispersion error taken into account, and these frequencies have been marked on the graph in the form of vertical dotted lines. In order to calculate the dispersion error in the triangular DWM, the same function is assumed for all directions of wave travel within the mesh. The average dispersion over 1000 directions evenly distributed around the circle is taken in order to achieve this function. This is not a good approach for tests involving the rectilinear DWM however (see section 4.4.6). For the case of the rectilinear mesh, only room modes are considered at relative frequencies (f/f_{update}) of less than 0.1, which have a small dispersion error (less than 1 %).

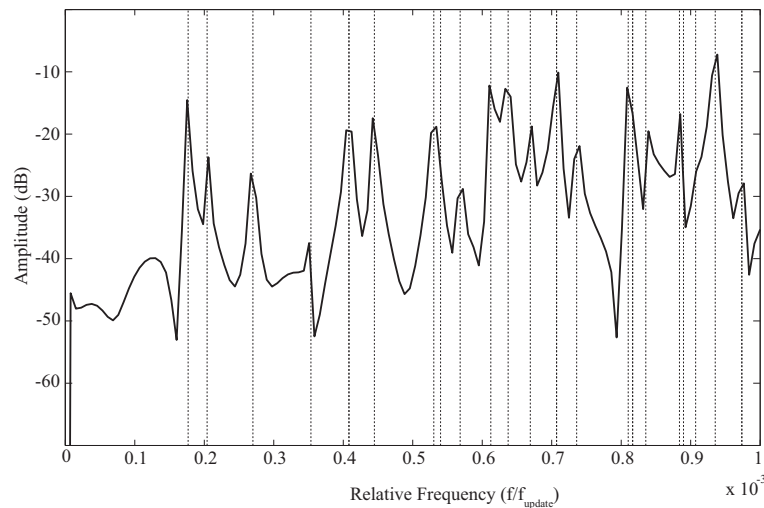


Figure B.2: Frequency Analysis of test output with the lowest 26 modal frequencies marked on.

- The test output signal is also checked for stability, and in the case where no boundary filters are implemented, it is checked to confirm that it is lossless. In order to do this, the root mean square of the signal between the 4000th

sample and the 8000th sample is taken and compared to the root mean square of the signal between the 8000th sample and the 12000th sample. An increase in more than 5 dB implies that there is a stability error in the model. Likewise, if no boundary filters are implemented, a decrease of more than 5 dB implies an error in the model, or that it is not lossless.

- Code displaying wave propagation in the mesh using computer graphics is implemented, and the mesh behaviour is checked visually during the mesh simulation. Figure B.3 shows a selection of screen shots taken during a diffusion coefficient measurement simulation for a flat plane boundary. The incident angle of the source signal relative to the normal of the boundary panel under test is -60° . Diffraction effects caused by the edges of the surface can clearly be seen in this example, as can the concentration of the reflected energy from the diffuser in the specular direction of travel.

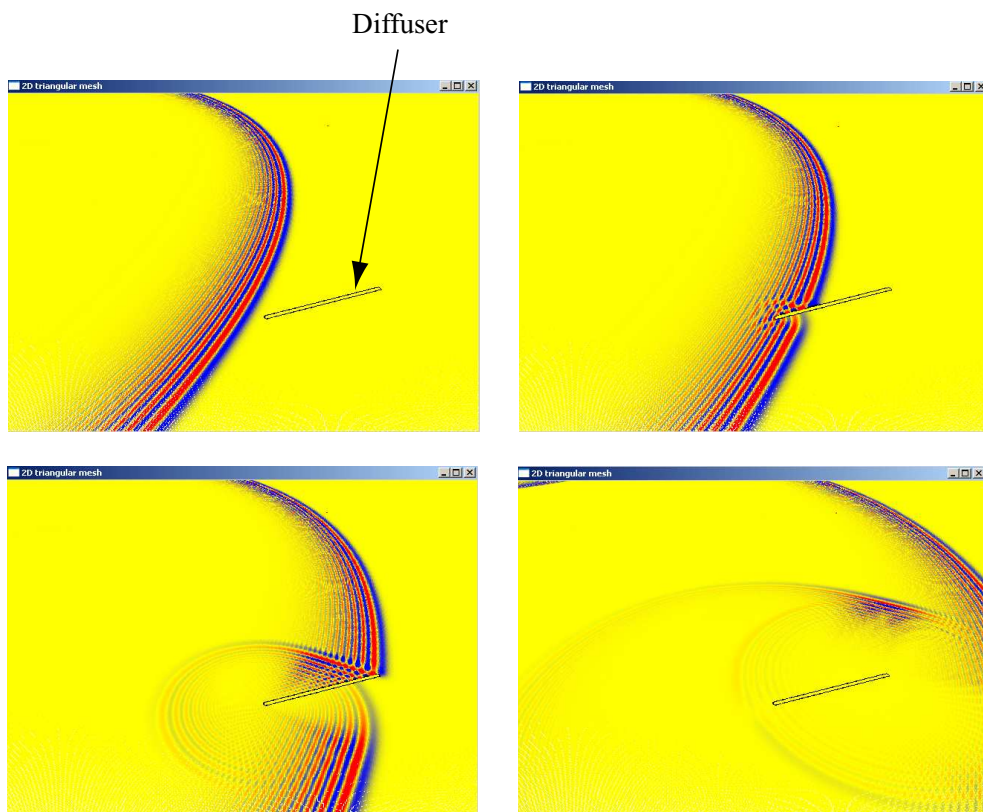


Figure B.3: Screen shots showing wave propagation during diffusion coefficient measurement simulation for a flat plane boundary, with an incident angle of -60° .

- Each simulation is run three times to ensure the results are consistent.

Appendix C

Accompanying CD-ROM

C.1 Directory Structure

Figure C.1 describes the directory structure and location of all files contained in the attached CD-ROM. The CD-ROM itself is labelled *Thesis_SBS*.

The directory **Auditory_Examples** contains all the listening demonstrations from the simulations described in section 6.10. The samples for both the 2-D and 3-D DWM simulations are split into two directories. All files in the directories entitled **R.04** were created using DWMs with the reflection coefficient r set to a value of 0.4, and similarly all files in the directories entitled **R.095** were created using DWMs with the reflection coefficient r set to a value of 0.95. Each file is in Microsoft WAVE format and its name describes the conditions used in its production. The first word in the file names refers to the *Sample Name* of the sample that is processed using the DWM impulse response and the second word after the underscore refers to the reflection coefficient used in the simulation. The next term in the name determines whether the sample was created using a 2-D mesh (2D) or a 3-D mesh (3D). In the final term (**DL_XX**) XX represents the maximum angle of diffusion used in the diffusion model which was implemented in order to create that particular sample, where $XX = 00, 15, 30 \dots 90$.

The files found in the folder **Test_Outputs** are the diffuser impulse responses calculated from the outputs of the simulations used to obtain the diffusion coefficients and results found in section 6.3. For each different diffuser implementation, the output wave files from the simulation are divided into folders named **Input_II** where $II = -80, -70, -60 \dots +80, +90$ is the incident angle (in degrees) of the input

used to obtain the impulse response. To save space on the CD-ROM only the results from half of the input incident angles are included in the cases where the diffusers are perfectly symmetrical. Within each of these folders the output files can be found for angles of reflection covering the whole semicircle with respect to the diffuser. The output files are named **Output_***JJ***.wav** where $JJ = -90, -85, -80 \dots +85, +90$ is the angle of reflection (in degrees) of the output. All files are in Microsoft WAVE format.

The names of the folders containing the test results for each of the different diffuser implementations is determined according to the naming convention described in section 6.3 and should be self explanatory.

An electronic copy of the thesis in pdf format, named *thesis.pdf*, is also included on the CD-ROM. This may be useful for reference.

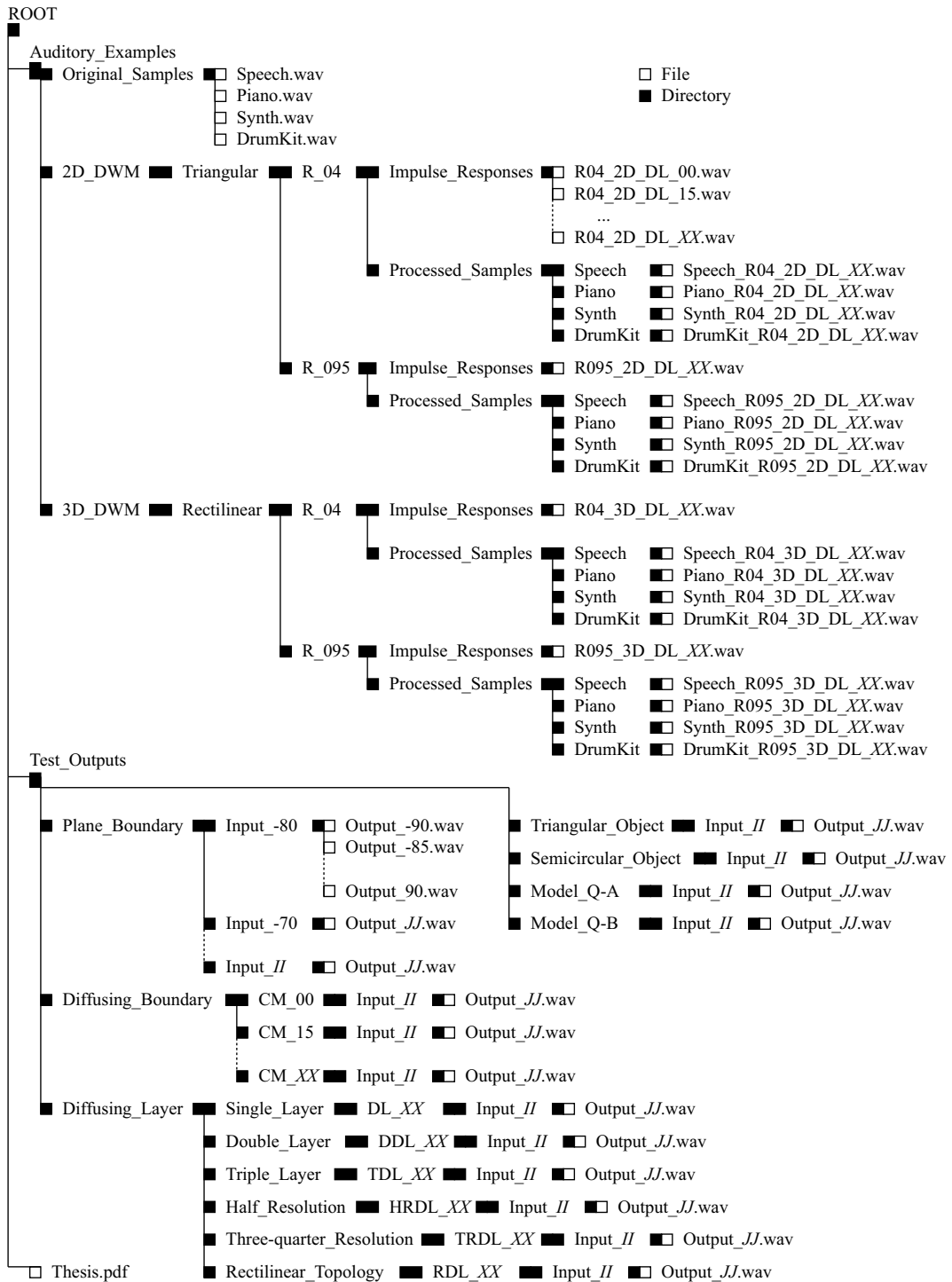


Figure C.1: Diagram describing the directory structure and location of files contained in the attached CD-ROM.

Bibliography

- [1] S. Shelley and D. T. Murphy, "Measuring diffusion in a 2-D digital waveguide mesh," in *Proceedings of the 8th International Conference on Digital Audio Effects (DAFx'05)*, Madrid, Spain, September 2005, pp. 249–253.
- [2] —, "Diffusion modelling at the boundary of a digital waveguide mesh," in *Proceedings of the 13th European Signal Processing Conference*, Antalya, Turkey, September 2005.
- [3] D. Murphy, A. Kelloniemi, J. Mullen, and S. Shelley, "Acoustic modeling using the digital waveguide mesh," in *IEEE Signal Processing Magazine*, vol. 24(2), 2007, pp. 55–66.
- [4] J. Mullen, "Physical modelling of the vocal tract with the 2D digital waveguide mesh," Ph.D. dissertation, University Of York, UK, 2006. [Online]. Available: <http://www-users.york.ac.uk/%7Edtm3/Download/JackThesis.pdf>
- [5] J. O. Smith, "Physical modeling using digital waveguides," in *Computer Music Journal*, vol. 16(4), Winter 1992, pp. 74–87.
- [6] —, *Principles of digital waveguide models of musical instruments*, M. Kahrs and K. Brandenburg, Eds. Boston, USA: Kluwer Academic Publishers, Boston/Dordrecht/London, 1998.
- [7] M. Kleiner, B.-I. L. Dalenbäck, and P. Svensson, "Auralization - an overview," in *Journal of the Audio Engineering Society*, vol. 41(11), November 1993, pp. 861–875.
- [8] D. E. Hall, *Musical Acoustic, An Introduction*. Wadsworth, 1980.
- [9] B.-I. Dalenbäck, M. Kleiner, and P. Svensson, "A macroscopic view of diffuse reflection," in *Proceedings of the 95th Audio Engineering Society Convention*, New York, October 1993, Preprint No. 3726.
- [10] M. R. Schroeder, "Binaural dissimilarity and optimum ceilings for concert halls: More lateral sound diffusion," in *Journal of the Acoustical Society of America*, vol. 65(4), 1979, pp. 958–963.
- [11] Kuttruff, *Room Acoustics*, 4th ed. UK: Taylor and Francis, 2000.
- [12] J. A. S. Angus, A. C. Marvin, J. Clegg, J. Dawson, and A. Knobloch, "The effect of acoustic diffusers on room mode decay," in *Proceedings of the 99th convention of the Audio Engineering Society*, New York, October 1995, Preprint No. 4116.

- [13] *Acoustics - Sound-scattering properties of surfaces - Part 1: Measurement of the random-incidence scattering coefficient in a reverberation room*, International Organization for Standardization Std. ISO 17 497-1:2004, 2004.
- [14] *AES information document for room acoustics and sound reinforcement systems – Characterization and measurement of surface scattering uniformity*, Audio Engineering Society Std. AES-4id-2001, 2001.
- [15] T. J. Cox, B.-I. L. Dalenbäck, P.D’Antonio, J. J. Embrechts, J. Y. Jeon, E. Mommertz, and M. Vorländer, “A tutorial on scattering and diffusion coefficients for room acoustic surfaces,” in *Acta Acustica united with Acustica*, vol. 92(1), 2006, pp. 1–15.
- [16] A. Krokstad, S. Strøm, and S. Sørsdal, “Calculating the acoustical room response by the use of a ray tracing technique,” in *Journal of Sound Vibration*, vol. 8(1), 1968, pp. 118–125.
- [17] J. B. Allen and D. A. Berkley, “Image method for efficiently simulating small-room acoustics,” in *Journal of the Acoustical Society of America*, vol. 65(4), April 1979, pp. 943–950.
- [18] L. Savioja, “Modeling techniques for virtual acoustics,” Ph.D. dissertation, Helsinki University of Technology, Espoo, Finland, 1999.
- [19] M. J. Beeson and D. T. Murphy, “Roomweaver: A digital waveguide mesh based room acoustics research tool,” in *Proceedings of the Conference on Digital Audio Effects (DAFx-04)*, Naples, Italy, October 2004, pp. 268–273.
- [20] D. T. Murphy and D. M. Howard, “2-D digital waveguide mesh topologies in room acoustics modelling,” in *Proceedings of the Cost G-6 Conference on Digital Audio Effects*, Verona, Italy, December 2000, pp. 211–216.
- [21] G. Campos and D. M. Howard, “A parallel 3-D digital waveguide mesh model with tetrahedral topology for room acoustic simulation,” in *Proceedings of the COST G-6 Conference on Digital Audio Effects (DAFX-00)*, Verona, Italy, December 2000, pp. 73–78.
- [22] A. Kelloniemi, P. Huang, V. Välimäki, and L. Savioja, “Hyper-dimensional digital waveguide mesh for reverberation modeling,” in *Proceedings of the 10th International Conference on Digital Audio Effects (DAFx-07)*, Bordeaux, France, September 2007, pp. 109–116.
- [23] S. A. V. Duyne and J. O. Smith, “Physical modeling with the 2-D digital waveguide mesh,” in *Proceedings of the International Computer Music Conference*, Tokyo, Japan, 1993, pp. 40–47.
- [24] A. Kelloniemi, V. Välimäki, and L. Savioja, “Simulation of room acoustics using 2-D digital waveguide meshes,” in *Proceedings of the IEEE International Conference in Acoustics, Speech and Signal Processing*, vol. 5, Toulouse, France, May 2006, pp. 313–316.
- [25] M. Hodgson, “Evidence of diffuse surface reflections in rooms,” in *Journal of the Acoustical Society of America*, vol. 89(2), February 1991, pp. 765–771.

- [26] I. Bork, "Simulation and measurement of auditorium acoustics - the round robins on room acoustical simulation," in *Proceedings of the Institute of Acoustics*, vol. 24(4), 2002.
- [27] S. Siltanen, T. Lokki, S. Kiminki, and L. Savioja, "The room acoustic rendering equation," in *Journal of the Acoustical Society of America*, vol. 122(3), 2007, pp. 1624–1635.
- [28] H. Kuttruff, "Simulierte nachhallkurven in rechteckraumen mit diffusem schallfeld," in *Acustica*, vol. 25, 1971, pp. 333–342.
- [29] K. Lee and J. O. Smith, "Implementation of a highly diffusing 2-D digital waveguide mesh with a quadratic residue diffuser," in *Proceedings of the International Computer Music Conference (ICMC)*, Miami, Florida, November 2004, pp. 309–315.
- [30] J. Laird, P. Masri, and N. Canagarajah, "Modelling diffusion at the boundary of a digital waveguide mesh," in *Proceedings of the International Computer Music Conference*, Hong Kong, October 1999, pp. 492–495.
- [31] D. M. Howard and J. Angus, *Acoustics and Psychoacoustics*. Focal Press, 1996.
- [32] L. E. Kinsler, A. R. Frey, A. B. Coppens, and J. V. Sanders, *Fundamentals of Acoustics*. John Wiley and Sons, Inc., 2000.
- [33] W. A. Yost, *Fundamentals of Hearing: An Introduction*. California, USA: Academic Press,, 2000.
- [34] *Acoustical Terminology*, American National Standards Institute Std. ANSI S1.1-1994, 1994.
- [35] M. L. Davis and S. J. Masten, *Principles of Environmental Engineering and Science*. New York: McGraw-Hill Companies, Inc., 2002.
- [36] F. A. Everest, *Master Handbook of Acoustics*. McGraw-Hill, 2001.
- [37] V. O. Knudsen and C. M. Harris, *Acoustical Designing in Architecture*. New York, USA: John Wiley and Sons Ltd, 1950.
- [38] C. Harris, "Absorption of sound in air versus humidity and temperature," in *Journal of the Acoustical Society of America*, vol. 40(1), jul 1966, pp. 148–159.
- [39] *Acoustics – Attenuation of Sound During Propagation Outdoors – Part 1: Calculation of the Absorption of Sound by the Atmosphere.*, International Organization for Standardization Std. ISO 9613-1:1993, 1993.
- [40] e. A. Isaacs, *A Concise Dictionary of Physics*. New York: Oxford University Press, 1990.
- [41] P. H. Parkin, H. R. Humphreys, and J. R. Cowell, *Acoustics, Noise and Buildings*, 4th ed. London, UK and Boston, USA: Faber and Faber, 1979.
- [42] M. Born and E. Wolf, *Principles of Optics*. Cambridge, UK: Cambridge University Press, 1999.
- [43] P. Haughton, *Acuostics for Audiologists*. Emerald Group Publishing, 2002.

- [44] T. J. Cox and P. D'Antonio, *Acoustic Absorbers and Diffusers: Theory, Design and Application*. Oxon: Spon Press, 2004.
- [45] D. Chu and T. Stanton, "Application of twerskys boss scattering theory to laboratory measurements of sound scattered by a rough surface," in *Journal of the Acoustical Society of America*, vol. 87(4), April 1990, pp. 1557–1568.
- [46] T. J. Cox and P. DAntonio, "Fractal sound diffusers," in *Proceedings of the 103rd Convention of the Audio Engineering Society*, vol. preprint 4578, New York, 1997, pp. Paper K-7.
- [47] J. J. Embrechts, D. Archambeau, and G. B. Stan, "Determination of the scattering coefficient of random rough diffusing surfaces for room acoustics applications," in *Acta Acustica united with Acustica*, vol. 87, 2001, pp. 482–494.
- [48] H. Nironen, "Diffuse reflections in room acoustic modelling," Master's thesis, Helsinki University of Technology, Finland, 2004.
- [49] J. J. Embrechts, "Broad spectrum diffusion model for room acoustics ray-tracing algorithms," in *Journal of the Acoustical Society of America*, vol. 107(4), April 2000, pp. 2068–2081.
- [50] M. R. Schroeder, "Diffuse sound reflection by maximum-length sequence," in *Journal of the Acoustical Society of America*, vol. 57(1), 1975, pp. 149–150.
- [51] P. D'Antonio and J. Konnert, "The reflection phase grating diffusor: Design theory and application," in *Journal of the Audio Engineering Society*, vol. 32(4), 1984, pp. 228–238.
- [52] Y. Ando, *Concert Hall Acoustics*. Springer-Verlag, 1985.
- [53] T. J. Cox and Y. W. Lam, "Prediction and evaluation of the scattering from quadratic residue diffusors," in *Journal of the Acoustical Society of America*, vol. 95(1), 1994, pp. 297–305.
- [54] W. R. T. Tenkate, "On the bandwidth of diffusors based upon the quadratic residue sequence," in *Journal of the Acoustical Society of America*, vol. 98(5), 1995, pp. 2575–2579.
- [55] T. J. Hargreaves, T. J. Cox, Y. W. Lam, and P. D'Antonio, "Surface diffusion coefficients for room acoustics: Free field measures," in *Journal of the Acoustical Society of America*, vol. 108(4), 2000, pp. 1710–1720.
- [56] J. H. Rindel, "Attenuation of sound reflections due to diffraction," in *Proceedings of the Nordic Acoustical Meeting*, Aalborg, 1986, pp. 257–260.
- [57] M. Vorländer and E. Mommertz, "Definition and measurement of random-incidence scattering coefficients," in *Applied Acoustics*, vol. 60(2), 2000, pp. 187–200.
- [58] *Acoustics - Measurement of sound absorption in a reverberation room.*, International Organization for Standardization Std. ISO 354:1985, 1985.

- [59] E. Mommertz and M. Vorländer, "Measurement of scattering coefficients of surfaces in the reverberation chamber and in the free field," in *Proceedings of the 15th International Congress on Acoustics (ICA95)*, vol. 60(2), Trondheim, 2000, pp. 187–200.
- [60] M. H. A. Gomez, M. Vorländer, and S. N. Y. Gerges, "Aspects of the sample geometry in the measurement of the random-incidence scattering coefficient," in *Forum Acusticum*, Sevilla, 2002, RBA-06-2002-IP.
- [61] T. J. Cox, "Predicting the scattering from reflectors and diffusers using 2d boundary element methods," in *Journal of the Acoustical Society of America*, vol. 96(2), 1994, pp. 874–878.
- [62] T. J. Hargreaves, "Acoustic diffusion and scattering coefficients for room surfaces," Ph.D. dissertation, University of Salford, 2000.
- [63] T. J. Cox and Y. W. Lam, "Evaluation of methods for predicting the scattering from simple rigid panels," in *Applied Acoustics*, vol. 40, 1993, pp. 123–140.
- [64] E. Mommertz, "Determination of scattering coefficients from reflection directivity of architectural surfaces," in *Applied Acoustics*, vol. 60(2), 2000, pp. 201–204.
- [65] D. A. J. J. Embrechts and G. B. Stan, "Determination of the scattering coefficient of random rough diffusing surfaces for room acoustics applications," in *Acta Acustica united with Acustica*, vol. 87, 2001, pp. 482–494.
- [66] J. D. Polack, X. Meynial, and V. Grillon, "Auralization in scale models: Processing of impulse response," in *Journal of the Audio Engineering Society*, vol. 41(11), November 1993, pp. 939–945.
- [67] B. M. Gibbs and D. K. Jones, "A simple image method for calculating the distribution of sound pressure levels within an enclosure," in *Acustica*, vol. 26, 1972, pp. 24–32.
- [68] J. Borish, "An extension of the image model to arbitrary polyhedra," in *Journal of the Acoustical Society of America*, vol. 75(6), June 1984, pp. 1827–1836.
- [69] U. R. Kristiansen, A. Krokstad, and T. Follestad, "Extending the image method to higher-order reflections," in *Applied Acoustics*, vol. 38, 1993, pp. 195–206.
- [70] U. Stephenson, "Comparison of the mirror image source method and the sound particle simulation method," in *Applied Acoustics*, vol. 29, 1990, pp. 35–72.
- [71] U. Svensson, R. Fred, and J. Vanderkooy, "Analytic secondary source model of edge diffraction impulse responses," in *Journal of the Acoustical Society of America*, vol. 106(5), 1999, pp. 2331–2344.
- [72] T. Lokki, P. Svensson, and L. Savioja, "An efficient auralization of edge diffraction," in *Proceedings of the AES 21st International Conference*, St. Petersburg, Russia, June 2002, pp. 166–172.

- [73] B.-I. Dalenbäck, "Room acoustic prediction and auralization based on an extended image source model," Ph.D. dissertation, Chalmers University of Technology, Gothenburg, Sweden, 1992.
- [74] B.-I. L. Dalenbäck, "Room acoustic prediction based on a unified treatment of diffuse and specular reflection," in *Journal of the Acoustical Society of America*, vol. 100(2), August 1996, pp. 899–909.
- [75] J. Borish, "Electronic simulation of auditorium acoustics," Ph.D. dissertation, Stanford University, 1984.
- [76] H. Kuttruff, "Auralization of impulse responses modeled on the basis of ray-tracing results," in *Journal of the Audio Engineering Society*, vol. 41(11), 1993, pp. 876–880.
- [77] A. Kulowski, "Algorithmic representation of the ray tracing technique," in *Applied Acoustics*, vol. 18, 1985, pp. 449–469.
- [78] M. Vorländer, "International round robin on room acoustical computer simulations," in *Proceedings of the 15th International Congress of Acoustics (ICA '95)*, Trondheim, Norway, June 1995, pp. 689–692.
- [79] I. Bork, "A comparison of room simulation software - the 2nd round robin on room acoustical computer simulation," in *Acta Acustica united with Acustica*, vol. 86, 2000, pp. 943–956.
- [80] C. L. Christensen and J. H. Rindel, "A new scattering method that combines roughness and diffraction effects," in *Journal of the Acoustical Society of America*, vol. 117(4), 2005, pp. 2499–2499.
- [81] A. Farina, "Ramsete - a new pyramid tracer for medium and large scale acoustic problems," in *Proceedings of EURO-NOISE 95 Conference*, Lyon, March 1995.
- [82] U. M. Stephenson, "Quantized pyramidal beam tracing - a new algorithm for room acoustics and noise immission prognosis," in *Acta Acustica united with Acustica*, vol. 82, 1996, pp. 517–525.
- [83] I. A. Drumm and Y. W. Lam, "The adaptive beam-tracing algorithm," in *Journal of the Acoustical Society of America*, vol. 107(3), March 2000, pp. 1405–1412.
- [84] T. Funkhouser, N. Tsingos, I. Carlbom, G. Elko, M. Sondhi, and J. West, "Modelling sound reflection and diffraction in architectural environments with beam tracing," in *Forum Acusticum*, Sevilla, September 2002.
- [85] R. R. Torres, U. P. Svensson, and M. Kleiner, "Computation of edge diffraction for more accurate room acoustics auralization," in *Journal of the Acoustical Society of America*, vol. 109(2), February 2001, pp. 600–610.
- [86] A. Farina, "Introducing the surface diffusion and edge scattering in a pyramid-tracing numerical model for room acoustics," in *Proceedings of the 108th Audio Engineering Society Convention (AES '00)*, Paris, France, February 2000, Preprint No. 5145.

- [87] M. F. Cohen, S. E. Chen, J. R. Wallace, and D. P. Greenberg, "A progressive refinement approach to fast radiosity image generation," in *ACM SIGGRAPH Computer Graphics*, vol. 22, no. 4. New York, USA: ACM, 1988, pp. 75–84.
- [88] M. Vorländer, "Simulation of the transient and steady-state sound propagation in rooms using a new combined ray-tracing/image-source algorithm," in *Journal of the Acoustical Society of America*, vol. 86(1), July 1989, pp. 172–178.
- [89] M. Monks, B. M. Oh, and J. Dorsey, "Acoustic simulation and visualization using a new unified beam tracing and image source approach," in *Proceedings of the Audio Engineering Society Convention*, Los Angeles, November 1996, pp. 153–174.
- [90] C. L. Christensen, *User's Manual of ODEON room acoustics program version 9.0*. Denmark: Brüel & Kjær, 2007.
- [91] Y. M. Lam, "On the parameters controlling diffusion calculation in a hybrid computer model for room acoustics prediction," in *Proceedings of the Institute of Acoustics (IoA)*, vol. 16(2), St Albans, UK, 1994, pp. 537–544.
- [92] C. L. Christensen, "Odeon - a design tool for auditorium acoustics, noise control and loudspeaker systems," in *Proceedings of Inst. of Acoustics, Reproduced Sound 17*, vol. 23(8), Stratford upon Avon, UK, November 2001, pp. 137–144.
- [93] CATT-acoustic software website. [Online]. Available: <http://www.catt.se>
- [94] J. R. Wright, "An exact model of acoustic radiation in enclosed spaces," in *Journal of the Audio Engineering Society*, vol. 43(10), October 2002, pp. 813–820.
- [95] M. Petyt, *Introduction to Finite Element Vibration Analysis*. Cambridge, UK: Cambridge University Press, 1990.
- [96] P. Macey, "Acoustic and structure interaction problems using finite and boundary elements," Ph.D. dissertation, Nottingham University, UK, 1987.
- [97] F. Ihlenberg, *Finite Element Analysis of Acoustic Scattering*. New York: Springer Verlag, 1998.
- [98] D. Colton and R. Kress, *Integral Equation Methods in Scattering Theory*. New York: Wiley, 1983.
- [99] Y. Zhang, M. Lee, J. Trevelyan, R. Adey, S. Niku, and C. Brebbia, *Acoustic diagnostic analysis of automobile passenger compartments*. Southampton, England: Computational Mechanics Publications,, 2000. [Online]. Available: <http://www.beasy.com>
- [100] A. Pietrzyk, "Computer modeling of the sound field in small rooms," in *Proceedings of the AES 15th International Conference - Audio, Acoustics and Small Spaces*, Copenhagen, Denmark, November 1998, pp. 24–31.
- [101] K. S. Yee, "Numerical solution of initial boundary value problems involving maxwell's equations in isotropic media," in *IEEE Trans. Antennas Propagat*, vol. 14, March 1966, pp. 302–307.

- [102] J. C. Strikwerda, *Finite Difference Schemes and Partial Differential Equations*. Pacific Grove, California, USA: Wadsworth and Brooks, 1989.
- [103] D. Botteldooren, "Finite-difference time-domain simulation of low-frequency room acoustic problems," in *Journal of the Acoustical Society of America*, vol. 98(6), December 1995, pp. 3302–3308.
- [104] L. Savioja, T. J. Rinne, and T. Takala, "Simulation of room acoustics with a 3-D finite difference mesh," in *Proceedings of the International Computer Music Conference*, Denmark, 1994, pp. 463–466.
- [105] L. Savioja, M. Karjalainen, and T. Takala, "DSP formulation of a finite difference method for room acoustics simulation," in *Proceedings of IEEE Nordic Signal Processing Symposium (NORSIG)*, Espoo, Finland, September 1996, pp. 455–458.
- [106] R. Courant, K. Friedrichs, and H. Lewy, "On the partial difference equations of mathematical physics," in *IBM Journal*, March 1967, pp. 215–234. [Online]. Available: <http://www.stanford.edu/class/cme302/classics/courant-friedrichs-lewy.pdf>
- [107] D. T. Murphy, "Digital waveguide mesh topologies in room acoustics modelling," Ph.D. dissertation, University Of York, UK, 2000. [Online]. Available: <http://www-users.york.ac.uk/~dtm3/Download/ThesisTotal.pdf>
- [108] S. Bilbao, "Wave and scattering methods of the numerical integration of partial differential equations," Ph.D. dissertation, Stanford University, USA, 2001.
- [109] S. Bilbao and J. Smith, "Finite difference schemes for the wave equation: Stability, passivity, and numerical dispersion," in *IEEE Transactions on Acoustics Speech and Signal Processing*, vol. 11(3), May 2003, pp. 255–256.
- [110] S. A. V. Duyne and J. O. Smith, "The 2-D digital waveguide mesh," in *Proceedings of the Workshop on Applications of Signal Processing to Audio and Acoustics (WASPAA'93)*, New Paltz, NY, October 1993, pp. 177–180.
- [111] —, "The 3-D tetrahedral waveguide mesh with musical applications," in *Proceedings of the International Computer Music Conference*, Hong Kong, 1996, pp. 9–16.
- [112] J. O. Smith, "A new approach to digital reverberation using closed waveguide networks," in *Proceedings of the International Computer Music Conference (ICMC)*, Vancouver, Canada, August 1985, pp. 47–53.
- [113] M. Karjalainen, P. Huang, and J. O. Smith, "Waveguide networks for room response modeling and synthesis," in *Proceedings of the 118th Audio Engineering Society Convention*, Barcelona, Spain, May 2005, Preprint No. 6394.
- [114] J. Escolano and F. Jacobsen, "A note on the physical interpretation of frequency dependent boundary conditions in a digital waveguide mesh," in *Acta Acustica united with Acustica*, vol. 93(3), may/june 2007, pp. 398–402.
- [115] M. Karjalainen and C. Erkut, "Digital waveguides versus finite difference structures: Equivalence and mixed modeling," in *EURASIP Journal on Applied Signal Processing*, vol. 7, June 2004, pp. 978–989.

- [116] J. O. Smith, III, "On the Equivalence of the Digital Waveguide and Finite Difference Time Domain Schemes," *ArXiv Physics e-prints*, Jul. 2004.
- [117] D. T. Murphy and M. J. Beeson, "The KW-boundary hybrid digital waveguide mesh for room acoustics applications," in *IEEE Transactions on Audio, Speech and Language Processing*, vol. 15(2), February 2007, pp. 552–564.
- [118] J. Huopaniemi, L. Savioja, and M. Karjalainen, "Modeling of reflections and air absorption in acoustical spaces – a digital filter design approach," in *Proceedings of the IEEE Workshop on Applications of Signal Processing to Audio and Acoustics (WASPAA)*, Mohonk, New Paltz, New York, October 1997, pp. 19–22.
- [119] A. Kelloniemi, "Frequency-dependent boundary condition for the 3-D digital waveguide," in *Proceedings of the 9th International Conference on Digital Audio Effects (DAFx '06)*, Montreal, Canada, September 2006, pp. 161–164.
- [120] F. Fontana and D. Rocchesso, "Signal-theoretic characterization of waveguide mesh geometries for models of two-dimensional wave propagation in elastic media," in *IEEE Transactions on Speech and Audio Processing*, vol. 9(2), February 2001, pp. 152–161.
- [121] S. J. Miklavcic and J. Ericsson, "Practical implementation of the 3d tetrahedral tlm method and visualization of room acoustics," in *Proceedings of the 7th International Conference on Digital Audio Effects (DAFx'04)*, Naples, Italy, October 2004, pp. 262–267.
- [122] F. Fontana, D. Rocchesso, and E. Apollonio, "Using the waveguide mesh in modeling 3-D resonators," in *Proceedings of the 3rd International Conference on Digital Audio Effects (DAFx'00)*, Verona, Italy, December 2000, pp. 229–232.
- [123] L. Savioja and V. Välimäki, "Reducing the dispersion error in the digital waveguide mesh using interpolation and frequency warping techniques," in *IEEE Transactions on Speech and Audio Processing*, vol. 8(2), March 2000, pp. 184–193.
- [124] —, "Interpolated rectangular 3-D digital waveguide mesh algorithms with frequency warping," in *IEEE Transactions on Speech and Audio Processing*, vol. 11(6), November 2003, pp. 783–789.
- [125] T. Laakso, V. Välimäki, M. Karjalainen, and U. K. Laine, "Splitting the unit delay - tools for fractional delay filter design," in *IEEE Signal Processing Magazine*, vol. 13(1), January 1996, pp. 30–60.
- [126] L. Savioja and V. Välimäki, "Improved discrete-time modeling of multi-dimensional wave propagation using the interpolated digital waveguide mesh," in *Proceedings of the IEEE International Conference in Acoustics, Speech and Signal Processing*, vol. 1, Munich, Germany, April 1997, pp. 459–462.
- [127] V. Välimäki and L. Savioja, "Interpolated and warped 2-D digital waveguide mesh algorithms," in *Proceedings of the COST G-6 Conference on Digital Audio Effects (DAFX-00)*, Verona, Italy, December 2000, pp. 201–206.

- [128] L. Savioja, "Improving the three-dimensional digital waveguide mesh by interpolation," in *Proceedings of the Nordic Acoustical Meeting*, Stockholm, Sweden, September 1998, pp. 265–268.
- [129] S. Bilbao, *Wave and scattering methods for numerical simulation*. Chichester, England: Wiley, 2004.
- [130] G. R. Campos and D. M. Howard, "On the computational efficiency of different waveguide mesh topologies for room acoustic simulation," in *IEEE Transactions on Speech and Audio Processing*, vol. 13(5), September 2005, pp. 1063–1072.
- [131] L. Savioja and V. Välimäki, "Reduction of the dispersion error in the interpolated digital waveguide mesh using frequency warping," in *Proceedings of the International Conference on Acoustics, Speech and Signal Processing*, vol. 2, New York, March 1999, pp. 973–976.
- [132] —, "The bilinearly deinterpolated waveguide mesh," in *IEEE Nordic Signal Processing Symposium (NORSIG'96)*, Espoo, Finland, 1996, pp. 443–446.
- [133] J. A. Laird, "The physical modelling of drums using digital waveguides," Ph.D. dissertation, Department of Electrical and Electronic Engineering, Bristol University, UK, November 2001.
- [134] D. T. Murphy, C. J. C. Newton, and D. M. Howard, "Digital waveguide mesh modelling of room acoustics: Surround-sound, boundaries and plugin implementation," in *Proceedings of Cost G-6 Conference on Digital Audio Effects (DAFX)*, Limerick, Ireland, December 2001, pp. 198–202.
- [135] D. T. Murphy and J. Mullen, "Digital waveguide mesh modelling of room acoustics: Improved anechoic boundaries," in *5th International Conference on Digital Audio Effects (DAFX-02)*, Hamburg, Germany, 2002, pp. 163–168.
- [136] A. Kelloniemi, L. Savioja, and V. Välimäki, "Spatial filter-based absorbing boundary for the 2-D digital waveguide mesh," in *IEEE Signal Processing Letters*, February 2005, pp. 126–129.
- [137] J.-P. Berenger, "A perfectly matched layer for the absorption of electromagnetic waves," in *Journal of Computational Physics*, vol. 114(2), October 1994, pp. 185–200.
- [138] W. C. Chew and W. H. Weedon, "A 3D perfectly matched medium from modified maxwell's equations with stretched coordinates," in *IEEE Microwave Opt. Technol. Lett.*, vol. 7, 1994, pp. 599–604.
- [139] J.-P. Berenger, "Three-dimensional perfectly matched layer for the absorption of electromagnetic waves," in *Journal of Computational Physics*, vol. 127(2), September 1996, pp. 363–379.
- [140] J. Huopaniemi, L. Savioja, and M. Karjalainen, "Modelling of reflections and air absorption in acoustical spaces a digital filter design approach," in *IEEE Workshop on Applications of Signal Processing to Audio and Acoustics (WASPAA)*, New Paltz, New York, USA, 1997.

- [141] F. Fontana, "Physics-based models for the acoustic representation of space in virtual environments," Ph.D. dissertation, Verona University, Italy, March 2003.
- [142] A. Kelloniemi, D. Murphy, L. Savioja, and V. Välimäki, "Boundary conditions in a multi-dimensional digital waveguide mesh," in *Proceedings of the International Conference on Acoustics, Speech and Signal Processing (ICASSP)*, vol. 4, Montreal, Canada, May 2004, pp. 25–28.
- [143] A. Kelloniemi, "Improved adjustable boundary conditions for the 2-D digital waveguide mesh," in *Proceedings of the Conference on Digital Audio Effects (DAFx-05)*, Madrid, Spain, September 2005, pp. 237–242.
- [144] —, "Improved adjustable boundary conditions for the 3-D digital waveguide mesh," in *Proceedings of the IEEE Workshop on Applications of Signal Processing to Audio and Acoustics (WASPAA-05)*, New York, USA, October 2005, pp. 191–194.
- [145] J. Laird, P. Masri, and C. N. Canagarajah, "Efficient and accurate synthesis of circular membranes using digital waveguides," in *Proceedings of IEE Colloquium on Audio and Music Technology: The Challenge of Creative DSP*, 1998, pp. 12/1–12/6.
- [146] L. Tsang, J. A. Kong, K.-H. Ding, and C. O. Ao, *Scattering of Electromagnetic Waves*. New York: John Wiley and Sons Inc., 2001.
- [147] P. Beckmann, *The Scattering of Electromagnetic Waves from Rough Surfaces*. New York: Pergamon Press, 1963.
- [148] D. Rocchesso and J. Smith, "Circulant feedback delay networks for sound synthesis and processing," in *Proceedings of the International Computer Music Conference*, Aarhus, Denmark, 1994, pp. 378–381.
- [149] J. Stautner and M. Puckette, "Designing multichannel reverberators," in *Computer Music Journal*, vol. 6(1), Spring 1982, pp. 52–65.
- [150] J. M. Jot and A. Chaigne, "Digital delay networks for designing artificial reverberators," in *Proceedings of the 90th convention of the Audio Engineering Society*, Paris, France, February 1991, Preprint No. 3030.
- [151] P. J. Davis, *Circulant Matrices*. New York Wiley, 1979.
- [152] D. Rocchesso and J. O. Smith, "Circulant and elliptic feedback delay networks for artificial reverberation," in *IEEE Transactions on Speech and Audio Processing*, vol. 5(1), January 1997, pp. 51–63.
- [153] R. M. Gray, *Toeplitz and Circulant Matrices: A review*. Hanover: Now Publishers Inc, 2006.
- [154] V. Authors, *Programs for Digital Signal Processing*. New York: IEEE Press, 1979.
- [155] E. W. Weisstein, <http://mathworld.wolfram.com/HanningFunction.html>. Wolfram Research Inc., 2008.

- [156] *Acoustics - Measurement of reverberation time of rooms with reference to other acoustical parameters.*, International Organization for Standardization Std. ISO 3382:2000, 2000.
- [157] A. Reilly and D. McGrath, "Convolution processing for realistic reverberation," in *Audio Engineering Society*, February 1989, Preprint No. 3977(13).
- [158] (Copyright 2005) RPG research. [Online]. Available: <http://www.rpginc.com/research/index.htm>
- [159] P. Cook and G. Scavone, "The synthesis toolkit (STK)," in *Proceedings of the International Computer Music Conference*, Beijing, 1999, pp. 164–166. [Online]. Available: citeseer.ist.psu.edu/article/cook99synthesis.html